Princeton Plasma Physics Laboratory

PPPL-

PPPL-

PPPL
PRINCETON PLASMA
PHYSICS LABORATORY

Princeton Plasma Physics Laboratory
Report Disclaimers

Full Legal Disclaimer

This report was prepared as an account of work sponsored by an agency of the United States Government. Neither the United States Government nor any agency thereof, nor any of their employees, nor any of their contractors, subcontractors or their employees, makes any warranty, express or implied, or assumes any legal liability or responsibility for the accuracy, completeness, or any third party's use or the results of such use of any information, apparatus, product, or process disclosed, or represents that its use would not infringe privately owned rights. Reference herein to any specific commercial product, process, or service by trade name, trademark, manufacturer, or otherwise, does not necessarily constitute or imply its endorsement, recommendation, or favoring by the United States Government or any agency thereof or its contractors or subcontractors. The views and opinions of authors expressed herein do not necessarily state or reflect those of the United States Government or any agency thereof.

Trademark Disclaimer

Reference herein to any specific commercial product, process, or service by trade name, trademark, manufacturer, or otherwise, does not necessarily constitute or imply its endorsement, recommendation, or favoring by the United States Government or any agency thereof or its contractors or subcontractors.

PPPL Report Availability

Princeton Plasma Physics Laboratory:

http://www.pppl.gov/techreports.cfm

Office of Scientific and Technical Information (OSTI):

http://www.osti.gov/bridge

Related Links:

U.S. Department of Energy

Office of Scientific and Technical Information

Fusion Links

Preliminary Physics Motivation and Engineering Design Assessment of the National High Power Torus Experiment (NHTX)*

Laboratory Directed Research & Development (LDRD)
Princeton Plasma Physics Laboratory (PPPL)
Fiscal Year 2007 Final Report
Issued: 29 September 2007
Revised: 8 February 2008

Edited by: R. Woolley

Authors:

C. Gentile
J. Menard
C. Neumeyer
S. Ramakrishnan
T. Stevenson
R. Woolley

Additional Contributors

W. Blanchard
R. Goldston
R. Maingi
S. Kaye
I. Zatz

Preface

In April 2006, Dr. Ray Orbach, Director of the DOE Office of Science, challenged the fusion community to "propose a new facility… which will put the U.S. at the lead in world fusion science." Analysis of the gaps between expected ITER performance and the requirements of a demonstration power plant (Demo) pointed to the critical and urgent need to develop fusion-relvant plasma-material interface (PMI) solutions consistent with sustained high plasma performance. A survey of world fusion program indicated that present and planned experimental devices do not advance the PMI issue beyond ITER, and a major dedicated experimental facility is warranted. Such a facility should provide the flexibility and access needed to solve plasma boundary challenges related to divertor heat flux and particle exhaust while also developing methods to minimize hydrogenic isotope retention and remaining compatible with high plasma performance.

Given this device mission, C. Neumeyer with contributions from others modified a previously developed ST systems code containing the basic physics and engineering algorithms for tokamak design while also including models of the available existing infrastructure at the PPPL site. While a high-performance PMI-focused device obviously need not be sited at PPPL, the PPPL site is sufficient to support the mission, and substantial cost savings could be achieved using the PPPL infrastructure already in place. The systems code was subsequently used in consultation with R. Goldston, J. Menard, and others to scan through parameter space searching for tokamak design points attractive for the proposed facility's high power heat flux plasma boundary physics experimental mission . At the same time, extensive studies of plasma equilibrium by J. Menard were made to identify poloidal field (PF) coil set geometries having the flexibility to provide the full range of shaping needed to investigate different advanced divertor designs.

After multiple scans using this systems code and calculations by other codes focusing in more detail on plasma behavior, and several meetings to discuss options, a preliminary design point was adopted, along with a name: the $\underline{N}$ational $\underline{H}$igh-power advanced $\underline{T}$orus e$\underline{X}$periment (NHTX). The machine features a plasma current of I_p=3.5 MA, toroidal field B_T=2T, major radius R_0=1m, plasma aspect ratio A=1.8, plasma elongation κ=2.7-3.0, plasma duration up to 1000 seconds, and sustained auxiliary plasma heating power of 50 MW. Its plasma current is initiated and ramped to flat top by a unidirectional OH solenoid and sustained non-inductively via neutral beams, radio frequency waves, and bootstrap effects. Its magnet systems use resistive water-cooled coil technology.

A Laboratory Directed Research and Development (LDRD) effort was funded at the 0.67 FTE level to investigate the engineering feasibility in key areas, with the goal of a final report at the end of FY07. Most of the key technical areas on which this report focuses were selected based on their novelty. Unless some confounding issue exists such as high cost, conventional design features applied successfully in past devices do not merit additional attention at this early point in the NHTX design. Instead, new experimental needs requiring solutions different from those used in the past have been studied here to find feasible approaches. The novel features investigated were chosen mainly to address needs for experimental flexibility and for cost control.

Section Authors

MISSION	**J.Menard, C.Neumeyer, R. Woolley**
SUMMARY HIGHLIGHTS OVERVIEW	**C.Neumeyer, R. Woolley**
ENGINEERING	
General Design Philosophy and design overview	**R. Woolley**
Plasma divertor, plasma exhaust, and vacuum pumping	**R. Woolley**
Outer vacuum vessel and inner first wall	**R. Woolley**
Magnets and their structural support systems	**R. Woolley**
Power Systems	**S.Ramakrishnan, C.Neumeyer**
Neutral Beam Injection	**T. Stevenson**
Site Cooling Systems	**R. Woolley**
RADIOLOGICAL ISSUES	**C. Gentile**
CONCLUSIONS AND RECOMMENDATIONS	**R. Woolley**

NHTX Assessment FY2007 R1

Table of Contents

Table of Figures

List of Tables

1   The Mission: Taming the Plasma-Material Interface

1.1   Mission Overiew

During 2007 there was significant effort within the U.S. fusion community through the FESAC priorities panel to identify gaps between the anticipated scientific achievements and fusion performance of ITER and what is needed for a successful demonstration power plant (Demo). The two most prominent gaps identified by the FESAC panel - plasma facing components and materials - fall under the theme of "Taming the plasma material interface". Another FESAC theme is "creating predictable high-performance steady-state plasmas". Importantly, the compatibility of stable steady-state high plasma performance with Demo-level divertor and first-wall heat fluxes and acceptably low tritium retention has yet to be demonstrated. Clearly, such integration requires an interdisciplinary approach involving both plasma physics and materials science. Present and proposed experiments will not explore this realm of sustained and controlled high power and particle exhaust due to insufficient pulse length, insufficient edge heat flux, or both. Recognizing the importance of developing unified solutions to the two research challenges embodied in the FESAC themes above, the National High-power advanced-Torus eXperiment (NHTX) is proposed with a mission to integrate a fusion-relevant high-power plasma-material interface with sustained high-performance plasma operation.

Given the NHTX mission, the methods and technical requirements are as follows:

- NHTX Method: fully diagnose, test, and evaluate PMI concepts, and assess their compatibility with high confinement, high beta, and steady-state operation.

- NHTX Technical Requirements:
  - sustain continuous high plasma heat flux (P/R)
  - operate for many plasma-wall equilibration times – 200-1000s
  - demonstrate exhaust handling, impurity removal, fuel re-injection
  - enable development of low tritium retention solutions
  - internal plasma facing surfaces at high temperature to simulate the first-wall conditions expected in reactors
  - full non-inductive plasma current drive, steady confinement fields
  - easy and rapid change-out of internal plasma-facing components
  - easy and rapid change-out of plasma divertor configurations/options
  - minimize device construction and operating cost

1.2 Physics Design

The fundamental areas needing research are the abilities of advanced divertor configurations to sustain the conditions enabling high overall plasma energy confinement (H-mode) while also continuously absorbing the plasma exhaust's heat, neutralizing its ions, and removing from the vacuum chamber the resulting gas including all of the significant impurities. These capabilities must be tested for long durations at appropriate levels of high heat flux plasma exhaust power. A useful metric for the sustained handling of plasma exhaust heat flux is P/R[†1] , the ratio of total plasma exhaust power P to the major radius R at which the plasma's poloidal divertor concentrates that exhaust. Systems studies (e.g., ARIES) have concluded that for fusion power to be economically competitive, fusion power plants will need P/R ratios near 100 MW/m or more. However, a successful ITER experiment will at best reach a sustained P/R ratio of 24 MW/m while other planned long-pulse experiments (KSTAR, EAST) will only reach 15 MW/m. Thus, the world fusion program's present plans do not include any experimental device capable of investigating sustained plasmas with the high exhaust heat flux intensity needed for fusion after ITER.

If a new facility will be developed to research plasma boundary issues concerning the plasma exhaust, it can and should be used to also investigate related issues. One crucial related issue for DT fusion devices is whether materials surrounding the plasma will absorb and retain excessive inventories of radioactive tritium. The new facility should be capable of isotope retention studies, and its licensed ability to use tritium would support the trace tritium experiments needed for accurate retention measurements. Further, a high first-wall temperature is required to simulate Demo conditions – in particular the impact of wall temperature on hydrogenic retention.

Preliminary systems studies by C. Neumeyer, R. Goldston, J. Menard and others indicated that a quasi steady-state compact experimental device operating at a P/R ratio of 50 MW/m or more could be constructed at PPPL while maximally leveraging the existing powerful infrastructure of US government property remaining from the successfully decommissioned TFTR experiment. For the NHTX mission, small size is a virtue while high fusion gain is unnecessary. Parametric studies including basic physics and engineering algorithms have scanned through ranges of major radius, R, aspect ratio, A, plasma current, Ip, and toroidal field, B_T, to identify designs for which the magnets can be powered, the plasma current can be non-inductively sustained, and the plasmas can without disrupting receive the full plasma heating power available at PPPL at the smallest plasma radius (in order to maximum P/R). Named the National High-power advanced Torus Experiment (NHTX), its parameters are I_p=3.5 MA, B_T=2 Tesla, R=1 m, A=1.8, κ=2.7-3.0, P_{heat}= 50 MW, durations ranging 200 to 1000 seconds. Smaller plasmas would have less capability to accept heat from plasma heating systems, while larger plasmas would challenge the approximately 300 MW site power limit, more than

---

[†] This P/R metric tends to be proportional to the true surface power density of the plasma exhaust, $P/(2\pi R\tau)$, since tokamak experiments show the plasma's power scrape-off layer thickness, τ, is relatively insensitive to machine size and other plasma parameters.

half of which will power plasma heating systems. The NHTX will use deuterium for most of its high heat flux plasma exhaust experiments.   However, although its expected fusion gain is < 1, it could also use tritium within the PPPL site's licensed limits. These limits are sufficient for purposes such as trace tritium experiments measuring hydrogen isotope retention and for short-pulse assessments of plasma instabilities excited by fusion alpha particles.

Details of the output data from the systems code which served as a starting point for the design development is given in Table 1.1 (physics related) and Table 1.2(engineering related).

Table 1.1: Physics Related Design Point Parameters

	DD	DT
R0[m]	1.000	
A_100	1.800	
A	1.871	
kappa	2.739	
delta	0.600	
qMHD	7.865	
qcyl	3.47	
qcyl/qcyl(A)	100.0%	
Ip[MA]	3.500	
Ip*A	6.3	
tflat[s]	1000.000	
tIp[s]	1001.050	
Bt(J)[T]	2.000	
Flux_total	1.86	
Beta_N_thermal	4.4%	3.8%
Beta_N_total	5.0%	5.0%
Beta_N/Beta_N(A)	100.0%	100.0%
Beta_T_alpha	0.0%	0.1%
Beta_T_nbi	2.0%	3.7%
Beta_T_thermal	14.3%	12.5%
Beta_T_total	16.3%	16.3%
Beta_P	141.9%	124.0%
xne[1/m^3]	1.92E+20	1.23E+20
fGW	56.1%	36.0%
fBS	77.0%	67.3%
Tempavg[keV]	3.7	5.1
HH98 (global)	1.30	1.30
Tau_E_98[sec]	0.08	0.07
Q	0.01	0.69
P_fusion [MW]	0.0	30.6
frad	7.8	0.1
Zeff	1.5	1.5
P_Brem[MW]	0.88	0.42
P_rad_core[MW]	0.0	0.0
P_aux[MW]	50.0	44.6
E_nbi[keV]	110	110
Gamma_CD[10^20*A/W-m^2]	0.050	0.068
P_CD[MW]	32.22	21.55
P/R	49	50

Table 1.2: Engineering Related Design Point Parameters

	DD	DT
turnsTF	20	
R_inner_leg_TF	0.287	
drfw[m]	0.100	
Itf[Amp per turn]	500000	
TF_packing	0.76	
Javg_TF_inner [A/m^2]	3.88E+07	
Javg_TF_outer [A/m^2]	5.84E+06	
TF_ripple	0.38%	
R_outer_leg_TF [m]	2.926	
dr_outer_leg_TF [m]	0.497	
dphi_outer_leg_TF [m]	0.345	
turnsOH	846	
Rinner_OH	0.301	
Router_OH	0.344	
Ioh[Amp per turn]	24000	
NSPSSOH	13	
Ioh_SOD[p.u.]	1.000	
Ioh_SOFT[p.u.]	0.000	
Ioh_EOFT[p.u.]	0.000	
OHESW_rated[sec]	0.685	
OH_packing	0.80	
J_OH[A/m^2]	1.31E+08	
P_tf[MW]	88	
P_oh[MW]	0	
P_pf[MW]	37	
P_aux_input [MW]	166	152
W_tf [MJ]	87616	
W_oh[MJ]	16	
W_pf[MJ]	36821	
W_aux[MJ]	165818	152546
P_grid[MW]	300	287
W_grid[MJ]	300535	287262
P_MG[MW]	308	308
S_MG[MVA]	316	316
W_MG[MJ]	1876	1877
W_tot_diss[MJ]	290256	276983
Mass TF_Inner [kG]	10336	
Mass TF_Outer [kG]	172651	
Mass OH [kG]	2810	
Mass PF [kG]	74	
Mass_Total [kG]	183061	

1.3   Fusion Fuel Cycle and Divertor Background

Figure 1.1 shows a block diagram of the flow of fuel and exhaust in a fusion power plant which is intended to help clarify the importance of plasma boundary physics research to fusion power development.
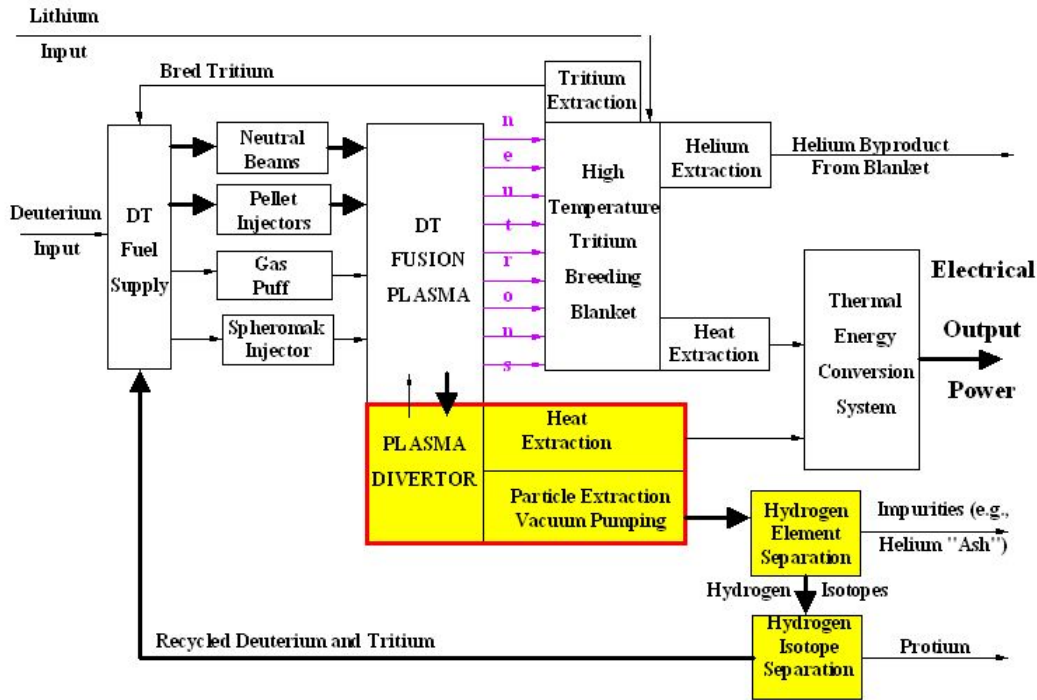
Figure 1.1: Fusion Power Plant Fueling Block Diagram

The large continuous flows through the diagram's loop of blocks colored yellow are a significant challenge for ITER. Solutions for Demo are not presently developed and demand plasma boundary physics research beyond what is now planned. Research is needed on the plasma divertor and its heat and particle extraction systems.

Deuterium and tritium isotopes of hydrogen will be continuously supplied to the thermonuclear plasma by a combination of fuel injection schemes. Some deuterium and tritium nuclei will fuse within the plasma to form an energetic helium ion and an energetic neutron in the D-T fusion reaction,

$$_1D^2 +\ _1T^3 \rightarrow\ _2He^4 +\ _0n^1 + 17.6\,\text{MeV}$$
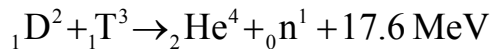
but most will leak from the plasma boundary without fusing. In addition to the main D-T fusion reaction, the following fusion side reactions will also occur in the plasma at rates well below one percent of the D-T fusion reaction rate.

$$_1D^2 + {}_1D^2 \rightarrow {}_2He^3 + {}_0n^1 + 3.27\,\text{MeV}$$

$$_1D^2 + {}_1D^2 \rightarrow {}_2T^3 + {}_1H^1 + 4.03\,\text{MeV}$$

$$_1D^2 + {}_2He^3 \rightarrow {}_2He^4 + {}_1H^1 + 18.3\,\text{MeV}$$
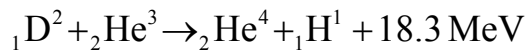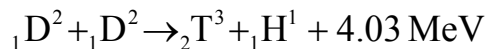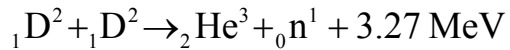
The side reactions can be ignored for many purposes but they will produce small amounts of protium and helium-3. The energetic neutrons produced by fusion will deposit their energy as heat within a surrounding fusion blanket, then will be captured by lithium nuclei there which in turn will immediately split into energetic tritium and helium nuclei, thus depositing even more heat in the blanket. The following nuclear reactions will occur in the blanket. The second of these, which only occurs for collisions with neutrons more energetic than 2.5 MeV, produces a triton without consuming a neutron and thus can boost the net tritium breeding ratio above unity.

$$_3Li^6 + {}_0n^1 \rightarrow {}_1T^3 + {}_2He^4 + 4.8\,\text{MeV}$$

$$_3Li^7 + {}_0n^1 \rightarrow {}_1T^3 + {}_2He^4 + {}_0n^1 - 2.5\,\text{MeV}$$
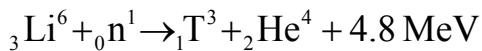
Extraction systems will remove the tritium and helium from the blanket, returning the bred tritium to be injected into the plasma to replace the tritium consumed by fusion while collecting the valuable helium byproduct. Fresh lithium will be supplied to the blanket to replace the lithium consumed by the tritium breeding reaction. Similarly, fresh deuterium will be continuously supplied to the plasma to replace the deuterium consumed by fusion.

All species of ions will continuously leak from the plasma at a rate about two orders of magnitude faster than the plasma's D-T fusion rate. They will be collected by flows in the plasma's scrape-off layer, then swept into the plasma divertor exhaust where they represent an extremely intense heat load for any surface they strike. The ions in the plasma exhaust will next be neutralized and their energy extracted as heat. The resulting flow of neutral atoms will then be pumped from the fusion reactor chamber to a remote location where impurities such as the helium-4 "ash" resulting from D-T fusion and the small amounts of protium helium-3 resulting from side reactions will be separated out. The remaining deuterium and tritium atoms will then be sent together back to the fueling system for re-injection into the plasma.

Thus, D-T fuel will recirculate from fuel injection systems into the plasma, out through the plasma divertor, through a purification system, then back to the injectors. The needed recirculation rate in this loop is not small; it is far greater than the rate at which fuel will be consumed. However, the plasma divertor's significance is not just the fact that it will need to accommodate large flows of fuel, impurities, and heat.   The plasma exhaust will control the main plasma's high fusion gain ability, both because it controls high confinement modes and because it will control impurities. Perhaps the plasma divertor exhaust should be termed the "plasma tail wagging the fusion dog".

Significant progress has been made in developing integrated divertor solutions for ITER utilizing flux expansion and impurity radiation for heat-flux spreading to reduce the peak divertor heat flux to 5-10MW/m². Such heat flux levels are in principle manageable utilizing actively-cooled Carbon Fiber Composite (CFC) tiles as proposed for ITER, but carbon erosion and co-deposition are serious issues for divertor lifetime and tritium retention, respectively. Solid metallic (W or Mo) divertor targets are also viable candidates for handling high divertor heat fluxes, but may also suffer from tritium retention problems in addition to accumulation of high-Z impurities and unacceptable radiation from the plasma core. Liquid metals such as Lithium may provide an integrated pumping and power handling capability, but the low evaporation temperatures of Li may make high-temperature divertor operation challenging. All of the above power handling materials are either marginally acceptable (or undeveloped) for ITER even under steady-state operating conditions, i.e. ignoring ELMs and disruptions which can dramatically increase the transient peak divertor heat flux. DEMO-level peak steady-state heat fluxes can be expected to be approximately 3-5 times higher than in ITER, and there are no demonstrated divertor solutions for this level of power exhaust. Thus, it is clear that DEMO-relevant PMI research is an important missing element in the present fusion research program.

Underlying the importance of this missing research program component is the fact that poloidal plasma divertors and their resulting plasma exhaust are essential to presently envisioned designs for future magnetically confined tokamak fusion reactors. Plasma divertors are crucial because they offer the following two benefits:

1) The overall plasma energy confinement essential for high fusion gain improves substantially when divertor operation is maintained in appropriate regimes;

2) A plasma divertor provides a mechanism to control plasma impurities.

The "H-mode" transition, in which overall plasma energy confinement may suddenly double or increase even more is usually associated with plasmas in which a poloidal divertor is operating, although its occurrence has also been documented in limiter plasmas lacking a poloidal divertor. Although this confinement regime transition is still not well understood, subtle plasma changes in the poloidal divertor region seem to have a controlling role in its inception and termination. Since most fusion power reactor design concepts assume the resulting enhanced energy confinement will always be in effect, they are tacitly assuming plasma divertors will operate continuously at very high plasma power levels in the particular local regime which confers high energy confinement. However, it is not at present known how to operate a divertor to obtain high energy confinement continuously at high power, or indeed whether a way exists.

For steady-state or very long pulse durations, tokamak plasmas act as leaky traps through which particles of both hydrogen isotope fuel and impurities flow. Since all types of atomic species are subject to leakage from a plasma through diffusion-like random walk processes, the key to steady-state plasma impurity control is to prevent exiting particles from immediately recycling back into the plasma. A plasma divertor provides a

mechanism to accomplish that feat by deflecting many of the exiting particles away from the adjacent reflective chamber walls. With an operating plasma divertor, particles exiting the plasma's nest of closed magnetic flux surfaces enter a surrounding "scrape-off" plasma layer in which many are swept by a prevailing plasma flow into the localized fan-shaped plasma exhaust located at the poloidal divertor. After the plasma exhaust particles' heat is removed and they are electrically neutralized, vacuum pumps can remove the resulting gas from the chamber. External systems can then separate the gas by species into the hydrogen isotopes to be continuously re-injected into the plasma versus the impurities to be discarded. However, although the conceptual outline of this continuously operating impurity control scheme may be clear, no actual system has ever been built to do this in sustained real-time operation.

2 Summary Highlights Overview of the NHTX Facility

2.1 Design Point

Parametric studies including basic physics and engineering algorithms[2] performed over a range of major radius, R_0, and aspect ratio, A, have identified an attractive design point maximizing the P/R ratio within site equipment constraints, as summarized in Table 2.1:

<div align="center">

TABLE 2.1: NHTX DESIGN POINT OVERVIEW PARAMETERS

Major Radius, R_0	**1.0m**
Aspect Ratio, A	**1.8**
Plasma Current, I_p	**3.5MA**
Toroidal Field, B_t	**2.0T**
Auxiliary Heating Power, P_{aux}	**50MW**
Pulse Length in D-D	**1000s**
Fusion Power in D-T	**30MW**

</div>

An isometric view of this design point showing magnetic coils and plasma appears in Figure 2.1. Figure 2.2 also shows 3 of the neutral beam auxiliary heaters. Figure 2.3 gives several plasma cross section views, showing flexibility in plasma shape control including variation in flux expansion at the divertor over a range of 3 to 30 times the midplane scrape-off-layer width. Figure 2.4 shows an elevation cross section. The demountable Toroidal Field (TF) system permits Poloidal Field (PF) coils to be located inside the TF bore close to the plasma, a situation which simplifies plasma shape control.
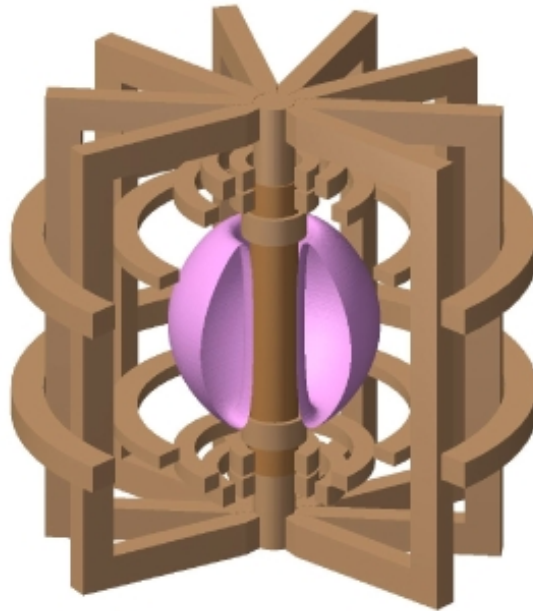
Figure 2.1 - Isometric View of NHTX Design Point Magnet Systems And Plasma

---

[2] C. Neumeyer, Y-K Peng, C. Kessel, P. Rutherford, "Spherical Torus Design Point Studies", PPPL Report No. 4165, June 2006
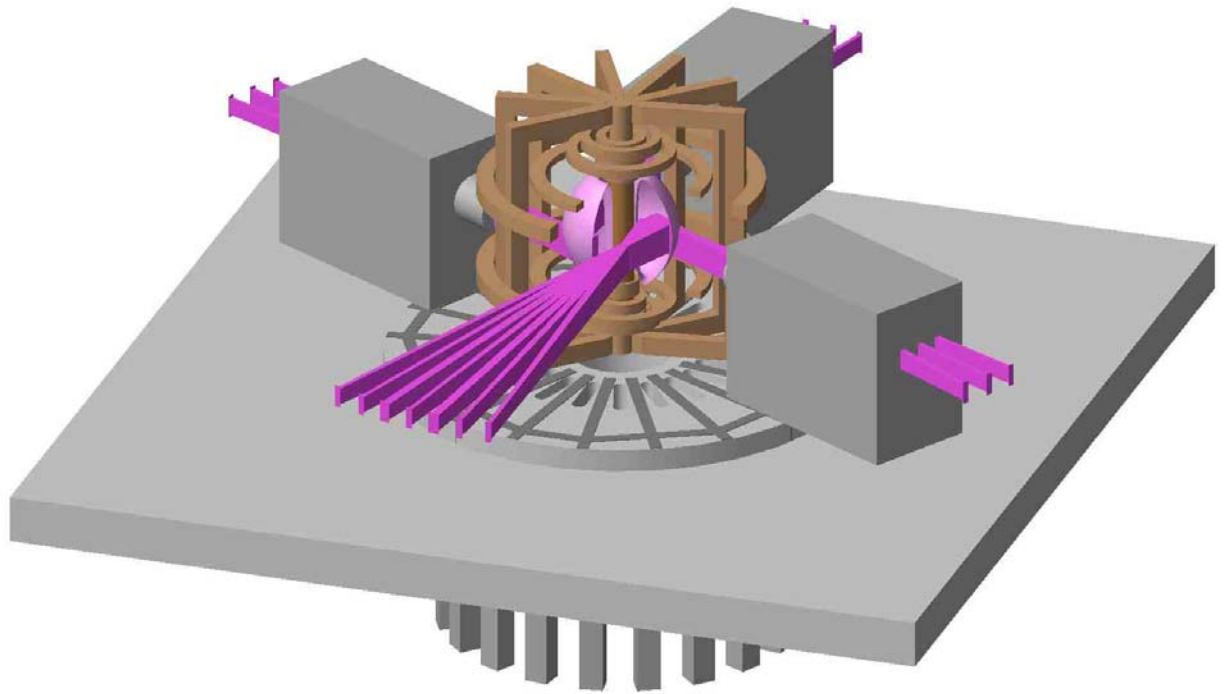
Figure 2.2: Isometric View of NHTX Installed on 102' Pedestal in TFTR Test Cell along with NBI lines, with various injection angles depicted
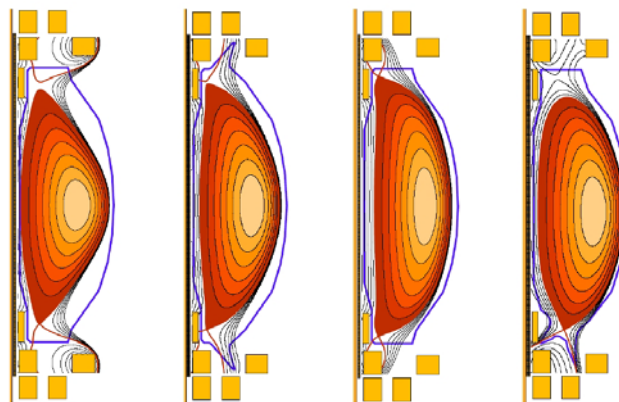
Figure 2.3 - Cross section views of NHTX plasma
showing (l to r) Double Null Divertor (DND) w/negative squareness, DND w/zero squareness, DND w/positive squareness, and ITER-like Single Null Divertor (SND)
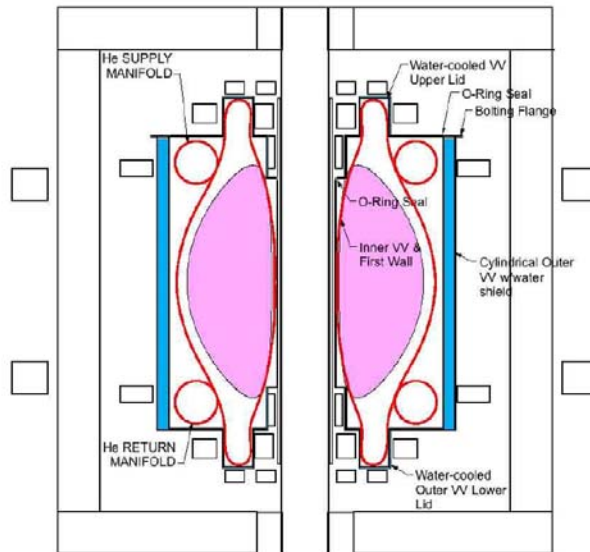
Figure 2.4 – Schematic Cross section of NHTX device

2.2 *Mission elements and chosen design solutions*

The following section highlights the main elements of the mission and the solutions which have been incorporated.

The primary constraint which, along with P/R optimization, led to the adopted design point is the PPPL site limit on power available from the local electric utility company ($\approx$300 MW). Plasmas able to continuously receive higher heating powers, P, within beta limits would need more power to operate their auxiliary plasma heating systems and their water-cooled magnet coils, while plasmas with smaller major radius, R, would suffer reduced confinement and a mismatch with existing neutral beam heating equipment.

High P/R

To maximize P/R the major radius of the machine is to be minimized. This also implies that the radius of the inner core of the device, containing the inner leg of the TF and the central solenoid (CS), should be minimized. For the CS, a limited inductive capability is assumed with a single swing of current to initiate and ramp the plasma current to flat top, with the CS current remaining at zero current for the remainder of the pulse. With this assumption for the CS, and the engineering algorithms in place for water cooled copper TF and PF coils, the systems code parameter scan indicates the minimum major radius which can handle 50 MW of auxiliary heating power occurs at R0=1.0m and that power handling vs. aspect ratio has a peak at A=1.8.

Non-inductive plasma current sustainment

With the CS providing initiation and ramp-up only, NHTX relies on non-inductive current drive (bootstrap, neutral beam injection (NBI), and radio frequency (RF)) for sustainment of the plasma current. To optimize the current drive capability of the NBI, two of the four existing TFTR NBI systems are positioned at the midplane elevation and two are located 25cm below the midplane. In addition, provision is included for adjusting the tangency radius of the beams +/-20cm with respect to the magnetic axis R0.

Long pulse

A 1000 second pulse length is chosen in order to conclusively exceed the equilibration time of plasma-wall interactions. There are several major design implications as follows.

> a. Water-cooled copper coils are used for the TF and PF. For water-cooling of the coils and other components the thermal inertial of a large (~500 kgal) quantity of water is required, which is adequate for the 1000 second pulse length. The water would be stored in a large tank or a tank farm, and cooling towers would be used to reject the heat in the period between pulses, based on a 1 hour repetition period.

> b. The required electrical input power is 300MW which, for the 1000 second pulse length, must be supplied directly from the grid.

> c. Since the TFTR NBI system was rated for short pulses it will require modification to run for 1000 seconds. A plan for this pulse length extension was developed and quantified during the TPX design activity.

> d. To cope with the plasma fueling, exhaust, and recirculation, an advanced system is required, envisioned to consist of multiple turbomolecular pumps of a design immune to high magnetic field, located close to the machine at the entrance to wide ducts at upper and lower ports between TF coil outer legs.

Flexible X-point Divertor Configurations

Multiple inner PF coils are included to provide a wide range of plasma shapes and divertor flux tube configurations.

Provision for Multiple Divertor and First Wall Experiments

The TF inner leg bundle, TF upper radial limbs and PF coils, and top lid of the cylindrical outer VV are removable via vertical crane access. Thus the divertor and first wall/ inner VV are readily removable and exchangeable via access by an overhead crane.

Hot Reactor-Relevant First Wall

The plasma-facing first wall is operated at reactor-relevant temperatures in the range from 300 C to 1000 C using a high temperature heat transfer medium such as helium. It is thermally isolated from the water-cooled 150 C outer vacuum vessel by the intermediate vacuum space plus thermally insulating mounts.

Capability for D-T Operation

The activation/contamination region is limited to the inner VV plus appendages such as the NBI ducts, etc. The ability to remove the inner VV and divertor assemblies by vertical crane is an advantage from a remote handling perspective. A water jacket outside the outer VV, in conjunction with the shielding of the TFTR Test Cell, provides the required neutron attenuation.

Low Cost

Cost is minimized by exploitation of the existing PPPL infrastructure (Test Cell, buildings, electric power, CS/PF AC/DC converters, and NBI). Simple design solutions are sought for the water-cooled copper coils and their support structures, as well as the outer VV.

2.3 Key Design Features

Key design features and summarized in this section, while their detailed developments are described in later sections.

Double Vacuum Vessel

As part of the NHTX mission to investigate plasma-wall interactions under conditions relevant to the design of future reactors, the NHTX first wall must operate at an elevated temperature nominally 600 C but potentially up to as high as 1000 C, substantially higher than prior devices which have operated with first walls as hot as 300 C (e.g. JET). The NHTX design will utilize a cold outer VV with an integral water-cooled jacket and a hot first wall structure, itself a closed toroidal vessel, located within the outer VV, thermally isolated by a small vacuum gap and by structural mounting standoffs constructed of thermally insulating ceramic material and Inconel bolts. An additional important feature of this configuration is that the region within the inner vessel will be sealed from the colder region in the space between the inner and outer vessels, thus eliminating impurity influx from the colder region to the plasma. The NHTX design permits the use of the overhead crane to lower the inner VV into the outer VV after first removing the upper TF/PF coil assembly and outer VV upper lid, such that the first wall can be readily exchanged as part of the experimental program. The structural mounting of the inner

vessel is an important issue since NHTX operations involving D-D or D-T will produce neutrons which will activate the structure causing it to emit gamma rays, and radioactive tritium may contaminate exposed surfaces. Thus, there would be significant radiation exposure to personnel entering the vessel. The solution chosen for NHTX, depicted in Figure 2.5, avoids the need for inner VV entry.
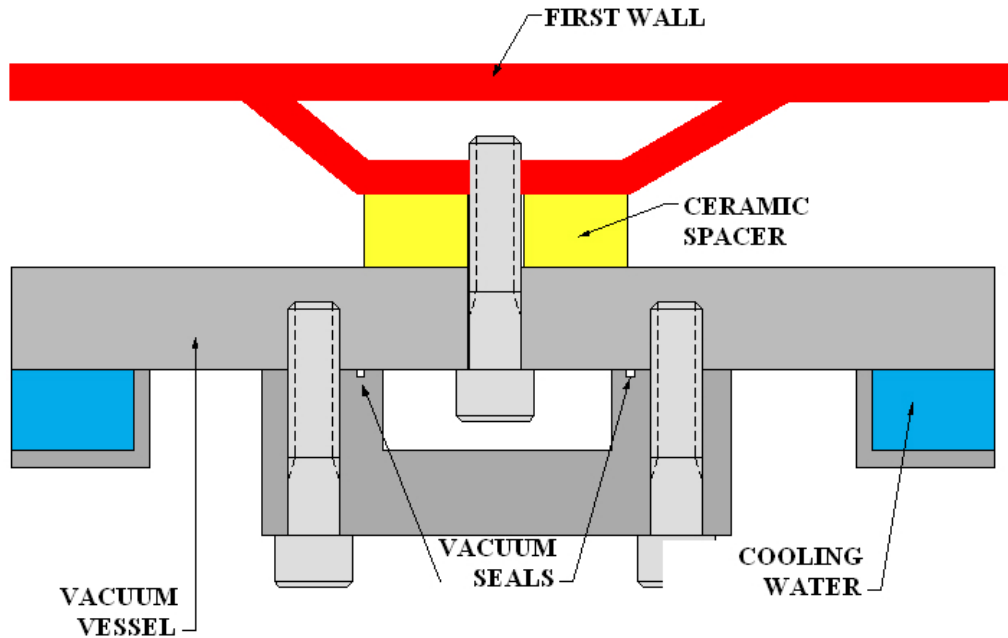
Figure 2.5: Inner VV (First Wall) Mounting Scheme

An additional issue is to provide access to the plasma space for NBI, diagnostics, etc., while maintaining separation of vacuum spaces between the two vacuum regions and allowing maintenance/assembly without personnel access to the inner VV. The NHTX solution is to provide special matching ports on the inner and outer VV as shown in Fig. 5. On the inward end of the bellows, an annular flange is mounted with the annulus extending into the port's cross-sectional area where it is accessible manually from outside. When preparing to change out the first wall these are disconnected, withdrawn from the inner VV and flattened against the inner wall of the outer VV.
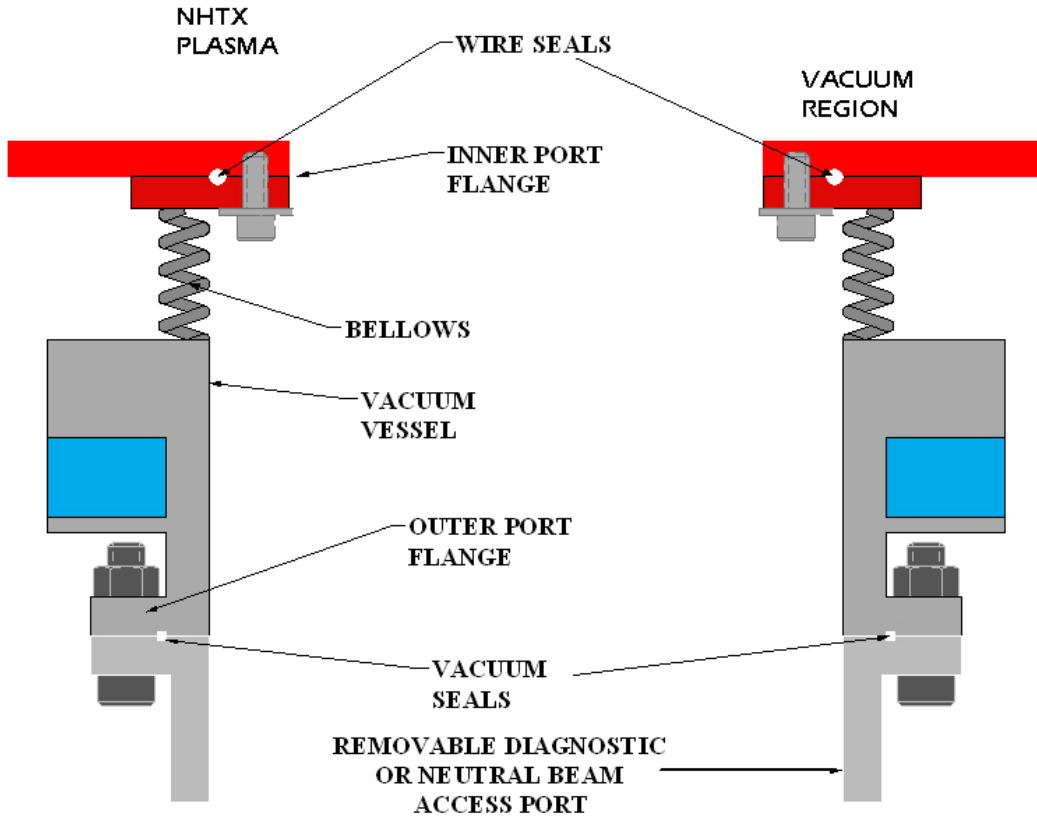
Figure 2.6: Scheme for Mating Ports between Inner and Outer VV

The heating/cooling system for the plasma's first wall will use high pressure helium flowing in many small, parallel tubes welded to the outside of the inner VV.

TF Structural Support
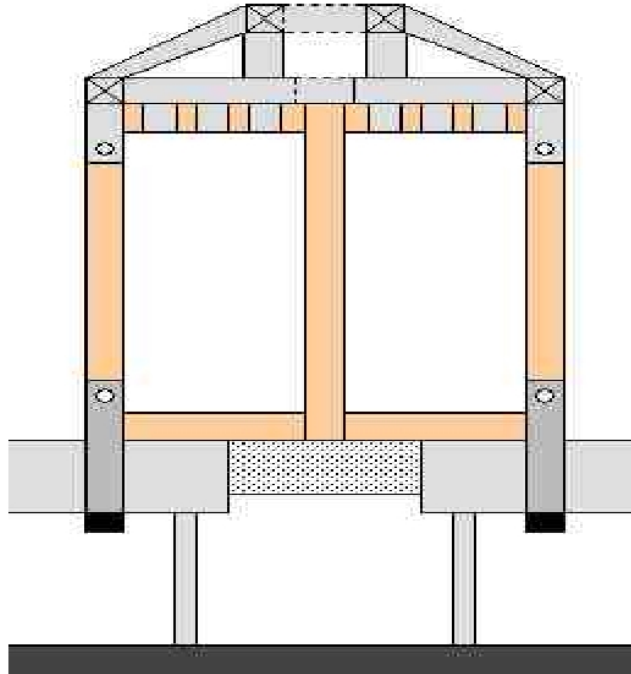
Figure 2.7: Concepts For TF Structural Support (Demountable Top, Existing Floor)
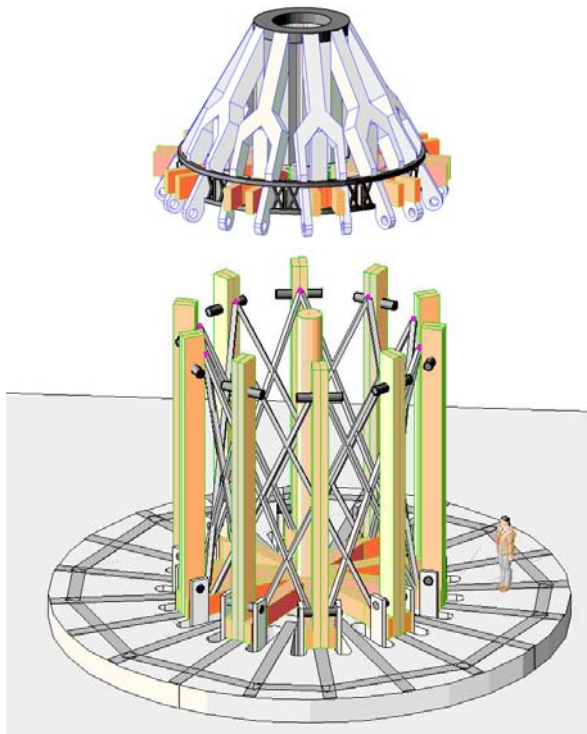
Figure 2.8: Details of Demountable TF Magnet System & Structure, With Umbrella Removed
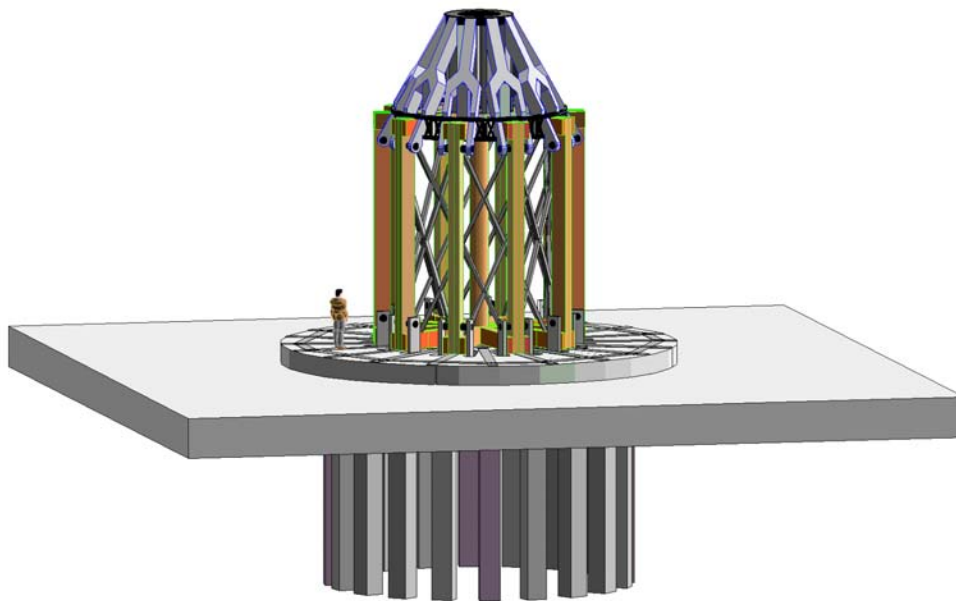
Figure 2.9: TF Magnets And Structure Details In Assembled Configuration

The in-plane magnetic pressure of the TF coil results in vertical forces on the upper and lower radial limbs totaling 23MN. The solution adopted by NHTX is to react those loads via the massive TF outer legs. The vertical forces are transferred to an umbrella structure on the top of the device and to a massive floor beam structure (within the pedestal on which TFTR was mounted). Using clamps and clevis pin joints the loads are transferred from these structures to the vertical limbs where the resultant stress is acceptable due to the massive cross section of the outer limbs. Out-of-plane forces are reacted via external "X" cross braces between adjacent TF outer legs.

TF Joint
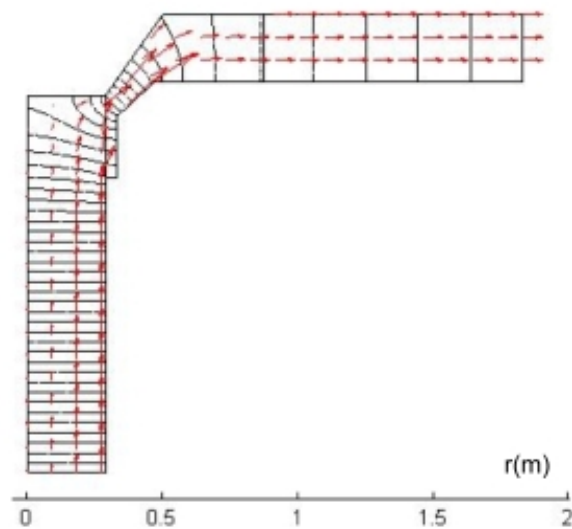
Figure 2.10: Current Flow and Voltage Contours Around Conceptual TF Joint

The demountable TF joint is a challenging aspect of the design, considering the high current, large forces, and thermal displacements. The solution chosen for NHTX is a lap joint which is designed to minimize variations in current density across the joint, to exploit the in-plane magnetic force to close the joint, and to align the pattern of current flow with the flux spilling out of the CS to minimize out-of-plane forces. In addition, by matching the thermal growth of the TF central bundle with the outer legs, issues due to differential expansion are minimized.

Coil Cooling

The TF and PF coils require aggressive water-cooling and will reach equilibrium temperature distributions in a time period much less than the 1000 second pulse length. The TF inner bundle will utilize multiple parallel cooling passages per turn. Each wedge shaped turn will be constructed from two pieces with milled grooves. Copper tubes will be placed in the grooves and the pieces joined by soldering.
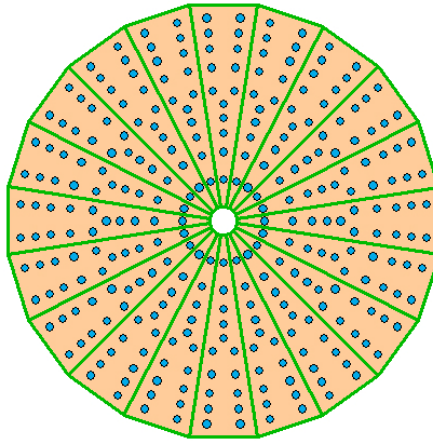
Figure 2.11: Midplane Cross Section of Inner TF Bundle

The PF coils can be cooled using conventional conductors extruded with internal cooling passages. However, for steady state water cooling, the maximum single water path length has to be limited to a small fraction of the total number of turns per coil. Therefore multiple cooling paths are required per coil. To obtain access to the multiple cooling path inlets and outlets the coils need to be wound with multiple conductors in hand.

A different PF coil design is also feasible in which each coil is implemented as a set of double-pancake subcoils wound from edge-cooled copper strip, with horizontal aisle gaps spatially separating the subcoils in order to provide external access to cooling paths. A cooling tube can be soldered into a groove machined into the strips' edges. This approach provides more coolant path access (e.g., half-turn) but sacrifices more conductor space for that access. Each of these two feasible steady-state designs has its advantages and disadvantages, so a detailed comparison of them for each PF coil must be carried out to choose the best.
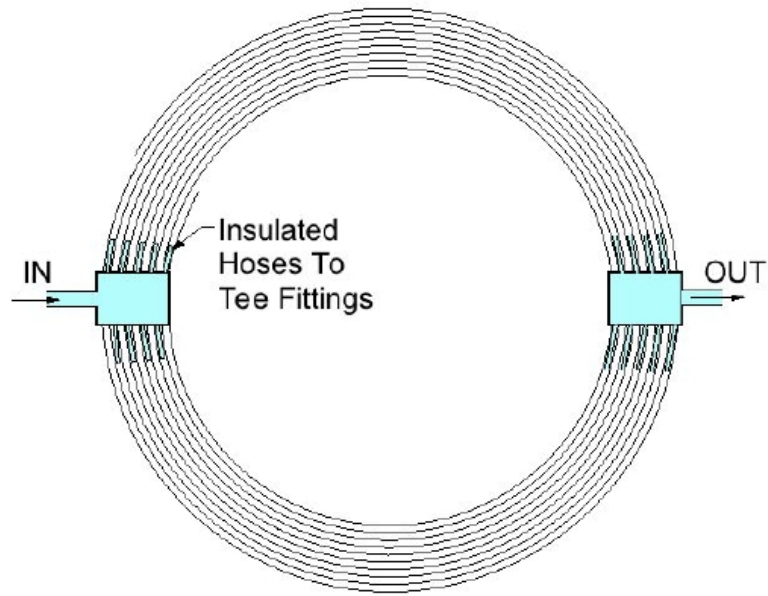
Figure 2.12: Optional Half-Turn Cooling Scheme for Outer PF Coils

Power Systems

Based on discussions with the local utility grid operator it was determined that 300MW of power could be obtained from the grid. The concept for the power supply system puts the relatively quiescent loads (TF and auxiliary heating) on the grid and the dynamic pulsed loads (CS and PF) on one of the two existing MG sets as summarized in Table 2.2.

<p align="center">**TABLE 2.2: NHTX DESIGN POINT POWER REQUIREMENTS**</p>

	Ramp (MW)	Sustainment (MW)
TF	96	88
CS	308	0
PF	100	37
Auxiliary Heating (NBI & RF)	0	166
Balance of Plant	10	10
Total MG	408	37
Total Grid	106	300
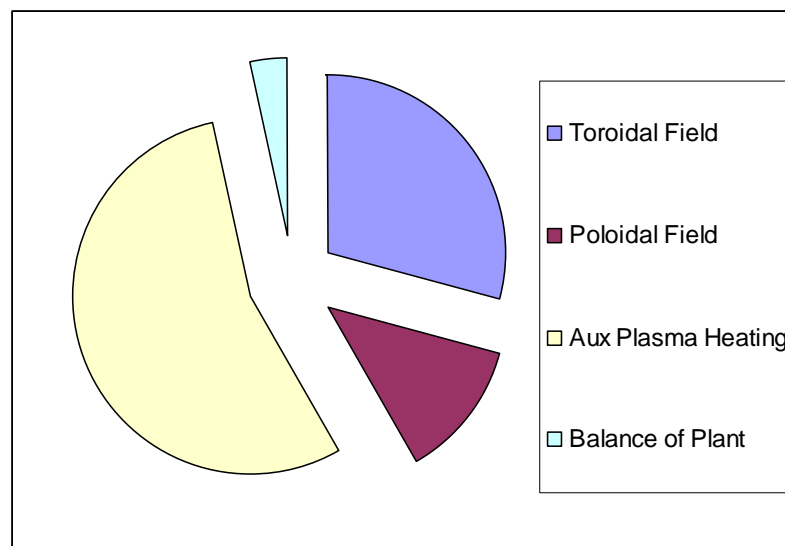
Figure 2.13: Design Point Electrical Power Requirements

To simplify the TF coil construction it was decided to minimize the number of turns (20) and use a very high current TF power supply (240V, 500kA) located close to the machine. For the CS and PF power supplies, existing AC/DC converters at PPPL can be reconfigured in series and parallel as required to supply the loads for 1000 second pulses, repeated once per hour. To take 300MW from the local 138kV grid connection, a combination of switched capacitors and Static Var Compensation (SVC) will be used for reactive compensation.

If the fusion community had a single vision of the future successful advanced divertor and associated first wall design, then a specialized experimental facility could be tailored

specifically to test it. However, that is not the present situation. In truth there are many proposed divertor and first wall design concepts advocated by different groups participating in fusion research. Although at present none are being adequately tested, a single facility dedicated to testing just one of them would be both inconclusive in finding the best solution and also potentially wasteful in its use of research monies. Therefore it is important that a new facility for research on fusion relevant plasma boundary physics be able to examine multiple advanced divertor and first wall concepts during its operating life. The NHTX should be designed with high heat flux sustained plasma experimentation as its primary objective, and it should also incorporate special features giving it the flexibility to efficiently conduct multiple experiments on multiple advanced divertor concepts. Beyond the obvious technical merits of such flexibility, it may be the only way to achieve a broadly supported consensus across the fusion community.

It is also important that a facility to research fusion relevant plasma boundary physics should be attractive from a cost perspective. The competition for research funds is fierce and seems likely to remain so in the near future even after ITER funding has peaked. The argument against such a facility that it could be delayed until later will certainly be made by research funding competitors outside fusion. Since ITER will itself provide some results on sustained high heat flux plasma divertor exhaust, and since results from a new facility experimenting with significantly higher P/R will not be used until later, i.e., for CTF or DEMO projects starting long after ITER has begun operations, funding competitors will claim that fusion can wait. The counter to their claim should be that the new facility will not cost much because it maximally leverages equipment which the US government already owns. Furthermore, funding delays would cause these present site credits to lose their value through depreciation, obsolescence and loss of the institutional expertise to maintain them, thus increasing the cost of researching plasma boundary physics later.

3   Engineering

3.1   General design philosophy and design overview

The sustainment of long duration quasi-steady tokamak plasmas has been an objective of research for many years. It has been shown that the most obvious difficulty, i.e., the sustainment of the plasma's toroidal current by non-inductive means, can be overcome by appropriately injected neutral beam particles, by properly launched radio frequency (RF) plasma waves, and by internal plasma current "bootstrap" effects arising during plasma heating. These techniques have been used in the past and can be successfully applied on the NHTX experiment. Although non-inductive sustainment of the full NHTX plasma current will not be easy and will be a significant design issue, the fact that plasma current has been non-inductively sustained before, albeit for short durations, justifies ignoring it in the present assessment. However, it will be necessary to upgrade the existing complement of neutral beam systems to allow quasi-steady-state long pulse neutral beam operation, and this upgrade is discussed in detail herein.   Most of the steady plasma heating power will be provided by the neutral beams, although some will be provided by RF systems.

Another aspect of long duration plasma maintenance includes maintaining its density by extracting the plasma exhaust particle flow and providing fresh hydrogen isotope fuel. Plasma exhaust schemes are the very subject of the facility's research, so the NHTX design must not limit investigations into different alternative approaches. However, there are not many physically possible ways to continuously pump the large flows of plasma exhaust particles, so they are discussed in detail herein.   Cryopumps at liquid helium temperature may not work well if located close to the intense radiation of a thermonuclear plasma, and their need for periodic regeneration in essentially a batch process would introduce problems for continuously operating fusion power plants. Today's commercially available turbomolecular pumps seem ideal except for the fact that they cannot be used in strong magnetic fields. Neither type of pump is adequate if located remotely from the plasma at the end of a long pumping duct.

The best approach for fusion power may be to develop turbomolecular pumps which will work in strong magnetic fields and to locate them adjacent to the fusion reactor's divertor. This turbomolecular pump technology development is certainly possible as evidenced by publications discussed in the later section of vacuum pumping, but at present industry has no market incentive to proceed without external funding. Alternatively, there may be a holistic solution for fusion power reactors in which free surfaces of flowing liquid lithium in the divertor chamber simultaneously provide both heat removal and most of the pumping.   The NHTX device provides an opportunity to experiment with both of these approaches. However, since the radiation environment of the NHTX will be far less than the radiation in a fusion reactor, it will also be feasible to locate liquid helium cooled cryopumps near its plasma divertor.   On the other hand, there will not be sufficient space around the NHTX vacuum vessel to attach pumping ducts large enough to accommodate its continuous particle flows using remotely located pumps of either type.

Continuous plasma fueling in the NHTX is expected to be done primarily by neutral beams, and by periodically injected frozen hydrogen pellets, but if necessary could be augmented with gas puffing. These systems are not novel, so they are ignored in the present document.

Yet another aspect of tokamak plasma sustainment is that the toroidal and poloidal field systems must operate continuously for pulse durations of up to 1000 seconds. Such continuous magnet operation in tokamaks has in recent years been pursued through the use of superconducting windings. However, for a variety of reasons the NHTX will not use superconducting windings but will instead use water-cooled normal resistive electromagnets. Resistive magnets operating near room temperature are less expensive to construct, require less thermal insulation and less radiation shielding, do not require long time periods for cool-down and warm-up, are utterly free from destructive "quench" events, and can be made demountable with internal electrical joints, thus providing superior access for experiment modifications or repairs. Water-cooled steady-state magnets are by no means new, having been used for various industrial purposes for more than a century. However, their use in long-pulse quasi-steady-state tokamaks along with demountable joints is new and is examined in some depth herein.

Maintaining the NHTX plasma for durations of 1000 seconds by the continuous use of high powered neutral beams, radio frequency systems and resistive magnetic field systems will require about 300 Gigajoules of electrical energy, far exceeding the 4.5 Gigajoule combined energy storage ratings of the motor-generator flywheel equipment remaining from the TFTR experiment. The plan for NHTX is to draw that power in real-time from the local electrical utility company, which has been consulted to determine necessary equipment additions. Although this is conventional engineering, it requires the active agreement and participation of an external organization but is absolutely essential for the NHTX. The electrical power system upgrade is therefore addressed in detail herein. The plan includes some off-site modifications and the installation of a new substation at PPPL's D-site to directly power both the neutral beams and a new high current dc power converter for the NHTX TF system. Existing thyristor rectifiers will operate the NHTX PF coil system from an existing motor-generator power source with some energy augmentation from the new substation.

Perhaps the most significant new requirements are that the plasma facing surfaces must operate at very high temperatures and that there must be sufficient flexibility to change-out those surfaces in order to experiment with different divertor schemes. The change-out process must be quick and easy such that its costs in terms of technician radiation exposure, schedule, and direct expenditures will not inhibit multiple sequential experiments involving different divertor and first wall concepts. Since it is not clear what the best plasma facing surface temperature will turn out to be, the facility needs to be able to experiment with a range of different controllable temperatures. The low end of that range is around 300 C while the high end may be 1000 C. At present it is expected that 600 C will be a frequent operating temperature.

No magnetically confined plasma device has ever before operated with such high temperature surfaces facing the plasma on all sides. Also, no experimental facility has ever before had the capability to quickly change out its plasma facing surfaces to replace them with an entirely different design. These are indeed novel requirements and they receive significant attention herein. The novel approach identified that meets both of these needs is to provide a water-cooled vacuum vessel with a removable upper lid and to provide a separate toroidal first wall capable of high temperature operation, to be inserted into the vacuum vessel from above using an overhead crane. Thermal insulation for the high temperature toroidal first wall is then provided by the vacuum space gap separating the two nested structures and by mounting standoffs that are thermally insulating. First wall change-out is accomplished by reversing the first wall's installation sequence, and it is made easy and quick by employing special fastening features. Adopting this approach requires that some new coupling schemes be used for external vacuum connections and it also increases the importance of quickly demountable TF system electrical joints.

The 50 MW cooling system for the very high temperature first wall, which must also provide heating to maintain its high temperature during the time intervals between successive plasma operations, is a completely new requirement. It gets substantial attention herein starting with a list of alternative ways to accomplish it. All of the possibilities make use of tubing attached to the side of the first wall facing away from the plasma to carry a heat transfer substance implementing forced convection, but they differ in the choice of that substance. This work tentatively adopts the use of high pressure, high temperature helium, and preliminary design calculations sizing the required helium systems are included. Unfortunately, the finding is that although such a system is likely feasible, its high pumping requirements make it quite expensive. It may be possible to dramatically reduce its cost by increasing the space allocated to helium flow tubes at the expense of another subsystem's allocated space, but that tradeoff has not yet been investigated.

To provide quick and easy demountability, NHTX high magnetic field TF electrical joints are not pierced by bolts requiring meticulously calibrated torques but instead are specially shaped so that the magnetic pressure from the toroidal field itself forces them closed. External clamps driven by high pressure gas cylinders provide additional closing forces important at low current. Special sizing of support structure members tailors their elastic compliance so that shear forces on the high magnetic field joints are minimized.

To reduce cost, the support for TF system electromagnetic forces relies on the massive pedestal steel and concrete structure remaining from the TFTR experiment, with minimal additions. Massive copper conductors used in the TF system to reduce resistive losses also serve as structural members wherever feasible.

Steady heat removal from TF and PF system conductors through water-cooling is accomplished by using many cooling water flow paths and keeping them short. This document examines construction layout details for each of these components. Local water manifolds on each component are essential to limit complexity when so many water connections are used. Although the design and construction of most TF and PF

components appears straight-forward, fabrication of the TF Central Bundle is less so. It appears feasible but may be difficult to construct.

The present PPPL site capability to absorb heat in cooling water does not extend to 300 MW for 1000 seconds once per hour for an eight hour day. The necessary upgrade includes very large water storage tanks, water pumps, and cooling towers. This is conventional engineering with no hidden pitfalls and so is only briefly outlined herein.

3.2 Plasma divertor, plasma exhaust, and vacuum pumping

Divertors are intended to boost energy confinement in the core plasma so that fusion reactors can be smaller than they would otherwise need to be with the "L-mode" confinement regimes typically occurring without divertors. Divertors also permit actively cycling the flow of exiting fusion fuel particles continually leaking from the plasma's edge through an external system rather than letting the particles passively recycle back into the plasma after reflective impacts on the vacuum chamber's walls. Directing the exiting particles through an external system before re-injecting them into the plasma provides the opportunity to remove impurities from the hydrogen isotope fuel. Such impurities include the helium "ash" resulting from fusion and heavier nuclei resulting from wall interactions.

Conditions in the high temperature cores of fusion reactor plasmas where most fusion reactions will occur are quite sensitive to conditions in the divertors, which must therefore be operated in regimes consistent with good plasma core performance. However, there are complicated requirements and constraints on divertor operation, so integrated, reactor-relevant solutions are sought. Fusion reactor divertors must receive and accept the thermonuclear plasma's intense plasma exhaust heat flow while also maintaining "H-mode" energy confinement in the plasma core and providing the pumped exhaust particle flow needed for sustained control of plasma impurities. Technologies used to implement divertors in fusion reactors must be consistent with acceptably low tritium inventories, and they should not require too frequent replacement of plasma facing components damaged in operation due to erosion or other mechanisms. Additionally, in a practical fusion reactor the fraction of output power fed back to operate the divertor and associated plasma exhaust purification and fuel recycling systems must be kept small.

The NHTX will be a test-bed to experiment with different advanced divertor schemes proposed to address plasma exhaust handling issues in subsequent fusion reactors. Different experiments testing different advanced divertor concepts will include their own systems to accommodate particles and heat loads. However, to maximize flexibility, NHTX systems should in principle be available as backup accommodating particles and heat loads if the specific systems being evaluated experimentally fail to perform as hoped. Therefore, the basic NHTX infrastructure will include equipment for vacuum pumping and for divertor/first wall heat removal.

3.2.1 Divertor particle flow vs. vacuum pumps and ducts

A plasma divertor collects and focuses into localized plasma exhaust fans the flow of atomic particles exiting the entire external surface of the plasma. For example, estimates have been made that a NHTX deuterium plasma with a volume of V=15.44 cubic meters could have an average density of $n=1.26*10^{20}$ atomic nuclei per cubic meter and an average "particle confinement time" of $\tau_p=0.45$ seconds. These are uncertain and approximate estimates but assuming their correctness, then the total leakage flow rate of particles exiting the plasma would be

$$nV/\tau_p=(1.26*10^{20})(15.44 \text{ m}^3)/(0.45 \text{ s}) = 4.33*10^{21} \text{ deuterium nuclei per second.}$$

A fusion power reactor will have a longer particle confinement time than the NHTX but will be larger with a more massive plasma, so its total leakage particle flow rate may be similar.

In terms of mass, this NHTX plasma exhaust flow rate would be 0.0144 grams per second. If the flow is not immediately recycled back into the plasma but instead is externally stored, then the amount of deuterium used over a 1000 second NHTX plasma operation would amount to a total of 14.4 grams. Under standard temperature pressure conditions this 14.4 grams of deuterium gas would fill a volume of 161.3 liters. Although these values may seem modest, a significant problem for fusion arises because of the high pumping requirements they impose and the difficulty of satisfying those requirements using existing technology. Significant pumping speeds are required since neutral densities in the divertor must be kept far lower than the standard atmospheric temperature-pressure Loschmidt density of $2.687*10^{25}$ molecules/m^3. If the density of neutrals at the divertor target is allowed to become too large, the overall energy confinement of the plasma core will not be maintained in a high energy confinement regime. Continuing the example, the vacuum pumping speed would need to exceed $(4.33*10^{21}/\text{s})/(10^{20}/\text{m}^3)=43.3$ m^3 /s =43,300 liters per second to keep the NHTX Divertor's deuterium neutral density below $10^{20}/\text{m}^3$. This very high vacuum pumping speed roughly matches the pumping speed of the ring cryopump system installed within the DIII-D vacuum vessel [Wesson].

A fundamental problem is that existing high speed vacuum pumping technologies cannot be deployed adjacent to the divertor of a fusion power reactor because magnetic, thermal, and radiation aspects of the reactor are incompatible with locating them there. On the other hand, even the best vacuum pumps become ineffective when deployed remotely from the divertor at the end of a long pumping duct.

3.2.2 Vacuum pumping considerations

Pumping speed and its relation to pumping duct conductance underlie the problems of divertor density control. The effective pumping speed of a combined duct and a pump located at the remote end of the duct is given by

$$S_e = \frac{CS_p}{C + S_p}$$

where S_e is the effective pumping speed of the combination of pump and duct, S_p is the actual pumping speed of the pump without the duct, C is the conductance of the duct, and all three of these quantities have consistent units of volume per unit time. This relation implies the effective combined pumping speed through a pumping duct will be less than either the pump's rating or the duct's conductance, whichever is less. It also hints that it is not useful to increase a vacuum pump's rating far beyond the conductance of its connecting duct since that increase may be costly but will provide little benefit in terms of improved pumping speed.

The conductance of a circular duct of length L and constant diameter D is given by the following approximate dimensional formula [Roth]:

$$C = 0.381 \sqrt{\frac{T}{M}} \left(\frac{D^3}{L + 1.33D} \right)$$

where C is the conductance in m³/s, L and D are in meters, T is the gas temperature in Kelvins, and M is the molecular weight of the gas in atomic mass units. For helium or deuterium gas (M=4) at a temperature of 20 C, this becomes

$$C = 3.261 \left(\frac{D^3}{L + 1.33D} \right)$$

Constant duct conductance contours are graphed versus duct length and diameter in the following plot, which was generated using the MATLAB computational cell .of Appendix A section 1.1.
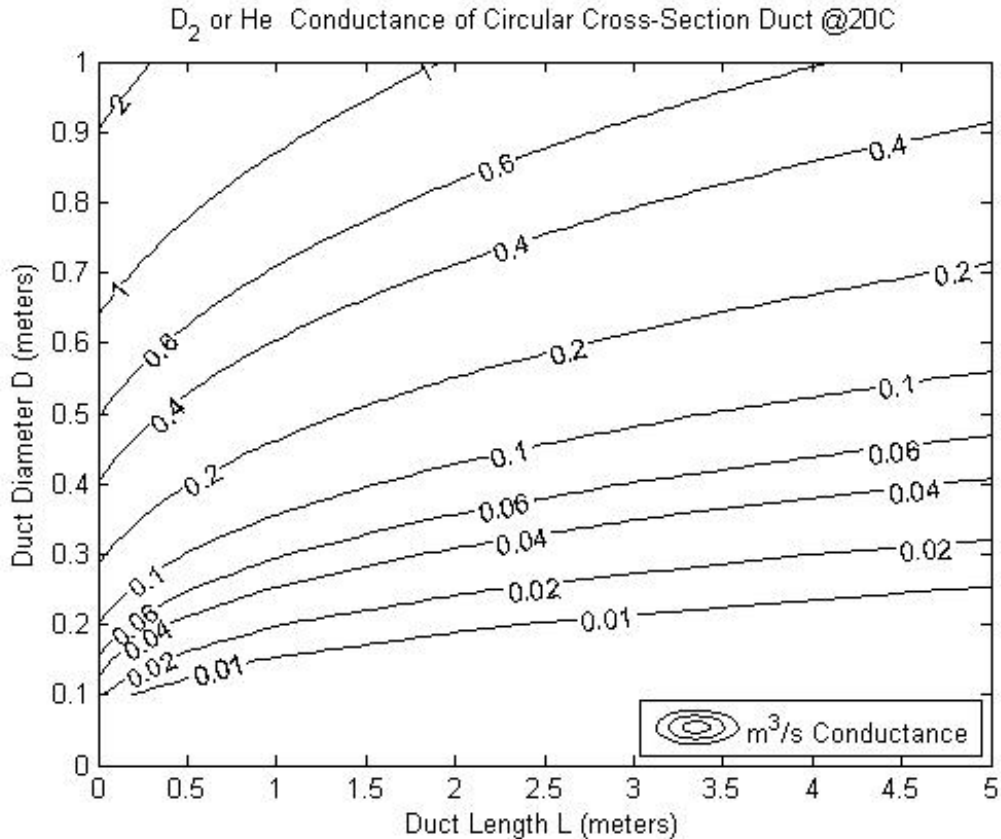
Figure 3.2.1: Pumping Conductance Vs. Duct Geometry

For example, a pumping duct with L=3 meters (i.e., about 10 feet length) and D=0.3 meters (i.e., about 1 foot diameter) has a room temperature deuterium conductance of only C=0.0259 m^3/s =25.9 liters per second. If a powerful high speed high vacuum pump rated at, say, 43,300 liters per second were deployed at the end of this duct, the effective pumping speed of the combined pump and duct together would remain slightly less than 25.9 liters per second. This illustrates the fact that ducts are a limiting factor for divertor pumping.

The flow of rarified gas through any duct is proportional to the difference between the gas pressures at the duct's two ends. In a high vacuum environment the pressures at both ends of a duct are very small, so the flow through the duct is similarly small. This is the fundamental reason that high vacuum pumping ducts are a severe bottleneck. In contrast to high vacuum pumping ducts, the forelines (also known as backing lines) which connect high vacuum pumps to backing pumps typically operate at higher pressures of 100 millitorr or more, so they are capable of developing a much higher pressure difference between their two ends. As a result, forelines may be long with comparatively small diameters without becoming a pumping bottleneck.

To attain higher divertor pumping speeds than permitted by ducts it is necessary both to use a high speed pumping technology for the high vacuum pumps and also to locate high vacuum pumps adjacent to the divertor without any significant duct length. .

Cryopump technology today provides the highest commercially available high vacuum pumping speeds in hydrogen. It also has been selected for use in the ITER program. However, it has deficiencies which make it an imperfect and clumsy choice for a fusion power reactor.

First, the high hydrogen pumping speed advantages of cryopumping require that the liquid helium cooled surfaces be located inside the vacuum vessel near the divertor, but the high temperature and intensely penetrating neutron and gamma ray flux of an operating fusion reactor makes that location impossible for liquid helium. On the other hand, the hydrogen pumping speed advantage of cryopumps would largely disappear if the pumps were instead located outside the vacuum vessel at the end of long, low-conductance pumping ducts.

Second, although cryopumps which use liquid helium to condense and freeze gases do indeed immobilize hydrogen isotopes well, they are less effective with the helium "ash" that will result from fusion, both in pumping speed and in capacity before saturation. Helium does not freeze on cold surfaces as does hydrogen and other gases. In order to pump helium, cryopumps must incorporate additional high surface area porous materials such as charcoal or zeolite which adsorb the helium as a surface monolayer in a process called 'cryotrapping' [Roth]. Helium has also been cryotrapped within argon frost, but measurements indicate a sticking coefficient of only 0.03 and more than 30 argon atoms per helium atom in the frost. Hydrogen and higher freezing temperature molecules can also interfere with helium adsorption making pumping unstable.

Third, cryopumps inherently operate in a batch mode rather than in the continuous operating mode of a fusion reactor, which is the focus of study in the NHTX.   Batch cryopump operation is adequate for a short pulse low duty cycle plasma experiment like DIII-D since plasma pulses can be halted during cryopump regeneration.   For a continuously operating fusion reactor, periodically halting the reactor to regenerate vacuum cryopumps is unacceptable.   Batch operated cryopumps would need to be replaced by a complex system of multiple cryopumps operating sequentially in separate chambers with timed valves for cyclic regeneration of one pump while others continue operating.

Fourth, cryopumps are inefficient in their use of energy. Exiting plasma ions may carry 10 eV or more energy as they are neutralized at their target, corresponding to temperatures above 100,000 Kelvins. The resulting neutrals may be significantly hotter than room temperature. Neutral gas freezing onto a cryopump's chilled surface transfers essentially its entire thermal energy into the cryopump's liquid helium coolant. The liquid helium also receives additional thermal energy arising from radiation, including nuclear radiation, and arising also from unavoidable heat leaks into the system. Removal of that acquired heat from the helium loop then requires vastly more electrical energy be

supplied to operate the helium refrigerator. The ideal thermodynamic limit requires that (300 K/4 K)=75 times as much electrical energy be supplied, but the limitations of practical equipment raise the ratio to several hundred. Since there will be a sustained flow of fuel in which each hydrogenic atom cycles through the plasma and the pumping system many times before fusing, a system based on cryopumps could consume excessive electrical power.

Although cryopumps may be a poor choice for fusion reactors, it would be possible to use cryopumps on the NHTX which will not generate very much fusion power. However, since the mission of NHTX is to look for reactor-relevant solutions to the plasma boundary physics issues concerning plasma exhaust, it would be better if the NHTX used an exhaust pumping scheme which extrapolates well to a fusion power reactor.

Turbomolecular pumps may provide a better pumping alternative for fusion power. The only deficiency of turbomolecular pumps is their susceptibility to magnetic fields. Turbomolecular pumps provide approximately the same pumping speed for helium as they provide for deuterium. They do not employ cryogens so in principle they could operate in a high radiation environment. They operate continuously so they do not introduce issues concerning batch cycling. They are also energy efficient.

The largest commercially available turbomolecular pumps individually develop pumping speeds in deuterium or helium of about 6,000 liters per second, i.e., about 6 m^3/s. As few as seven of these pumps operating in parallel could in principle provide about the same pumping speed for deuterium as the DIII-D ring cryopump mentioned earlier while also providing a similar pumping speed for helium. However in reality, commercially available turbomolecular pumps are adversely affected by magnetic fields. Typical manufacturer's guidelines restrict ambient magnetic field strength at the pumps below 50 gauss. Therefore, each pump must either be very well shielded magnetically or located far enough away from the magnetically confined plasma that the magnetic field at its location is weak.

Past practice in fusion research has usually located turbomolecular pumps remotely from magnetically confined plasmas. For a pump to be outside the TF region implies a pumping duct length of several meters, and even more pumping duct length could be needed to attenuate poloidal fields. For past and present experiments involving brief plasma durations followed by long times between pulses, there may be sufficient time between the plasmas to pump out the gas through long pumping ducts before the next pulse begins. However, this will not be adequate for continuous plasma operation. Locating turbomolecular pumps (or any type of pump, for that matter) remotely from the tokamak at the end of long pumping ducts greatly reduces their effective pumping speeds. For a large turbomolecular pump with pumping speed 6 m^3/s deployed at the end of a duct, constant contours of effective pumping speed at the vacuum vessel are graphed versus duct length and diameter in the following plot, which was generated using the MATLEB computational cell .of Appendix A section 1.2.
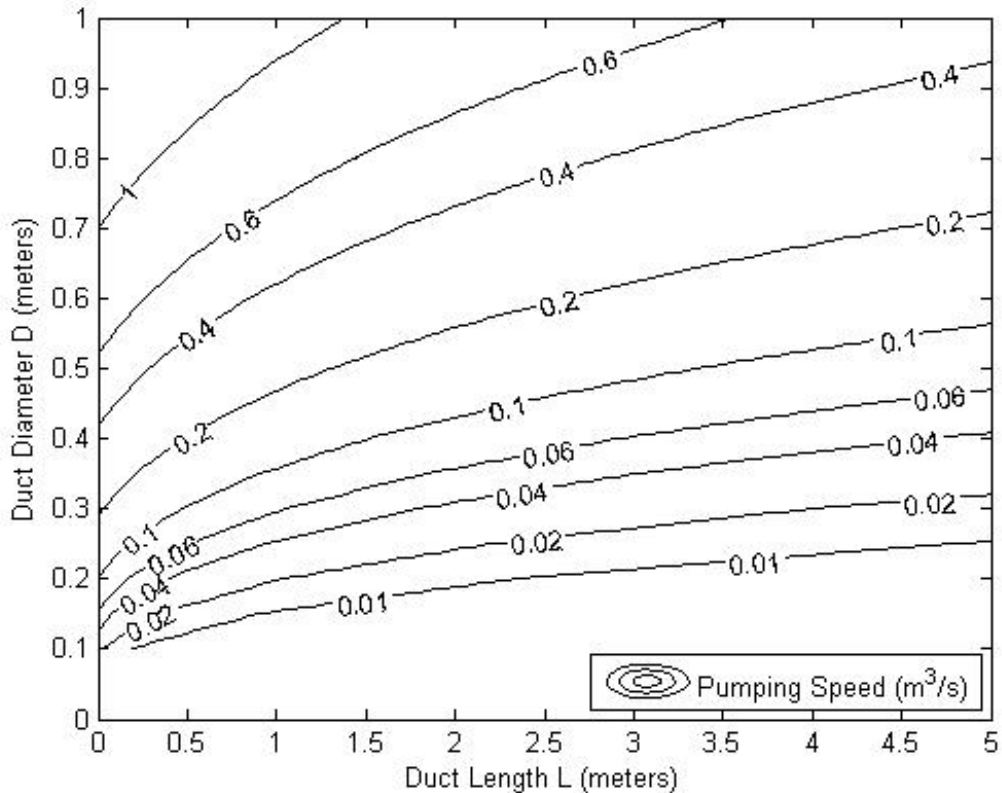
Figure 3.2.2: Effective Pumping Speed of a Remotely Located Vacuum Pump

The plot shows that the effective pumping speed of even the largest commercially available turbomolecular pump becomes quite small if the pump must be located at the end of a pumping duct in a region far enough from the plasma that magnetic fields are small.

However, the situation regarding turbomolecular pumps may not be quite so bleak. It should be noticed that the fundamental operating principles which make turbomolecular pumps possible do not in any way involve magnetic fields. The pumps' operations are based simply on the fact that during the brief time molecules rest in a monolayer on a moving surface before re-evaporating, momentum is transferred from the moving surface to the molecules. On a fundamental level, turbomolecular pumps are simply arrays of alternating axial stages of rotating disk and plate surfaces cut by angled slots or grooves.

The technical problems with operating any of the commercially available turbomolecular pumps in a high magnetic field environment all arise because of the particular ways the pump designs have been implemented. In spite of this, the designs have been commercially successful because the majority of turbomolecular pump users do not want to use them in strong magnetic fields. The fusion researchers who would benefit from eliminating magnetic issues do not represent a large market.

The most severe magnetic susceptibility issue arises because commercially available units all use metallic rotors. The use of metal is a manufacturing convenience to limit cost, since non-metallic rotors could alternatively be used if their strength were sufficient for high speed and their surfaces were specially shaped for the pumping task. Stationary magnetic fields perpendicular to the rotor axis or time-varying magnetic fields aligned with the axis each generate electric fields in the rotor which in electrically conductive metallic rotors cause unwanted eddy currents to flow. The eddy currents in turn heat the rotors. Exacerbating the situation, commercially available units are also not designed with any effective way to remove this electromagnetically generated heat from their vacuum-insulated rotors, so rotor failures can eventually occur due to the combination of high temperature and the mechanical stress arising from rotation. This type of failure has been reported in magnetic fields as weak as 100 gauss, and 50 gauss is quoted as the safe operating level. A second magnetic susceptibility issue arises in some turbomolecular pumps which employ magnetic bearings to actively levitate their rotors instead of using conventional lubricated bearing surfaces. In spite of their advantages, magnetic bearings can fail to work in a strong external magnetic field. A third issue arises because each commercially available turbopump includes its own electric motor to drive its rotor as part of the pump assembly. These electric motors have not been designed to work in a strong external magnetic field since most of the customers purchasing them do not care about that issue.

There has not been much effort expended to develop turbomolecular pumps suitable for operation in close proximity to magnetic fusion reactors, and no manufacturers hint of any such possibility in their advertising literature. This is as should be expected because with most magnetic fusion plasma experiments involving only short, low duty cycle pulses in which negligible quantities of helium are produced through fusion, the market need justifying expenditures to develop such pumps has not yet materialized.   However, there have been some efforts along these lines. The July 1987 issue of J. Vac. Sci&Tech. A:Vac.,Surfaces, and Films contained an article written jointly by [Murakami, Abe, Morii, Nakaishi, Hata] from JAERI and Mitsubishi Heavy Industries, Ltd reporting on such an effort. With the title, "**Performance test of a ceramic rotor developed for turbomolecular pumps for fusion use**", it reported on a test machine consisting of a ceramic rotor assembly made of high electrical resistivity silicon nitride, gas bearings with a spiral-groove seal, and a gas turbine to power the turbomolecular pump instead of an electrical motor. Their test machine provided good pumping performance while utterly avoiding any magnetic or electrical components, an approach which is consistent with its operation in direct proximity to the plasma divertor of a fusion power reactor. They totally eliminated the magnetic susceptibility issue. Unfortunately, although their approach would be ideal for fusion power reactors, it did not confer any advantage for most turbomolecular pump users so it has not been developed into a marketed product.

Other approaches to allowing turbomolecular pump operation in magnetic fields may also be possible. The stationary metallic plates used in today's turbomolecular pumps could be redesigned to include internal coolant passages while materials capable of higher temperature operation could be substituted in the rotating disks, so that the resulting radiative cooling would allow more eddy current heating of the rotors to occur without

failure. In another approach, higher resistivity metallic materials could be used for the rotors. Yet another approach would specially shape the metallic rotors and their slots to reduce eddy currents. Also, a gas turbine is not the only possible replacement for the electrical motor driving the rotor, since alternatively a long rotating drive shaft could operate it from a distant motor. It may alternatively be feasible to provide active magnetic shielding to cancel a strong magnetic field, thus allowing even today's commercial turbomolecular pumps to be used.

It is likely that with sufficient focused funding, e.g., several million dollars, turbomolecular pumps can be developed capable of operating in direct proximity to the divertor region of a continuously operating magnetic fusion power plant. Since turbomolecular pumps otherwise have excellent characteristics, i.e., they pump helium well, they could operate in an intense radiation environment, and they are energy efficient, this reactor-relevant approach using a new turbomolecular pump design suitable for fusion should be pursued as the baseline approach for NHTX machine infrastructure.

Alternatively, cryopumps could be used in the NHTX, but their non-relevance for fusion power reactors and the fact that their behavior is very different from the appropriate turbomolecular pump technology for fusion makes cryopump usage unwise.

The basic NHTX vacuum pumping infrastructure design concept will provide 10 ducts exiting the vacuum vessel from the lower divertor region and another 10 ducts exiting the vacuum vessel from the upper divertor region. Ducts exiting the vacuum vessel at the divertor protuberances will be of rectangular cross section 0.15 m tall and 0.50 m wide, consistent with the allocated space for PF coils surrounding the divertor regions. Such small cross section ducts would compromise pumping speeds if they were high vacuum pumping ducts with pumps located at their distant ends remote from the vacuum vessel. Therefore, the pumps will instead be located at the vacuum vessel boundary.

A turbomolecular pump of a new design which will be able to reliably operate in strong magnetic fields will be located in the entrance to each of these ducts. Each will pump neutrals from the divertor region of the vacuum vessel, with the turbomolecular pump's exhaust entering its associated duct. Thus, these ducts will not be high vacuum pumping ducts but instead are forelines in which higher pressure exhaust gases flow. They are therefore compatible with very high pumping speeds in the divertor. They will connect to backing pumps located in the basement, and these backing pumps in turn will pass their exhaust to PPPL's gas processing systems which can separate out helium and each hydrogenic isotope including tritium.

In addition to the new design for turbomolecular pumps which will be part of the NHTX infrastructure, individual advanced divertor experiments may provide their own divertor particle pumping schemes to be tested. For examples, one such scheme may include cryopumps. At least one other scheme will include using a liquid lithium free surface to pump hydrogen species by the liquid lithium while also absorbing the exhaust heat.

3.2.3 Fuel separation systems

Hydrogen isotopes are best separated from non-hydrogenic impurities by the use of filters known s "palladium leaks". These commercially available components typically include long helically coiled tubes of a palladium- silver alloy located inside a pressure-tight surrounding enclosure. With the tubes at an appropriate elevated temperature, the gas which includes a mix of hydrogen isotopes with non-hydrogenic impurities to be filtered is flowed at high pressure into one end of each tube. Its hydrogen dissolves in and flows through the palladium tube walls, entering the lower pressure volume surrounding the tubes, from which the purified hydrogen is continuously pumped. The non-hydrogenic gases are left behind in the tube, and they exit from the tube's other end along with a much lower hydrogen content than the gas entering the tube. Multiple stages can reduce the hydrogen content at the final outlet to negligible levels.

In an operating fusion power reactor, it will <u>not</u> be necessary to separate the tritium from the deuterium in the plasma exhaust, since in any event they will both be continuously re-injected into the plasma which would instantly re-mix them. However, if all the hydrogenic isotopes in the plasma exhaust were simply returned to the plasma, then the protium which does not fuse under these conditions but results from side reactions would eventually build up to intolerable levels. Excess protium confined in the plasma implies less confined deuterium and tritium, so the D-T fusion reaction rate would decline towards zero. Therefore, it is necessary to do some isotope separation in order to remove enough of the protium that its equilibrium level in the plasma remains low.

The best approach to avoid excess protium in a future D-T fusion power reactor is not yet clear. The facts that that protium production rates are small and that some protium content in the plasma is tolerable, together imply that simplified fuel processing may be possible. It may be best to completely separate isotopes and remove the protium in only a small portion of the circulating flow, passing along the rest of the circulating flow without isotope separation. Alternatively, there may be a way to separate out the protium from the stream without separating the deuterium and tritium from each other, and to obtain a high throughput with a low inventory in the process.

Although the NHTX will not be a fusion power reactor, it will produce some fusion. The normal D-D plasmas planned for most NHTX operations will produce some protium and helium-3 impurities via the D-D side reactions while also yielding smaller additional amounts of protium and helium-4 via deuterium reactions with the small amounts of tritium and helium-3 bred within the plasma. In addition, the NHTX will be capable of operating with deuterium/tritium 50/50 plasmas for reduced plasma durations, during which helium-4 will be produced from D-T at a higher rate than in D-D plasmas. Although none of these operations will produce impurities at rates approaching their production in a future fusion power reactor, the NHTX will provide an opportunity to study proposed fusion fuel separation schemes.

3.2.3.1 Divertor exhaust heat

In order to accommodate different experiments testing different advanced Divertor schemes, the NHTX first wall cooling system infrastructure will be able to remove the full 50 MW of plasma heating power deposited on it in the most spatially concentrated profiles anticipated. The poloidal distributions of heating have been roughly estimated [R.Maingi, 4April'07] as follows:

Table 3.2.1: Plasma Heat Deposition Spatial Distribution Estimates

	Plasma Operating Mode	% Power On Centerstack	% Power On OuterWall	% Power On UpperDivertor	% Power On LowerDivertor
1	DND negative squareness	45	5	25	25
2	DND zero squareness	20	10	35	35
3	DND positive squareness	15	15	35	35
4	LSN ITER-like	20	20	10	50

Since the NHTX first wall will have about 62 m^2 of internal surface area, its spatially averaged value of sustained power density at the full 50 MW plasma heating power will be about 0.8 MW/m^2. However, the peak sustained power density will be far higher. R.Maingi estimated that if the total heat load were limited to 30 MW, the sustained peak local power density would exceed 40 MW/m^2 in double null configurations and would be even higher in the single null configuration. If one linearly extrapolates this estimate to the planned total plasma heating power of 50 MW, the resulting peak local heating density would exceed 67 MW/m^2 in double null configurations and would be even higher in the single null configuration. It will be challenging for each advanced Divertor scheme to be tested on NHTX to accommodate such high local heat fluxes, but that will be part of their set of design issues.

The cooling system which NHTX will provide will be capable removing the full 50 MW of bulk heating deposited in the first wall. It is assumed that the heat deposition profile will not be too peaked, i.e., that it will be approximately axisymmetric without large toroidal variations and that its poloidal power breakdown into zones will not be more concentrated than the estimates given in the above table. However, the machine infrastructure will not itself accommodate sustained localized heating intensities of 40 MW/m^2 , or 67 MW/m^2 , or 100 MW/m^2. Such high heat fluxes will need to be accommodated as part of the experiments themselves.

3.2.3.2 *Example of advanced divertor*

Note: This section does not describe the NHTX infrastructure. Instead, it discusses aspects of a particular advanced divertor experiment which should be tested in the NHTX.

Among the different advanced divertor schemes to be tested in the NHTX, it is likely that some will not directly involve free-surface lithium flows in the divertor region. On the other hand, the use of lithium confers some important advantages, so there are strong incentives to try it. The hope is that liquid lithium may provide a single holistic solution to multiple problems by its superior abilities to absorb hydrogen isotopes, accept high heat flux, remove heat and hydrogen isotopes through forced convection, and renew flowing surfaces without any permanent damage from erosion.

It is expected that at least one of the advanced divertor schemes to be tested by the NHTX will investigate the use of free-surface molten lithium flows in the NHTX Divertor region. The particle control reasons for using liquid lithium there were bolstered by the 2002 Nuclear Fusion paper by Baldwin, Doerner, Luckhardt and Conn, **"Deuterium retention in liquid lithium"**, which had the following abstract:

> **Measurements of deuterium retention in samples of lithium exposed in the liquid state to deuterium plasma are reported. Retention was measured as a function of plasma ion dose in the range 6×10^{19}–4×10^{22} D atoms and exposure temperature between 523 and 673K using thermal desorption spectrometry. The results are consistent with the full uptake of all deuterium ions incident on the liquid metal surface and are found to be independent of the temperature of the liquid lithium over the range explored. Full uptake, consistent with very low recycling, continues until the sample is volumetrically converted to lithium deuteride. This occurs for exposure temperatures where the gas pressure during exposure was both below and slightly above the corresponding decomposition pressure for LiD in Li.**

It had long been suspected that liquid lithium could be an effective sink for hydrogen ions, since the formation of lithium hydride is exothermic. On the other hand, hydrogen gas is slow to combine with lithium. However, this work showed experimentally that all hydrogen ions striking the liquid lithium surface immediately became trapped in the liquid instead of being recycled as gaseous neutrals. The liquid lithium can also compactly hold in solution a very large quantity of hydrogenic atoms, so it provides an effective high temperature way to capture hydrogenic particles exiting the plasma without using a cryopump. Furthermore, the liquid lithium with its dissolved hydrogen can be flowed through the vessel in a continuous process.

Liquid lithium also can absorb large amounts of heat. Its surface evaporation rate in a vacuum is not large for temperatures up to 450 C, and over one megajoule is absorbed by each kilogram of liquid lithium in raising its temperature from 200 C to 450 C. Therefore, the entire 25 MW heat load estimated for the single null lower divertor could be absorbed by a lithium flow of only 25 kg/second, i.e., about 50 liters per second, with incoming lithium at 200 C and the exiting lithium (along with its load of hydrogenic isotopes) at 450 C.

A 450 C lithium outlet temperature is also reactor relevant in than it is more than hot enough to economically operate a thermal conversion system for the generation of electricity. Although present day fossil fuel electrical generation systems use slightly higher steam temperatures in supercritical coal-fired plants and use considerably higher temperatures in turbine systems burning natural gas, the steam temperature in most nuclear fission power plants is slightly below 300 C.

The obvious way to configure a single null lower (SNL) Divertor using liquid lithium is to replace the solid neutralizer plates used in existing divertors by an axisymmetric free-surface of lithium flowing poloidally downwards over a slanted solid surface into a sump region at the vacuum vessel's bottom. The two plasma Divertor exhaust fans of the particular SNL plasma equilibrium shape calculated for the NHTX may be best accommodated by a single liquid lithium flowing surface extending from a ring of lithium nozzles located on the inner wall above the inner strike location to a lower ring of sump drains located at a larger major radius past the outer strike region. For a lithium flow depth of 25.4 mm (i.e., 1 inch) the flow speed needed at a 1 meter major radius neutralizer target location for a 25 kg/sec lithium flow able to absorb 25 MW of heat would be only 0.31 m/s, i.e., about 1 foot per second. At such a low speed, MHD effects will be small. The flowing stream of liquid lithium cannot be damaged by high localized heat flux or by plasma erosion from the incoming fan of ions since it has no solid structure to damage and it is continually renewed by fresh incoming fluid. Transient localized high temperatures in the lithium as it flows through the plasma exhaust's target circle will be rapidly dissipated by fluid convection mixing processes in addition to thermal conduction.
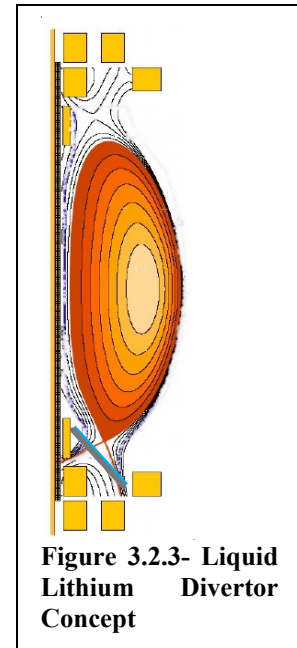
Figure 3.2.3- Liquid Lithium Divertor Concept

Flowing liquid lithium will be subject to MHD effects, although these will be small in slow speed flows. Moreover, for the NHTX configuration these will have simple solutions. The MHD concern about lithium splashing during OH-driven startup will be addressed by not commencing lithium flow until the OH plasma startup transients have finished and the plasma approaches a quasi-steady-state condition. .

There is a MHD concern over how to eject unpressurized liquid lithium at the lithium loop's full flow rate from the vacuum vessel into exit drain pipes in which back pressure will be produced both by fluid friction and MHD effects. The concern is that the natural gravity-driven draining rate may be too slow since the weight-density of 450 C molten lithium is only $\rho g= (491\ kg/m^3)(9.766\ m/s^2)=4,795\ N/m^3$. Excessive fluid depth may be needed in the sump in order to develop enough pressure to force fluid to exit through sump drains at the needed 50 liter per second drainage flow rate.

This concern will be addressed by driving radially directed electrical current galvanically through the liquid lithium sump in the bottom of the vacuum vessel. The JxB interaction of that injected current with the toroidal field will act as an electromagnetic pump, thus providing the liquid with an electromagnetic downwards force in addition to its own

weight. For instance, a current density of only 2.4 A/cm^2=24 kA/m^2 flowing radially in the lithium sump across the B=2 Tesla toroidal field would create a force field there of JXB=48,000 N/m^3. This is more than ten times the weight density of the lithium and it adds to the lithium's weight in helping to force it down through the drains. However, this current density is so low that its resistive voltage gradient in the liquid lithium would be only 8 millivolts per meter and its power dissipation in the liquid lithium would be only 188 W/m^3..

The free-surface liquid lithium flow, which will be axisymmetric and poloidally directed and thus will cross through the toroidal magnetic field, will generate through its motion a VxB electric field directed normal to its free surface. However, there is no external circuit to carry bulk current flowing normal to the surface, so MHD effects will not be strong. They are not eliminated entirely though since the MHD-generated electric field strength will vary between different radial locations, both because toroidal field strength varies with location and because the lithium flow velocity may also be non-uniform. These variations in the MHD-generated electric field strength normal to the surface can be reduced by limiting the major radius range of the free-surface flow, but they cannot be eliminated altogether. The resulting spatial gradient of the flow-generated electric field is a second order effect but it will drive circulating poloidal electrical currents within the liquid lithium. The JxB forces from these circulating currents may somewhat modify the shape of the flowing lithium's free surface from the shape it would otherwise assume without a toroidal field. These effects are not expected to severely disrupt the flow.

Figure 3.2.4: InSitu EM Pump
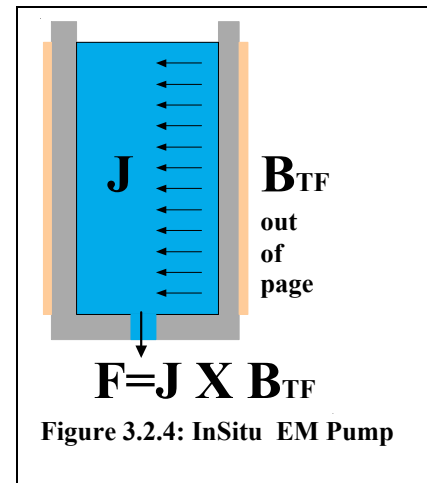
Since the free-surface liquid lithium flow will serve as the neutralizer target for the scrape-off layer flowing along magnetic field lines into the divertor's fan-shaped plasma exhaust, it logically follows that the weak poloidal magnetic field at the free surface cannot be tangent to the surface and may have a non-zero perpendicular component there. The electric field resulting from the VsB interaction between the flowing liquid lithium and this perpendicular poloidal magnetic field component will therefore also produce some toroidally directed currents in the lithium. The combined effects of induced toroidal and poloidal distributed currents in the flowing lithium interacting with the toroidal and poloidal magnetic fields are quite complicated and have not yet been determined. However, since these combined effects are simply the passive response of the system to stationary magnetic fields and gravity, it seems likely that their combined effect will be to modify the flow to more closely follow the spiraling total magnetic field lines as the liquid lithium descends. Thus, it is expected that some toroidal swirl motion may appear in the flow.

Notwithstanding the fact that MHD effects will occur, it is expected that they will not disrupt the free-surface flow and that the flow will instead be a continuous downward

fluid motion over a slanted solid surface from the higher elevation ring location where the lithium is introduced to the sump location at the bottom where it drains.

MHD pressure drops in the pipes bringing fresh lithium into the vacuum vessel will be overcome by pumping hard and by adopting favorable plumbing strategies. The pressure drops arise because the VXB electric field generated in the flowing liquid is different from the zero electric field produced in the stationary conducting pipe surrounding it, and this difference can cause distributed electrical currents to circulate between them. Those electric currents also interact with the magnetic field to produce a JxB back-pressure opposing the fluid motion. Such MHD pressure drops can be reduced for any given flow rate by using larger diameter pipes so that relative speed differences between the pipes and their contents are reduced. They are also dramatically reduced if either the pipes themselves or a coating applied on the pipes' inner walls is electrically insulating. Insulating materials exist which can do this job but investigations 20 years ago did not succeed in finding insulating coatings for metal pipes capable of surviving long-term high temperature contact with flowing lithium.

In addition to recent interest in using liquid lithium in free-surface flows within divertors, there has been interest for a long time in using liquid lithium to implement tritium-breeding blankets. In the blanket application, liquid lithium flowing in pipes must carry the bred tritium to extraction systems while also carrying the heat from fusion to thermal conversion systems. One of the proposals resulting from this long-term interest was documented in the 1995 Fusion Engineering And Design paper by Sze, Mattas, and others, **"Tritium recovery from lithium, based on a cold trap"**. This was not the first published proposal that a cold trap be used to remove bred tritium from lithium, but it was the first to suggest that sparging with other hydrogen isotopes could lower the retained tritium to arbitrarily low levels, and to propose that this system be tried out on ITER (which is not at present planning to do so).

A system based on the utterly simple cold trap principle could be implemented to continuously remove hydrogenic isotopes from a liquid lithium stream leaving the NHTX divertor. The principle is based on the facts that lithium and hydrogen combine to form the ionic compound, lithium hydride, and that the saturation solubility of hydrogen isotopes in liquid lithium is an increasing function of temperature.
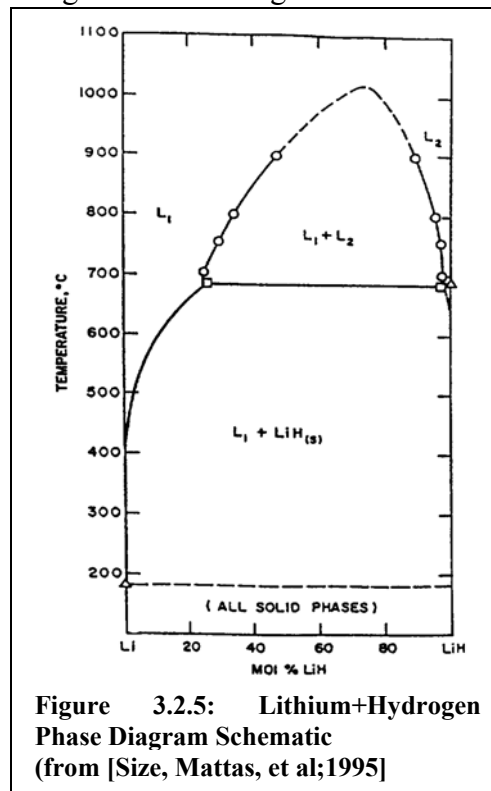
Figure 3.2.5: Lithium+Hydrogen Phase Diagram Schematic (from [Size, Mattas, et al;1995]

Figure 3.2.5, from the 1995 paper, roughly illustrates the combined phase diagram of lithium and hydrogen. Between lithium's 182 C melting temperature and lithium hydride's 688 C melting temperature, the diagram is divided into three regions. The left region represents a single liquid in which hydrogen is dissolved in liquid lithium as the H⁻ ion. The central region represents a mixture of solid lithium hydride and liquid lithium in which the hydrogen concentration is at its saturation point.   The right hand region, which only extends slightly below 688 C, represents a single liquid of mostly lithium hydride in which dissolved lithium has depressed its melting point temperature. The diagram above 688 C is not important for this discussion, but on its left it continues the liquid phase in which hydrogen is dissolved in liquid lithium. On the right it continues the other liquid phase in which lithium is mixed with liquid lithium hydride. The middle region represents two immiscible liquids, i.e., liquids which separate instead of mixing. Above the consolute temperature near 1000 C, there is a single liquid phase.

It is important to understand that no distinction is made between hydrogen dissolved in lithium and dissolved lithium hydride within the left hand side region.   They are considered identical.

Between 182 C and 688 C, the boundary between the left and central regions in Figure 3.2.5 represents the saturation solubility of hydrogen in lithium. Various investigators have measured this solubility curve. Shpil'rain's model [OHSE] is

$$\ln\left(n_H{}^{Sat}\right) = E - \frac{F}{T}$$

where the temperature is in Kelvins. His regression fit values are as follows:

Table 3.2.2: Regression Fit Parameters for Hydrogen Solubility in Molten Lithium

Isotope	E	F (Kelvins)	Exp. Range (Kelvins)
Protium	15.476	5360	523-775
Deuterium	15.047	5112	472-771

A MATLAB plot of his solubility model follows, as generated by a MATLAB cell in Appendix section 1.3:
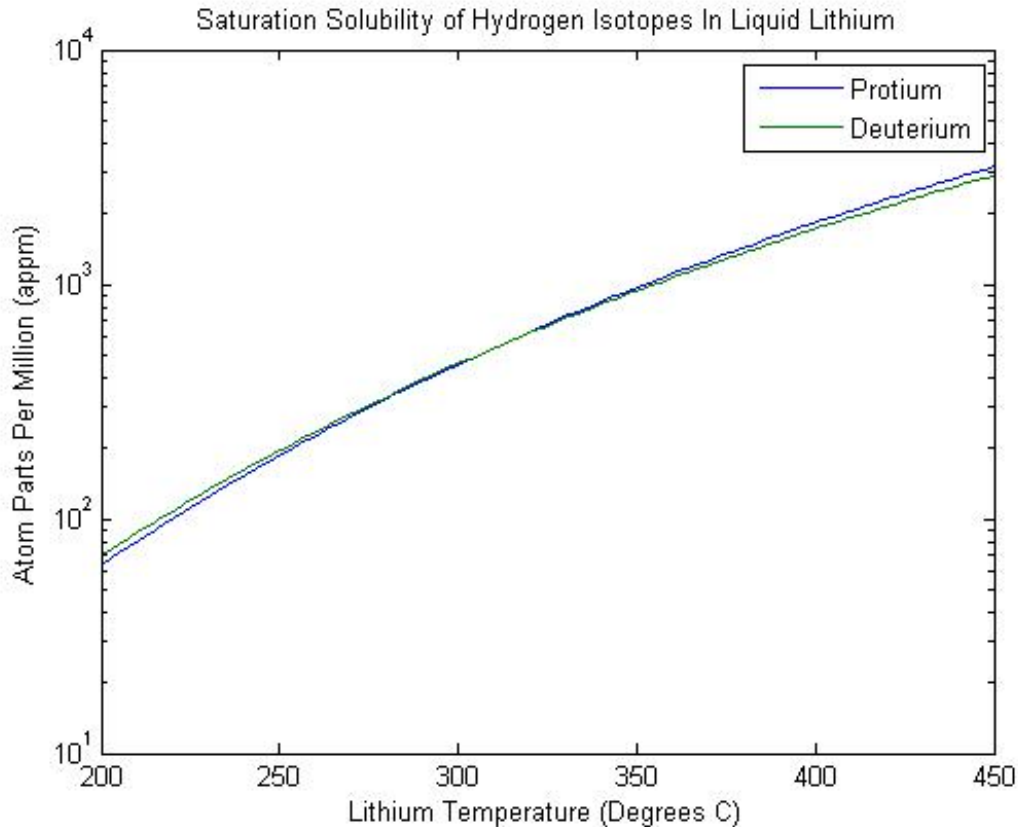
Figure 3.2.6: Regression Curves for Hydrogen Solubility in Molten Lithium [OHSE]

R. Causey's 2002 review paper in J. Nuclear Materials, "**Hydrogen isotope retention and recycling in fusion reactor plasma-facing components**", lists reference publications giving alternative experimentally determined formulae for the solubility curves.

The important point about the solubility is that it increases with temperature. If liquid lithium exiting the NHTX divertor at 450 C contains dissolved hydrogen isotopes at a concentration higher than hydrogen's 200 C solubility, then when the temperature of the lithium is subsequently cooled to 200 C the excess dissolved hydrogen leaves the solution. However, it does not evolve into a gas. Instead it forms solid lithium hydride crystals which precipitate out. These solid crystals simply appear, suspended in the fluid. However, whereas the density of molten lithium at 200 C is 513 kg/m^3, the 200 C density of solid lithium hydride incorporating protium has been measured as 757 kg/m^3, so lithium hydride incorporating the heavier deuterium or tritium isotopes of hydrogen must have even higher densities of about 850 kg/m^3 and 950 kg/m^3, respectively. Since for any mix of hydrogenic isotopes the solid crystals will be denser than the liquid lithium in which they appear, they can be quickly separated out by a centrifugal separator. After separation, the solid lithium hydride can be decomposed to release its hydrogen isotopes by one of two possible approaches. If it is raised above its 688 C melting temperature, an electric current passed through the resulting liquid lithium hydride electrolyzes it so that

its hydrogen isotopes immediately evolve at the positive electrode as separated gas. Alternatively, even without electrolysis the hydrogen can be slowly released from the hydride at a net decomposition rate depending both on temperature and on the partial pressure of hydrogenic gas in contact with the lithium hydride. For instance, at the oft-quoted LiH decomposition temperature of 850 C, a hydrogen gas pressure of one standard atmosphere is needed to halt LiH decomposition. After the hydrogen isotopes have been removed from the lithium, if needed they can be separated from each other by standard methods, e.g., the Tritium Purification System (TPS) remaining from the TFTR experiment uses cryogenic distillation columns.

The cold trap is not the only way to separate hydrogen from lithium. For example, complete separation can eventually be achieved by simply holding hot molten lithium in a high vacuum for a time during which its dissolved hydrogen outgasses and is pumped away. This slow process can be hurried along by using an yttrium getter. The advantages of the cold trap separation method are its extreme simplicity and the fact that no significant process time is required. It can be implemented as part of a continuously operating process without any batch components.

The 1995 paper's proposed system also included use of a regenerative heat exchanger. If a fusion power plant's thermal conversion system design did not require cooling its liquid lithium all the way down to 200 C, then a regenerative heat exchanger could still do so and then reheat the lithium back to its incoming temperature with very little energy loss. Thus, the possible use of a regenerative heat exchanger decouples the design of this hydrogen extraction scheme from a fusion power plant's thermal conversion design.

A previously identified concern regarding the use of the cold trap separation scheme for breeding blankets was that although the 200 C hydrogen solubility in liquid lithium is small, it is not zero. In the 1995 paper the 200 C solubility was assumed to be 440 appm for the three hydrogenic isotopes, although the paper mentioned a publication asserting that its value for deuterium is lower. The Shpil'rain model from [OHSE] asserts the 200 C solubility is only about 70 appm, so there are clearly some quantitative discrepancies to be sorted out. However, from a qualitative standpoint the concern is clear. Since some hydrogen would be retained in solution in the lithium after leaving the cold trap, this might allow an excessively large tritium inventory to build up within a large breeding blanket system. The 1995 paper by [Sze, Mattas et al], in considering a 700 tonne lithium breeding blanket, proposed that protium be deliberately added to the lithium as a dilutant. Since lithium's 200 C hydrogen solubility does not discriminate in any major way between hydrogen isotopes, this strategy would reduce the tritium inventory retained in lithium to as low a level as desired consistent with the associated cost of a higher throughput hydrogen isotope separation system.

A liquid lithium advanced divertor experiment for the NHTX would have far less lithium than a fusion reactor, perhaps less than 0.1 tonnes. Such a small quantity of lithium may not pose a tritium inventory concern when used with the cold trap scheme for separation of hydrogen isotopes from the lithium. However, if it were a concern then the isotopic dilution strategy could provide an approach to accommodate it.

3.3   Outer vacuum vessel and inner first wall

An overview of the vacuum vessel and first wall design for NHTX is as follows. An inner first wall structure will be mounted within an outer vacuum vessel. The plasma-facing first wall will operate in thermally steady state conditions at high temperature while absorbing 50 megawatts of heat from the plasma it encloses.   A small fraction of that 50 MW will radiate outwards from the first wall through the vacuum gap surrounding it which is provided as thermal insulation between it and the outer vacuum vessel, then will be intercepted and absorbed by the outer vacuum vessel. Flowing water in a water jacket will remove that radiated and reabsorbed heat from the outer vacuum vessel. At the same time, a gaseous or liquid fluid coolant substance flowing in pipes attached to the first wall will remove the remainder of the 50 MW heat.

As part of the NHTX mission goals to experimentally investigate plasma-wall interactions under conditions relevant to the design of a future fusion demonstration reactor or later electricity-producing fusion reactors, the NHTX first wall must operate at an elevated temperature. Elevated temperature may improve tritium retention issues while increasing thermal conversion efficiency, but may also increase costs and create other difficulties.   The optimal first wall temperature for economical future fusion power is presently unknown so it is appropriate for the NHTX to be able to investigate first walls with a range of different elevated temperatures. The upper part of that temperature range will be breaking new ground in magnetic fusion experiments.   Although some experimental devices have operated with first walls as hot as 300 C, there is consensus that 300C is too cold. The design target first wall temperature for NHTX is still under discussion, with temperatures of 800 C sometimes quoted and even 1000 C mentioned. At present it is expected that 600 C will be adopted as the typical operating temperature for the NHTX first wall, but there would be merit in NHTX being able to experiment with its first wall operating at temperatures higher than 600 C. An advanced divertor incorporating a liquid lithium free surface would likely operate at 450 C.

Table 3.3.1: Colors Emitted By Hot Metallic Objects

Visible Color	Approximate Temperature		
	°F	°C	Kelvins
Faint Red	930	500	770
Blood Red	1075	580	855
Dark Cherry	1175	635	910
Medium Cherry	1275	690	965
Cherry	1375	745	1020
Bright Cherry	1450	790	1060
Salmon	1550	845	1115
Dark Orange	1630	890	1160
Orange	1725	940	1215
Lemon	1830	1000	1270
Light Yellow	1975	1080	1355
White	2200	1205	1480

*from Process Associates of America

The experience base at PPPL in high temperature operation of experimental magnetically confined plasma devices includes bake-out with vacuum vessel temperatures approaching 150 C, the limiting maximum temperature for reusable vacuum seals relying on the special type of synthetic rubber known commercially as Viton™. Any vacuum ports operating at temperatures above 150 C will need to adopt a different vacuum sealing technology. The most common such technique uses sacrificial O-rings made of soft metal wire compressed by a knife-edge within a circular groove in the annular flange surrounding each high temperature vacuum port.

However, sealing the vacuum boundary may be the least of the technical difficulties introduced by the adoption of a high design temperature for the first wall. To fully appreciate this it may be useful to review the visible colors of light radiated by objects in the temperature ranges proposed for the NHTX first wall, as summarized in Table 3.3.1. First walls operating within the temperature range from 600 C to 800 C will be red-hot, glowing brilliantly in temperature-dependent hues of red. Even higher temperature first walls operating e.g. at 1000 C would be well past the red-hot range. Clearly, a large red-hot NHTX vacuum vessel directly contacting air would transfer an enormous amount of heat into the air. With such a heat leak it would be almost impossible to keep the vessel hot. A second issue is that a red-hot vacuum vessel would pose a fire hazard and threaten nearby equipment, e.g., PF & TF coils. A traditional single-walled vacuum vessel exposed to the test-cell air would be inadequate. In theory it is possible to surround a hot vacuum vessel with closely fitting non-flammable thermal insulating material in order to reduce the heat leak. This approach is taken for situations in which the vessel is to operate at temperatures up to 300C. However, it would be difficult at much higher temperatures because of the limitations of available thermal insulating materials.

The solution for NHTX is to adapt existing technologies developed for similarly high temperature applications. The starting point is today's commercially available vacuum furnaces, used industrially for a variety of metal melting processes involving ranges of temperatures considerably hotter than 600C. In these, a water-cooled vacuum vessel operates near room temperature to develop a high vacuum internally, thus providing excellent thermal insulation for the region inside it. It is hard to find better thermal insulation than a vacuum. However, to further improve the thermal insulation for very high internal temperatures it is common to also employ a radiation barrier by suspending one or several sheets of thin refractory metal (e.g., molybdenum) in the vacuum space between the cold walls of the vacuum furnace and its central hot region. The central region of a vacuum furnace typically contains an ac electrical induction coil to heat metal, a high temperature crucible to hold the molten product, and other equipment.

The NHTX design will follow the vacuum furnace design pattern by adopting a cold outer vacuum vessel with an integral water-cooled jacket. The NHTX deviation from a cylindrical vacuum furnace lies mostly in its toroidal geometry. The hot NHTX first wall structure will be located within the NHTX outer vacuum vessel, thermally isolated from it by a small vacuum space gap and by structural mounting standoffs constructed of thermally insulating ceramic material and Inconel bolts. Thus, the outer vacuum vessel will protect external equipment from being damaged by heat from the red-hot plasma-

facing first wall. It is envisioned that the outer vacuum vessel will normally operate at room temperature, but its temperature could also be raised if necessary to approach 150 C by using heated pressurized water in its cooling jacket.

For a first wall temperature of only 600 C, it will not be necessary to use additional radiation barriers within the vacuum space. That might change for a 1000 C first wall.

Although it would be possible to implement the first wall in pieces as separate panels not connected to each other, that approach would be flawed because it would permit direct flow of material between the plasma volume and the cold spaces located behind the first wall panels. Since it will never be feasible to bake out the outer vessel to temperatures approaching the operating temperature of the first wall, the use of separate unconnected panels to implement the first wall would doom NHTX to suffer an unstoppable flow of undesired impurity material into and from the plasma. It would also provide a reservoir for an unwanted inventory of radioactive materials such as tritium to accumulate.

Instead, the NHTX first wall will be implemented as a vacuum-tight toroidal chamber nested inside the toroidal outer vacuum vessel. External vacuum pumping systems will pump separately on the vacuum space gap between it and the outer vessel, in addition to pumping on its own internal space. This unconventional design configuration entirely eliminates issues of impurity migration to or from locations behind the first wall, but it introduces other issues, each of which is accommodated in the NHTX design through the application of straight-forward but unconventional design features.

It should be noticed that since vacuum pumping systems will simultaneously pump on both the inside and the outside of the first wall structure, it will never be subjected to any significant pressure difference across it. It may therefore perhaps be feasible to construct the first wall structure from multiple thin pieces of metal which are bolted together so that any leak paths where they join have acceptably low vacuum pumping conductance. However, it is expected that different first wall structures will be prepared for different experiments, and no optimal construction scheme has been identified.

Figures 3.3.1a and b depict a horizontal cross section through the NHTX, with the second providing an expanded view of an inner of the first.   They shows the inner TF, OH solenoid, water-cooled vacuum vessel, red-hot first wall, plasma, first wall and vacuum vessel again with a thick water layer to augment neutron shielding. The PF coils shown outside the vacuum vessel are above and below the midplane.
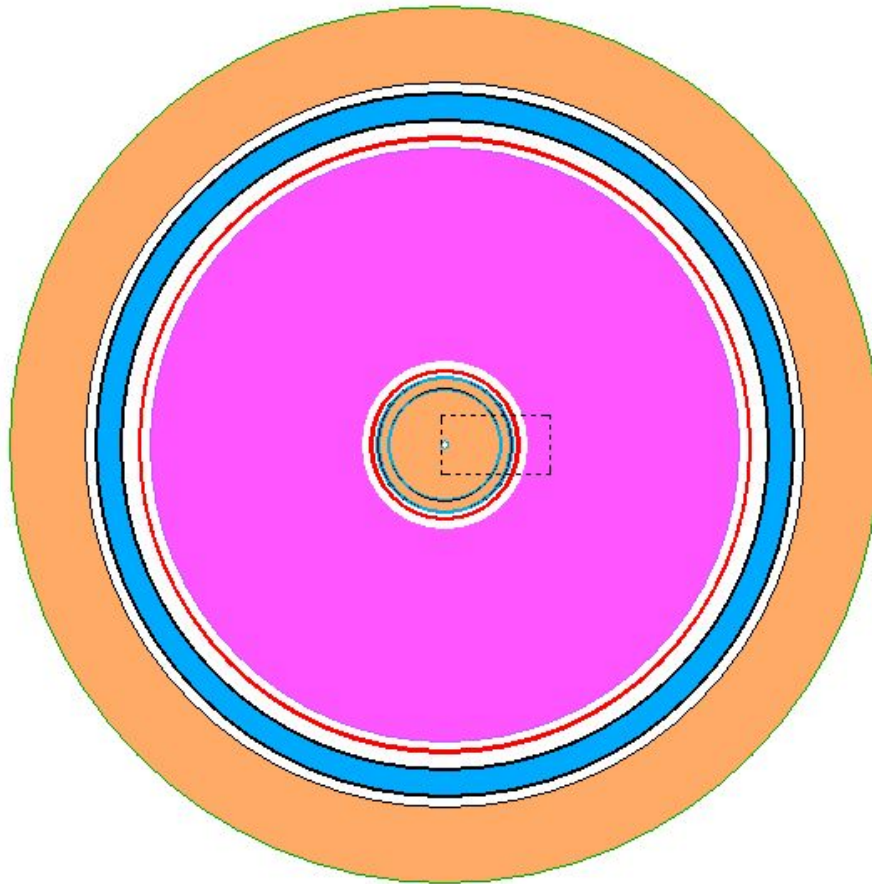
Figure 3.3.1a: NHTX Radial Build
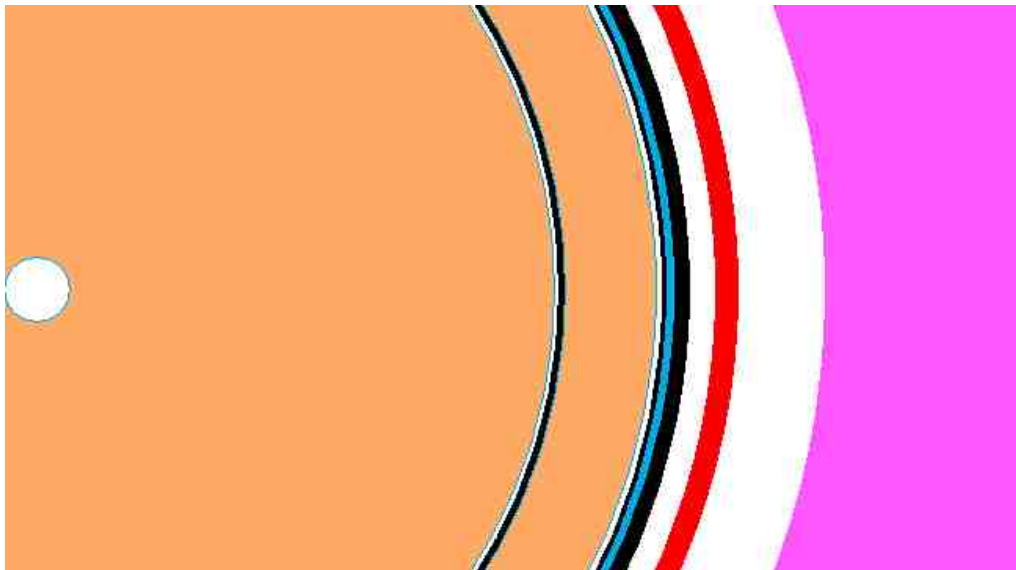
Figure 3.3.1b: Expanded Central Portion Of NHTX Radkal Build On Midplane, Including Inner TF Conductors, OH Solenoid, Water-Cooled Vacuum Vessel, Red-Hot First Wall, and Plasma

The radial build design layout is listed in Table 3.3.2.

Table 3.3.2: NHTX Radial Build On Midplane

Seq. No.	System	Details	Radial Thickness (millimeters)	Radial Range (millimeters)_
1	none	hole	18.2	0<R<18.2
2	Inner TF	Conductors & Insulation	272.6	18.2<R<290.8
3	none	TF/OH assembly gap	3.2	290.8<R<294
4	OH solenoid	OH tension tube	3.6	294<R<297.6
5	OH solenoid	OH Insulation	3.8	297.6<R<301.4
6	OH solenoid	OH conductor	43	301.4<R<344.4
7	OH solenoid	OH Insulation	3.8	344.4<R<348.2
8	none	OH/VV assembly gap	3.8	348.2<R<352
9	Outer Vacuum Vessel	Water Jacket Wall	3	352<R<355
10	Outer Vacuum Vessel	Cooling Water	3	355<R<358
11	Outer Vacuum Vessel	Structural Wall	10	358<R<368
12	Gap	Vacuum Space For Thermal Insulation	14	368<R<382
13	Hot First Wall	Helium Carrying Pipes	6	382<R<388
14	Hot First Wall	First Wall Structure	6	388<R<394
15	Gap	Plasma/wall clearance	50	394<R<444
16	PLASMA	Last Closed Flux Surface	1111	444<R<1555
17	Gap	Plasma/wall clearance	50	1555<R<1605
18	Hot First Wall	First Wall Structure	6	1605>R>1611
19	Hot First Wall	Helium Carrying Pipes	6	1611<R<1617
20	Gap	Vacuum Space For Thermal Insulation	83	1617<R<1700
21	Outer Vacuum Vessel	Structural Wall	10	1700<R<1710
22	Outer Vacuum Vessel	Cooling &Shielding Water	120	1710<R<1840
23	Outer Vacuum Vessel	Water Jacket Wall	10	1840<R<1850
24	none	Airspace Gap	50	1850<R<1900
25	(*) PF Coils	(*) PF5U2 & PF5L2 Coil Shadows	(*)400	(*) 1900<R<2300

(*) PF5U2 & PF5L2 Are Not Actually On Midplane; They Are Above and Below It By ≥1.2 meters

Arising from the configuration choice, the first issue to confront is how to get the toroidal first wall inside the toroidal outer vacuum vessel. The NHTX answer is to provide a fully demountable coil system so that all coils above the vacuum vessel can be easily removed, and to design the outer vacuum vessel to have a removable upper lid and a cross section such that the crane can reach all internal points. Thus, the NHTX design will use the overhead crane to lower the toroidal first wall structure into the outer vacuum vessel after first removing the outer vacuum vessel's upper lid. A key benefit of this design approach is that the first wall can be easily and quickly changed out in order to experiment with different first wall schemes.

Figure 3.3.2 depicts the NHTX vacuum vessel and first wall as an elevation section.
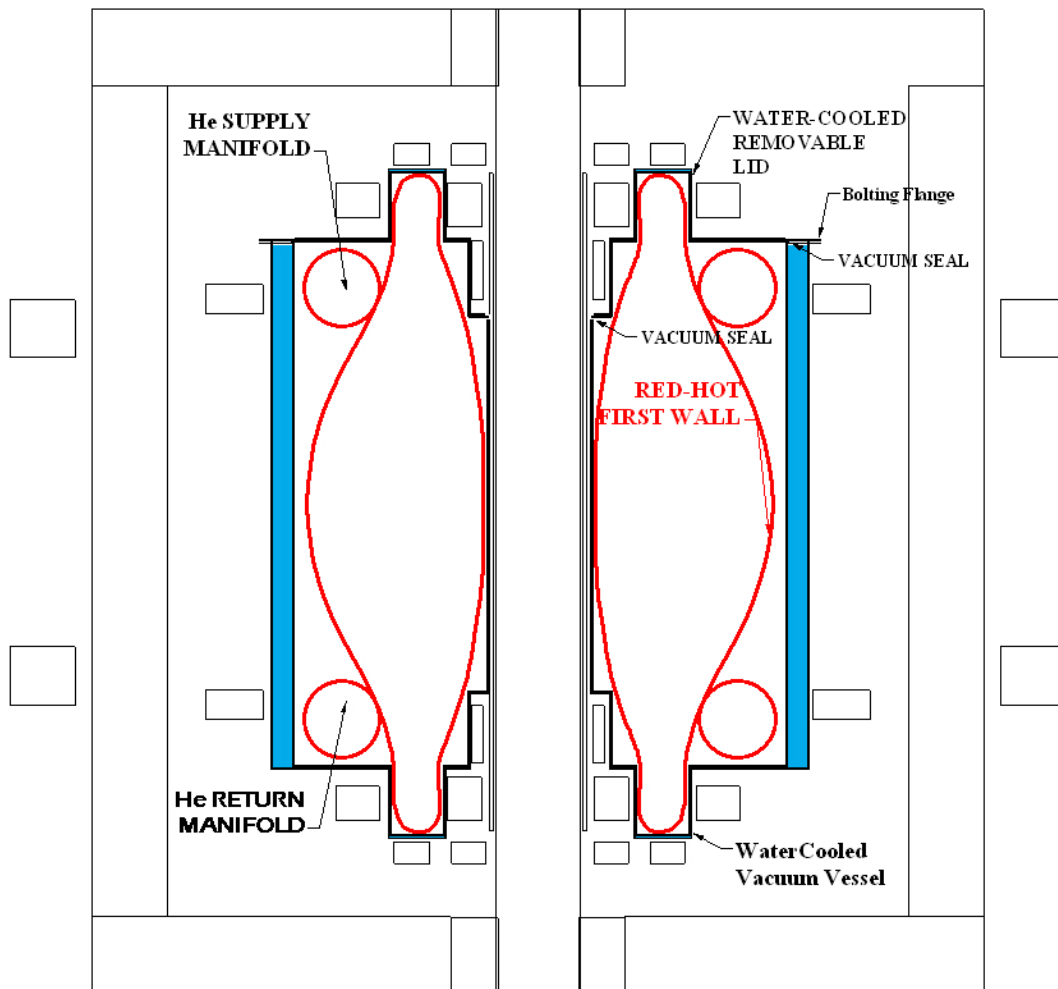
Figure 3.3.2: NHTX Elevation Cross Section Schematic Diagram

A second issue to confront is how to mechanically attach (or disconnect) the inner sealed toroidal first wall to the outer vacuum vessel without requiring that technicians personally enter the structure. This structural mounting issue is important since NHTX operations involving deuterium or deuterium plus tritium will produce neutrons which will activate the structure so that it subsequently emits gamma rays, and since radioactive tritium may contaminate exposed surfaces within the outer vacuum vessel. Thus, there could be significant radiation exposure to anyone who must enter the vessel after extended NHTX operations have started. The simple solution chosen for NHTX, depicted in Figure 3.3.3, avoids the need for any such vacuum vessel entry. Inconel bolts, chosen because of their low thermal conductivity, are inserted from outside the outer vacuum vessel through appropriately sized bolt holes each of which is centered within a tiny vacuum port flange. Inside the outer vessel, each of these bolts passes through a hole in a ceramic standoff, then into threaded holes in a leaf spring which is part of the first wall structure. After

NHTX Assessment FY2007 R1

tightening each bolt from outside, the flange surrounding each bolt head will then be sealed by covering it with a vacuum port cover which compresses a vacuum seal. between flanges. This assembly procedure will be reversed to disconnect the first wall, again without requiring personnel entry inside the vacuum vessel.

A main point of Figure 3.3.3 is that the NHTX outer vacuum vessel will include holes through its wall so that personnel may structurally attach or disconnect the first wall from a vantage point on the outside. Leaks through these structural bolt holes are avoided by extending the vacuum boundary beyond the bolts via a layer of additional sealed vacuum ports. Thus, these bolts will be in vacuum during NHTX operations.
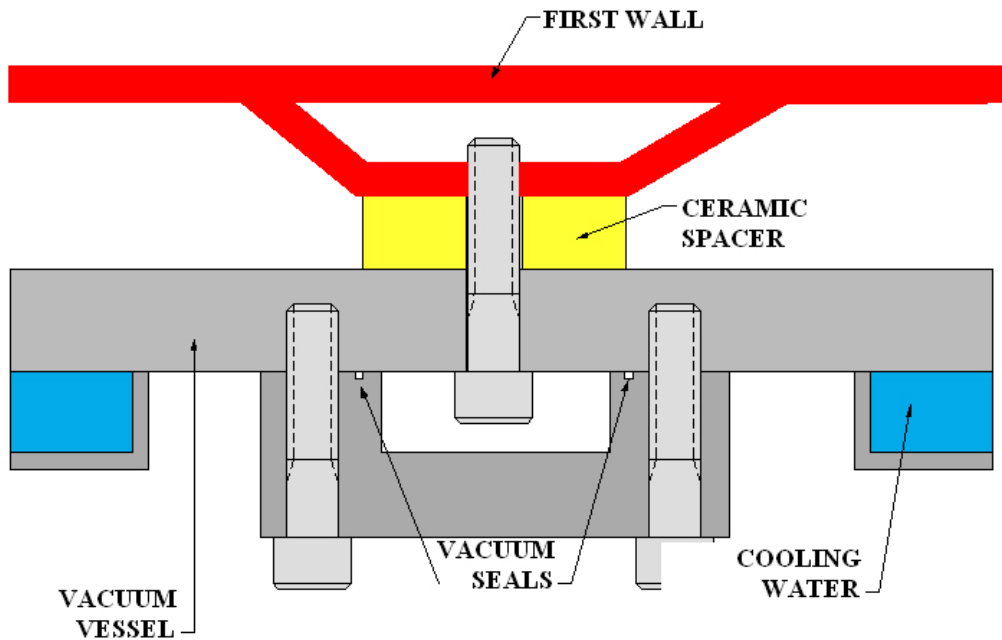
Figure 3.3.3: NHTX First Wall Mounting Inside Vacuum Vessel With External Attachment

A third issue to confront is how to provide external access to the plasma space for neutral beams or plasma diagnostics while maintaining the separation of vacuum spaces between the two vacuum regions, i.e., inside and outside the toroidal first wall. The NHTX solution (as proposed by PPPL engineer W. Blanchard) is to provide at each access port location special matching flanges on the first wall and the outer vacuum vessel. In this design, the first wall flange has tapped bolt holes aligned with a second mating annular flange that is attached to a short internal bellows which in turn connects it to the inside of the outer vacuum vessel wall. This is illustrated in Figure 3.3.4. This outer annular flange is mounted on the bellows with the annulus extending into the port's cross sectional area where it is accessible once the removable diagnostic or neutral beam access port is removed. When preparing to change out the first wall, all of the access port mating flanges will be disconnected and their bellows compressed to retract their outer vacuum vessel flanges and hold them close to the outer wall. This will create a spatial gap providing the clearance needed for removal of the first wall structure.
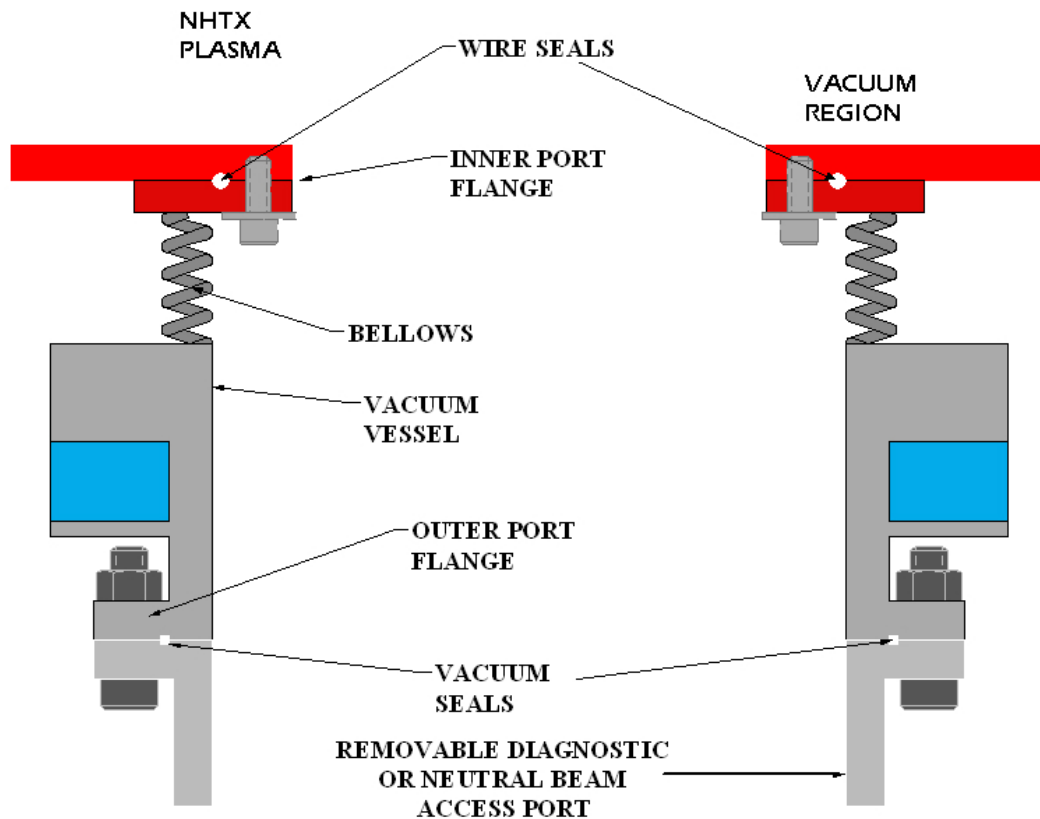
Figure 3.3.4: Matching Ports In Vacuum vessel And In First Wall

During NHTX plasma operations lasting for durations of up to 1000 seconds, the plasma will be continuously heated by 32MW from neutral beam systems in addition to another 18 MW from radio frequency systems. The resulting 50 MW of plasma heating power plus any contribution from thermonuclear fusion alpha particles must also exit the plasma. As a result, the plasma will deposit that heat on the first wall structure, so it will be necessary to actively cool the hot first wall at a 50 MW rate during operation to prevent it from overheating.   On the other hand, during the longer time intervals between successive NHTX operations it will be necessary to supply some heat to the first wall in order to prevent it from cooling down, thus maintaining it at its designed operating temperature.   Furthermore, in the event that the plasma heating suddenly and perhaps unexpectedly stops, the first wall's temperature should not change much.   Thus, for NHTX it is not adequate to only provide electrical heating as done in a vacuum furnace. It is instead necessary to implement a full heating/cooling system for the hot first wall.

During plasma operations the NHTX first wall will operate in thermal steady state conditions at a nominal temperature of 600C while absorbing 50 megawatts of heat from the plasma it encloses. A small fraction of that 50 MW will radiate outwards from the first wall through the vacuum gap provided as thermal insulation, then will be absorbed by the vacuum vessel's inner wall. Flowing water in a water jacket will remove that radiated and reabsorbed heat from the vacuum vessel. A gaseous or liquid fluid substance

flowing in tubes attached to the first wall will remove the remainder of the 50 MW from the first wall. The use of tubes to contain the coolant has the advantage that coolant pressurization can be maintained by mechanical stresses in the tubing without requiring construction of special pressure-tight heat exchanging manifolds.

3.3.1   First wall construction

According to the Specialty Steel Industry of North America (SSINA) internet site, type 304 stainless steel can be used for intermittent service temperature applications up to 870 C and for continuous service temperature applications up to 925 C, if proper stress de-rating factors are used. The following table is reproduced from their internet site.

Table 3.3.3: Maximum Service Temperatures of Steel Alloys
Generally Accepted Service Temperatures

Stainless Steel Material	Intermittent Service Temperature	Continuous Service Temperature
Austenitic		
304	1600°F (870°C)	1700°F (925°C)
316	1600°F (870°C)	1700°F (925°C)
309	1800°F (980°C)	2000°F (1095°C)
310	1900°F (1035°C)	2100°F (1150°C)
Martensitic		
410	1500°F (815°C)	1300°F (705°C)
420	1350°F (735°C)	1150°F (620°C)
Ferritic		
430	1600°F (870°C)	1500°F (815°C)

The necessary stress de-ratings are very large at the high ends of these ranges. The following plot, also from the SSINA internet site, provides some idea of the de-rating.

Hot-Strength Characteristics (2)
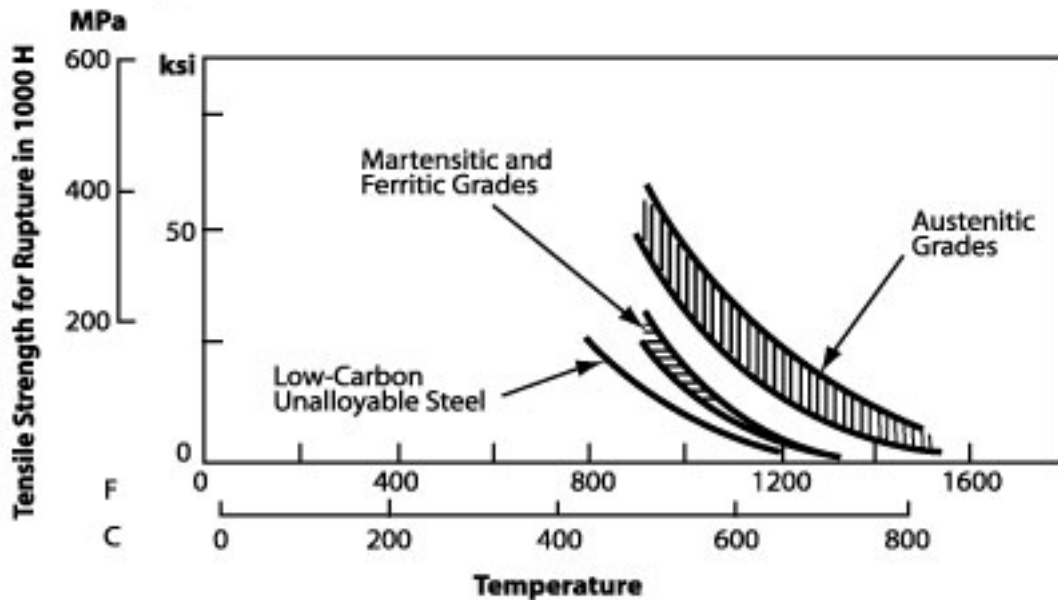
General comparison of the hot-strength characteristics of austenitic, martensitic and ferritic stainless steels with those of low-carbon unalloyed steel and semi-austenitic precipitation and transformat ion-hardening steels.

Figure 3.3.5: Steel Alloy Temperature Derating Curves (from SSINA internet site)

This plot of the 1000 hour rupture stress vs temperature restates the fact that steels are fundamentally not high temperature materials since they lose most of their strength at moderate temperatures which are far below their melting points. However, it also shows that austenitic stainless steels retain more strength at any temperature than the others. Since the NHTX first wall application will not require extreme strength, it appears likely that stainless steel can be used to construct it. However, the NHTX first wall should survive more than 1000 hours, so stresses must be kept well below these plots.

Since type 304 or 316 stainless steel would be much less expensive to use than a refractory metal like molybdenum and since the planned first wall working temperature is only 600 C, it is planned that the first wall material will be stainless steel. If needed, other types such as the more expensive type 310 stainless could raise the service temperature limit above 1000 C, according to the SSINA's service temperature table, although it must have a very low stress capability there.. If even higher temperatures are needed then a refractory metal could be used. For example, the first wall could be constructed from a molybdenum alloy such as TZM, although its cost would be far more.

In the allocated radial build on the midplane of NHTX, there are two midplane intersections with the first wall, i.e., inner and outer intersections.. Each is a composite of two joined layers. The plasma facing side layer is the first wall structure and the layer on the side away from the plasma is a network of pipes. Each of these two layers is nominally 6.35 mm=1/4 inches thick so their composite is ½ inch thick.

According to the space allocation, the first wall structural layer can be made from standard ¼ inch sheets of metal either cut into strips, bent, and then welded, or alternatively stamped (i.e., "formed") to produce the proper toroidal first wall shape. The helium-carrying pipes can be standard ¼ inch outer diameter seamless stainless steel tubing. The tubing must be attached to the backside of the first wall in some way which provides good thermal conduction between them and results in a composite assembly ½ inch thick. Although the best joining method is unclear, one idea is to vacuum braze them together using copper as the braze material, since stainless steel does not melt below 1360 C but copper, which is highly conductive, melts at 1083 C. Such use of vacuum brazing may require that the tubes be first inserted in grooves machined in the first wall structure, in which case the thickness of the stainless steel sheet should be increased to ½ inch to maintain the combined thickness of the sheet and the helium carrying pipes mounted on it.

The two ends of each separate piece of first wall tubing will be connected respectively to inlet and outlet gas manifolds mounted on the first wall. Each gas manifold will extend toroidally around the first wall and the tubing will predominately in the poloidal direction between the manifolds, although tubing will also need to curve around first wall ports or other penetrations. Although the schematic cartoon of the first wall depicts only two such gas manifolds (i.e., one inlet and one outlet), there may be advantages to using more. More manifolds would allow the first wall to be constructed from separately cooled subassemblies which could be bolted together when they are inserted into the NHTX. In would also allow shorter tubing runs, which would enhance cooling.

Although much of the first wall structure can be designed for low stresses, the tubes carrying pressurized coolant will unavoidably be stressed. The internet web site for one tubing manufacturer, Swagelok, includes their recommendations for the choice of working pressure. For ¼ inch o.d. type 304 stainless steel seamless tubing with the nominal wall thickness of 0.035 inches, their recommended working pressure for operating at room temperature is 5,100 psig. They also give recommended de-rating factors vs. temperature but their de-rating factor table stops at 1000 F (i.e., 538 C). At that temperature their recommended pressure de-rating factor is 0.69 for type 304 stainless (but 0.76 for type 316 stainless). Applying their recommended type 304 stainless steel 538 C derating factor of 0.69 to their room temperature working pressure of 5100 psig results in 3519 psig. Probably this is not enough derating for operation at 600C so we lower the target helium working pressure value to 200 bar= 20 MPa, equivalent to about 2900 psig and a de-rating factor of 0.57. More de-rating should be applied if temperatures above 600 C are needed.

It is possible to use stainless steel tubing of larger diameter. Swagelok tubing is available for the same or even higher working pressures in 3/8, ½, 5/8, and ¾ inch diameters, and is also available with only slightly lower working pressure in 7/8 and 1 inch diameters. In addition, there are also metric sizes and there are other tubing manufacturers. However, such use of larger diameter tubing in the first wall would require changing the radial build layout by reducing space allocated for the TF Central Bundle or the OH solenoid.

3.3.2   Heat radiated from inner first wall and outer vacuum vessel cooling

The toroidal first wall is expected to have an external surface area of about A=62 m^2. A black body surface radiates heat according to the rule:

$$E_{bb} = A\sigma T^4$$

where   s   is the Stefan-Boltzmann constant, s=5.670E-8 W m^{-2} Kelvin^{-1}, and T is the temperature in Kelvins. Then if the first wall behaved as an ideal black body it would radiate heat to the vacuum vessel at the following rate:

$$E_{bb} = (62)(5.670E - 8)(873)^4 = 2.04E6 \approx 2\,\text{MW}$$

However, typical emissivities of stainless steel in this temperature range are about 0.5, so the radiated heat will actually be about half of this value, i.e., about 1 MW.

Between NHTX plasma "pulses" it will be necessary to supply the first wall with 1 MW of heat in order to maintain its 600C temperature with this radiative cooling.

The following MATLAB graph, generated in the Appendix shows the expected radiated heat rate versus first wall temperature, assuming that the emissivity of the first wall and the vacuum vessel surfaces facing it are each 0.5 and that the vacuum vessel is at 27 C.
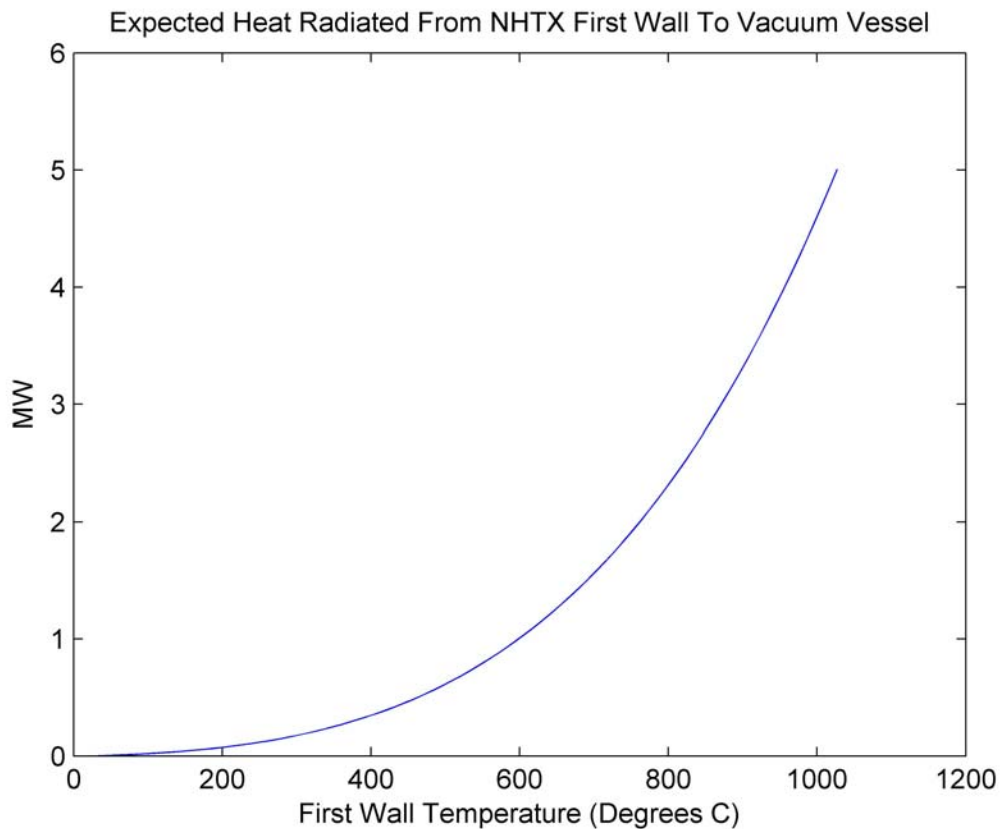
Figure 3.3.6: Outer Vacuum Vessel Heat Load Vs. Inner First Wall Temperature

If we allow a 24 C temperature rise in the cooling water, about 10 liters per second or equivalently about 160 gpm of water flow is sufficient to absorb the expected 1.0 megawatt heating. This is a modest water flow rate. Given the assigned radial build, the highest water speed implied by that flow is 3 m/s, occurring within the 3 mm (i.e., approximately 1/8 inch) gap allotted for water cooling in the vacuum vessel's inner wall. The major radius there is 0.3565 meters so the cross sectional area of that gap is 67.2 cm^2. The entire 10 liters/second flows upwards through half of that cross section then return downwards in the other half. At other locations within the vacuum vessel's water jacket the water speed will be lower. There is ample margin to increase vacuum vessel cooling if needed. The water flow rate and temperature rise could each be more than tripled from these values, thus increasing vacuum vessel cooling tenfold before confronting difficult constraints.

3.3.3   Pros and cons of different substances for cooling the first wall

Although the recommended first wall cooling system uses helium, alternatives have been considered and should be considered further since helium is not unequivocally superior. They are discussed in this section.

With only 1 MW of heat radiated from the first wall, almost all of the 50 MW deposited in the plasma and transferred to the first wall during operations must be actively removed by forced convection of some liquid or gaseous coolant fluid through cooling passages in the first wall. It is not clear what coolant fluid substance is best for this heat removal task, so several are discussed here. Different heat removal schemes may be tried as an adjunct to the NHTX experimental investigations into plasma wall interactions.

It should be realized that 50 MW of high temperature heat removed from the first wall is an asset that can be used to drive a thermal conversion system yielding useful power in the form of electricity or mechanical work. In PWR fission power plants, electricity is generated with typically 33% energy conversion efficiency using steam at a temperature slightly below 300C. A 600C heat source could drive a more efficient conversion process, so perhaps as much as 25 MW might be generated from first wall heat. If this available power were recovered it would more than offset the pumping power needed to circulate the coolant fluid. On the other hand, the NHTX capital cost would be reduced if this power were simply discarded.

Liquids as coolant fluids have the advantage of having much higher densities than gases. This makes their pumped circulation relatively simple to implement. However, it is not possible to convert high temperature heat into mechanical or electrical work using only a liquid. If it is desired to also recover the available work energy from the high temperature heat, then a liquid heat transfer fluid would need to be augmented by an additional gaseous thermal conversion fluid. Thus, in the trade-off between possible liquid and gas coolants, liquids may need less expensive equipment for simple heat removal while gases may optimize higher efficiency designs in which work energy is recovered from the high temperature heat. .

3.3.3.1 Liquid coolant options for the first wall

Pressurized liquid water is generally an attractive liquid coolant to use at temperatures below 300C, and perhaps may be used up to 372C. It is the cheapest, most available and most environmentally benign liquid and it also has a high specific heat. Pressurization can maintain water in a liquid state at elevated temperatures up to water's critical point, which is about 372C and 215 bar. However, at higher temperatures regardless of pressure, water only exists as the gas known as steam. Liquid water could in principle be used to cool a 600C pipe if the pipe were short and the flow speed were so fast that the water temperature never approaches 600C, but if that flow unexpectedly slowed or stopped the pipe could explode. Thus, liquid water will not be used in the NHTX first wall.

Several commercial heat transfer liquids are available with usable temperature ranges extending above 300C. However, no commercial heat transfer liquids are available for use from room temperature up to 400C, much less up to 600C.

No candidate nonmetallic liquids with a temperature range from room temperature up to 600 C were identified.

3.3.3.1.1 Single phase liquid coolants (all liquid metals)

Three liquid metals were identified which remain liquid through most of the temperature range from room temperature to 600 C, i.e.,

(1) Hg, elemental mercury,
(2) NaK, the eutectic mixture of elemental sodium and potassium, and
(3) Ga, elemental gallium.

Each of these liquid metals has been used in the past as a heat transfer liquid in specialized applications. As metals they are sufficiently good electrical conductors so that each would suffer some pressure loss from MHD effects while flowing through first wall pipes in NHTX magnetic fields. Each is chemically active to some degree and, depending on materials compatibility, temperature and pressure, may attack or embrittle confining solid boundaries. Each would become activated by the NHTX neutron flux, so would subsequently emit gamma rays for a period of time.

Although mercury boils at 357C at atmospheric pressure, additional pressurization can suppress its boiling up to its critical point at 1750 Kelvins and 1720 bars. For example, if pressurized to 400 psig (i.e., about 27 bars), liquid mercury does not boil below 621C. Thus, pressurized mercury could be used as a liquid metal coolant for the 600 C NHTX first wall. Mercury is available in large quantities and is relatively inexpensive. Mercury is not combustible or flammable, it is resistant to corrosion, and it does not react violently with most chemicals (excepting acetylene and ammonia). Although mercury does activate, it does not have extremely long lived activation products. The most onerous isotope produced by neutron absorption in mercury appears to be Hg-203, a gamma ray emitter with a 46.6 day half-life. On the negative side, mercury is toxic in small doses

because of its severe poisonous effects on the human nervous system, so it is an environmental hazard if leaked or spilled.

NaK, consisting of 78% potassium and 22% sodium, is liquid at atmospheric pressure from -12.6 C to +785 C.   Thus, NaK could be used to cool the NHTX first wall without pressurizing it above 1 bar.   NaK can be prepared in essentially unlimited quantities and is not particularly expensive. Each of the two elements comprising NaK are normally found in the human body so small leaks or spills of NaK would not have the same degree of toxicity exhibited by mercury. However, hot NaK is highly flammable if it is allowed to contact either air or water. Both sodium and potassium are activated by neutrons, forming K-42, a gamma ray emitter with a 12.36 hour half-life and Na-24, a gamma ray emitter with a 15 hour half-life, but no longer-lived radioactive isotopes.

Gallium metal is liquid at temperatures almost down to room temperature since it melts at 29.9 C, i.e., about 86F.   At a pressure of 1 bar it boils at 2,403 C. Thus, gallium liquid at atmospheric pressure could be used to cool the 600 C NHTX first wall and could still be used without modification even if the first wall temperature were increased well above 1,000 C. Gallium is not regarded as particularly toxic, as evidenced by the facts that neither OSHA nor NIOSH have gallium exposure limits and that gallium has medical applications. Gallium is not combustible, and although it does react with air producing corrosion products, it does not burn. Gallium is activated by neutrons, forming Ga-72, a gamma ray emitter with a 14.1 hour half-life, and some other isotopes with shorter half-lives. The most negative aspect of gallium is that it is quite expensive.

3.3.3.1.2 *Liquid coolants which solidify in cold part of temperature range*
Other liquid coolant options would become possible if it is not required that the coolant remain liquid at room temperature.   There are quite a few substances which are solid at room temperature but are liquid in a temperature range including the 600 C targeted first wall temperature.   However, it should be recognized that choosing to use such a substance imposes burdens on NHTX design and operation. The NHTX would need to have special provisions to avoid freezing of the coolant during all anticipated eventualities and other special provisions to drain first wall coolant volumes before their cooldown to room temperature and to reheat them by some other means before restart.

3.3.3.1.3 *Additional liquid metals*
Some of the additional liquid metal coolants which would become possible if permitted to be solid at room temperature are as follows:

(1) Li, elemental lithium,
(2) Na, elemental sodium,
(3) Pb, elemental lead, and
(4) Pb eutectic mixtures with other metals, e.g.:
    (a) PbLi, a eutectic mixture of lead and lithium,
    (b) PbBi, a eutectic mixture of lead and bismuth.

Lithium melts at about 180.5 C, with small variations for isotopic composition or impurities. At 1 bar pressure it boils at 1,342 C. Thus, liquid lithium at atmospheric pressure could be used to cool the NHTX 600 C first wall and could even accommodate increases of first wall temperature to well above 1000 C. Lithium's electrical conductivity implies that flowing it in the NHTX magnetic field through first wall tubes would entail some pressure losses due to MHD effects. Lithium is available in essentially unlimited quantities and is relatively inexpensive since it is used industrially in batteries and in several other applications. Lithium compounds are not toxic in small quantities and even have medicinal applications, but since lithium is not normally found in the human body it is suspected of being toxic in large doses. Molten lithium is highly active chemically and is flammable in air, in water, in carbon dioxide, and in nitrogen. Molten lithium is compatible with some solid metals but attacks others, e.g., aluminum. Under neutron bombardment some lithium is converted to tritium and helium, but no gamma rays result. Lithium is not otherwise activated by neutrons.

Sodium melts at 98 C. At 1 bar it boils at 883 C. With some pressurization it would remain liquid above 1000 C. Thus, liquid sodium could be used to cool the NHTX 600 C first wall and could accommodate some increase of first wall temperature above 600 C. Sodium is available in essentially unlimited quantities and is inexpensive. There is extensive experience using liquid sodium as a heat transfer fluid. Sodium compounds are not particularly toxic since sodium is found normally in the human body. Sodium has the highest electrical conductivity of all liquid metals, so in the NHTX it would suffer larger MHD flow losses than other candidate fluids, thus increasing its required pumping power. Molten sodium is chemically active and flammable in air or water (but not in carbon dioxide or nitrogen). It is activated by neutrons, producing a gamma ray emitter with a 15 hour half-life.

Lead melts at 327 C. At 1 bar pressure it boils at 1,755 C. Thus, liquid lead at atmospheric pressure could be used to cool the NHTX 600 C first wall and could even accommodate increases of first wall temperature to well above 1000 C. Its low electrical conductivity among metals ensures that its use would not result in high MHD pumping losses. Lead has been used for many applications since Roman Empire days, it is industrially available today in essentially unlimited quantities, and it is inexpensive. Lead is not flammable so it poses essentially no fire hazard. Although lead can accumulate in food chain organisms and in the human body, it apparently serves no biological purpose and it has toxic effects. Molten lead exposed to the air can produce toxic vapors. Leaks or spills would therefore be judged hazardous to humans and to the environment. Activation by neutron capture in lead is not a significant issue. The main product, Pb-209, decays to stable bismuth with a 3.28 hour half life without emitting any gamma rays. The only gamma ray emitter product, an isomeric form of Pb-207, decays to a stable state with a half-life less than one second.

Lead-bismuth eutectic mixtures have been used extensively as coolants in experimental nuclear fission applications. A lead-lithium eutectic mixture has been proposed for experimental modules in the ITER project because it is a nonflammable liquid which carries the lithium material needed for tritium breeding.

3.3.3.1.4 Non-metallic liquids

Molten salts form the other set of liquid coolant options which are solid at room temperature. An important difference between molten salts and molten metals is that the electrical conductivity of molten salts is far less than that of molten metals. As a result, MHD drag effects on the pumping requirements for molten salt liquid coolants in the NHTX first wall would be negligible.

There are many possible molten salt candidates. A common one that has been considered extensively for fusion reactor tritium breeding blankets is a eutectic mixture of lithium fluoride, LiF, and beryllium fluoride, BeF_2, which has sometimes been called FLiBe. Although this could be considered for NHTX, it is not necessary or desired for NHTX to breed tritium so other molten salt candidates could also be considered. Molten salt candidates for a different application were recently surveyed in a 2006 report, **"Assessment of Candidate Molten Salt Coolants for the NGNP/NHI Heat-Transfer Loop"**, ORNL/TM-2006/69, by D.F.Williams of Oak Ridge National Laboratory.   The following molten salt summary table is reproduced directly from that document.

Table 3.3.4: Summary of the properties of candidate coolants for the NGNP/NHI heat-transfer loop

Salt	Formula weight (g/mol)	Melting point (ºC)	900ºC vapor pressure (mm Hg)	Heat-transfer properties at 700ºC			
				ρ, density (g/cm3)	$\rho*Cp$, volumetric heat capacity (cal/cm3-ºC)	μ, viscosity (cP)	k, thermal conductivity (W/m-K)
LiF-NaF-KF	41.3	454	~0.7	2.02	0.91	2.9	0.92
NaF-ZrF4	92.7	500	5	3.14	0.88	5.1	0.49
KF-ZrF4	103.9	390	1.2	2.8	0.7	<5.1	0.45
LiF-NaF-ZrF4	84.2	436	~5	2.92	0.86	6.9	0.53
LiCl-KCl	55.5	355	5.8	1.52	0.435	1.15	0.42
LiCl-RbCl	75.4	313	--	1.88	0.4	1.3	0.36
NaCl-MgCl2	73.7	445	<2.5	1.68	0.44	1.36	0.5
KCl-MgCl2	81.4	426	<2.0	1.66	0.46	1.4	0.4
NaF-NaBF4	104.4	385	9500	1.75	0.63	0.9	0.4
KF-KBF4	109	460	100	1.7	0.53	0.9	0.38
RbF-RbF4	151.3	442	<100	2.21	0.48	0.9	0.28
This table is reproduced from ORNL/TM-2006/69 by D.F. Williams							

Clearly, all but one of these molten salt liquids could be used at temperatures up to 900 C without pressurizing the coolant above 1 bar. Their volumetric heat capacities are within a factor of two of water, and their viscosities are not excessive. It seems appropriate that if liquid coolant substances are to be considered that are solid at room temperature, then the Table 3.3.4 candidates should each be considered for possible use in NHTX.

3.3.3.2   Gaseous coolants

Although when using liquid coolants it is typically necessary to restrict the upper end of the operating temperature range in order to avoid boiling and the subsequent reduction in heat transfer, the situation with most gaseous coolants is different. For gaseous coolants the upper end of their usable temperature range is set by the decomposition or ionization of the gas or by failure of the confining structure. For most gases, decomposition or ionization occurs at a temperature far higher than the operating temperature.

Gaseous coolants have far lower mass densities than liquid coolants and their volumetric heat capacities are therefore correspondingly far lower than those of liquid coolants. Gaseous coolants are typically used at higher pressures than liquid coolants in order to increase their low densities, and their gas flow velocities are typically significant fractions of the sound speed instead of several meters per second. However, in spite of their use of high pressure and high speed, gas cooling typically requires larger passages for cooling flow than liquid coolants for identical heat removal missions. It is also common when using gases for heat transfer to employ extended surfaces (i.e., fins) to increase the surface area between the gas and a solid surface within a limited volume.

Many different gaseous substances could alternatively serve to remove heat from the NHTX first wall. Among them, the two that are discussed further herein are super-heated steam and helium. Each of these gases is remarkably safe compared to alternatives. Steam is attractive both because it is cheap and because commercial off-the-shelf industrial equipment is available to do the entire job, including even the extraction of work energy from the heated steam if that is desired. Helium is attractive because it has special inertness properties. Although both gases should be seriously considered for cooling the NHTX first wall, helium is the recommended choice because its inertness gives it a superior flexibility to accommodate different experiments.

3.3.3.2.1 Steam
Super-heated steam at temperatures higher than water's 372 C triple point temperature can serve as a heat transfer gas, absorbing heat from hotter contacting surfaces while flowing past them. Steam supplied at 300 C or 400 C to tubes embedded in the 600 C NHTX first wall could flow through the tubes, then exit them at a temperature near 600 C. Subsequently, the steam would be cooled either in an external heat exchanger or in a steam turbine followed by a heat exchanger, then would be recompressed and returned to the first wall tubes.

Steam has a high specific heat. It is cheap and readily available in unlimited quantities. It has no environmental consequences if spilled, it is not toxic, it cannot burn, and it would not by itself represent any safety hazard beyond the high temperature first wall heat it would carry. Radiologically, the oxygen in the steam would be activated by NHTX neutrons but the resulting nuclides have a very short half-life.

Super-heated steam is similarly heated in tubes in coal-fired plants driving supercritical thermal conversion systems. According to the March 2006 issue of the online publication, Energy-Focus, the maximum steam temperature in new supercritical coal-fired plants deployed in the 1980s reached 500 C, with typical thermal conversion efficiencies then reaching 48%. The publication goes on to report that since the 1980s there has been significant progress in further extending the maximum steam temperature and pressure so that today the new "ultra-supercritical" steam parameters available for purchase for the newest coal-fired plants have reached 600 C and 300 bar. This temperature matches the expected NHTX first wall operating temperature.

Although there are several steam turbine manufacturers, a review of the internet website of one particular manufacturer, Siemans, did find a steam turbine with almost those high parameters. Siemans' STS-700 steam turbine product line for applications between 10 MW and 130 MW accepts steam at 585 C and 165 bar. The system is not physically small, since as shown on the Siemans internet site the turbine, condenser, and generator together are 22 meters long, 15 meters wide, and 6 meters tall. The turbine's mass alone is 85 tonnes. Although this may appear large, it is a standard off-the-shelf commercial product well suited for recovering the work energy from cooling the NHTX first wall if the first wall were operated at about 600 C. Siemans also sells the associated pumps and other equipment needed to circulate the water and steam in a coal-fired power plant which would be needed as infrastructure for cooling the NHTX first wall using ultra-supercritical steam. It seems likely that as much as 25 MW of the total 50 MW first wall heat load could be converted to electricity for other NHTX uses in this fashion.

Superheated steam could alternatively be used for cooling the first wall even if no work energy were recovered from it. With no turbine, such a system would have a far lower cost. The fact that superheated steam is commercially used on an industrial scale implies that the associated pumps, heat exchangers and other equipment routinely needed to handle it are manufactured and could be purchased off-the-shelf for the NHTX application.

The only negative aspect of using steam as a heat transfer substance is that like many other substances it is chemically active. The oxygen in hot steam can react with metal in the walls of tubes confining it, forming rust or other corrosion products and releasing some free hydrogen. Different metals are corroded at different rates, but corrosion rates are typically accelerated by high temperature operation.

3.3.3.2.2 Helium
Since helium is a gas, the high temperature energy transferred into it from cooling the high temperature first wall could be thermally converted into work to produce electricity or operate other systems. It would only be necessary to operate the helium loop as a closed Brayton cycle, with turbocompressor and turboexpander stages separated on one side by the hot first wall structure and on the other side by a cold heat exchanger dumping the waste heat into the environment. However, there are no commercial off-the-shelf high power turbines and compressors designed specifically for use in helium. The market does not produce them since there is little demand and lower cost alternatives are available. Other turbomachinery might be adapted for helium use but such custom modifications do not seem worth their costs for only this NHTX application. Thus, helium cooling will certainly not attempt to recover work energy from the NHTX first wall's high temperature heat.

Helium has very high specific heat and thermal conductivity, facts which help make it an excellent heat transfer fluid among gases. However, the main advantage of helium cooling for the NHTX first wall application is that helium gas is a truly inert substance. As a noble gas it does not chemically interact with any material and it has no biological effects on living organisms. Its use guarantees no adverse materials compatibility issues

and no fire hazards. It can even be used safely in direct contact with such chemically active substances as molten lithium. Since its atomic number is only 2, if it were to leak out into the plasma it would not have the same deleterious effect on energy confinement as a high atomic number impurity, and its lack of chemical activity implies it would not be retained by plasma-facing material surfaces. Furthermore, in contrast to other noble gases helium is also inert to activation by neutrons. Thus, regardless of the nuclear or chemical environment, any accidental release of helium coolant is guaranteed to have no safety or environmental impact whatsoever. It is even difficult to imagine any hazards to equipment imposed by helium use. The only negative aspect of helium is its expense. In addition to its initial cost, helium will leak away through passages so narrow that other gases do not leak through them.

3.3.4   Options for the cooling system's overall configuration

Since gases are compressible, it is possible to configure a thermal conversion system to directly extract work energy from the heated gas coolant. With a liquid coolant, such extraction of work energy would require coupling an additional gas loop to the liquid loop. The extraction of work from a gaseous first wall coolant could follow the Brayton Cycle which is configured according to the following schematic diagram. The gas would circulate in a loop, cycling between a high pressure heat exchanger in thermal contact with the plasma first wall and a low pressure heat exchanger in contact with the environment (e.g., the outdoor air). The pressure difference would be maintained by a turbocompressor and a turboexpander mounted on a common shaft. Because expander work exceeds compressor work, the turbine would drive both the compressor and an additional electrical generator which would produce electrical power for other uses.
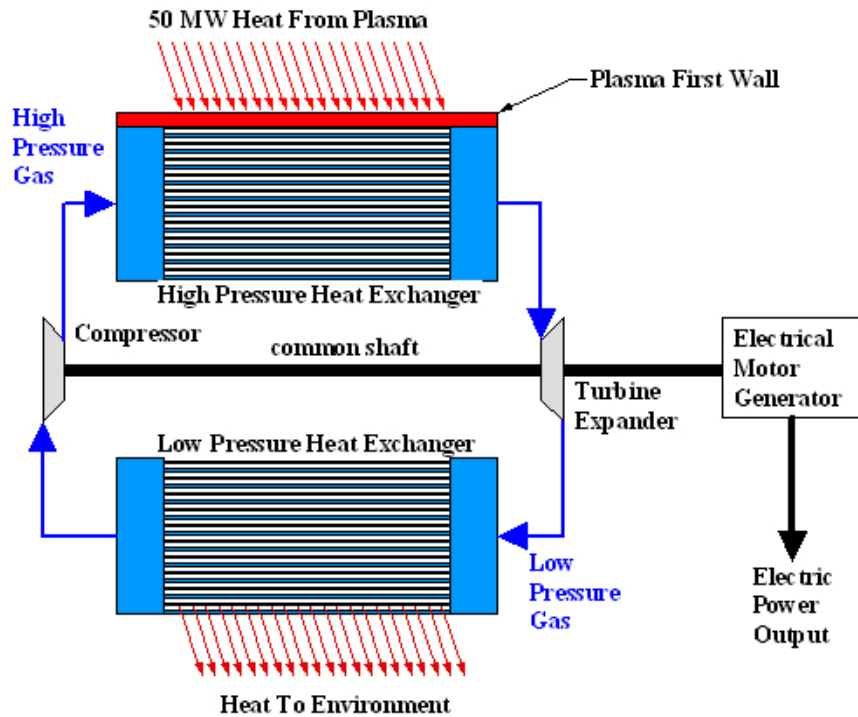
Figure 3.3.7: First Wall Cooling System With Work Recovery

Although this could certainly be accomplished, it is likely not cost-effective to recover useful work from the high temperature first wall heat.. In order for this scheme to work the rotating turbocompressor and turboexpander components must be capable of providing a sufficiently large ratio between the high and low gas pressures so that the corresponding adiabatic temperature changes they produce in the gas by compression and expansion approximately match the difference in temperatures between the first wall and the external environment. Furthermore, the rotating components must produce their pressure ratio with sufficiently low energy losses that they approximate adiabatic processes. Components capable of such operation are expensive. In their normal power-plant use their high cost is defensible based on their continuous production of power, but NHTX will only operate with a low duty cycle. In addition, a system relying on this scheme for first wall cooling would likely be configured for only a small range of first wall operating temperatures, thus reducing experimental flexibility to try out different first wall temperatures.

The following schematic diagram depicts a gas cooling scheme for the NHTX first wall which does not attempt to recover useful work from the high temperature heat. With only terminology changes this schematic could also describe a liquid cooling scheme .
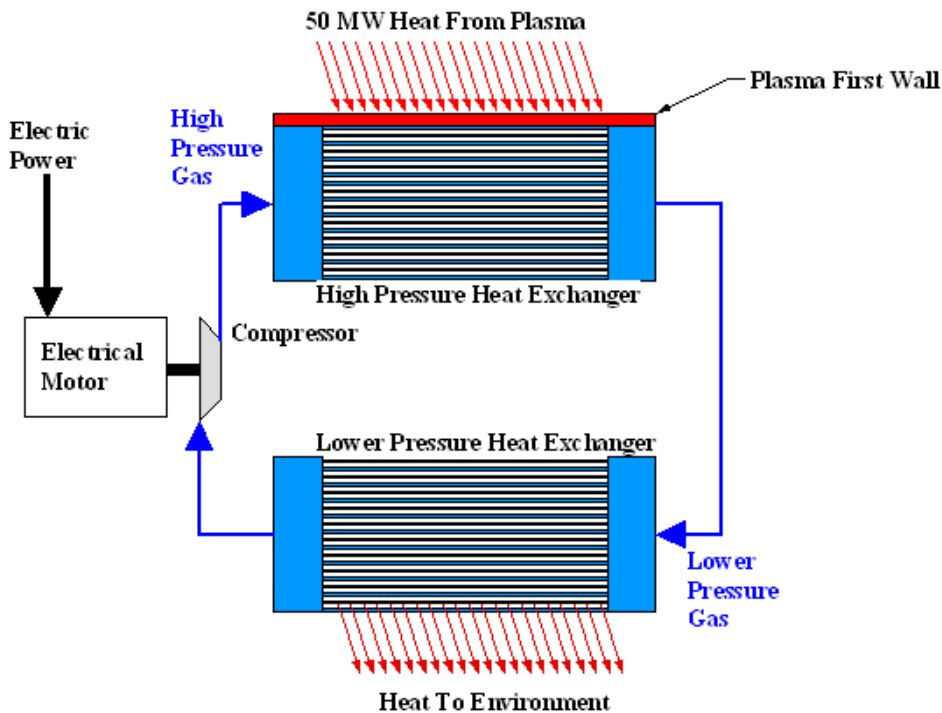
Figure 3.3.8: First Wall Cooling System Without Work Recovery

In this scheme the low pressure gas portion of the loop has been eliminated along with the turbine expander. Gas pressure is everywhere high, with the only pressure variations

resulting from flow friction effects which make the pressure slightly higher at the first wall's heat exchanger and slightly lower in the external heat exchanger. The small pressure drop developed in the loop implies that a small compressor can be used, although there would be a high background pressure for bearings and rotary seals to withstand. Since there are no thermodynamic constraints, any inexpensive compressor technology could be used even if not particularly energy-efficient.

Although it is expected that the NHTX will be operated for long durations lasting up to 1000 seconds in which the plasma and plasma-facing surfaces essentially reach steady-state conditions, control of the first wall temperature will require more than a steady-state cooling system design. The heat load from the plasma to the first wall will vary transiently, increasing from zero before plasma initiation to 50 MW after the plasma has been started, and later decreasing from 50 MW back to zero when the plasma is terminated. In addition to these large step changes in heating power, there may be other transient first wall heat load variations for particular NHTX plasma experiments.

The desired NHTX first wall thermal control system behavior is to hold the plasma first wall temperature as close to a constant value as practical, regardless of the transient variation in its heat load. If a high mass flow rate liquid coolant were used, it might be sufficient to continue supplying coolant to the first wall at a constant temperature and flow rate and to simply accept the resulting small first wall temperature changes as the heat load is cycled. However, the lower heat transfer available with gas cooling implies hundreds of degrees of temperature difference between the gas and the first wall in order to remove 50 MW of heat. Thus, if the gas coolant were supplied to the first wall at a constant temperature the first wall temperature would change by hundreds of degrees when the plasma heating is started or stopped.

For a cooling system using a gas to more precisely regulate NHTX first wall temperature, the temperature of the gas supplied to cool the first wall must be dynamically controlled to vary inversely in tandem with changes in the total plasma heating power. As the plasma heating is increased the temperature of the supplied first wall cooling gas should proportionally decrease so that the resulting first wall temperature remains constant. However, there are practical difficulties in dynamically maintaining this balance so transient temperature regulation of the first wall will be only approximate.

The main practical problem is that the natural time scales for heating and cooling variations are different. Plasma heating systems are capable of increasing their heating power through their full range in milliseconds or less, but cooling a gas requires more time. The option of censoring fast changes in plasma heating power so that gas temperature can keep up with it is unattractive since that would restrict plasma control.

There is a design option of controlling the supplied gas temperature in a way similar to how water temperature is adjusted in a bathroom shower by adjusting the mix of cold and hot water drawn from different sources. Separate reservoirs of cold and hot gas could be available for first wall cooling and could be mixed through dynamically adjustable valves in order to quickly change the temperature of gas coolant supplied to the first wall.

However, a careful examination of the necessary associated system details suggests that this dual gas approach would be excessively complicated and expensive to implement.

The best design option may be to adopt a strategy of anticipatory control of gas temperature to match *expected future* (e.g., several seconds later) plasma heating power, and to combine that strategy with a gas cooling system whose cooling action can be quickly (e.g., in several seconds) adjusted through a wide range. For the cooling of liquid or gas fluids hotter than 100 C, heat rejection based on rapid water evaporation is possible. Liquid water could be sprayed directly onto the outer surfaces of heat rejection cooling tubes where it would flash into steam, thus cooling the tubes almost instantly and as a result quickly changing the cooling of the gas flowing inside the tubes as the water spray rate is changed. Sudden changes in the water spray rate would cause a very rapid change in the temperature of the cooled gas flow emerging from the tubes. This scheme is depicted in the following schematic diagram. This diagram also shows electrical heaters to be operated when the plasma heaters are off during the time intervals between NHTX plasma "pulses" in order to offset radiant heat losses from the first wall and thus maintain the first wall's high temperature without plasma heating.
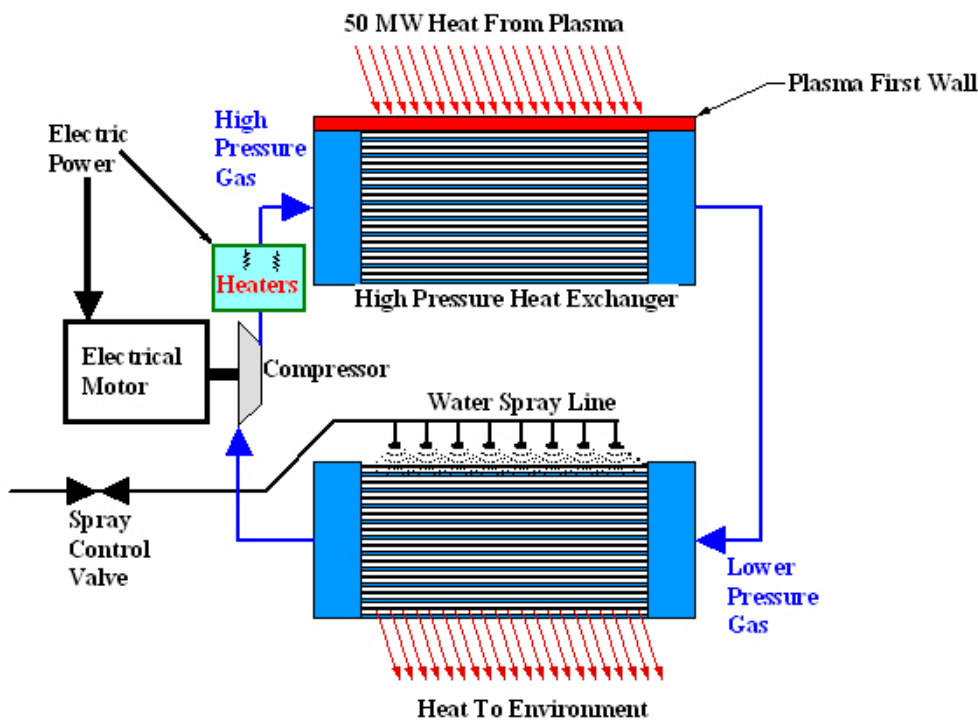
Figure 3.3.9: First Wall Cooling With Quick Response to Heating Changes

3.3.5   Analysis of cooling the first wall with helium
The present section documents some calculations evaluating the prospects of first wall cooling using helium. Differential equations for high speed gas flows in a duct with both friction and heat transfer are solved numerically. Its results show that helium cooling

within the allocated space appears feasible but additional space allocated for cooling might allow improved thermal performance.

Analysis of cooling is in general more complicated for a gas coolant than for a liquid coolant. For cooling with an incompressible liquid, the heat transferred to the liquid from the duct's walls by thermal conduction and by friction is matched by the liquid's temperature rise, and the liquid's pressure drop and flow rate can be determined by separate calculations. In contrast, the compressibility of gases intimately links their temperature and pressure effects. The pressure drop directly produced in a subsonic gas flowing in a duct by friction with the duct walls causes the gas to expand (i.e., according to the ideal gas law) which in turn causes the gas flow speed to accelerate as it progresses along the duct. As the gas expands it also cools due to internal adiabatic thermodynamic effects, so the temperature of the expanding flowing gas can be colder at downstream locations in a duct than it is at the duct entrance. Friction with the duct walls also adds some heat which increases gas temperature and thereby increases its volumetric expansion, thus accelerating the gas to even higher speeds as it progresses. Heat transferred optionally through the duct's walls to the gas increases this gas acceleration process further, so the gas velocity, temperature and pressure at the duct's exit can depend sensitively on the heat transferred through duct walls. On the other hand, the quantity of heat transferred depends sensitively on the difference between gas temperature and duct wall temperature as well as on the gas velocity. Thus, the necessary sophistication of accurate heat transfer calculations for compressible gases is greater than for incompressible liquids.

To accurately analyze a first wall cooling system using helium requires a simultaneous mathematical treatment of the helium's pressure, temperature, flow speed, wall friction, and heat transfer from the wall. It turns out to be useful to transform from these variables to a different equivalent set in which the differential equations can be stated more simply. The 1-D differential equations solved numerically for this present analysis follow the textbook, Compressible Fluid Flow by Michel A. Saad, and in particular, this text's section 6.10 FLOW IN A FRICTIONAL CONSTANT AREA DUCT WITH HEAT TRANSFER. Instead of directly analyzing changes in gas flow speed, Saad's equations transform variables to state the speed evolution in terms of changes in the local Mach number, M, the ratio of gas flow speed to the local speed of sound which itself varies with gas temperature. Instead of directly analyzing changes in gas temperature the equations are stated in terms of changes in the "total temperature", T_o , sometimes alternatively called the "stagnation temperature", which is the temperature that the local gas would reach if it were adiabatically brought to rest. Saad's differential equations follow.

Evolution of Mach Number:

$$\frac{dM^2}{M^2} = \frac{\left(1+\kappa M^2\right)\left(1+\frac{\kappa-1}{2}M^2\right)}{1-M^2}\frac{dT_o}{T_o}$$

$$+\frac{\left(\kappa M^2\right)\left(1+\frac{\kappa-1}{2}M^2\right)}{1-M^2}\frac{4f}{D}dx$$

Evolution of total gas temperature:

$$\frac{dT_o}{T_w-T_o} = \frac{4h_c}{\rho v c_p D}dx$$

In these equations, x denotes the distance along the duct from the duct entrance, κ is the specific heat ratio which for helium is the constant value $\kappa=5/3=1.6667$, D denotes the hydraulic diameter of the duct, i.e., 4 times the area of its inner cross section divided by its inner perimeter, T_w is the wall temperature of the duct, ρ, v, and c_p are respectively helium's gas density, speed, and specific heat at constant pressure, h_c is the heat transfer coefficient governing heat flow from the walls to the helium gas, and $4f$ is Moody's friction factor, an empirical function of Reynolds number and wall roughness. Regrettably, there are two technical traditions for the definition of Moody's friction factor, frequently represented as f for liquids while the same quantity is represented as $4f$ for gases, as appears here. Either can be used if internal consistency is maintained.

Helium gas density obeys the ideal gas law:

$$\rho = \frac{p}{RT}$$

where p is the gas pressure in Pascals, T is the gas temperature in Kelvins, and the gas constant for helium is R=2077.1 J/kg-Kelvin

Conversion from Mach number to gas speed requires the speed of sound, which varies with true gas temperature according to the following formula:

$$c_s = \sqrt{\kappa RT}$$

Conversion from total temperature to true temperature is given by:

$$T = \frac{T_o}{1+\frac{\kappa-1}{2}M^2}$$

Energy conservation requires the local heat transferred must match the local increase in gas energy density in terms of its total temperature:

$$d\dot{Q} = \dot{m}c_p dT_o$$

To close these equations the heat transfer coefficient must be further defined. An approximate relation which is frequently invoked in analyses of heat transfer to gases is

Reynolds Analogy:

$$\frac{h_c}{\rho v c_p} = \frac{f}{2}$$

which expresses the heat transfer coefficient in terms of Moody's friction factor. Substituting this into the temperature evolution equation gives:

$$\frac{2dT_o}{T_w - T_o} = \frac{4f}{D} dx$$

Instead of manually using the famous graph of Moody's friction factor, computer calculations use one of the approximations to it that have been developed. For turbulent flow portions of the graph and for smooth duct surfaces, the one used here is due to vonKarmen-Nikuradse. This approximation is transcendental and can be solved numerically for the friction factor $4f$ via Jacobi iteration.

$$\sqrt{4f} = \frac{1}{2\log_{10}\left(\mathrm{Re}_D \sqrt{4f}\right) - 0.8}$$

where Re_D is the local Reynolds number of the flow, given by

$$\mathrm{Re}_D \equiv \frac{\rho v D}{\mu} = \frac{4\dot{m}}{\mu(\mathrm{Perimeter})}$$

$$= \frac{4}{\pi} \frac{\dot{m}}{\mu D} \quad \text{for circular ducts}$$

where v is the gas speed, mdot is the mass flow rate which is constant along the duct, and μ is helium's viscosity which varies as a function of its temperature as shown in the following plot.
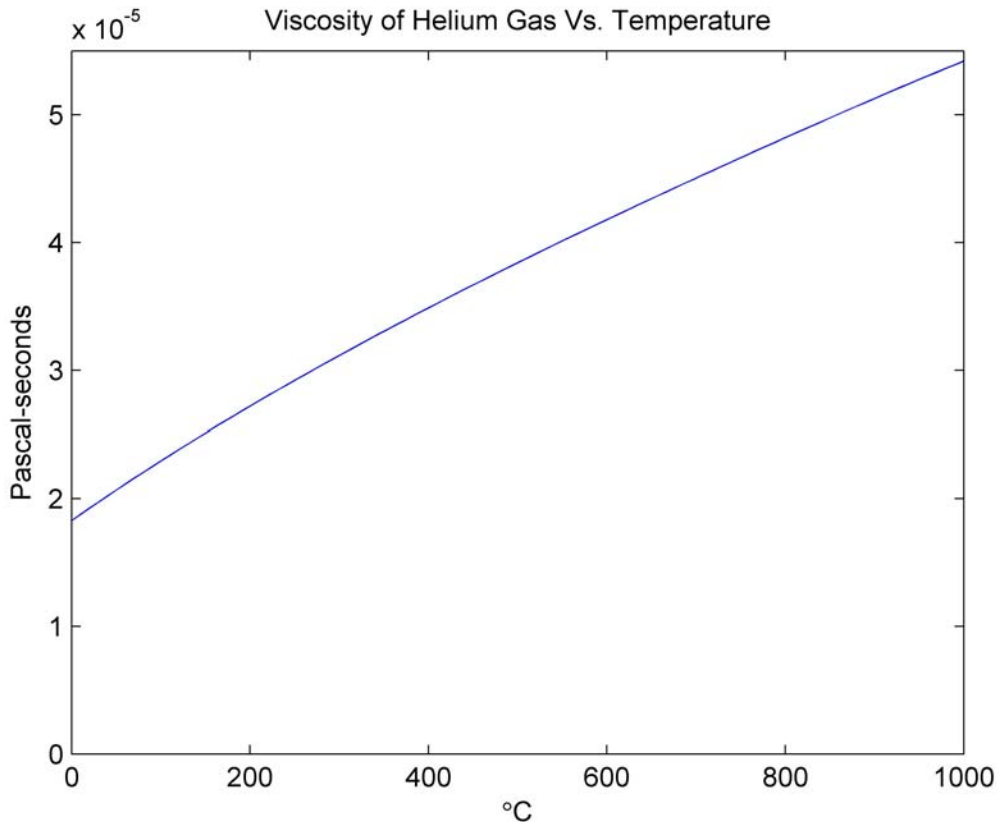
Figure 3.3.10: Helium Gas Viscosity Vs Temperature

Thus, the Reynolds number only varies along the constant area duct because of changes in gas viscosity, which in turn is only affected by gas temperature. We note that the Reynolds number of 200 bar=20 MPa helium at 873 Kelvins=600 C flowing in a circular duct of D=4.572 mm at a speed of 828.7 m/s is $Re_D=10^6$.

The Appendix documents MATLAB code which numerically solves these differential equations which describe duct flow with friction and heat addition for particular cases. The following contour plot interpolates between results of 360 different solution cases computed by that code in order to show the performance of cooling systems configured with 6-meter lengths of tubing having an I.D. of 4.572 mm, with the helium inlet gas pressure fixed at 200 bar consistent with the capability of commercially available quarter-inch O.D. stainless steel tubing operating at 600 C. Since the poloidal perimeter of the first wall is almost 10 meters, it is expected that 6 meter tubing lengths could be sufficient if two toroidal gas manifolds are used, i.e., one inlet and one outlet.

Each of these calculations began by assuming values from a 15 X 24 grid of gas temperatures and gas speeds at the inlet to a single 6-meter long tube, and assumed the tube wall was held uniformly at 600 C. Each calculation then solved for the profiles along the tube length of Mach number, total gas temperature, friction, gas speed, true gas temperature, gas pressure, and local heat flow. For each case the calculated total cooling rate integrated along the entire tube was then divided into 50 MW to determine how

many tubes would be needed to absorb the total first wall heat load. Taking the coverage area of each tube on the first wall to be the product of its 6-meter length and its 0.00635 meter outer diameter, the total coverage of all the tubes needed for 50 MW cooling was calculated as the product of the number of tubes times the coverage area of one tube. The total mass flow was then calculated as this number of tubes times the mass flow rate of one tube. Total pumping power was calculated under the assumption that exiting gas is first isobarically cooled to the gas inlet temperature then isothermally recompressed to 200 bar. Therefore the pumping power was calculated as the product of the total mass flow rate, helium's gas constant, the absolute gas temperature at the inlet, and the natural logarithm of the pressure ratio.

Axes in the following contour plot are the assumed duct entrance conditions, i.e., the helium inlet's temperature and speed. For 50 MW total heat removal, the calculated pumping power needed is indicated by the dashed red contours while the calculated first wall area coverage by the bundle of tubes is indicated by solid black contours. It should be noted that the total NHTX first wall area is only about 62 m^2 minus missing areas for ports and other penetrations, so all coverage area contour values greater than about 50 m^2 would require tubing to be configured in multiple layers. However, the present NHTX space allocation provides only enough room for a single layer of quarter-inch O.D. tubing, so coverage values greater than 50 m^2 imply a NHTX space allocation redesign.
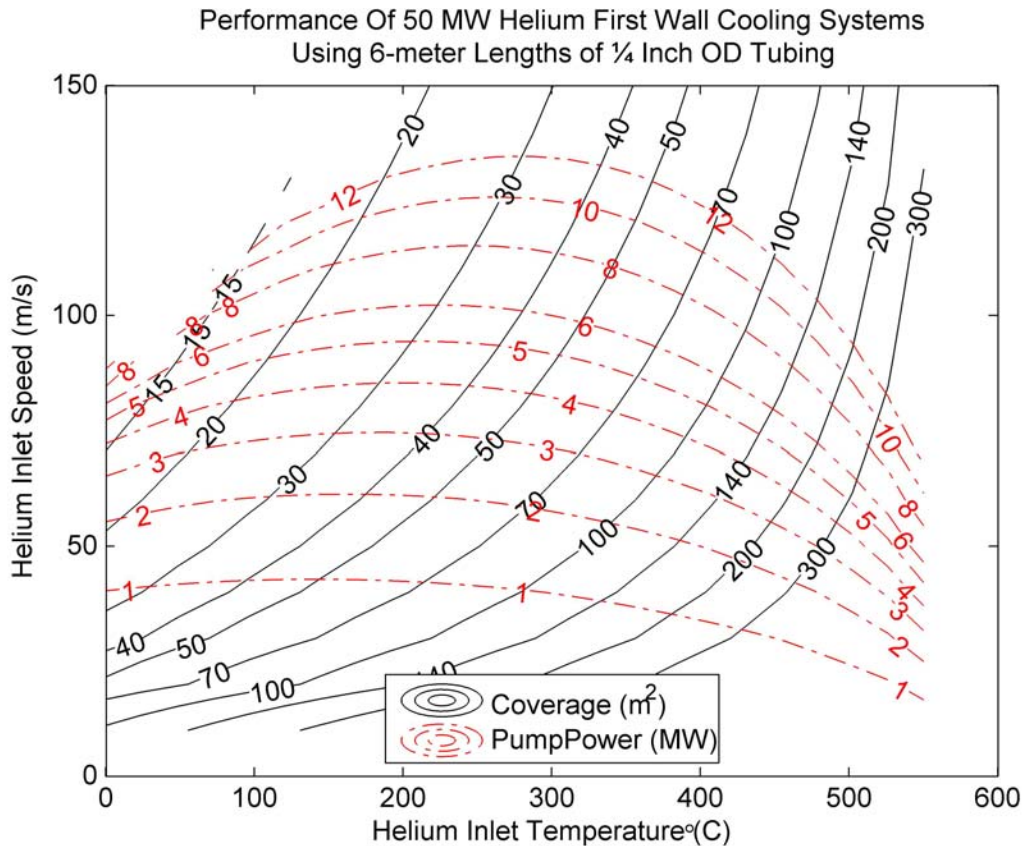
Figure 3.3.11: First Wall Cooling By He Gas in 6 Meter Lengths 0.25 Inch OD Tubes

The situation is different if we instead use 2-meter lengths of quarter-inch O.D. tubing to cool the first wall.   We note that would require at least six appropriately located toroidal manifolds in order to use 2-meter tubing lengths, and there may not be sufficient allocated space for six toroidal manifolds or for large access pipes to reach them from ports, especially on the inboard side of the plasma.   Nevertheless, a summary plot interpolated from 360 calculated cases of options using 2-meter lengths of the tubing is as follows:
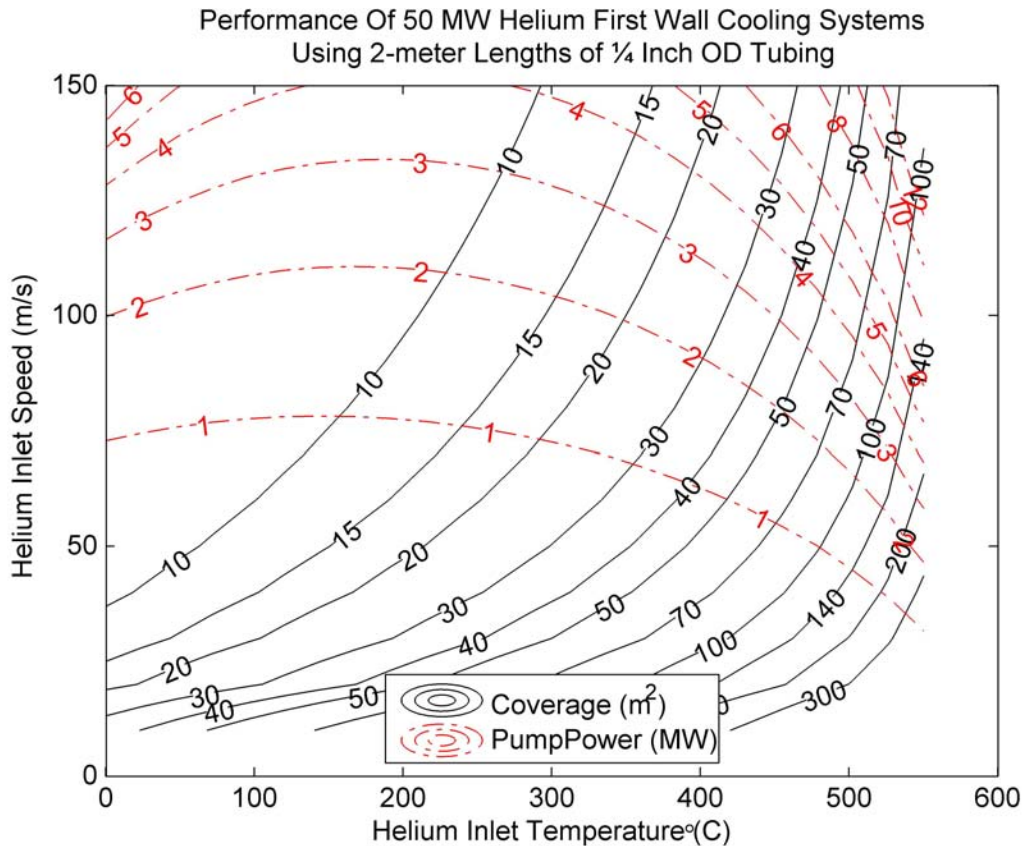
Figure 3.3.12: First Wall 50 MW Cooling By He Gas in 2 Meter Lengths 0.25 Inch OD Tubes

An inspection of calculated profiles along tube duct lengths calculated for particular cases shows they predict most of the cooling will occur near the tube's entrance rather than distributed evenly along the tube's length. For example, the following graph shows the calculated profiles of Mach number, total temperature, and linear cooling density versus position for a 6-meter length of quarter0inch O.D. tubing with gas entering the tube at a 100 C temperature and 100 m/s speed. These are inlet conditions for which the previous contour plot for 6-meter tubing lengths asserts 50 MW of heat removal can be accomplished with less than 20% of the first wall covered by tubes. The following graph shows that within those tubes most of the heat would be removed by only the small part located near entrances.

Duct Flow With Friction And Heat Addition
Inlet Helium 200 bar 100°C 100 m/s, Duct Diameter 4.572 mm
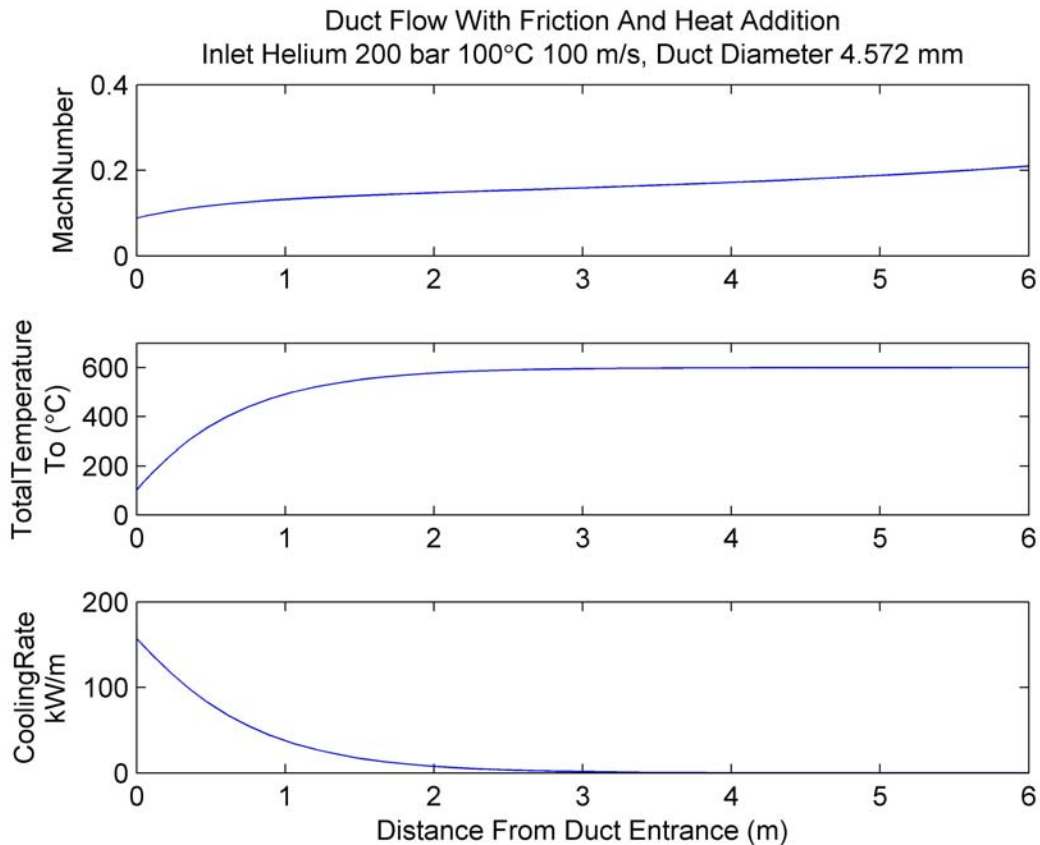
Figure 3.3.13: Helium Gas Cooling Profiles for Particular Design Example

To understand this, it should be noticed that for constant values of the friction factor, the temperature evolution equation predicts an exponential approach of gas total temperature to a constant wall temperature as the gas moves down the duct, with an e-folding "decay" length of $D/(2f)$. For Reynolds numbers in the range between 10^5 and 10^7, which essentially covers the entire range of interest for first wall helium gas cooling, the value of $(2f)$ from Moody's graph for smooth pipes only varies from about 0.004 to 0.009. Therefore, for a quarter inch O.D. tube with inner diameter 4.572 mm the e-folding distance for equilibration of total temperature to a constant wall temperature would be in the range from 0.5 meters to 1.1 meters. This suggests that quarter-inch OD tubing lengths as long as 6 meters or even 2 meters would inefficiently concentrate most of their cooling action within the first meter closest to their entrances. This result suggests that shorter tube lengths would be more effective, which is also consistent with a comparison of the two contour plots, i.e., the plots describing cooling system performance with 6-meter and with 2-meter tubing lengths.

However, there is not enough modeled detail here to conclude that nonuniform cooling is a problem. The actual tubing temperature profile will not be constant as assumed in this analysis but instead will vary along the duct's length as a result of the nonuniform power deposition profile and other effects. It may be better to locate tubing duct entrances close to expected high heat flux locations, e.g., near divertor strike locations. Also, temperature drops in the first wall structure due to heat conduction will alter this result

and may partially smear out the high heat transfer cooling zones into larger regions. Thus, the present analysis should be interpreted only as confirming feasibility that a helium gas cooling system for the first wall could globally remove the full 50 MW of heat. The cooling system still needs to be designed in its full 3D detail and a full 3D thermal analysis of it including spatial profiles of deposited heat needs to be performed. But it may turn out to be necessary to change the space allocation in order to provide more room for helium flow pipes and manifolds in order to achieve an effective design.

3.4 Magnets and their structural support systems

3.4.1 Overview

The NHTX toroidally shaped plasma is confined by the same general type of magnetic field structure that is common to all tokamaks. Nominally, such structures are rotationally symmetric, i.e., the magnetic field components, (B_r, B_φ, B_z), when expressed in a particular (r, φ, z) cylindrical NHTX coordinate system, each vary as functions of (r, z) only, independent of φ. Such cylindrically symmetric magnetic field functions are usually considered to be the vector sum of a Toroidal Field component, $(0, B_\varphi, 0)$, and a Poloidal Field component, $(B_r, 0, B_z)$, where each component is a function of (r, z) only. This decomposition into toroidal and poloidal components neatly simplifies magnetic field production into separable pieces. As with all tokamaks, comparable magnitude toroidal currents flow in the plasma and in a system of Poloidal Field magnet coils external to the plasma in order to generate the Poloidal Field. Separately, the Toroidal Field results from poloidal currents flowing mainly in the Toroidal Field Magnet System, but is also locally affected by poloidal current components flowing in the plasma.

As in most tokamaks the NHTX Toroidal Field magnet system actually is not perfectly axisymmetric. Its use of 10 outer legs returning Toroidal Field magnet system currents confers a ten-fold rotational symmetry instead of axisymmetry. However, the system conductors' geometry guarantees that the resulting Toroidal Field "ripple" departures from axisymmetry are small in the vicinity of the plasma.

By designing each magnet system as multiple turns electrically insulated from each other and connected in series, the current driven through magnet coil leads can be kept within ranges for which electrical power converters are commercially available at reasonable cost. Multiturn designs are therefore used in the NHTX for both the Poloidal and Toroidal magnetic field systems. The numbers of turns chosen for the Poloidal Field components are selected to match capabilities of the existing thyristor power conversion modules available at the PPPL site. Twenty turns are used in the Toroidal Field system.

The Poloidal Field (PF) magnet coils in the NHTX are located inside the Toroidal Field (TF) system adjacent to the plasma, thus providing superior flexibility to configure different plasma experiments while also reducing out-of-plane forces on the TF system components. However, since the two magnet systems are then linked, this requires either that they must be wound in place or that one of them must be demountable with internal electrical joints. In the NHTX, the Poloidal Field system is configured with complete Poloidal Field coils while the Toroidal Field magnet system is configured with modular conductors joined by demountable electrical joints.

All NHTX magnet systems are constructed from Oxygen Free High Conductivity (OFHC) copper conductors. All operate near ambient temperature and are water-cooled. Except for the "OH Solenoid" coil which only briefly operates at high field for plasma initiation, all other magnet components employ water-cooling designed to permit them to operate in thermally steady-state conditions at their full magnetic field capability. The

use of water-cooled copper instead of superconductors for NHTX magnet systems confers the following advantages:

- Copper conductors allow an internal Poloidal Field coil set (since demountable superconducting joints have never been developed).
- Copper conductors avoid the expensive engineering development needed for superconducting magnet designs.
- Copper conductors allow inexpensive magnet construction.
- Copper conductors avoid any possibility of superconductor quench events and the need to detect and mitigate them with additional expensive equipment.
- Copper conductors operating at ambient temperature reduce the need for radiation shielding and thermal insulation between the plasma and magnet components.
- Copper conductors operating at ambient temperature avoid the need for expensive cryogenic refrigeration systems.
- Copper conductors operating at ambient temperature avoid the need for the very long lost-time durations needed with superconducting magnet systems for cool-down to cryogenic temperature or for warm-up to room temperature.

The only disadvantages incurred by the NHTX use of water-cooled copper conductor magnet technology are the costs associated with the high electrical power dissipation in the magnets. During the magnets' operations, sufficient electric power must be purchased from the local electric utility company and drawn in real time from the electric power grid without causing excessive grid voltage transients. It also must be converted and conditioned by local equipment to the proper voltage and current levels to drive the magnets. At the same time, pumped cooling water flowing at high speed must remove heat from the magnets as fast as the heat appears there due to power dissipation in the copper. The heated cooling water which exits from the magnets must flow into a large external holding tank, which must later be recooled during the time intervals between successive NHTX experiments by rejecting heat to the atmosphere via cooling towers. Each of these is somewhat costly. However for the NHTX, which is expected to confine a plasma for less than two percent of each operating year and for which auxiliary plasma heating systems will consume more power from the electrical grid than the copper magnets, these costs associated with the water-cooled copper magnets are less expensive than alternatives using superconductors.

Design issues with NHTX copper magnets include:
- magnet and support system construction methods and costs,
- support of primarily magnetic forces and the resulting mechanical stresses,
- demountable electrical joint design details and the resulting joint performance,
- total electric power dissipation,
- external access between magnets to plasma (e.g., for neutral beams, vacuum pumping, plasma diagnostics, etc.)
- heat removal via forced convection cooling water.

To some extent, each of these design issues has been faced and addressed in previous tokamak designs. To the extent feasible, magnet construction will use proven methods adapted as needed for the NHTX mission, and will use standard size materials which do

not require special manufacturing. At the chosen design point, no steady magnetic field strength exceeds 7 Tesla, so mechanical support requirements and materials stress limits do not need to approach any technological challenges. Various demountable joint designs have been deployed on different tokamaks in the past and have sometimes proven challenging, so a new demountable joint design is proposed herein for the NHTX.

Perhaps the most novel aspect of the NHTX magnet designs is that they must operate thermally in steady-state at their full design field. However, this is not really a new situation. Industrial water-cooled copper magnets for many years have been designed for full steady-state operation but few have been deployed in closed-confinement fusion research. On the other hand, Toroidal Field systems for tokamaks have been designed for thermally steady operation at a *reduced* field level. For instance, the TFTR's Toroidal Field system which was design rated at 5.2 Tesla for pulsed operation was also required to operate at 1.0 Tesla in thermal steady-state.

Steady operation of copper electromagnets implies costs for the electric power. Given any fixed design for a toroidal plasma's geometry and confining magnetic field, the amount of electric power needed to steadily operate resistive magnets producing that field varies in inverse proportion to the volume allocated for their copper conductors. Therefore, the NHTX will use massive copper conductors in order to limit electric power.

A magnet design with the lowest possible total electric power would need to totally surround the plasma with thick layers of insulated conductors. However, that would not permit any external access to the plasma. Thus, there is an inherent trade-off between minimizing magnet electric power dissipation and providing access to the plasma. The design point plasma and magnet parameters chosen for NHTX reflect the results of a trade-off study apportioning space between the Toroidal Field magnet system's outer legs and the existing neutral beam plasma heating systems remaining from the TFTR project, which have a fixed beam geometry that cannot be adjusted. Widths and depths of the ten Toroidal Field system's outer legs were chosen so that neutral beams from the existing equipment can intercept the plasma at desired tangency radii with some flexibility for adjustments. These width and depth dimensions were then adopted for the remainder of the Toroidal Field magnet system's current return paths, reduced only to taper as needed in their approach to the central axis where the Toroidal Field system conductors are assigned to fill all available space. Electrical power dissipation in the Toroidal Field system is then fixed by this geometry.

As of the present time, no similar trade-off study has yet been made between assigning space to the NHTX magnet systems versus assigning it to vacuum pumping ducts, plasma diagnostics, radio frequency heating systems, or any other NHTX equipment. It is conceivable that such studies might find it advantageous to further reduce the space allocated to copper magnets and accept the associated increase in electrical power dissipation in favor of allocating more space to a different NHTX system.

3.4.1.1 General Considerations For Water-Cooled Copper Electromagnets

Thermally steady-state removal of heat by cooling water flows is an essential design aspect of each magnet system conductor, excepting the OH Solenoid used only for plasma startup. It is therefore discussed here. For the design of thermally steady-state water-cooled coil systems, the thermal quantities of interest are the conductor's peak temperature and the conductor's average temperature. The peak temperature is important because it must not exceed capabilities of coil materials, of which the most limiting is typically the insulation. Insulation materials for wound magnet coils are now becoming available which maintain their properties at temperatures up to 150C, so 150C may be taken as the design limit for peak copper temperature. Ceramic insulation materials with higher temperature limits are excluded from consideration because they are brittle and would therefore require special magnet design and construction features.

Average conductor temperature is not similarly constrained but is important because copper's electrical resistivity increases linearly with temperature as per the following plot, causing electrical power consumption to increase in direct proportion. For example, a magnet operating at an average conductor temperature of 75C consumes about 20% more electrical power than it would at 25C carrying the same electrical current.
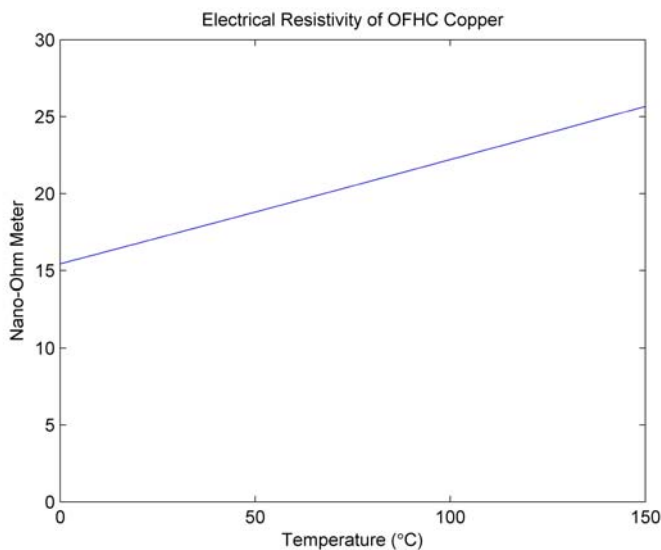
Figure 3.4.1: Temperature-Dependent Copper Resistivity

Each location in a water-cooled coil steadily operating with constant current develops its own characteristic temperature elevated above the temperature of the supplied cooling water. The temperature rise of each location over the temperature of the supplied cooling water can be analyzed by approximations decomposing it into the sum of three separate component parts:

   (1) Bulk temperature rise of the flowing cooling water,
   (2) Film heat transfer temperature drop from copper to water, and
   (3) Cross-conductor temperature gradient due to copper's thermal conductivity.

Although it is only approximate, this thermal decomposition is important because for approximate design calculations each component part of the temperature rise can be simply estimated without considering the others in detail. Heat flow is modeled as flowing through the copper in a plane perpendicular to the cooling water flow direction, then through the film into the water. Of course, later design verification analyses should confirm results with full 3D analyses modeling nonlinear properties and phenomena.

Bulk temperature rise of the cooling water is a simple ratio of P, the power dissipated in the conductor being cooled, divided by the product of water's specific heat capacity with the mass flow rate of water in the cooling passage. The heat capacity of water in the temperature range between 10C and 70C is about 4180 J kg^{-1} Kelvin^{-1}, while water's density is about 990 kg m^{-3}. Assuming that cooling water is supplied to magnets at 10C and exits the magnets at about 70C, the bulk water temperature rise of 60C would absorb about $2.5*10^8$ J/m^3 of thermal energy. Thus, each liter per second of cooling water flow could remove about 250 kW of heat. Cooling water speeds commonly used in past designs for magnet systems have frequently been about 3 m/s but some have been as high as 10 m/s, the target water speed adopted for magnets in the NHTX. It should be noted that even at 10 m/s, a single circular cross section coolant passage would need to be 11.3 millimeters in diameter in order to carry water flows as large as 1 liter per second. At that speed a one millimeter diameter coolant passage would carry slightly less than 0.008 liters per second, so could only remove about 2 kW with a 60C bulk temperature rise. However, this 60C temperature rise implies there would be a location near the water exit where the film heat transfer temperature drop and the cross-conductor temperature gradient drop must each be added to the 70C exit water temperature without the resulting sum exceeding the 150C insulation temperature limit. That may be difficult to achieve in some situations. It may be necessary in design situations with large film heat transfer temperature drops or with large cross-conductor temperature gradient drops to decrease the bulk water temperature rise by further increasing water flow.

To estimate the other two temperature drop components, which correspond to heat flowing perpendicular to the water flow direction, it is useful to calculate the linear heat transfer density, P/L, where P is the total heat dissipated in the conductor being cooled and L is the water cooling path's length. This ratio quantifies the intensity of heat flowing to the water in the plane perpendicular to the water flow direction.

The thermal flux transferred through the film to the water (in W/m^2) is equal to the (P/L) ratio further divided by the cooling passage's perimeter, (πD). The film heat transfer temperature drop is then calculated as the ratio of this thermal flux divided by the film heat transfer coefficient. In turn, the film heat transfer coefficient varies as a function of hydraulic flow conditions and is augmented greatly by turbulence in the flow. Heat transfer coefficients are significantly poorer without turbulence, so it is important to ensure that cooling flow is turbulent. Turbulent flow can occur with Reynolds numbers as low as 3,000, but is guaranteed to always occur for Reynolds numbers at or above 10,000. Thus, water-cooled magnet designs should guarantee the Reynolds number exceeds this turbulence threshold, i.e. :

$$\mathrm{Re} \equiv \frac{VD}{\nu} \geq 10^4$$

where V is the bulk average speed of the flowing water, D is the hydraulic diameter of the cooling passage, and ν is water's kinematic viscosity which varies as a function of temperature as per the following plot.
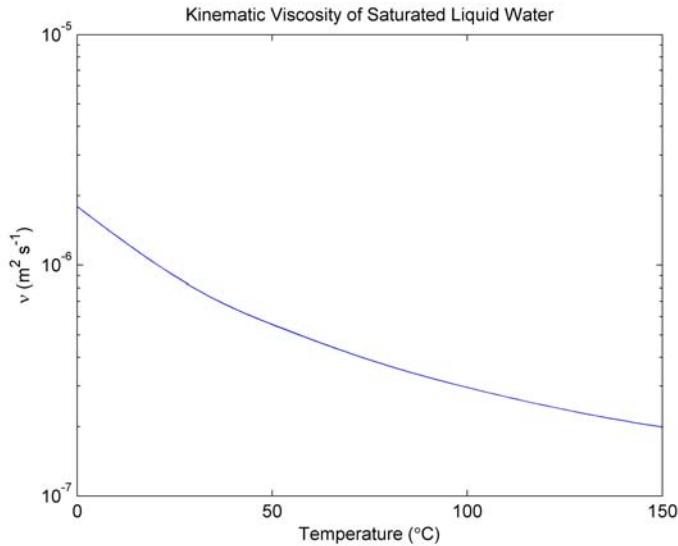
Figure 3.4.2: Temperature-Dependent Viscosity of Cooling Water

A minimum cooling passage hydraulic diameter must be exceeded in order to guarantee turbulent flow:

$$D \geq 10^4 \frac{\nu}{V} \tag{2}$$

To numerically estimate this minimum diameter we use approximate average values. Assuming again that cooling water is supplied to coils at 10C and exits at 70C, the average temperature of water within the cooling passages contacting the conductor would be about 40C. The kinematic viscosity of water at 40C is about $\nu = 7*10^{-7}$ m^2/s, which we use as typical. Substitution of these values gives a minimum diameter to guarantee turbulence of 0.7 millimeters if the flow speed is V=10 m/s. This constraint is easily met with practical sizes for cooling passages, so good turbulent heat transfer is assured for the chosen water speed.

For turbulent flow conditions in liquids, the film heat transfer coefficient is estimated by first invoking the Dittus-Boelter correlation:

$$Nu = 0.023\,\mathrm{Re}^{0.8}\,\mathrm{Pr}^{0.4}$$

where Nu is the Nusselt number, Re is the Reynolds number and Pr is the Prandtl number, which varies with water temperature. The heat transfer coefficient is then defined in terms of the Nusselt number as follows:

$$h = \frac{k_w}{D} Nu$$

where k_w is the thermal conductivity of water, another temperature dependent quantity. Combining these relations together, using the actual nonlinear water properties, and fixing the water flow speed at V=10 m/s yields the following contour plot of the film heat transfer coefficient versus water temperature and flow path hydraulic diameter:
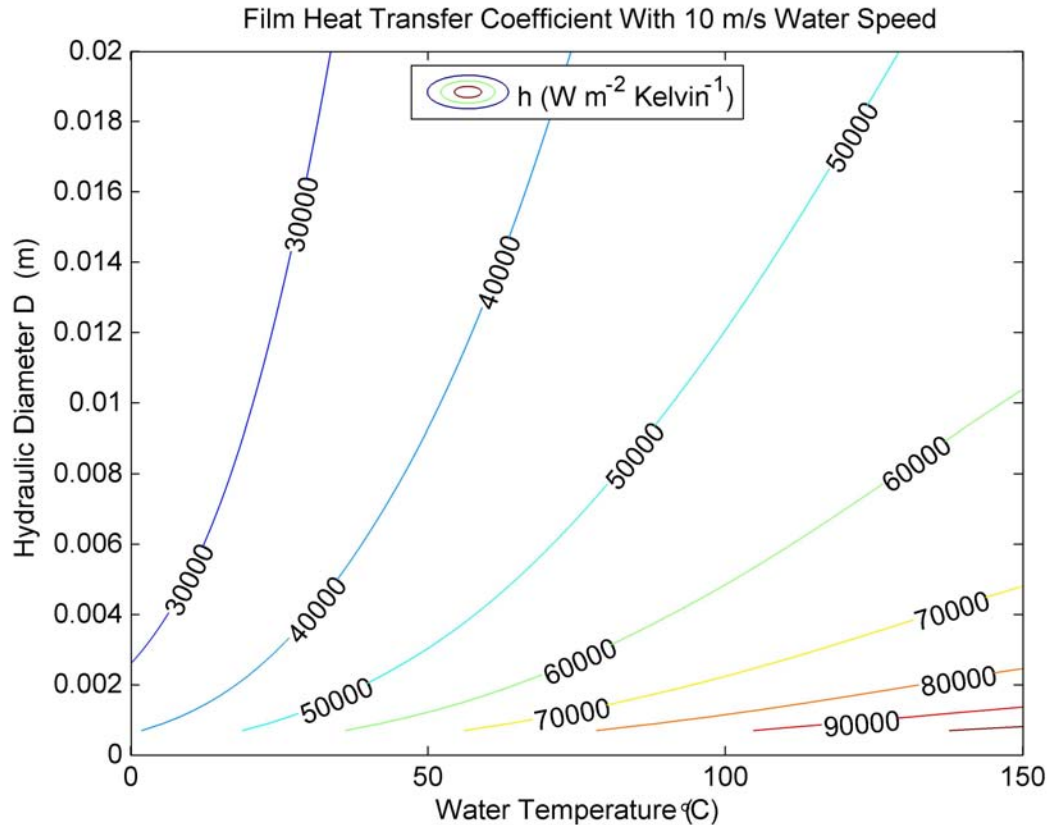
Figure 3.4.3: Heat Transfer Coefficient To 10 m/s Water Vs Temperature, Hydraulic Diameter

This plot shows that for the 10C-70C range of expected water temperatures and for practical water cooling passage diameters of several millimeters, the flow passage average film heat transfer coefficient would vary in the approximate range from 30 to 60 kW m^{-2} Kelvin^{-1}. To illustrate this by an example, a single circular cross section D=11.3 millimeter diameter passage carrying cooling water at 10 m/s would have a 40C mid-temperature range heat transfer coefficient of roughly h=37 kW m^{-2} Kelvin^{-1}. In order to develop a film temperature drop of 30C the linear heat transfer rate would need to be:

(P/L)=πDh(ΔT)=π(0.0113 m)(3.7*10^4 W m^{-2} Kelvin^{-1})(30 Kelvin)= 39.4 kW/m

Thus, heat would need to be transferred to the water at a linear rate of almost 40 kW/m in order to develop a film temperature drop of 30C. A group of smaller diameter cooling passages with the same total cross section would provide a larger total heat transfer area, so a smaller film temperature drop would result at identical linear cooling rates.

The cross-conductor temperature gradient is determined both by the steady heat flux in the copper and by copper's thermal conductivity which varies slightly with temperature as per the following plot. If the copper's heat flow direction is also perpendicular to the direction of electrical current flow as well as to the direction of water flow, then the electric current will nonuniformly redistribute itself towards the colder, less resistive copper regions adjacent to the cooling passage. However, for rough estimating purposes current redistribution can be ignored along with variations in the thermal conductivity, which can be approximated by the constant value, K=400 W/m-Kelvin.
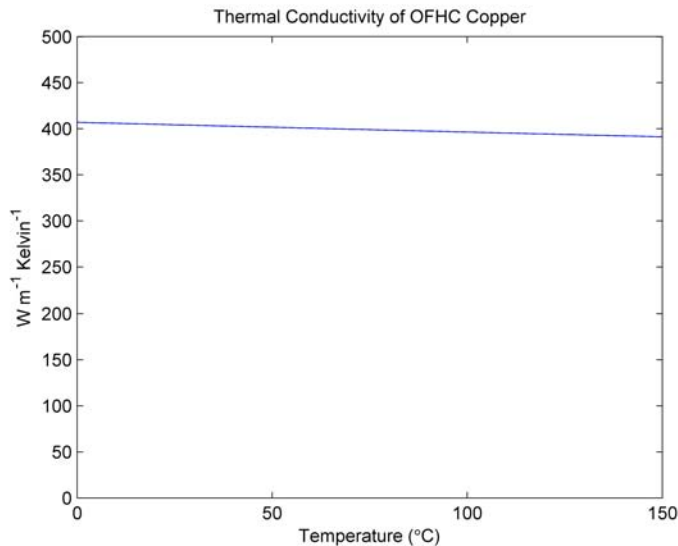
Figure 3.4.4: Thermal Conductivity of Copper Vs. Temperature

Then, the temperature rise due to the cross-conductor temperature gradient in the copper can be estimated as a geometry-dependent factor which depends on the shape of the copper cross-section in the plane perpendicular to the water passage, multiplied by the ratio of the linear heat transfer density, P/L, divided by copper's thermal conductivity, K. We note that the quantity, P/(LK), is a temperature difference with units of degrees (or Kelvins). Two extreme geometries present themselves for heat flow, and each has a closed-form solution. In one the heat flows everywhere in a uniform direction while in the other it everywhere converges radially. For a strip-shaped copper cross-section cooled on one edge so that heat flow is essentially one dimensional, the maximum temperature rise in the copper under the approximations of constant electrical resistivity, constant thermal conductivity, and constant current density is as follows:

$$\Delta T_{\text{Strip}}^{\text{Cu}} = \left(\frac{s}{2w}\right)\left(\frac{P}{LK}\right)$$

where w denotes the strip's width and s denotes the distance between its cooled and uncooled edges. With the same approximations applied to an annular copper cross-section cooled only on its inner surface so that heat flow is essentially radial and

cylindrically symmetric, the maximum temperature rise in the copper is given by the following:

$$\Delta T_{Annulus}^{Cu} = \frac{1}{4\pi}\left(\frac{2r_o^2 \ln(r_o/r_i)}{r_o^2 - r_i^2} - 1\right)\left(\frac{P}{LK}\right)$$

where r_i and r_o denote respectively the inner and outer radii of the annulus. The two geometry-dependent coefficients can each be plotted against the conductor cross-section's aspect ratio, where aspect ratio is defined in both cases as the distance between the cooled and uncooled sides divided by the width of the cooled side. Thus, the aspect ratio is (s/w) for the strip and $(r_o\text{-}r_i)/(2\pi r_i)$ for the annulus:
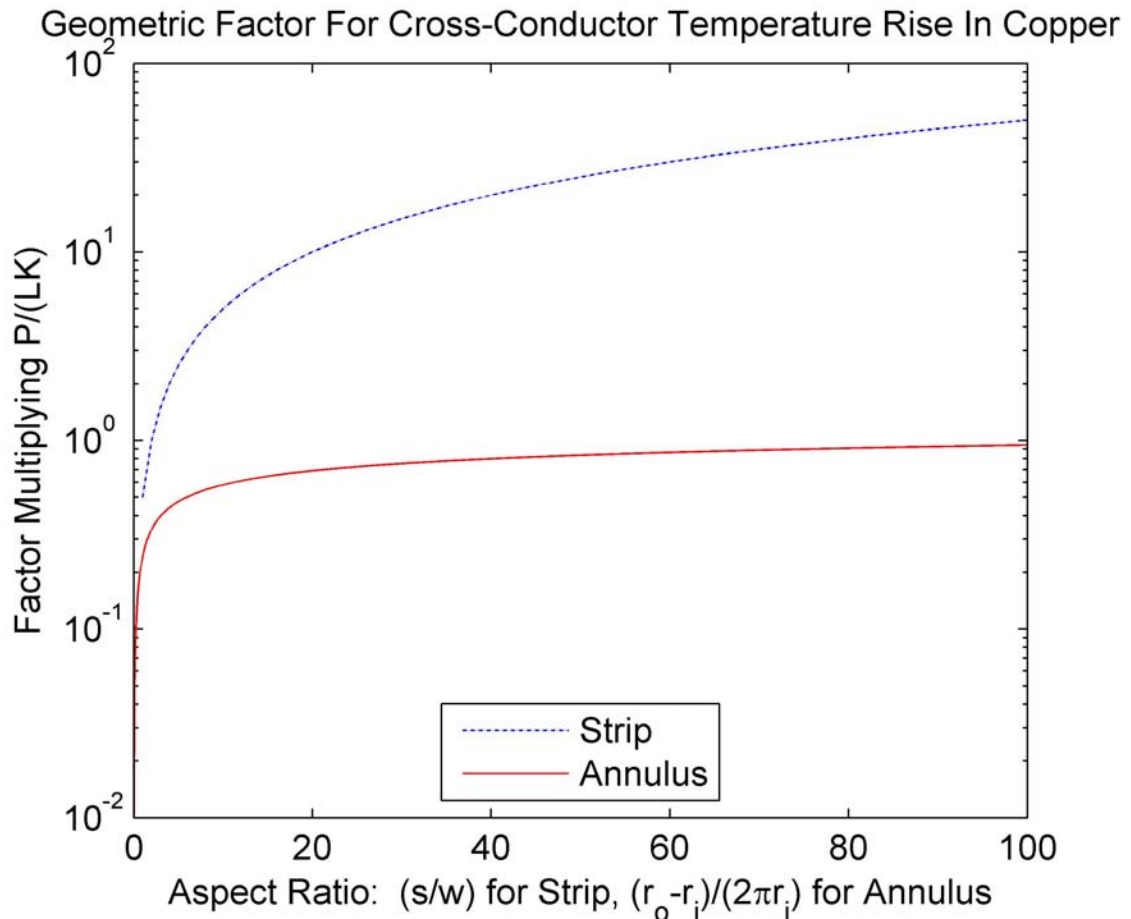
Figure 3.4.5: Normalized Cross-Conductor Copper Temperature Rise Factors

For instance, suppose a conductor's P/L linear heat transfer density was 4 kW/m. Then

P/(LK)=(4 kW/m)/(400 W/m-Kelvin) = 10 C.

If that conductor's cross section were an annulus with aspect ratio 10, e.g., with inner radius 0.159 cm so that its inner circumference would be 1 cm and with an outer radius of

NHTX Assessment FY2007 R1

10.159 cm, then the factor as plotted would be 0.58, so the cross-conductor temperature rise in the copper would be (0.58)(10)= 5.8 Kelvins. On the other hand, if the conductor were instead a rectangular cross-section strip with the same aspect ratio of 10, e.g., a strip 1 cm wide and 10 cm from cooled edge to uncooled edge, then the factor would be 5 so the cross-conductor temperature rise in the copper would be (5)(10)= 50 Kelvins.

The plot and this example show that annular centrally cooled cross sections typically have lower cross-conductor temperature rises in the copper than edge-cooled rectangular strip cross-sections. This is one reason that extruded hollow conductor technology is frequently used for water-cooled magnet coils. However, edge-cooled strips can have advantages for construction and for cooling water access, so they may be used in magnet systems where the linear power density is sufficiently low.

Water-cooled copper conductors with other geometrical shapes may have heat flow patterns intermediate between these two extremes. For instance, a conductor with multiple internal cooling passages will have radially converging heat flows near to each cooling hole but may have nonradial heat flows in other regions. Under the same approximations of constant electrical resistivity, thermal conductivity, and current density, 2D numerical thermal analyses of the cross-section perpendicular to the water flow will predict each such configuration to have peak cross-conductor temperature rises intermediate between the two extremes.

3.4.2   Toroidal Field (TF) Magnet System

3.4.2.1   TF System Overview

The toroidal field (TF) system for the NHTX includes 20 water-cooled turns each carrying 500 kA of steady dc current, thus together carrying the total central threading current of 10^7 ampere-turns (i.e., 10 MAt) which is needed to generate the 2.0 Tesla toroidal field at the NHTX plasma's major radius of 1 meter. The TF system geometry as defined in the original design point study is illustrated by Figure 3.4.6. Each of the TF components with rectangular shaped cross-sections includes two turns and has the same allocated current carrying cross-sectional area 0.3446 m wide toroidally by 0.4971 m in the perpendicular direction. The central cylindrical component has an outer radius of 0.287 m and a central hole of radius 0.0182 m. The entire TF assembly of Figure 3.4.6 is 7.0 meters tall.

During the course of the present LDRD investigations, the TF shape has changed
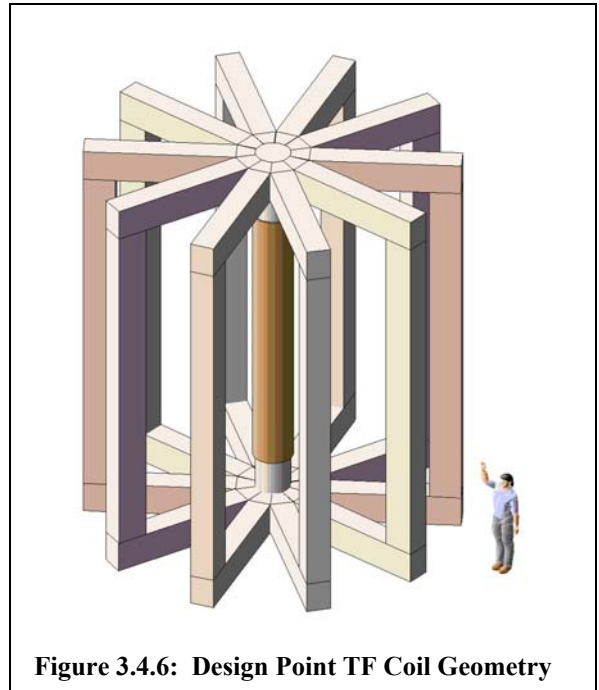
Figure 3.4.6: Design Point TF Coil Geometry

slightly from this form at the TF system's demountable electrical joints which are located at the rectangular corners. The outer joints will make contact in the toroidal direction while the inner joints will involve some vertical curvature. However, in broad terms there has been no major change from the Figure 3.4.6 scheme.

The TF system is implemented using current carrying component modules which individually are not complete coils but together form the 20 turn TF system when connected together through their contacting electrical joints. The different current-carrying module types in the TF system are summarized in Table 3.4.1.

Important issues for the TF system include construction methods and their costs, the implementation of demountable electrical joints, electrical power dissipation, steady-state heat removal by flowing water coolant, and the associated structural support systems. It should be mentioned that the TF Central Bundle carries a current density 6.65 that of the other TF modules, so it dissipates power at a power density $(6.65)^2$=44.2 times as high.

Table 3.4.1: NHTX TF System Current Carrying Modules

Module Type	Number Of Modules Of This Type	Number of Partial Turns Per Module	Number of Electrical Joints Per Module	Current Density at Full TF* (MA/m^2)	Net E-M Force on Each Module (MN)	Weight of Each Module (MN)
TF Central Bundle	1	20	40	38.800	0	0.050
TF Upper Radial	10	2	4	5.838	2.32 up	0.043
TF Outer Leg	10	2	4	5.838	2.22 radial	0.101
TF Lower Radial	10	2	4	5.838	2.32 down	0.043

*This does not correct for cooling channels or insulation, so actual current densities are higher.

3.4.2.2 Implementation Of TF Electrical Joints

The NHTX TF system will have inner TF joints and outer TF joints, both at the top and at the bottom. With 20 turns, there will be 40 inner joints and 40 outer joints. These each will carry 500,000 amperes of steady TF current while operating in a significant magnetic field environment. They also should be easily demountable and easily reassembled. Clearly, these joints are important and critical areas worthy of careful design attention.

The NHTX inner TF joints should avoid the problems seen in other projects such as the NSTX project which used a right-angle bolted "flag" joint design. That design failed in a spectacular arc and fire, and although subsequently rebuilt with improvements, remained vulnerable due to its basic configuration. Its perpendicular corner unavoidably developed large magnetic shearing forces and failed to generate any magnetic clamping force holding the joints closed. The perpendicular corner also produced extremely nonuniform current densities which in turn drove excessive local heating of the corner. To support the large shear forces at the joints it was necessary to cut holes in the joints for bolts, which reduced current carrying area and further magnified nonuniformities in current distribution due to joint pressure concentrations around each bolt. The NHTX toroidal field strength will be higher than the NSTX and the electrical current passed through its joints will also be higher, so its magnetic forces and stresses will therefore be considerably greater. It therefore should use a more robust approach.

In addition, it is intended that upper TF joints in the NHTX must be readily demountable. Because support for the NSTX perpendicular joints was so difficult it was necessary for it to rely on multiple load paths acting in parallel. Assembly or disassembly of its overall support structure including its multiple "flag box" and "shear shoe" supports and including precise torquing of the through-bolts clamping each joint closed, is a labor-intensive process requiring many technician hours of activity in close proximity to the machine. For the NHTX it is desired that instead it will be feasible to disassemble and reassemble the upper field systems without incurring much personnel exposure to radiation, even though the machine will have become activated due to its exposure to neutrons during many steady plasma experiments each lasting up to 1000 seconds.

The NHTX design approach adopted for its inner TF electrical joints will rely on external clamping forces to hold the joints closed so that they can be quickly disassembled and reassembled when necessary. Magnetic effects will contribute to those clamping forces, which will also be augmented by mechanical clamps for low magnetic field operation. Single load paths will be sufficient without requiring load sharing between multiple load paths. No through-bolts will penetrate joints, so their full areas will be used.

This NHTX approach of relying on external clamping rather than on through-bolts to hold joints closed requires that electromagnetic forces acting on joints must be accurately anticipated and carefully controlled or countered. In-plane forces on the inner joints can be engineered to act in beneficial directions by special shaping to control the current flow path, while shaping can also minimize peak out-of-plane forces. Structural support systems with careful controlled elasticity coefficients can be designed so that their deformations are minimized at the joint locations.

A "lap-joint" followed by a gentle curve provides a better design for the NHTX TF joints. In a cylindrically symmetric configuration the shape itself generates radial magnetic clamping forces forcing the joint closed while also reducing vertical magnetic shearing forces developed near the joint. The clamping force density at full TF is approximately

$$(7 \text{ Tesla})(5*10^5 \text{A}) = 3.5*10^6 \text{ N/m}) = 20,000 \text{ pounds/inch}$$

at the top of each upper TF joint, decreasing as the current passes through the contact, reaching zero on the plasma side of the joint. Since the joint has no corner, the current density relaxes to a configuration which is

Figure 3.4.7: TF Lap-Joint Concept

approximately uniform over the joint area. The configuration's curved shape in the poloidal plane even provides some strain relief. In addition, this configuration implies no "trapping" of an OH coil solenoid (e.g., as in designs of C-MOD or MAST), because the TF Central Bundle has no radial protuberances.

Out-of-plane electromagnetic forces on the TF near the joint can be minimized by conductor shaping. As shown in the following four flux plots, the poloidal magnetic field near the NHTX TF inner joints is small during sustained plasma operations.
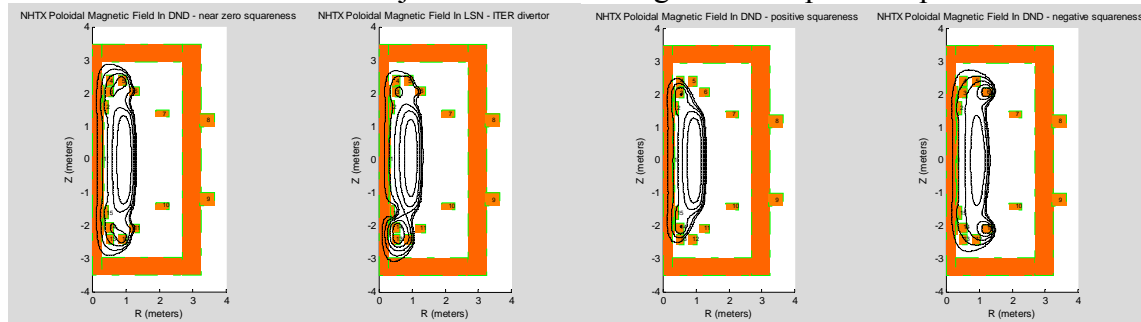
Figure 3.4.8 (a-d): Magnetic Flux Plots Including TF Joint Regions During Plasma Operations

However, the OH field during startup is strong in the TF joint region.
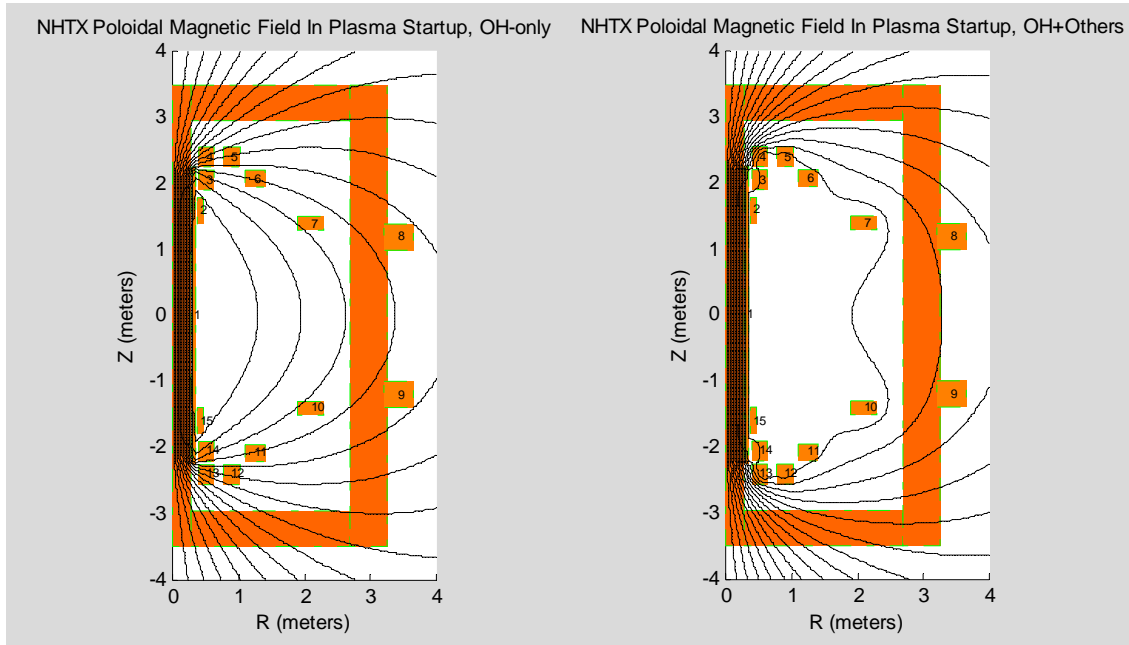
Figure 3.4.9(a,b): Magnetic Flux Plots Including TF Joint Regions During Plasma Startup

A strategy to reduce peak out-of-plane forces in the TF joint region is to design the TF conductors so that the TF current follows lines of poloidal magnetic flux. The following plot shows such a shape:
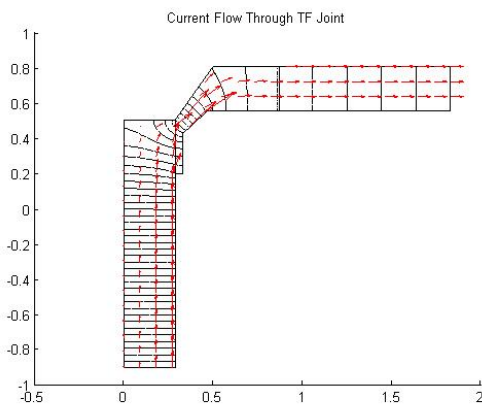
Figure 3.4.10: Analysis of TF Lap-Joint Concept

Here, constant voltage contours are shown in black while the red arrows show TF current streamlines. The point is that this lap-joint configuration results in current streamlines which closely follow the poloidal magnetic flux contours at plasma startup, thus reducing the peak out-of-plane forces at the inner TF joints. Electrical current flows smoothly through the joint without concentrating. Interaction between the TF system current and the toroidal magnetic field strongly forces the joint closed. With this configuration the

entire joint is useful, since current density is relatively uniform and no bolt holes cut through the joint. Joint pressure is uniform without any bolts to locally concentrate it.

The overall best TF joint shape has not been determined in this LDRD effort. It should be found by a design optimization process. What has been determined is that TF joint shaping of the type shown here can provide significant performance advantages and thus should be pursued in a detailed NHTX design.

However, although joint shaping can provide a magnetic clamping force to hold the joint closed, that magnetic clamping force will not function at low TF currents and field levels. To provide a force keeping the inner joint closed at low TF currents, pneumatic springs with a common N_2 supply will balance mechanical clamping forces between the 20 upper and 20 lower joints. The diagram depicts a poloidal plane view of one such pneumatic spring pushing against a toroidal ring (whose cross section is shown as a black square) in order to hold closed an upper inner joint. A variety of manufacturers make compact high pressure gas springs designed to operate as such remotely controllable pistons. For instance, Hyson sells gas springs using a 2000 psi N_2 supply pressure, with different spring models providing stroke distances ranging from 0.5 inches to 5.0 inches and with diameters ranging up to 5 inches with controllable clamping forces ranging up to 15,000 pounds.
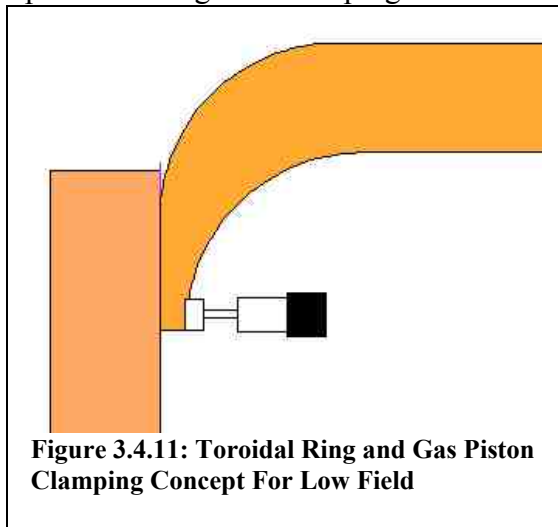
Figure 3.4.11: Toroidal Ring and Gas Piston Clamping Concept For Low Field

As depicted in the nearby diagram showing in plan view ten TF Lower Radials, ten TF Outer Legs, and the TF Central Bundle, the NHTX TF outer joints connecting between the TF Outer Legs and the TF radials will be implemented on the two outer toroidal sides of the TF Outer Legs. The two turns of each TF Radial will separate and straddle its associated outer leg to form the electrical contacting joints. This especially simple demountable joint configuration requires that each Radial and each Outer Leg have no more than two turns, which is the main reason why the two-turn outer leg design and its resulting 20-turn TF system has

Figure 3.4.12: TF Lower Radials Straddle TF Outer Legs To Form Outer Lower Electrical Joints.
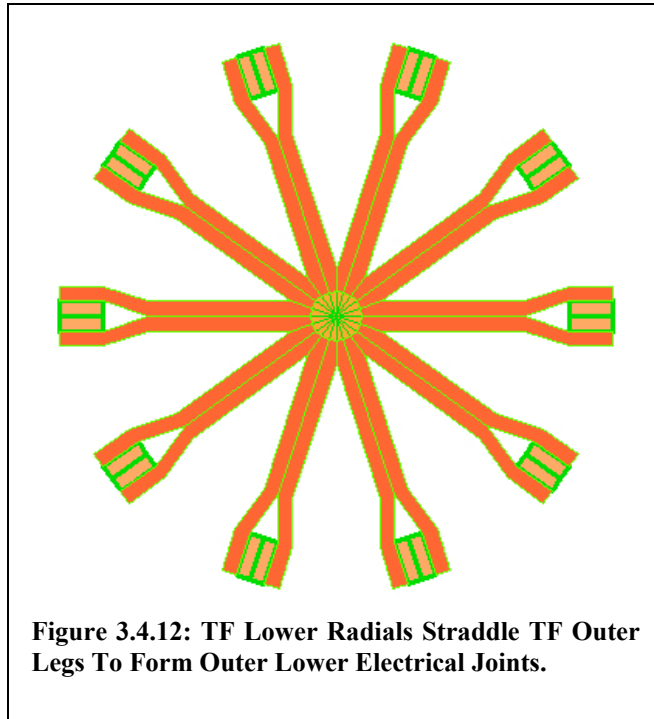
been adopted. These outer joints, which are readily accessible and for which space is not severely constrained, will be held closed by external mechanical clamps (not shown) which will squeeze each "sandwich" formed by a TF Outer Leg and the two separated turns of a TF Radial which straddle it. Although the diagram shows the lower radials and their joints, the upper radials will be the same except for their inclusion of a flexible region. The outer upper electrical joints will be identical to the outer lower ones.

3.4.2.3   TF Central Bundle

3.4.2.3.1   Construction of TF Central Bundle

The NHTX TF Central Bundle has the highest power dissipation of any TF or PF coil module, and indeed dissipates more power than all the other TF or PF system modules combined. It occupies most of the prized space in the center of the NHTX device. It is also complicated and may be difficult to construct. For these reasons it certainly is worthy of significant design attention.

The TF Central Bundle has the approximate shape of a 7 meter tall 0.287 meter radius solid cylinder with a small central cylindrical hole of 0.0182 meter radius. Although it is mostly copper, it is covered by a thin layer of insulation everywhere except for water fittings protruding from its top and bottom and electrical joint contacts visible on its sides near its top and bottom.

A horizontal cross section through its middle as depicted in Figure 2 shows it is divided in the toroidal direction into 20 different pie-shaped copper conductors separated by thin sheets of electrical insulation.   Each conductor subtends 18 degrees toroidally about the central axis, so each is almost 9 cm wide (i.e., about 3.5 inches wide) at the TF Central Bundle's outer radius. However, if the side insulation in Figure 3.4.13 were stripped away a vertical view would reveal that the turns are not prismatic in shape but instead are slightly twisted into a helical

Figure   3.4.13:NHTX   TF Central Bundle

configuration between the side joints. This twist rotates conductors by one 18 degree turn width about the cylinder's central axis while running between upper and lower joints, thus providing within the TF Central Bundle the "clocking" needed to connect TF turns in series with each other and with the TF power supply. We note that although this twist exacerbates the difficulty of constructing the TF Central Bundle, alternative designs implementing the TF "clocking" elsewhere, e.g., in the TF Lower Radials, seem to pose more severe problems.

Although most of the external surface of the TF Central Bundle is covered with electrical insulation, external electrical joints are located on its outer radius near its top and bottom. Each electrical joint is implemented within an 8 cm wide rectangular region of bare copper centered in the external side face of its conductor, leaving about 1 cm of surface insulation remaining between exposed copper rectangles to accommodate "creepage" by

electrically separating adjacent turns. Each contact is implemented as a shallow indented region machined in the copper, thus forming a female connection which would mechanically limit excessive relative sideways motion of the contacting male pin of a TF Radial module. The machined surface of each contact is flat and oriented in a vertical plane while its edges are flared for mating alignment purposes.
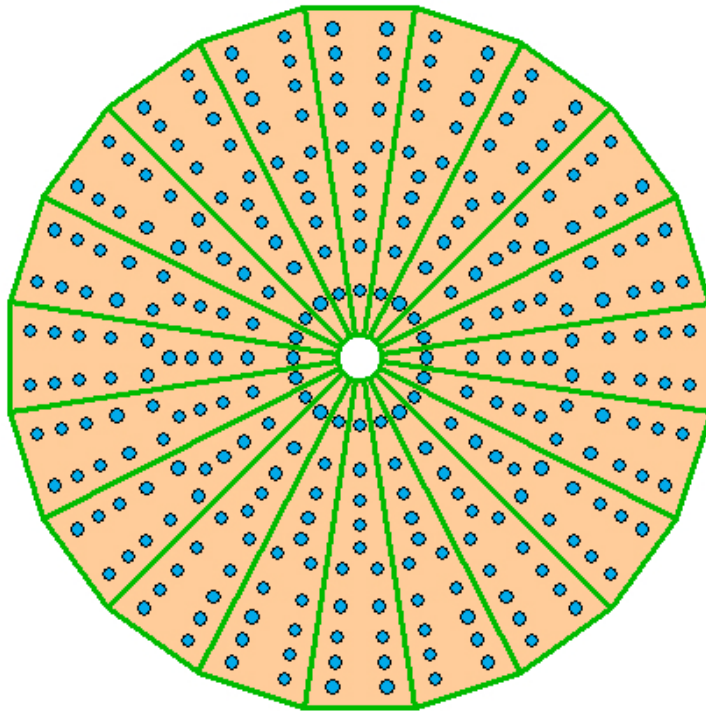
Figure 3.4.14: TF Central Bundle Horizontal Cross Section (20 Turns,15 Cooling Tubes/Turn)

Each of the 20 turn conductors in the TF central bundle is itself an assembly requiring a somewhat complicated construction. Each 18 degree wide conductor is fabricated from two 9 degree wide halves in which five semicircular grooves must be machined in the facing sides to provide space for ¾ inch outer diameter copper cooling tubes. In addition to these grooves, machining also must excavate regions at the turn's top and bottom surfaces past the external electrical joints in order to hold internal water manifold boxes attached to the turn's multiple internal cooling tubes. Each of these internal water manifolds has an external 2 inch diameter water hose fitting protruding vertically from its end of the turn in order to accommodate the 180 gpm flow of cooling water which that turn will need at full power.   After the external electrical contact indentations are also machined, the two halves are then helically bent to produce the precise plastic deformation needed for the 18 degree twist.   The internal copper tubes and attached manifolds are next inserted into the machined grooves, then all are soldered together to form a single conductor assembly.   After turn insulation is externally applied to each of the 20 conductor assemblies they are fitted together and overwrapped with external surface insulation to form the TF Central Bundle module. If epoxy resin and fiberglass insulation are used, injection and curing at elevated temperatures may also be required.

3.4.2.3.2 TF Central Bundle Thermal Performance Calculations

The ratio of the TF Central Bundle's total current at the full designed field for NHTX divided by its total geometric cross section area is the average current density value of $3.88*10^7$ A/m^2.   This is significantly higher than the current densities of other components, and it implies a high density of dissipated electrical power. The TF Central Bundle's actual current density is higher still since some of its geometrical cross section is used for insulation and some to carry cooling water. Thus, among the NHTX magnet components the TF Central Bundle is the most difficult to steadily cool.

Total power dissipation in the 20-turn TF Central Bundle at full field is expected to exceed 60 MW, but it may be as high as 70 MW or more depending on the effectiveness of its cooling in minimizing copper temperature averaged over its 3D volume. An initial turn layout design using five ¾ inch outer diameter copper tubes of 0.065 inch wall thickness embedded within each turn was not successful. At a 10 m/s cooling water flow speed in the five tubes, 9.75 liters per second of cooling water entering at 10C would exit at 85C after absorbing 3 MW of heat from the single turn's copper. However, a 2D analysis of heat conduction, through the copper in directions perpendicular to the TF current and through the water surface film (for which the Dittus-Boelter heat transfer correlation was used) predicted that within the turn's cross section, some locations distant from the cooling tubes would be up to 190C hotter than the entrained water, as shown in the following plot. For cross-sections near the water exit, this implies peak copper temperature would reach 85C+190C=275C, which exceeds the capability of many conventional insulations and might even cause the copper to slowly anneal.
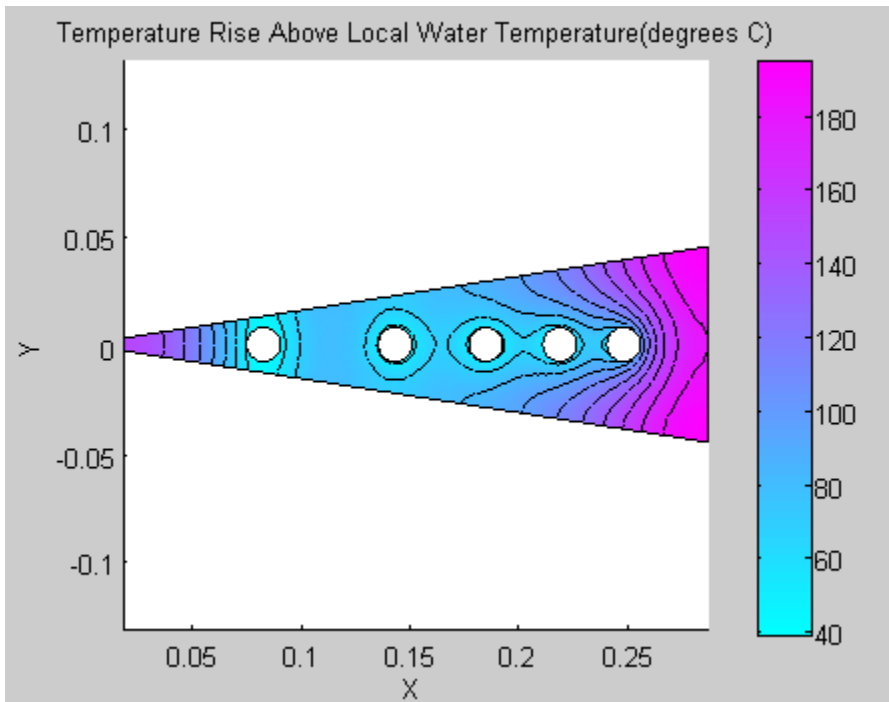
Figure 3.4.15:   Inadequate, Initially Investigated 5-Hole Cooling Of A TF Central Bundle Turn

An improved cooling layout was then examined in which 15 copper tubes each having ½ inch outer diameter and a wall thicknesses of 0.049 inches would be embedded within

each TF Central Bundle turn. At 10 m/s water speed this raises total water flow in each turn to 12.28 liters per second, so cooling water entering at 10C would exit at 69C after absorbing 3 MW of heat. The 2D perpendicular heat flow was analyzed for several different spatial arrangements of the cooling tubes within the turn cross-section. Among them, the tube arrangement copied below showed a peak temperature rise from the entrained water temperature as low as 70C.   (Please note the two contour plots have different color contour scales.)   Since the entrained water temperature near the exit would be near 69C, this implies a peak copper temperature near 139C. This hot-spot value would be acceptable for many types of insulating material which could be employed in the TF Central Bundle, and it is sufficiently cool that the copper itself would not anneal as a result.
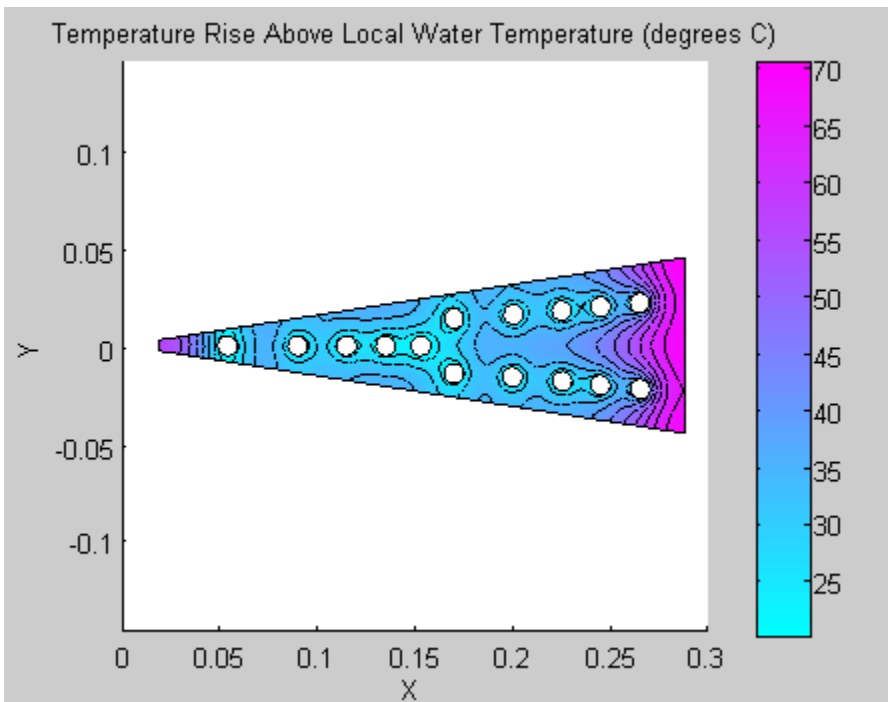
Figure 3.4.16: Acceptable 15-Hole Cooling Of A TF Central Bundle Turn

Careful comparison of the two design layout analyses reveals that the reduction in peak temperature resulted mostly from the reduction of the maximum distance for heat to be conducted through the copper to reach the nearest cooling passage. The slightly increased water flow rate and the slightly increased film heat transfer area and coefficient also helped but were not decisive changes. Thus, further reduction in peak copper temperature could result if the number of cooling passages in each turn was raised even higher than fifteen and they were spatially distributed in a uniform pattern over the cross section. Although a 3D thermal analysis was not carried out, it should be noted that these results imply the average copper temperature in the TF Central Bundle will be considerably cooler than 139C.   The average water temperature would be close to 40C and the temperature rise from the water to most locations in the cross section is in the 30C to 40C range, so the 3D average copper temperature would likely be between 70C and 80C. Thus, this result confirms that the TF Central Bundle can be adequately cooled,

but more detailed design calculations are needed to accurately quantify and optimize its performance.

3.4.2.3.3   TF Central Bundle Cooling Water Pressure Drop

The pressure drop in the TF Central Bundle tubes is estimated via the Darcy-Weisbach head-loss formula:

$$\Delta p = f(\mathrm{Re}, \varepsilon) \frac{L}{D} \frac{\rho V^2}{2}$$

where D, ρ, and V are as defined previously, L is the length of a tube, and f is a dimensionless friction factor which has been empirically studied and found to depend on Re, the Reynolds number of the flow and on ε, tubing's per unit surface roughness, in a manner summarized by Moody's well-known diagram.   For turbulent flow (i.e., for Re>>3000) in smooth pipes (i.e., for ε=0) , Moody's diagram may be approximated by VonKarmen's equation:

$$\frac{1}{\sqrt{f}} = 2\log_{10}\left(\mathrm{Re}\sqrt{f}\right) - 0.8$$

Jacobi iteration is used to numerically solve for f given a particular value of Re.

The pressure drop calculation done here uses tabulated water properties but approximates the water temperature as a constant value along the tube (whereas actually the water temperature varies continuously along the tube's length). The result is as follows:
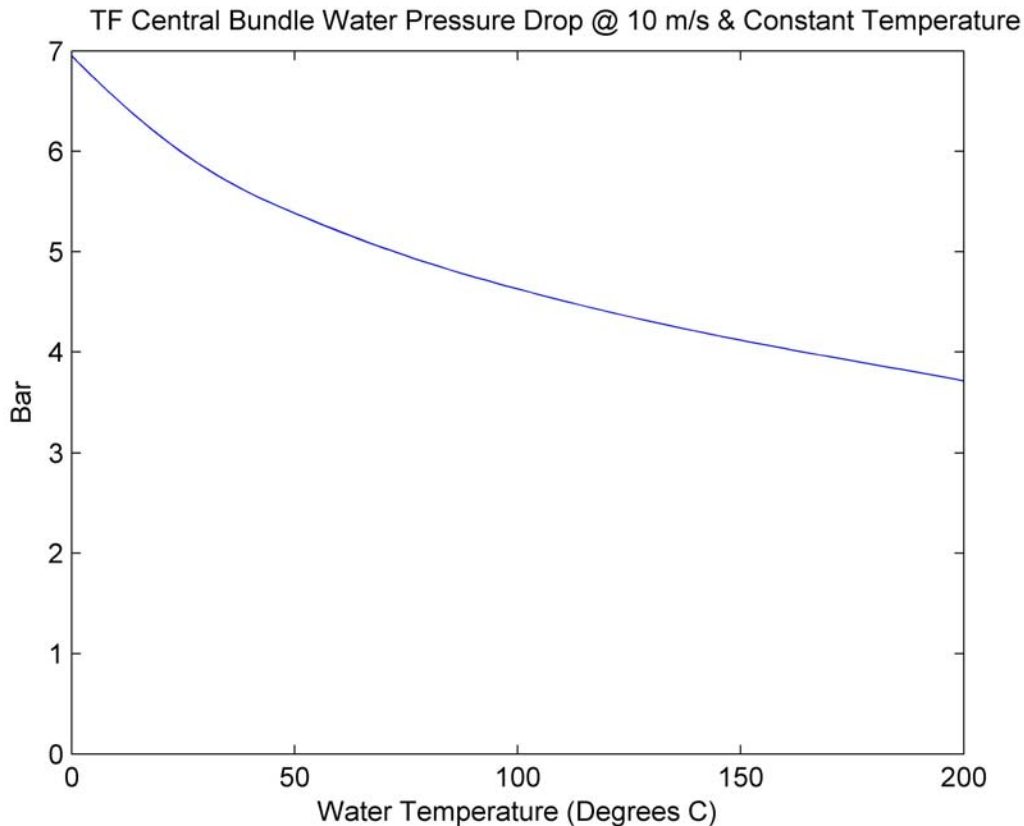
Figure 3.4.17: TF Central Bundle Pressure Drop Vs. Constant Temperature

This plot shows for 10 m/s water speed vs. the assumed constant water temperature, the calculated pressure drop using Bar units, where 1 bar=10^5 Pascals is slightly less than one standard atmosphere. Of course, the actual water temperature will not be a constant but instead will vary along the length of a coolant tube, so this plot is only approximate and requires interpretation. However, with inlet temperature 10 C and outlet temperature 70 C, the true pressure drop will be between 5.0 bar and 6.5 bar, the plotted values corresponding to constant water temperatures of 10 C and 70 C respectively. A reasonable estimate of the true pressure drop may be the plot's prediction for the 40 C average temperature of entrained water, i.e. about 5.6 bar (which is equivalent to about 81 psi).

3.4.2.3.4 TF Central Bundle Cooling Water Flow & Pumping

As stated earlier, with 15 tubes per turn the cooling water flow per turn is 12.28 liters per second. Thus the total water flow for all 20 turns of the TF Central Bundle is
    (20)(12.28 liters/sec)=245.6 liters/second = 0.2456 m^3/s.

In the US Customary units frequently used for water flow, this is 3,892.8 gpm.

<u>Pumping Power</u>
Mechanical power transferred to the water by a pump is the product of pressure drop times flow, i.e.,
(560000 Pa)(0.2456 m^3/s)=137.5 kW.

Electrical power for the pump is this mechanical power value divided by the net combined motor and pump efficiency, which together will be in the vicinity of 90%. Thus, electrical power for pumping the cooling water through the TF Central Bundle will be about 150 kW.

3.4.2.3.5 Structural Supports For TF Central Bundle

Although the TF Central Bundle is subjected to the strongest toroidal field values, the net electromagnetic forces on it will cancel out due to its cylindrical symmetry and so are nominally zero. When the entire TF system is in its assembled operational configuration, the external joints with the TF Radials on the sides of the TF Central Bundle near its top and bottom will provide stabilizing restraint against any force imbalance that might arise due to dynamic imbalances. The TF Central Bundle is expected to be able to internally withstand, based on its own strength, the internal stresses resulting from electromagnetic loading. Thus, its structural support requirements are limited to supporting its own weight of 0.05 MN= 11,200 pounds.   For that support, its base will rest on an insulated plate with twenty insulated holes through which the hose fittings for the individual turns will extend. That plate, in turn, will be supported from below by structural connections to the basement floor.

3.4.2.4   TF Radials And TF Outer Legs

3.4.2.4.1 Construction Scheme
The TF Radials and the TF Outer Legs have very large copper cross sections of 0.4971 m by 0.3446 m.   Each turn's cross section is 0.4971 m by 0.1723 m. To inexpensively fabricate the copper turns of TF Radials and TF Outer Legs, they will be constructed as laminations of many copper plates, each of which will first be cut 0.4971 m wide in the direction perpendicular to the current flow direction. For example, if standard quarter-inch .thick copper plate were used, then 27 sheets of the copper plate would have a combined thickness of (27)(0.00635 m) = 0.171 m when the plates are stacked together. The remaining thickness will be provided by solder applied to "tin" plate surfaces, then when the assembly is heated to the appropriate temperature the solder melts to join the stack of plates into a single rigid slab. .

Cooling provisions will be provided by edge cooling as described in the next section. The construction features for edge cooling require that a slot first must be machined into the edge of each plate prior to assembly of the module, then a seamless tube to carry cooling water is inserted into that slot and soldered into place. Before the stack of separate plates is soldered together the ends of all tubes surrounding the stack should first

be soldered to pressure-tight manifolds for the incoming and exiting water. Then additional copper sheets can be soldered onto the plate stack edges to protect the tubes there from any accidental damage. This will result in a rigid metal turn assembly made mostly from copper plate but also including some tubing and some solder. Finally, external insulation will be wrapped or otherwise applied onto the exterior surfaces of the turn assembly in all places except for the external electrical joints, and to turns are joined together in some nonconductive way to form a module.

3.4.2.4.1.1 Shapes OF Flexible Radial Conductors In The TF System

This section describes results of an approximate analysis of the flexes portion of the TF Upper Radials based on a modified version of beam equations. The purpose of this analysis was to approximate the spring constant for flex shapes. No attempt was made to include the interaction of the bent shapes with the magnetic field. The analysis revealed that the overall spring constant of the constant conductor cross-section flex assembly is proportional to the square of the thickness chosen for each of the leaves which it incorporates, and that there may be a conflict in choosing their thickness between the need for a low spring constant and the need for steady cooling.

The smallest standard sized copper tubing which appears capable of implementing edge cooling of copper flexes is type ACR tubing with an outer diameter of 1/8 inch. Using this type of tubing, the thinnest flex leaves compatible with soldering the tubing into a groove in the edge of each strip would be about 3/16 inch thick. However, the analysis shows that when using 3/16 inch thick leaves the expected spring force of the flex assembly for each TF Upper Radial would be $6*10^5$ N, which seems excessive. A more manageable maximum spring force of $7*10^4$ N would require restricting the individual leaf thicknesses to about 1/16 inch. Unfortunately, this is too thin to implement edge cooling using a soldered-in cooling tube for each flexible leaf. Therefore,

As discussed earlier, a pivotal issue for the NHTX TF System is the design of its electrical joints. A new design approach is necessary to allow for easy and frequent crane access to the inside of the NHTX vacuum vessel by removing upper PF and TF coil components and the vacuum vessel's lid. Conventional bolted joints would either need extensive radiation exposure of personnel or the development of expensive remote handling features. The approach taken is instead to hold all TF joints closed during NHTX operation by the action of external clamps or presses augmented by the electromagnetic forces which naturally arise due to TF electrical current flows. Therefore, the structural support system must minimize vertical deflections at the inner joint locations, with its elastic compliance carefully tailored so that deflections occur elsewhere. With this design approach there are no bolts penetrating the electrical joints , thus avoiding the need for painstaking and time consuming care in joint assembly and disassembly.   The external clamps or presses can be quickly deactivated to permit removal and reassembly of upper components, then quickly reactivated for electrical operations.

The resulting associated design issue which must be addressed is how to ensure that the upper inner TF joints remain closed when the TF System is energized. Each of the TF Outer Legs develops a large force pushing it radially outwards. This radial force is not an issue at the bottom where the TF Outer Legs will be firmly anchored to the floor, but there will be radial motion if the TF Outer Legs at the top. Although structural supports will resist the radial force, there will be a small radial deflection of the outer legs due to elastic compliance of the structural supports. As will be discussed later, this radial deflection, whose size is expected to be about 3 mm, i.e., about 1/8 inch, is an essential part of the structural design which is deliberately exploited to optimize the upper vertical structural support for inner joints. Therefore, the upper radial deflection of the TF Outer Legs must not be eliminated by using excessively stiff structural members.   However, the TF Outer Legs' radial deflection at the top does as a result require a special flexible design for the TF Upper Radial modules.   Since the electrical joints between the outer legs and the radials are not sliding joints, the outer portion of each TF Upper Radial must also deflect radially outwards when the TF system is energized. However, it is essential that the inner portion of a TF Radial must not move radially outwards since that would open the inner joint. Thus, the TF Upper Radials must deform, extending radially under the full TF load by about 3 mm.

Since each TF Radial will be constructed from parallel stacked copper plates and since the stacked plates will be bent toroidally so that the two turns can straddle the TF Outer Legs, the design solution is to shape the TF Upper Radials so that they can flex in the radial direction.   By bending the radial plates in shapes permitting compliant radial flexing with relatively small force, the outer portion of the TF radials will be able to move radially outwards while the inner TF joint remains firmly closed.

Simplified Mathematical Model For A Thin Bent Plate
To investigate the elastic compliance of a stack of bent copper plates it is sufficient to analyze a single plate, provided that the plates do not bind or otherwise interact with each other. Small air gaps separating individual plates within the bend regions will avoid binding. For an individual bent plate, a simplified elastic compliance analysis can be carried out via 1-D ordinary differential equations derived as an extension of the beam equations. To derive them, we assume the bent plate has a uniform thickness which is small compared to its length, L, measured along its curved, bent path in the horizontal XY plane and also small compared to its unbent width, w, in the vertical Z direction. With no dependence on Z, we can concentrate on the shape in X and Y.   The plate can be modeled by a finite curve of curvilinear length, L, representing the plate's center line with the understanding that the plate extends a distance $\tau/2$ to each side of that center line.   If we further label one end of the curve as the starting end, then any point on the curve can be uniquely represented by S, its curvilinear distance measured along the curve from the starting end, where $0 \leq S \leq L$. Then any chosen shape for the curve can be represented by specifying the two parametric functions, X(S) and Y(S) which jointly give the coordinates for each point on the curve, (X(S), Y(S)).

A unit vector tangent to the curve at any point, S, has the components

(X'(S), Y'(S))=(dX(S)/dS, dY(S)/dS).

This allows the unique definition of a curve direction angle, θ(S), as
       (cosθ(S), sinθ(S))=(X'(S), Y'(S))

which varies along the curve. We note that with θ(S) measured in radians its derivative, θ'(S)=dθ(S)/dS is the reciprocal of the curve's local radius of curvature.

We also note that if *θ(S)* has been specified then it is not necessary to separately specify X(S) and Y(S) since these can be computed from θ(S) and the coordinates of the starting end:

$$X(S) = X(0) + \int_0^S \cos\theta(S)dS$$

$$Y(S) = Y(0) + \int_0^S \sin\theta(S)dS$$

To extend the beam model to this configuration, we shall model the system of balanced elastic forces within the bent plate as lying entirely in the XY plane and entirely characterized by the three functions, T(S), V(S), and M(S).   If the bent plate were cut at any location, S, on the curve and the region from the starting end to that cut point were retained while the rest of the plate beyond the cut were discarded, then it would be necessary to externally apply a force and moment to the cut end in order to remain in balance without further motion or deformation. The necessary applied forces include the tension component T(S) directed along the curve's local direction and the shear force component V(S) directed perpendicular to the curve's local direction.   It is also necessary to apply at the cut end a torque about the Z direction called the bending moment M(S).

In the case where there is a lateral force per unit curvilinear length or q(S) applied to the bent plate, these obey the following equations.

$$\frac{dV(S)}{dS} = q(S) + T(S)\frac{d\theta(S)}{dS}$$

$$\frac{dM(S)}{dS} = V(S)$$

$$\frac{dT(S)}{dS} = -V(S)\frac{d\theta(S)}{dS}$$

We note that in the conventional model for straight beams, the curvature terms involving dθ/dS are absent and the tension which in the straight beam case is constant is also ignored. However, for curved thin beams they become the primary phenomena to model. However, the curvature changes with loading and thus is a dependent variable that must

be determined as part of the solution. Since it appears in the differential equations as products with other dependent variables, the system of equations becomes nonlinear.

In the conventional model for straight beans, only the local rotation and deflection of a nominally straight beam's centerline are determined. The elastic deformations in response to both tension and shear are ignored   The same approach is taken here, except that here the situation is more complicated.   In both cases the change in local curvature is proportional to the bending moment, but here that change is added to an underlying nonzero curvature which exists without any applied loading.

We represent the shape of the unloaded but bent beam as $\theta_0(S)$ and the shape of the loaded beam as $\theta(S)$. Then the rule relating deformation to loading is

$$\frac{d\theta(S)}{dS} = \frac{d\theta_0(S)}{dS} + \frac{M(S)}{EI}$$

where E is Young's modulus of the beam material and I is the moment of inertia if the plate's cross section for bending in the XY plane around the Z direction. For this case, Young's modulus for copper is about 1.25E11 Pa and the moment of inertia is given by

$$I = \frac{\tau^3 w}{12}$$

For the TF Radials' height of w=0.4971 m and plate thickness of τ=0.375" =9.525 mm, the moment of inertia would be
    I=(0.4971 m)(0.009525)^3/12 = 3.58E-8 m^4
so that
    EI=4,474.7 N-m^2

If we ignore out-of-plane lateral loading, the system of equations becomes as follows:

$$\frac{d\theta(S)}{dS} = \frac{d\theta_0(S)}{dS} + \left(\frac{12}{Ew\tau^3}\right)M(S)$$

$$\frac{dV(S)}{dS} = q(S) + T(S)\frac{d\theta(S)}{dS}$$

$$\frac{dT(S)}{dS} = -V(S)\frac{d\theta(S)}{dS}$$

$$\frac{dM(S)}{dS} = V(S)$$

$$\frac{dX(S)}{dS} = \cos\theta(S)$$

$$\frac{dY(S)}{dS} = \sin\theta(S)$$

These can be rewritten in an equivalent form in which there are not dependent variable derivatives on the right hand side:

$$\frac{d\theta(S)}{dS} = p(S) + \left(\frac{12}{Ew\tau^3}\right)M(S)$$

$$\frac{dV(S)}{dS} = q(S) + T(S)\left(p(S) + \left(\frac{12}{Ew\tau^3}\right)M(S)\right)$$

$$\frac{dT(S)}{dS} = -V(S)\left(p(S) + \left(\frac{12}{Ew\tau^3}\right)M(S)\right)$$

$$\frac{dM(S)}{dS} = V(S)$$

$$\frac{dX(S)}{dS} = \cos\theta(S)$$

$$\frac{dY(S)}{dS} = \sin\theta(S)$$

where q(S) was defined previously and

$$p(S) \equiv \frac{d\theta_0(S)}{dS}$$

As presented in the Appendix, this system of ordinary differential equations was coded into a MATLAB algorithm which was numerically solved using MATLAB's existing routines for solving boundary value problems. The following graph shows the calculated plan view shape of a single 3/16 inch=4.8 mm thick by 0.4971 m tall flexible copper leaf under no-load conditions and under 8400 N (i.e., 1885 pounds) of tensile force, which results in a calculated deflection of approximately 3 mm.
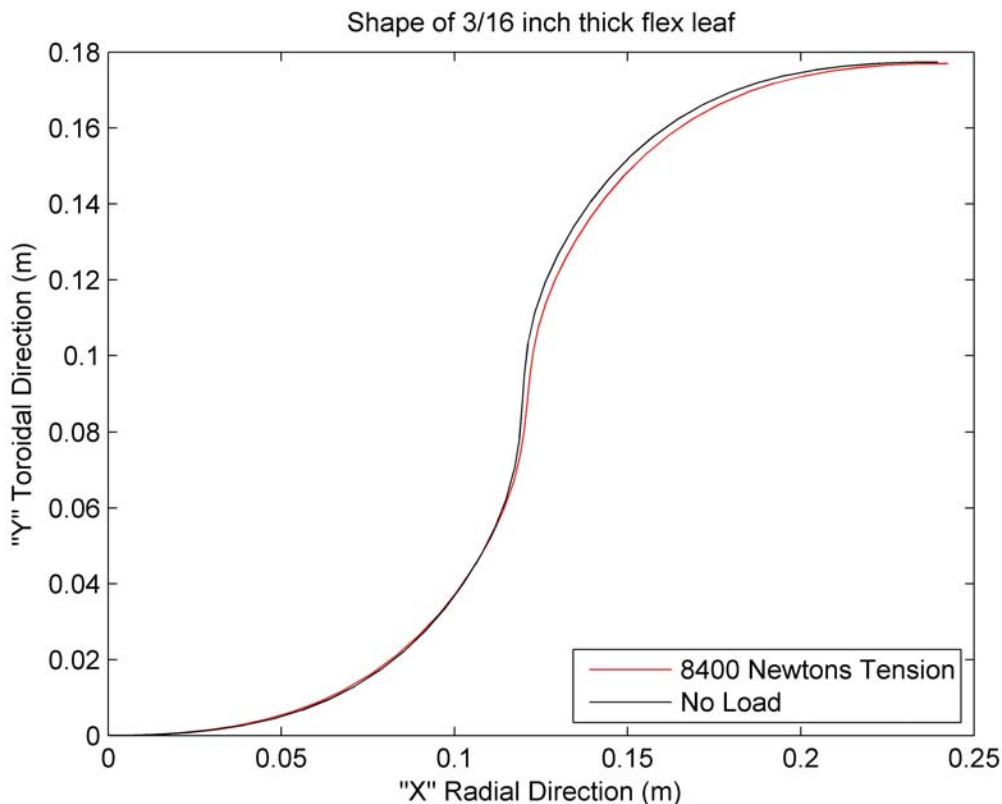
Figure 3.4.18: Calculated Shapes of TF Flexes With and Without End Force Loads

However, 36 such leaves would be required to match the full width of each TF turn, so 72 flex leaves of this thickness would be required for each TF Upper Radial. The following diagram depicts in plan view two of the TF Upper Radials, each incorporating 72 of these 3/16 inches thick flex leads..
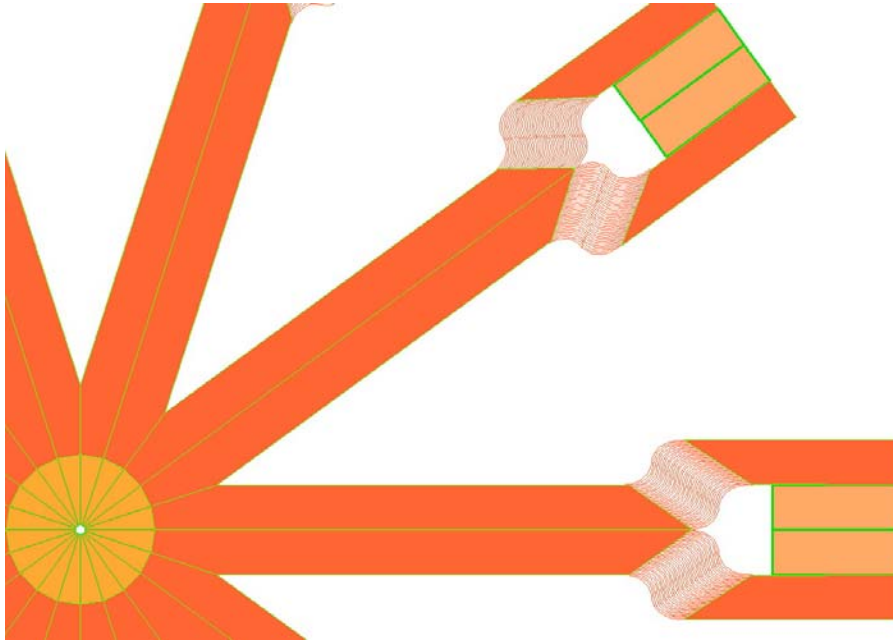
Figure 3.4.19: TF Upper Radials Incorporating 3/16 Inch Thick Flexes.

With 72 flex leads, the total expected spring force needed for 3 mm extensions of the flexes in each TF Upper Radial, based on the stiffness calculation, would be

$$(72)(8400 \text{ N})=604,800 \text{ N}=135,771 \text{ pounds.}$$

Commercially available high pressure gas cylinder springs develop forces up to 15,000 pounds per cylinder, so 30,000 pounds of mechanical clamping force is expected to be available for the two turns of a single TF Upper Radial module. That is considerably less than 135,771 pounds. Additional clamping force would also be produced by magnetic effects, depending on details of the shaping of the inner TF joints. Indeed, since with the lap-joint shape the two turns of a TF Upper Radial can together develop 40,000 pounds per inch of clamping force at the top of their joints and an average of 20,000 pounds per inch over the joints' full vertical extent, the magnetic effects may be sufficient for using this spring constant. It is conceivable that the total mechanical plus magnetic clamping force may be adequate for the use of 3/16 inch thick copper leaves, which then could be edge-cooled using cooling water flowing in standard sized copper tubing. This question has not yet been resolved during the present LDRD effort.

It also seems possible that a detailed analysis might instead show the available mechanical plus magnetic radial clamping force for the inner joint to be insufficient when using 3/16 inch thick flexible copper leaves. If that turns out to be the case, then a larger

number of thinner flexible leaves must be used. For instance, using 216 copper leaves each 1/16 inch thick per TF Upper Radial would maintain the same constant total cross-section of the copper but would reduce the spring force at 3 mm extension by almost a factor of ten, so that a single commercially available pneumatic cylinder remotely operated by high pressure nitrogen could keep the inner upper TF joints closed without any help from the magnetic clamping pressure that will also be present. However, then a different system for cooling the 1/16 inch thick flex leaves in thermal steady-state would need to be designed since they would be too thin for soldering standard sizes of cooling tubes into grooves machined in their edges. If this turns out to be necessary, one possible cooling system concept for such thin flexes might be to immerse each entire turn assembly of 108 flexes in its own bath of flowing water contained inside an enclosing flexible rubber skin. Ends of the flexible water container where it would be penetrated by the non-flexible portions of the TF Upper Radials would need to be made water-tight by some means, such as perhaps compression by external hose clamps.

3.4.2.4.2 Edge-Cooling Analysis Applicable to TF Radials and TF Outer Legs

Edge-cooling is frequently inferior thermally to the use of extruded hollow conductors wound with short flowpath lengths, but is preferred nonetheless because of its simpler construction. For this reason it will be used in portions of the NHTX TF system which carry relatively low current density. Other situations are also possible where edge-cooling's ability to use very short flowpaths makes it more effective thermally.

It turns out that for the rectangular cross section geometry it is possible to carry out a general analysis of edge-cooling including the nonlinear properties of copper and current redistribution effects.   This section outlines the analysis and summaries its results.

Figure 3.4.20 : Geometry Of Edge-Cooled Conductor

Figure 3.4.10 shows the general geometry of an edge-cooled current-carrying conductor as analyzed herein, along with geometric variables used in the analysis.   The conductor bar's height is denoted by h and its width is denoted by w. Locations along its height are denoted by the variable y which is zero at the bar's center. Locations along its width are denoted by the variable, x. Locations along the bar's length are denoted by the variable, z. A current of I amperes flows in the bar in the z direction. The blue regions shown in Figure 3.4.10 located above and below the bar represent cooling water flowing along the bar's edge, absorbing heat from the bar as it flows.
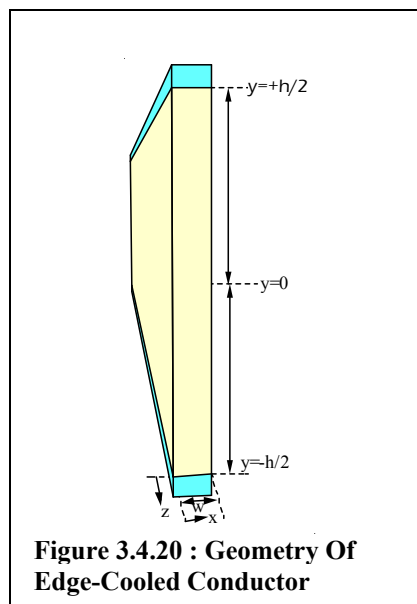
In steady edge-cooling, heat produced within the electrical conductor by resistive heating flows by thermal conduction to the water located at the conductor's top or bottom. Since there is no heat sink on the conductor's sides, there is no heat flow in the x direction.

Heat is modeled as entirely flowing in the y direction. As a result, the heat conduction problem becomes one dimensional, described by an ordinary differential equation with the single independent variable, y. Since copper resistivity changes with temperature it may vary over the cross-section. With possibly a large conductor temperature variation as a function of y at a particular z section, the electrical resistivity may be quite nonuniform across that section. The electrical response will naturally redistribute the current away from the hotter, higher resistivity regions towards the cooler regions which have lower resistivity. The present analysis calculates how the current redistributes itself as a function of this resistance nonuniformity in copper strips.   To do this, the approximation assumption is made that across any cross-section perpendicular to z there is a single electrical field value in the z direction, independent of y, although that field value is permitted to vary as a function of the z location. Although the methodology could apply to any metallic conductor, for this analysis we assume the metal is OFHC copper. Two nonlinear functions of temperature are important, i.e., copper's thermal conductivity K(T) and copper's electrical resistivity η(T). The following differential and integral equations define the problem for any particular section, z. Heat conduction in the y direction is related to the thermal gradient as follows:

$$q(y) = -K(T(y))\frac{dT(y)}{dy}$$

$$q(0) = 0$$

where zero heat flow through the center of the bar follows from symmetry.
The spatial rate of change of heat flow is the local electrical heating, i.e.:

$$\frac{dq(y)}{dy} = \eta(T(y))(J(y))^2$$

where J(y) is the local value of the nonuniform electrical current density, given by

$$J(y) = \frac{E}{\eta(T(y))}$$

The total current, I, obeys

$$I = w \int_{y=-h/2}^{y=+h/2} J(y)dy$$

so therefore it follows that the electrical field at any section is given by:

$$E = \frac{I}{w \int_{y=-h/2}^{y=+h/2} \frac{dy}{\eta(T(y))}}$$

Putting these equations together we arrive at the following single integrodifferential equation which describes the performance of edge-cooling with a copper conductor:

$$\frac{d}{dy}\left(K(T(y))\frac{dT(y)}{dy}\right) = -\left(\frac{I}{w}\right)^2 \frac{1}{\eta(T(y))\left(\int_{y=-h/2}^{y=+h/2} \frac{dy}{\eta(T(y))}\right)^2}$$

with the two boundary conditions that

$$\frac{dT(y)}{dy}\bigg|_{y=0} = 0$$

$$T\left(y = \frac{h}{2}\right) = T_{edge}$$

)

We note that because of symmetry, T(y)=T(-y) so it is not necessary to numerically solve for the temperatures in the lower half of the conductor bar, and the integral can also be taken over a nonnegative domain. The defining equation can then be rewritten as follows:

$$\frac{d}{dy}\left(K(T(y))\frac{dT(y)}{dy}\right) = -\left(\frac{I}{w}\right)^2 \frac{1}{\eta(T(y))\left(2\displaystyle\int_{y=0}^{y=+h/2}\frac{dy}{\eta(T(y))}\right)^2}$$

One can prove that the peak copper temperature satisfying this integrodifferential equation does not depend on h, the height of the conductor. Peak copper temperature with edge cooling depends on only two quantities, the copper's edge temperature, Tedge, and the electrical current per unit width, I/w. This dependence is shown by the following plots, based on numerical solutions of the differential equations by MATLAB algorithms summarized in the Appendix.
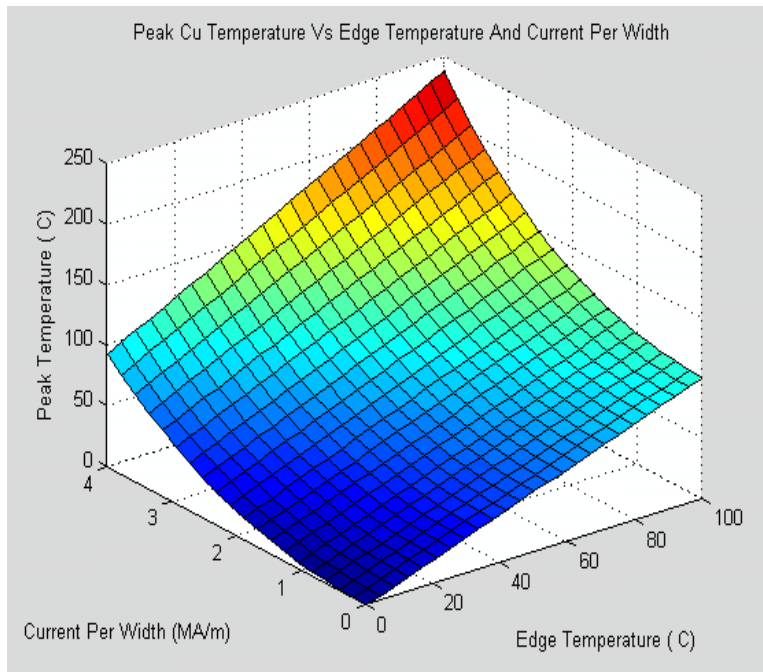
Figure 3.4.21 Peak Edge-Cooled Cu Temperature Vs Edge Temperature and Current Per Width
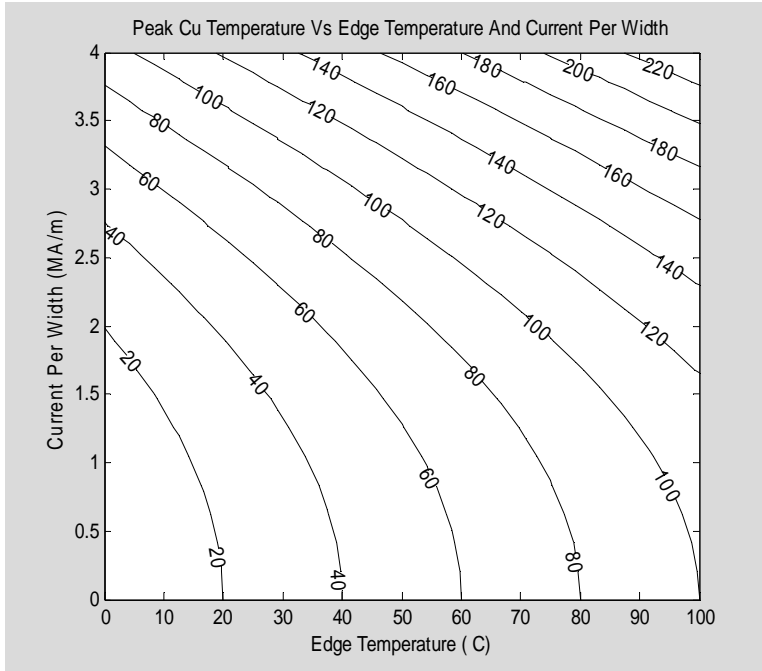
Figure 3.4.22 Contour Plot of Peak Edge-Cooled Cu Temperature

For the TF Radials and the TF Outer Legs, the ratio of current to width is
        (I/w)=(1E6 A)/(0.3446 m) = 2.90 MA/m.

This defines a horizontal line almost three quarters of the way up the contour plot of copper temperature. It asserts, for instance, that if edge cooling can keep the edge copper temperature of the TF Radials and the TF Outer Legs below 50C, then the peak copper temperature will not exceed 100C.

3.4.2.4.2.1 Thermal Hydraulic Calculations For The TF Radials

The TF radials extend radially from R=0.287 m to the outer edge of the outer legs at R=3.1746. Neglecting the flaring of the two turns in each radial, that indicates the total length is about 3,1746-0.297=2.888 m. The height of the constant height portion of each radial is 0.4871 and the width of each turn in a TF Radial is 0.1723 m, so the cross sectional current carrying area per turn is A=(0.4871 m)(0.1723 m)=0.08393 m^2. Estimating the average temperature-dependent copper resistivity as roughly 2E-8 ohm-meter, the resistance of each turn component in a TF Radial would be about
    (2E-8 ohm-m)(2.888 m)/(0.08393 m^2)=0.6742E-6 ohm

We note this may an overestimate since part of the 2.888 m length does not carry the full current which transfers sideways to the TF Outer Leg through part of that length, and since also the inner part of the TF Radial has a larger vertical extent at the joint with the TF Central Bundle, especial with special lap-joint shaping features. However, with this approximation we estimate the dissipation in one turn of a TF Radial as:
        P=(5e5 amperes)^2(0.6742E-6 ohm)=1.686E5 W

Thus, each TF Radial component of each turn would dissipate about 168.6 kW. Since there are 40 such components for the 20 turns, the total dissipation in all the radials is estimated to be about 7 MW.

We will consider fabricating each turn component of each TF Radial, excepting the flex region of the upper radials, from 18 sheets of 3/8 inch=0.375" thick copper placed in vertical orientations. In the upper and lower edges of each sheet a groove is machined to accept inserted copper tubing of 0.250" outer diameter. Such precisely sized tubing, available as type ACR tubing (manufactured for air conditioning service) has an inner diameter of 0.190"=4.826 mm. The different tubes cooling different sheets would be connected hydraulically in parallel.

The total length of this each tube in each TF Lower Radial would be then about (2.888 m)(18)(2)=104 m. The total surface area of the wetted perimeter of each tube would be
   (104 m)(0.004826 m)π= 1.576 m^2.

Assuming a water speed in these tubes of 10 m/s, the volumetric flow rate in any single section through a single tube would be
   (10 m/s)(0.004826 m)^2 *π/4=0.183 liters per second.

Assuming the 18 adjacent tubes on each edge of a TF Lower Radial turn carry parallel flows, the total coolant flow through an 18-tube section would be (18)(0.183 liters/ s)=3.29 liters/s=52 gpm. If this were the total flow in the entire radial turn component, the bulk water temperature rise would be about 168.6E3/4.186E6/0.00329=12.24 C. This is acceptably low, so this approach will be adopted.
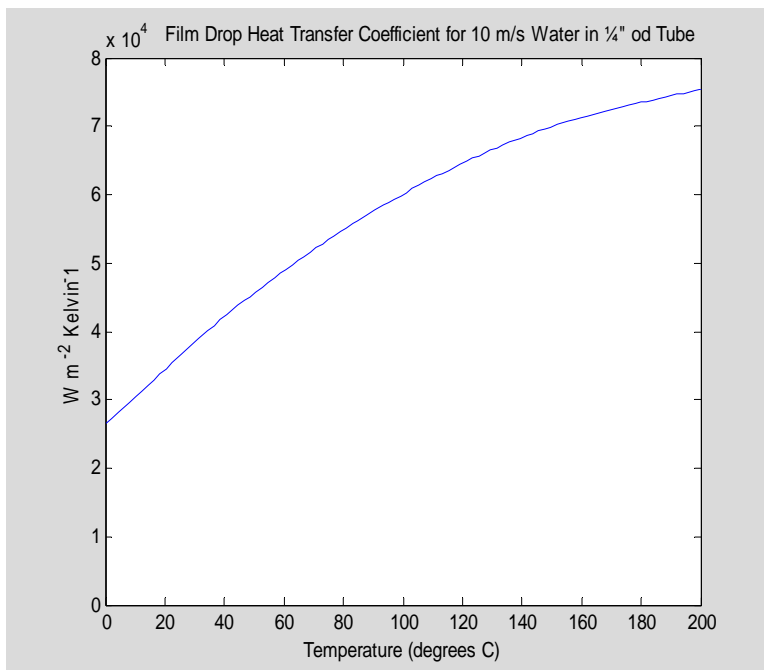
Figure 3.4.23 Heat Transfer Coefficient For 10 m/s Water In Standard ¼ inch OD Tubing

With cooling water supplied at 10 C and rising by 12.24 C within the radial turn assembly, the average temperature of entrained water will be about 16 degrees C. As shown on the above plot, for that temperature the heat transfer coefficient will be about 30,000 W m^{-2} Kelvin^{-1}. Then. using the tube wall heat transfer surface area of 1.576 m^2 and the heating power of 168.6 kW, the temperature drop from the copper to the water through the heat transfer film is estimated as

(168.6E3 W)/(30,000 W m^{-2} Kelvin^{-1})/(1.576 m^2) = 3.57 degrees C

Therefore, the temperature of the upper and lower cooled copper edges of each radial turn component range from 10+3.57=13.57 C near the water inlet to 10+12.24+3.57=25.8 C near the water exit. The average temperature of the copper edge is midway between these, i.e., about 20 C.

The 500 kA TF turn current spread over the 0.1723 m width of a radial turn component results in a current to width ratio of (5E5 amperes)/(0.1723 m)=2.9 MA/m=29 kA/cm. Analysis of the temperature gradient in the copper with this current ratio and with 20 C edges on top and bottom shows the peak temperature in the copper remains slightly less than 70 C and the bulk average copper temperature is near 55 C.

IF we model the water properties as being at a single water temperature, the pressure drop can be calculated as a function of water temperature as shown in the following graph. Actual water temperature will be nonconstant within the cooling passage, so the actual pressure drop will be intermediate between the values plotted for inlet and exit water temperatures.
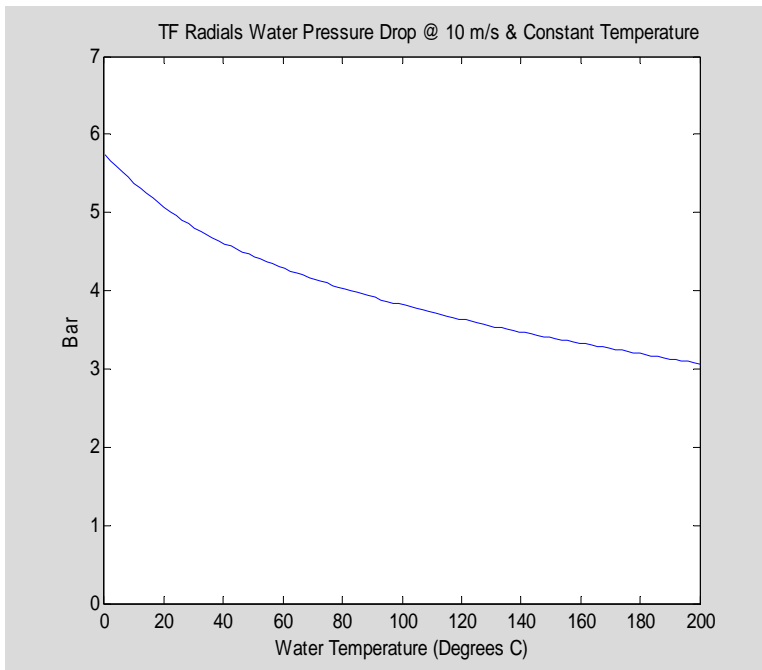
Figure 3.4.24 : Cooling Water Pressure Drop In TF Radials

Thus, the expected pressure drop in cooling water within each of the TF Lower Radial turns is about 5 bars, i.e., about 72 psi.

Results for the TF Upper Radials will be similar, but somewhat different based on the different cooling arrangement for the flexes region.

3.4.2.4.2.2 Thermal Hydraulic Calculations For TF Outer Legs
The TF outer legs will be constructed in the same manner as the TF Lower Radials by using 3/8 inch thick sheets of copper . Since the cross section of outer leg turns precisely matches that of the radial turn components, the heat dissipated per unit length, the film drop, and the temperature rise in the copper due to gradients will be identical. However, the length of each outer turn is 7 meters, which is 2.4 times as long as a radial. To compensate for this the inner and outer edges of the outer legs will have separate cooling water supply and return connections instead of routing a single coolant path around the perimeter as done for the TF Radials. Thus, the total cooling water flow for each outer leg *turn* will be (2)(3.29 liters/s)=6.58 liters/s=104 gpm.   Pressure drops for cooling the outer turns will be as follows:
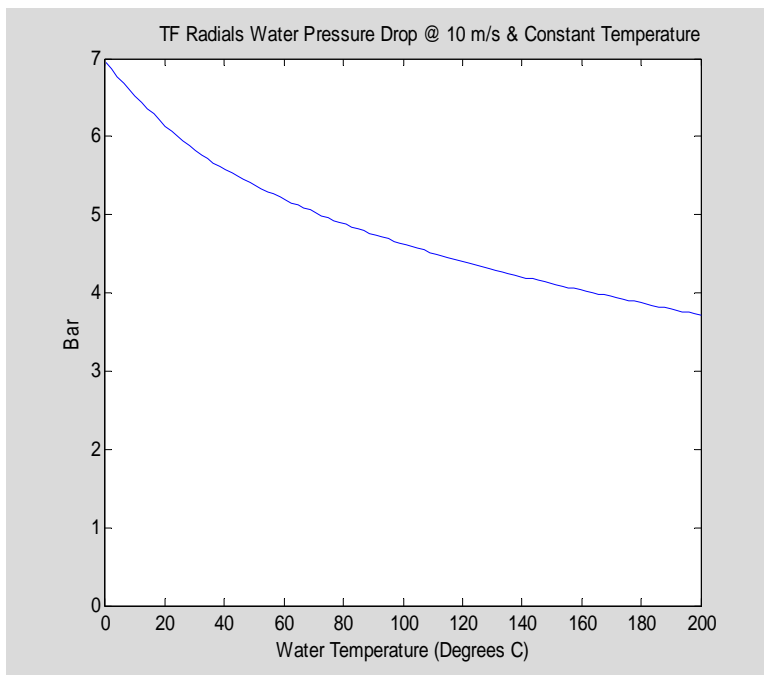
Figure 3.4.25 : Cooling Water Pressure Drop In TF Outer Legs

Thus, the required pressure drop to pump coolant through the TF outer Leg cooling tubes will be about 6 Bar, i.e., about 87 psi.

3.4.2.5 In-Plane TF-only Self-Forces

Because electromagnetic forces between currents flowing in components of the TF and PF systems are much greater than the component weights, they drive most of the design requirements for structural support. Approximate calculations of electromagnetic forces as presented here are useful guides for the initial design of the structural support system. More accurate force calculations which more precisely consider current flow details will later inform the final design.

In the absence of poloidal fields, the electromagnetic self-forces on TF system components are directed within each component's particular poloidal plane. As discussed in later calculations below, simultaneous PF coil operation leaves these TF self-forces unchanged but creates additional out-of-plane force components directed toroidally, perpendicular to the poloidal plane.

As, as illustrated in the Figure 3.4.26 cartoon, uniform density electromagnetic forces push each TF Outer Legs radially outwards while nonuniform density vertical forces push the TF Upper Radials and the TF Lower Radials away from each other. Because the vector sum of the stronger but
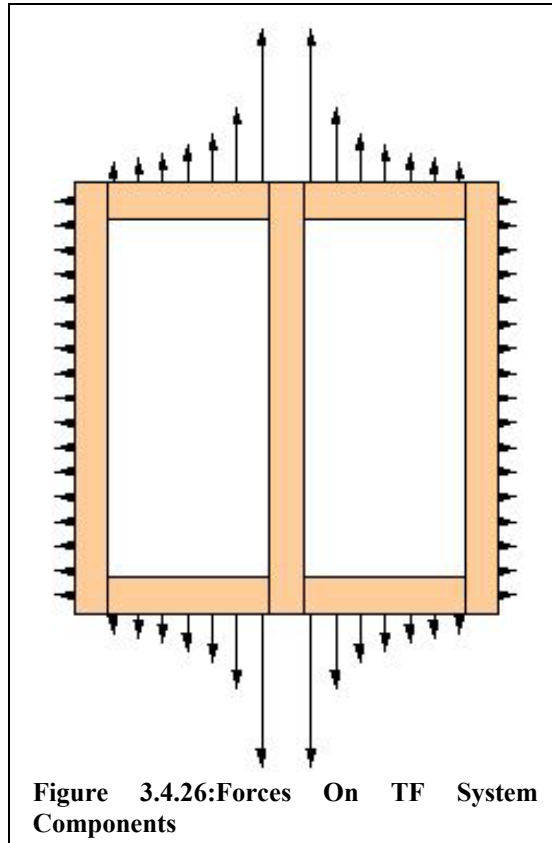
Figure 3.4.26:Forces On TF System Components

balanced electromagnetic forces acting on the TF Central Bundle is zero, those forces do not require external structural support and are not depicted here.

3.4.2.5.1 Toroidal Magnetic Field Approximation

For the purpose of initial approximate calculations of the TF self-force, TF currents are abstracted as being axisymmetric and flowing only in poloidal planes with no toroidal direction component anywhere. That modeling representation mathematically guarantees that the resulting calculated magnetic field is toroidally directed and that interaction forces are in poloidal plane directions. Basically, this ignores TF ripple effects. The assumption of axisymmetry is an approximation since the TF system is not truly axisymmetric but instead exhibits 10-fold rotational symmetry. The assumption of no toroidally directed current ignores the slight helical twist about the machine's central axis of symmetry which is planned in the TF Central Bundle, and is also in error locally where

the two turns of each TF Radial diverge from each other toroidally.   However, the effects of these deviations are not large and are ignored in this approximation.

With the modeling assumption of axisymmetry the cylindrical coordinate system is appropriate. The two cylindrical coordinates (r,z) refer equally well to a point location in a poloidal half-plane or to a particular horizontal circle coaxial with the cylindrical symmetry axis of radius r and vertical location z.   If the total TF system current in ampere-turns which threads through the interior of any such circle is denoted as $I_{thread}(r,z)$, then the toroidal field strength at (r,z) is:

$$B_{TF}(r,z) = \frac{\mu_0}{2\pi r} I_{thread(r,z)}$$

where μ_0 is the permeability of free space, which in SI metric units is $4\pi*10^{-7}$ henrys/meter. Thus, in this approximation the toroidal field is nonzero in the toroidal region bounded by the TF Central Bundle, the TF Upper and Lower Radials, and the TF Outer Legs, while it is zero everywhere beyond those components.

Taking the calculated toroidal field at the centerline of current flow in each conductor as representative for the purpose of calculating forces, this results in the magnitude of the force per unit length on each TF turn being expressed as

$$\frac{dF}{ds} = \frac{\mu_0}{4\pi r} n_{TF} I_{TF}^{2}$$

Here, dF/ds is the lineal force density in newtons per meter per turn, n_{TF} is the number of turns in the TF system, and I_{TF} is the TF current per turn.   For the NHTX device, n_{TF} =20 turns and I_{TF} =$5*10^5$ amperes/turn. The lineal force per unit length is directed in the poloidal plane perpendicular to the local direction of TF current flow and away from the enclosed toroidal field region.

3.4.2.5.2   Radial Force On TF Outer Legs

Each of the TF Outer Leg components is 7 meters tall and has inner and outer radii of R_{inner}=2.6775 and R_{outer}=3.1746 m, respectively. For approximate force calculations the centerline is taken as the average of these, i.e., $R_{OLcenter}$=2.92605 m.   Applying the above formula yields an outer leg running lineal force density per turn of
   dF_{OL}/ds = 170,879 N/m/turn.

The TF current does not run the entire length of the outer leg since it must be transferred in and out through electrical joints which have finite extent. These outer TF joints have the same vertical heights as the TF radials, i.e., each is 0.4971 m tall. Approximating the current as being full between the centers of these joints and zero beyond the centers, the length of the current path for the purpose of calculating force is:
   7 m – 0.4971 m/2 -0.4971 m/2 = 6.5029 m.

Then, the total electromagnetic force on each TF outer leg is
       F_{OL}=(6.5029 m)(170879 N/m/turn)(2 turns)=2.222 MN

which is about one-half million pounds. It is directed radially outwards away from the NHTX central symmetry axis.

3.4.2.5.3 *Vertical Separating Force Between TF Upper And Lower Radials*

Each of the TF Upper Radials and/or TF Lower Radials extends radially from the TF Central Bundle at R=0.287 to its corresponding TF Outer Leg, where the center of the interfacing electrical joint is at R=2.926 m.   Current in the Radials is modeled here as being entirely in the radial direction, notwithstanding the fact that actually there is a vertical component to the current direction in the vicinity of the inner TF joints due to the increased vertical extent there. Therefore, the lineal density of the vertical force in each turn of a TF Radial is given by

$$\frac{dF_{TFRadial/turn}}{ds} = \frac{\mu_0}{4\pi r} n_{TF} I_{TF}^{\;2} = \frac{5*10^5 \; \text{N}}{\text{r}}$$

and the total vertical lineal force density for an entire TF Radial including both of its turns is

$$\frac{dF_{TFRadial}}{ds} = \frac{\mu_0}{4\pi r} n_{TF} I_{TF}^{\;2} = \left(10^6 \; \text{N}\right)\frac{1}{\text{r}}$$

The integrated total vertical force acting on each TF Radial is then approximately:
.

$$F_{TFRadial} = \left(10^6 \; \text{N}\right) \int\limits_{r=0.287\,\text{m}}^{r=2.926\,\text{m}} \frac{dr}{\text{r}} = \left(10^6 \; \text{N}\right)\ln\left(\frac{2.926 \; \text{m}}{0.287 \; \text{m}}\right) = 2.322 \; \text{MN}$$

Thus, the total electromagnetic vertical force on all ten TF Upper Radials is together 23 MN or equivalently 5.2 million pounds pushing vertically upwards, while an equal but opposite vertical electromagnetic force pushes the TF Lower Radials downwards. We note that this is a significantly large vertical separating force, equal to the combined weight of about 1000 large SUVs.

For some simplified structural calculations it is useful to determine a single equivalent line of action for each distributed force, since this concept preserves the torque attributes of a force distribution when the force distribution is approximated by its net vector sum. It is obvious from vertical symmetry that the line-of-action of the radial forces acting on each TF Outer Leg is a radial line located on the vertical midplane. For the vertical forces acting on a TF radial, the line of action is a vertical line located at a major radius of :

$$r_{loa} = \frac{\left(10^6 \; \text{N}\right) \int\limits_{r=0.287\,\text{m}}^{r=2.926\,\text{m}} r\frac{dr}{\text{r}}}{\left(10^6 \; \text{N}\right) \int\limits_{r=0.287\,\text{m}}^{r=2.926\,\text{m}} \frac{dr}{\text{r}}} = 1.137 \; \text{m}$$

3.4.2.6   TF Structural Support Scheme

3.4.2.6.1   Use Of Existing TestCell Floor Remaining From TFTR

The NHTX will be located in the same Test Cell which previously housed the TFTR experiment. It will be mounted on the existing circular 12 meter (40 ft) diameter pedestal which is elevated 2 ft above the surface of the surrounding 4 ft thick reinforced concrete floor. Embedded in the concrete of the pedestal is an extremely strong nonmagnetic steel structure including a network of 20 evenly spaced radial beams with webs six feet tall extending between their upper and lower flanges.   Each radial beam is further supported by steel columns on piers sunk beneath the concrete floor of the basement below the Test Cell.   We note that such beams exceed the typical sizes and strengths used in large bridges.   These beams all terminate in a central ring girder whose 2.6 meter inner diameter is at present an empty hole open to the basement.   NHTX will make use of the ring girder's features remaining from TFTR for transferring large vertical forces to support new structural components to be located within its central hole

The capability of this existing steel structure far exceeds what is needed to radially transmit the 23 MN of vertical separating force between the TF Outer Legs and distributed locations in the TF Lower Radials. It not only has ample strength, it also is so rigid that its deflections under NHTX electromagnetic loading will be negligible.

The TF Outer Legs will be used to structurally transmit the 23 MN vertical separating force between the bottom and top of the NHTX field coil systems.   To do this, each of the ten outer legs must carry a tension of 2.3 MN. Since the total copper cross

Figure 3.4.27: Existing Steel Structure In Floor

sectional area of the two TF turns in each outer leg is (0.3446 m)(0.4971 m)=0.1713 m^2, the uniform average tensile stress developed in the outer legs for this role is only:

  (2.3 MN)/(0.1713 m^2)=13.4 MPa=1.9 ksi.

This is a very low average tensile stress, far lower than the typical capability of full hard copper. The copper strain at this low tensile stress is 13.4 MPa/125GPa = $1.07*10^{-5}$, so the vertical elongation of the outer legs resulting from this stress would be

  (7 m)($1.07*10^{-5}$)=0.75 mm

if the entire TF Outer Leg's 7 meter height were in tension.

The vertical separating forces will be coupled into the TF Outer Legs through insulated steel pins penetrating in the toroidal direction through circular holes in the copper conductors. These pins will be longer than the holes through which they are inserted so they will extend beyond the TF Outer Legs on both sides toroidally. There they will be mechanically coupled to additional steel structures through a clevis connection. The plan for NHTX is to use ten of the beams in the pedestal floor by positioning each TF Lower Radial and each TF Outer Leg directly

Figure3.4.28: TF Vertical Support Conceptual Scheme

atop one of them. As shown in Figure 3.4.27, there are existing racetrack shaped penetrations in the floor between beams through which the structural connections will be made. Clevis type double connections to the lower pins will protrude through 20 such penetrations in the floor to the basement below where as shown in Figure 3.4.28 each will be tightened around the underside of its beam with a clamp able to transmit 2.3 MN = 516,000 pounds.
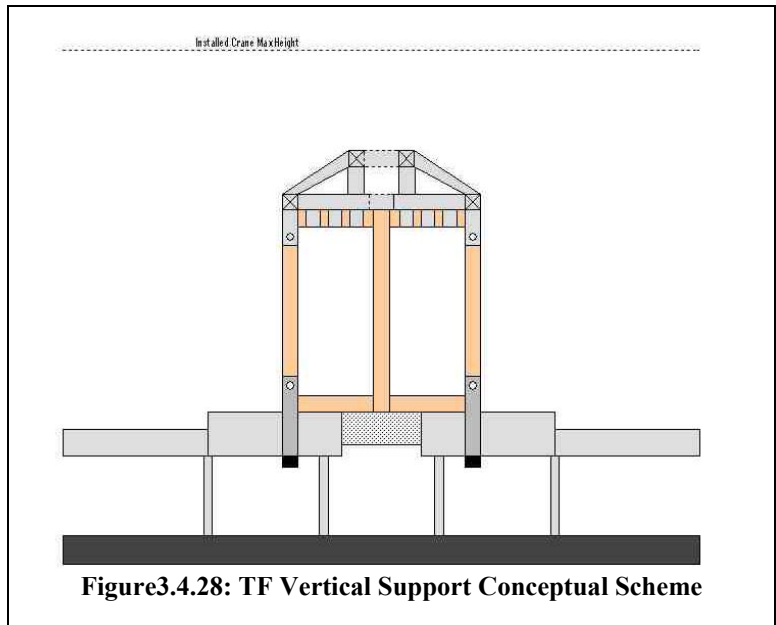
3.4.2.6.2 Load Transfer Pins For TF Outer Legs

The use of pins to transfer tensile loads between plates is unavoidably accompanied by some stress concentration in the plates. While the stress distribution and its peak can be numerically calculated for any particular set of dimensions, the stress concentration factors as functions of dimension ratios were long ago compiled in published works such as [Peterson] from which the following plot was extracted.
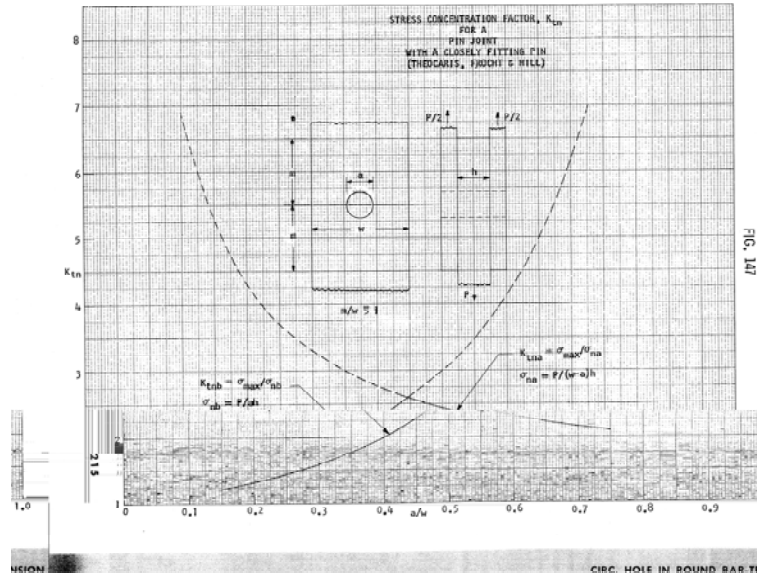
Figure 3.4.29: Stress Concentration Factors For Circular Pin In Hole [Peterson]

Renormalizing his data to express the stress concentration factor in terms of the average stress without correcting for the pin and hole results in the following MATLAB plot.
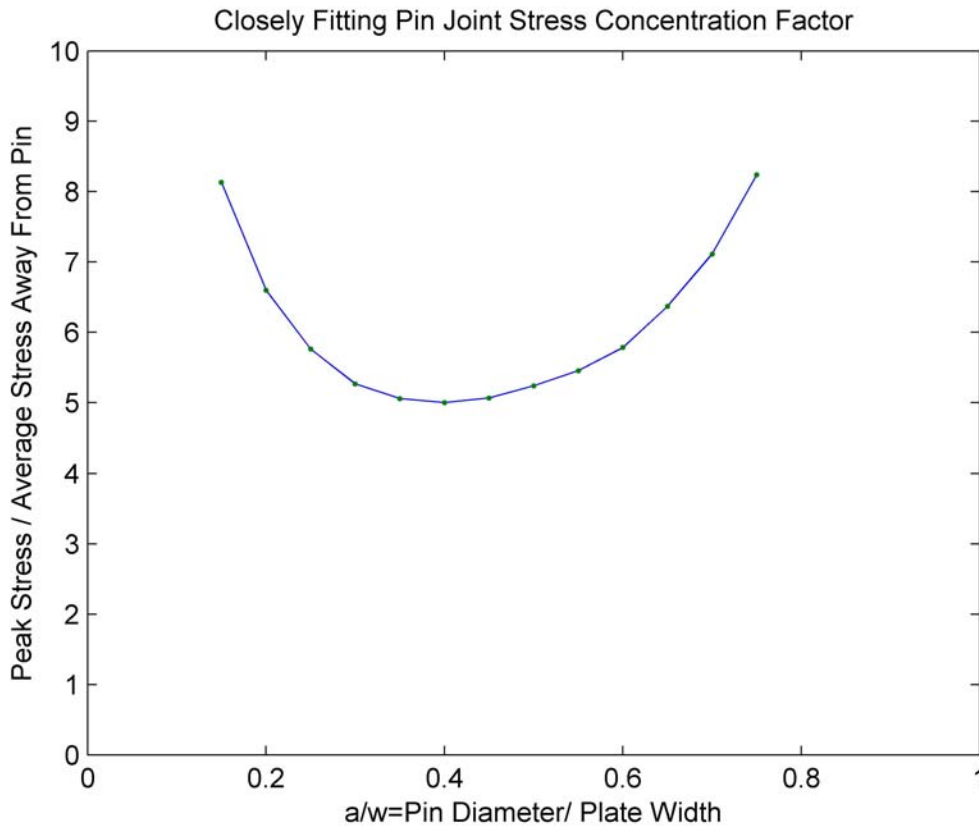
Figure 3.4.30: Stress Concentration Factors Restated For Constant Stress Distant From Pin

Thus, the minimum peak stress in the copper occurs if the pin diameter is 40% of the plate width, and is 5.0 times the ratio of total tensile force on the plate to the total cross sectional area of the plate not adjusted for the pin and hole. That ratio is simply the average tensile stress carried in the outer legs, which as stated earlier is 13.4 MPa=1.9 ksi. Applying this minimum stress concentration factor of 5.0 to it shows that for the most favorable pin diameter choice, the peak local concentrated copper stress near the pin would be (5)(1.9 ksi)=9.5 ksi. .This minimum peak copper stress situation occurs for a pin diameter 40 % of the plate's width, i.e., or (0.40)*(0.4971 m) = 0.199 m. Other choices of pin diameter would increase the peak copper stress. However, the minimum of this function is a very broad one and the peak copper stress is nowhere near copper's limit, so this calculation does not provide much guidance on the selection of pin diameter.

However, the pin will also be stressed and its peak stress depends more strongly on its diameter. The following diagram shows a TF Outer Leg mounted at the proper major radius on one of the steel beams in the pedestal's floor, between two of the racetrack-shaped penetrations to the basement. As indicated, the distance between centers of the penetrations at the major radius appropriate for the lower pin is 0.935 meters. This will be the distance between the Clevis fork's arms connecting the pin to the basement.

Each cylindrical pin's length is thus divided into regions based on loading. The middle 0.3446 meters of each pin will be pulled upwards with a smoothly distributed total force of 2.3 MN. On either side of that middle section there will be no load pressure for a distance, then 0.4675 m from the center each side will have a concentrated 1.15 MN force pulling downwards towards the basement.

In this situation the pin acts as a horizontal beam with vertical loading. Assuming the upwards force on the pin is evenly distributed within the TF Outer Leg, the maximum bending moment in the pin is trivially calculated as:

$M_{max}=(0.4665-0.1723)*(1.15E6)+(0.1723)*(1.15E6)/2 = 4.374*10^5$ Newton-meters.

Now, the peak stress of a beam in bending is given by

$$\sigma_{max} = \frac{M_{max}}{S}$$

where S is the beam's section modulus, i.e., its moment of inertia divided by the maximum section distance to its neutral axis. For a cylindrical pin, the section modulus is

$$S = \frac{\pi R^3}{4} = \frac{\pi D^3}{32}$$

where R and D are the pin's radius and diameter respectively. Combining these and solving for the pin diameter gives:

$$D = \sqrt[3]{\frac{32 M_{max}}{\pi \sigma_{max}}} = \sqrt[3]{\frac{4.455E6 \text{ Nm}}{\sigma_{max}}}$$

Using this formula, to limit the peak bending stress in the pin to 138 MPa (i.e., about 20 ksi) its diameter would need to be 0.318 m. Such a pin would be 64% of the radial width of the TF Outer Leg. Such a large pin would be acceptable but it seems that a smaller pin would be better since it would not restrict the electrical current flow as much. Therefore, the relationship is plotted in the following MATLAB graph:
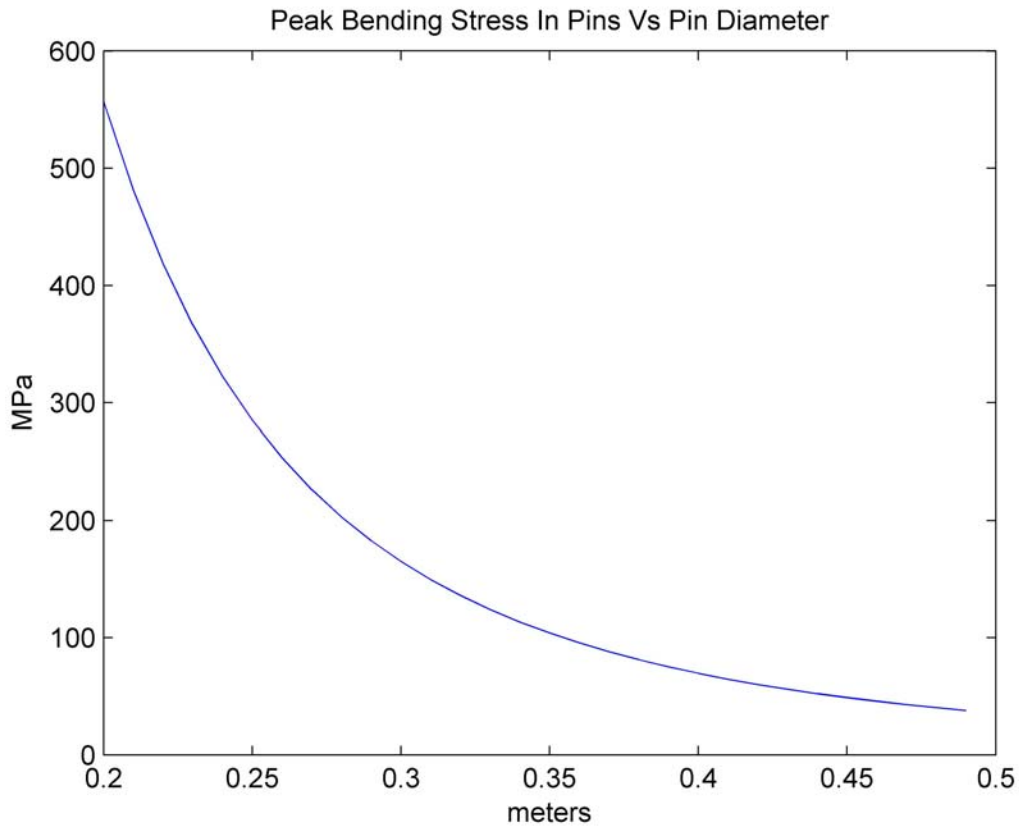
Figure 3.4.31: Maximum Pin Stress Due To Bending Vs. Pin Diameter

We note that average stress in the highest stress section through the pin would be much lower than this value, which only applies for the peak bending stress "fiber" most distant from the pin's neutral axis. For this type of service it may be acceptable to operate stainless steel pins to a peak local bending stress near 200 MPa, in which case the pin diameter could be as little as 0.28 m. However, there are other materials which could alternatively be used for these pins which can withstand far more stress. For instance, Inconel 718 pins could operate with peak stresses above 600 MPa, so if Inconel pins were used the pins could be as little as 0.20 m (i.e., about 8 inches) in diameter. This choice is attractive since it would minimize peak copper stress while leaving plenty of copper cross section through which the TF current can flow around the pin. Thus, it is tentatively recommended that the load transfer pins in the TF outer legs be of Inconel and be about 0.2 meters (i.e., about 8 inches) in diameter.

3.4.2.6.3   Radial Support of TF Outer Legs

Because of their large size, the TF Outer Legs will be fabricated as a laminate of many thin copper plates. After cutting holes through each plate to accommodate the pins and then modifying each plate's edges for edge cooling, a stack of plates is soldered together to form a turn assembly which is next wrapped with turn insulation. Each TF Outer Leg results from joining two turn assemblies.

The thin copper plates used to fabricate the TF Outer Legs will have been cold-worked by rolling them to uniform thickness, so they can be expected to exhibit typical "full hard" yield point stresses instead of the lower yield point stresses typical of softer extruded copper. Each TF Outer Leg includes two copper turns with a combined cross section extending 0.4971 m in the radial direction and 0.3446 in the toroidal direction. Since each turn will be constructed as a stack of plates each of which has the full 7 m height and the full radial extent of 0.4971 m , it follows that the moment of inertia in bending of each TF Outer Leg cross section opposing radial deformations is
   I=(0.3446 m)(0.4971)^3/12=3.5275E-3 m^4.

Each TF Outer Leg will be restrained against outward radial motion at concentrated simple support locations near the Outer Leg's top and bottom. The beam-like rigidity of the TF Outer Leg conductors will limit their deformation and resulting deflections at other locations.   The largest resulting radial deflection of the copper will be at the midplane, where it is given by the following formula (from Roark, Table 3 formula 2e):

$$\delta_{max} = \frac{5L^4 w}{384EI}$$

where
w=(170,879 N/m/turn)(2 turns) = 341,758 N/m,
I=0.0035275 m^4,
E=1.25*1011 Pa for copper,
L ≤ 7 m (depending on support locations)

The largest possible midplane deflection would result from locating the supports at the very top and bottom in which case we would have L=7 m as a limiting case. With this substituted the maximum midplane deflection becomes 0.0243 m.   Peak stress in the "fiber" most distant from the neutral axis would then be:

$$\sigma_{max} = \frac{M_{max}c}{I} = \frac{wL^2 c}{8I}$$

$$= \frac{(341,758 \text{ N/m})(7 \text{ m})^2 (0.4971 m/2)}{8(0.0035275 \text{ m}^4)} = 147.5 \text{ MPa}$$

$$= 21.36 \text{ ksi}$$

This is not too large a value for the maximum fiber stress in "full hard" copper. However, this value is not entirely accurate. It is an overestimate of peak bending stress since it is not feasible to radially restrain a TF Outer Leg from its very top edge, and furthermore the radial restraints must avoid interfering with the outer TF electrical joints.

Since the full TF current does not flow all the way to the top and bottom of each TF Outer Leg and since the upper restraint will also not be at the top, better estimates result from incorporating those details. Since the situation then deviates from the general case, general formulas from Roark's compendium do not apply and the ordinary differential equations for ideal beams must be solved numerically. As presented by Popov's textbook the follow differential are valid for describing small deflections of a straight beam:

$$\frac{dV(s)}{ds} = q(s)$$

$$\frac{dM(s)}{ds} = V(s)$$

$$\frac{d\theta(s)}{ds} = \frac{1}{EI(s)} M(s)$$

$$\frac{dy(s)}{ds} = \theta(s)$$

Here, the position of a particular cross section perpendicular to the beam's straight length is denoted by the independent variable, s, which represents distance along the beam's axis. The lineal force density of the perpendicular loading applied to the beam at location s is q(s). The total shear force acting across a particular cross section is V(s), and the bending moment, M(s), characterizes how axial tension or compression varies linearly across that cross section.   The small angle of deflection from the unloaded axis of the beam is θ(s) in radian units, and the actual deflection distance of the beam at location s is y(s). The material comprising the beam has a Young's elastic modulus value of E, and the shape of the beam's geometrical cross section at the location denoted by s is characterized by its moment of inertia about the axial plane through its neutral axis, I(s).

The loading q(s) must include all the applied forces including the forces of restraint necessary to maintain static equilibrium.

TF Outer Leg loading is modeled as resulting from uniform vertically directed current flowing between the centers of its upper and lower joints. Thus, the estimated total E-M radial force is

(6.5 m)(341,758 N/m)=2.22 MN

We assume this is restrained by two inward radial forces, one acting at the very base of the TF Outer Leg where restraints mounted on the pedestal floor will prevent the TF Outer Legs from sliding, and the other acting 6.2 meters higher on a pin through the outer leg. The physical laws requiring a balance of both forces and moments then imply that the upper pin radial force component must be 1.25 MN while the lower force is 0.97 MN. Incorporating these loads, the resulting calculated beamlike deflection of each TF Outer Leg is calculated by a MATLAB code cell documented in the Appendix, resulting in the following graph figure. In its plots, q is the local loading force density on the TF Outer Leg in newtons per meter, V is the internal shear force in newtons, M is the internal bending moment in newton-meters, θ is the local angular rotation in radians due to bending, and Y is the local radial deflection in meters.
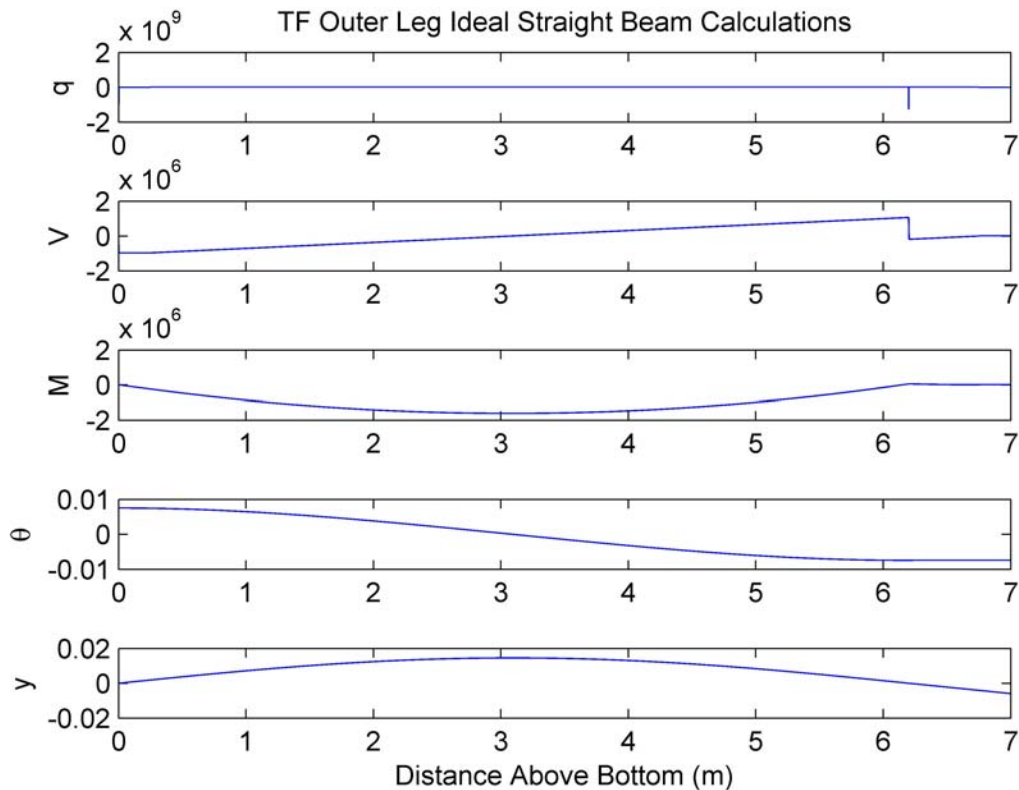
Figure 3.4.32: TF Outer Leg Beam Analysis Results At Full In-Plane TF Loading

Thus, the ideal straight beam differential equations predict that at full TF loading with unyielding radial restraints located at the TF Outer Leg's base and the upper pin, its peak local radial deflection of 14.6 mm (i.e., 0.57 inches) occurs near its middle 3.093 m up from its bottom. The maximum local stress produced in the copper by the bending moment is 113.44 MPa, equivalent to about 16.43 ksi, and it occurs on the outer edge of the TF Outer Leg at about the same elevation. Actually, the TF Outer Leg restraint will be relatively unyielding at its base, but the upper pin will only be radially restrained by the umbrella structure which will elastically deform by a measurable amount. Thus, actual peak outer leg deflection will exceed 14.3 mm.

3.4.2.6.4 Support Of TF Lower Radials

The following diagram depicts TF Lower Radials in plan view superimposed on the underlying pedestal floor. The two turns of each component are angled away from each other forming a V shape as they approach the TF Outer Legs in order to straddle them and implement a clamped joint there. The visible break in a turn conductor of one of the radials is the site where the TF power supply feeds TF current in and out of the system through buswork connected from below.
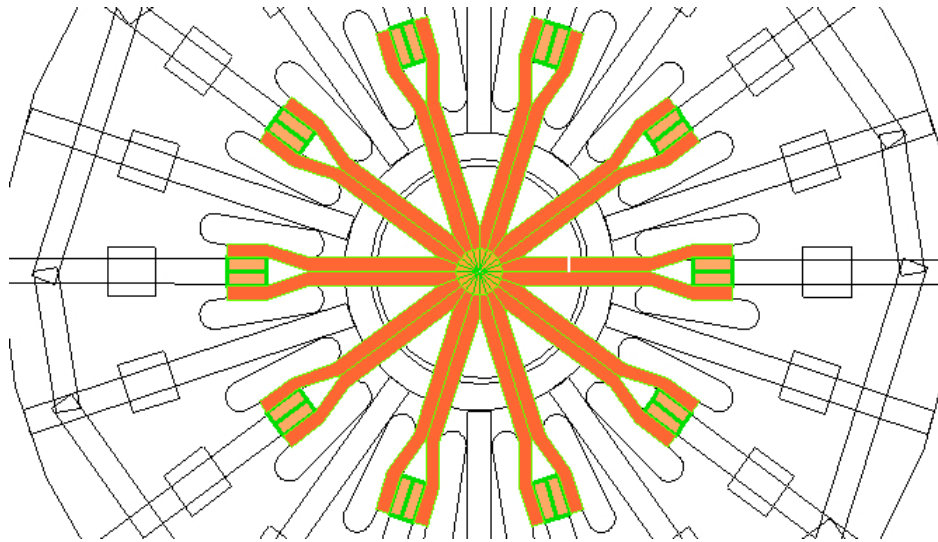
Figure 3.4.33: TF Lower Radials Will Be Supported By The Floor

Because of their large thickness, it is expected that each turn conductor of the TF Radials will be fabricated as a laminate of thin copper plates. Each plate will be bent to form its desired shape as shown in the plan view diagram, then after cooling provisions are added to the external edges of each plate the entire stack of plates will be soldered together to form a structurally stiff turn assembly. External electrical insulation will be applied to complete the component assembly.

The electromagnetic force on the TF lower radials mainly pushes them down against the pedestal floor and the new structure inside the pedestal's ring girder which will be attached to it. The TF Lower Radials will thus be directly supported against vertical magnetic forces by the pedestal floor. Braces mounted on the floor (not shown) will provide support for the smaller sideways forces on the TF Lower Radials arising from their magnetic interaction with poloidal fields.

3.4.2.6.5 Umbrella Structure

The situation is different for the top of NHTX for which it will be necessary to design and build an umbrella structure. That umbrella structure must be far less massive than the floor's network of steel beams embedded in concrete, but must also radially transmit the 23 MN vertical separating forces between the TF Outer Legs and the TF Upper Radials. in addition to accommodating out-of-plane forces. It must be sufficiently strong for the loads, but it will not be feasible for it to be so massive that its deflections would be negligible.

The requirement that the umbrella structure must also be capable of quick and easy removal and reassembly is another complicating constraint.

Because of the approach taken for the inner TF joint design, it would be best if the deflections under load of the umbrella structure would compensate for and cancel out the

vertical elongation under load of the TF outer legs. Thus, although the TF outer legs would "grow" vertically by about 0.75 mm as the TF is ramped up to its full field, the umbrella structure ideally would change its shape in such a way that it would lower the inner end of the TF Radials with respect to their outer end by a compensating 0.75 mm. This design goal is useful because if it were achieved it would make the inner TF joints robustly unaffected by changes in toroidal field.

It would also be best if the angular deflections under load canceled out at the TF inner joint, so that there would not be any tendency for the joint to pitch and thus partially open under load.

It appears that the only way to achieve these design goals is to harness outward radial motion of the top of the TF Outer Legs. Some small outward radial motion will occur because of the elastic compliance of the upper radial support structures. If the umbrella structure is sufficiently tall and stiff, the outward radial motion of the TF Outer Legs' tops can push down on the TF Upper Radial at its inner TF joint.   On the other hand, if it is too compliant then the radial motion would be accommodated by stretching of the structure, with no "dishing".

3.4.2.6.6 Vertical Support For TF Upper Radials By The Umbrella Structure
We continue in this section to apply simplified analytical models to investigate design possibilities. Although to evaluate the final NHTX design a full 3-D finite element mechanical and thermal analysis will be appropriate, the approaches used herein use 1-D or even 0-D approximations in order to sort out different possibilities and synthesize a promising design.

To develop the truss/ring layout for the umbrella structure, we focus on a single TF Radial. At full toroidal field, the total vertical electromagnetic force on each TF Radial of 2.3 MN directed upwards has an effective line of action located at a major radius of R=1.137. The mechanical restraining force transmitted by the TF Outer Legs has an equal magnitude directed downwards but has a line of action at a major radius of R=2.926 m. The two forces thus form a couple which applies an in-plane torque of to the TF Upper Radial in a direction such that its inner end would rotate up while its outer end would rotate down.   Its magnitude is as follows:
   $(2.3 \text{ MN})(2.926 \text{ m} - 1.137 \text{ m}) = 4.1147 * 10^6 \text{ N-m}$

From the very limited set of feasible options for countering this torque, the NHTX design employs horizontal forces. In order for the umbrella structure to generate and apply an equal but opposite torque it employs a toroidal restraining ring located above the inner side of the TF Upper Radial which operates in tension to apply an inward directed radial force.   This ring's inward radial force magnitude matches the magnitude of a different outward directed radial force which has a lower line of action. The outward directed radial force could in principle be generated by a second restraining ring operating in compression at a lower elevation, but in the NHTX design case there is a more convenient source for it. Each TF Outer Leg electromagnetically develops its own

outward directed radial force in direct proportion to the vertical force on its associated TF Radial, and the same circular pins which couple the vertical separating force through the TF Outer Legs can also transfer this radial force.

If the upper and lower pins through each TF Outer Leg located symmetrically above and below its center were both used for radial restraint of the TF Outer Legs, each pin would transfer half of the 2.22 MN radial force developed in its TF Outer Leg, i.e., 1.11 MN. Then, to generate a torque which balances the vertically directed couple, the lines of actions in the new horizontal couple would need to be vertically separated by $(4.1147 * 10^6$ N-m $)/(1.11 * 10^6$ N$) = 3.70$ meters.

Thus, in that case the umbrella's inner ring would need to be located at an elevation 3.7 meters higher than the TF Outer Leg's upper pin in order to avoid the necessity of using a second restraining ring to generate an additional large radial force.

However, radial restraint of the TF Outer Legs will not be vertically symmetric since the lower radial restraint will not use the pin. Instead, the steel beams in the floor will provide radial restraint for the TF Outer Legs through short, rigidly attached clamps. Thus, the lower radial restraints will be located essentially at the bottoms of the TF Outer Legs. Choosing to center the upper pin 0.8 meters below the TF Outer Leg's top guarantees no direct interference between that pin and the nearby joints, but does change the radial restraint forces. For static equilibrium the lower restraint force with a radial line of action through the bottom of its TF Outer Leg is reduced to 0.97 MN while the upper restraint force with its radial line of action through the pin 0.8 meters below the TF Outer Leg's top is increased to 1.25 MN. It then follows that to generate the balancing torque in the structural supports without requiring a large radial force from a second toroidal ring requires that the inner ring must be located above the upper pin by a vertical separation of

$(4.1147 * 10^6$ N-m $)/(1.25 * 10^6$ N$) = 3.292$ meters.

Thus, the inner ring should be located vertically 3.292-0.8=2.492 meters higher than the top of the TF Outer Leg, i.e., 9.492 meters above the level of the pedestal's surface. It will provide a 1.25 MN inwards radial restraint force to the planar support structure of each TF Upper Radial.

The transmission of the in-plane vertical force between the TF Outer Leg's upper pin and the distributed load on the TF Upper Radial will be accomplished using a truss structure. An efficient shape for that support structure is the associated finicular curve computed for the particular load distribution to be supported, as presented in Timoshenko & Young's classic 1945 textbook, Theory Of Structures. A familiar example of a funicular curve is the catenary curve used in the design of suspension bridges, but different shapes are appropriate for different load distributions.

The plot below shows in black the ideal finicular curve calculated to provide distributed vertical support for a TF Upper Radial along its entire radial extent. This calculation is

performed by a MATLAB cell documented in the Appendix for the distributed TF-only electromagnetic force distribution acting on a TF Upper Radial. The plot's axes represent cylindrical coordinates but the vertical coordinate has been displaced to display the vertical distance above the top of the TF Upper Radial. This funicular curve's horizontal tangent direction at its upper inner end is consistent with it being anchored there to the inner toroidal restraining ring which can only exert a purely radial force on it. The curve's slope at its outer lower end matches the vector direction of the total restraining force from the TF Outer Leg's upper pin. The vertical lines (green) connecting the funicular curve with the top of the TF Upper Radial represents structural truss link elements transmitting purely tensile or compressive vertical forces.
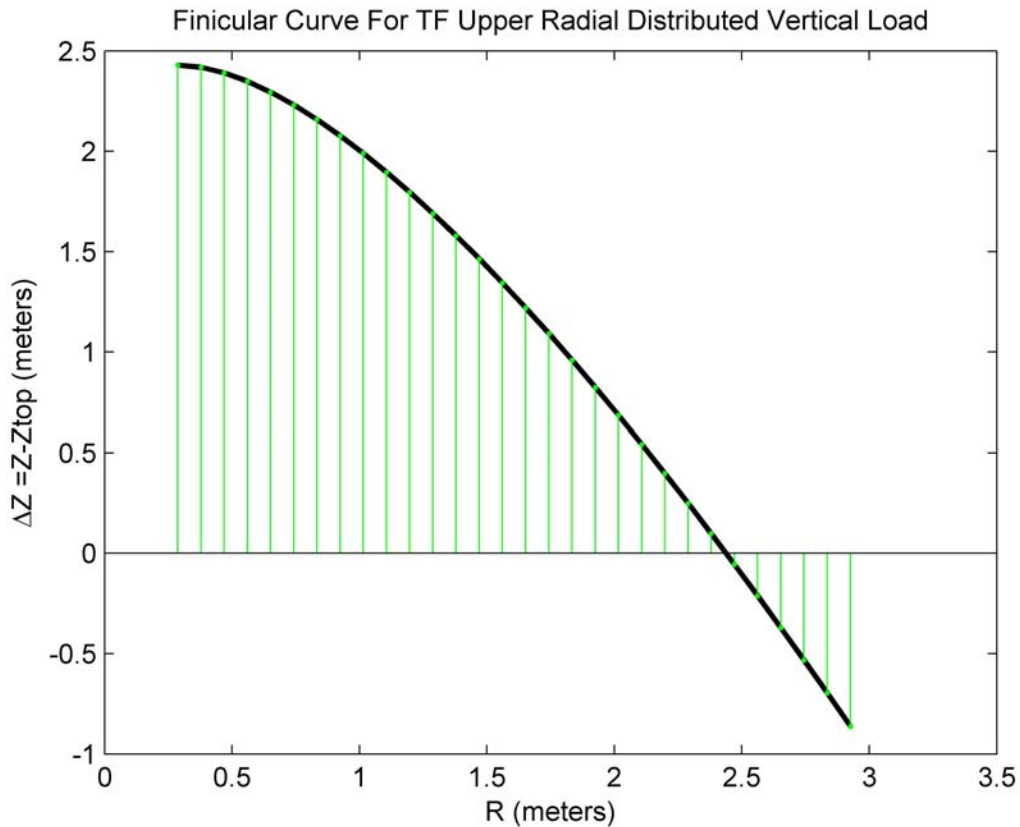
Figure 3.4.34: Finacular Shape Could Support A Nonrigid TF Upper Radial

There are no triangular truss elements shown in the figure because if they were present they would be inactive, i.e., the assumed loading distribution would result in their carrying zero tension or compression. On the other hand, triangular bracing elements should be included in appropriate places in an actual truss design in order to accommodate possible variations in loading and to provide structural stability.

In spite of the fact that this funicular curve shape would efficiently support the distributed loading of a TF Upper Radial, it is not adopted for the NHTX design because it

represents "overkill". It wastefully fails to make use of the inherent strength which the TF Upper Radial would already have. Indeed, the many vertically oriented link elements shown in green on the figure could in combination support a different TF Upper Radial design having almost no internal structural strength of its own. However, it is planned to construct each TF Upper Radial component from a stack of vertically oriented plates, in which each plate extends vertically from the bottom to the top of the allocated volume. This type of construction strongly resists deformations due to vertical force distributions.

A simpler structural support design results from choosing a small set of support locations and relying on the beam-like stiffness of each TF Upper Radial to limit internal inplane deflections and stresses at other locations. The minimum number of support locations capable of restraining a rigid body in static equilibrium against in-plane forces is two. However, it is planned that the TF Upper Radials will incorporate a flexible internal section in the radial interval from r=2.1 m to r=2.7 m, so some distributed inplane support must be provided for that flex section where internal stiffness is reduced. This will be accomplished by way of a radial beam at the top surface of each TF Upper Radial extending (at least) over the interval,
    $2.0 \text{ m} \le \text{r} \le 3.1746$.

For these reasons, each TF Upper Radial is divided into two disjoint intervals for the purpose of external support, and three locations are chosen to vertically support these intervals.   The flex region needs an adjacent beam to provide firm external support. Therefore, there are funicular support locations allocated at both ends of the flexes, i.e., at R=2.0 m and R=2.6 m.. The inner support location could be located at various different places due to the rigidity of the TF Upper Radial there. Therefore, it is important to examine the effects of different choices.

The discrete forces to react at the three support locations are determined through the following procedure, which tends to minimize internal stress required at location (2). (Step a) First, vertical forces at locations (1) and (2) which are statically equivalent to the distributed vertical E-M forces on the TF Upper Radial over the interval $0.287 \text{ m} \le \text{r} \le 2.0 \text{ m}$, are calculated .
(Step b) Second, forces at locations (2) and (3) are similarly calculated, statically equivalent to the distributed vertical E-M forces on the TF Upper Radial over the interval $2.0 \text{ m} \le \text{r} \le 3.1746 \text{ m}$.
(Step c) Finally, the two forces separately calculated for location (2) are summed.

Ideally, the deformation under TF-only loading of the TF Upper Radial and its support system should not only compensate for the 0.75 mm elastic growth of TF Outer Leg height, but it should also include an angular deformation such that the pressure profile of the TF inner joint remains unchanged.   This angular deformation is accomplished by forcing the joint boundary value of beam angle to be zero while adjusting parameters to obtain a 0.75 mm vertical deflection at the outer joint.

These TF Upper Radial support calculations were implemented in a MATLAB computation cell model in the Appendix, integrated with solution of the differential

equations for deflections of a straight beam representing the TF Upper Radial. The beam model was run for different choices of r1, the radius of the inner support. It was found that in order for the TF Upper Radial's deflection as predicted by beam theory to compensate for the approximately 0.75 mm extension of the outer leg resulting from its carrying the vertical separating load, the inner support for the TF Upper Radials with this model would need to be located at r1=0.83 meters. .
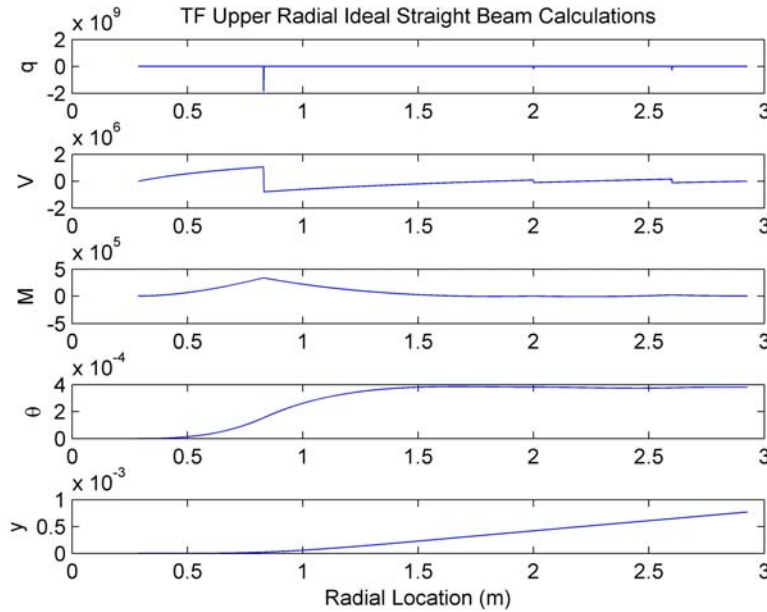
Figure 3.4.35: Beam Calculation In-Plane Results For TF Upper Radial
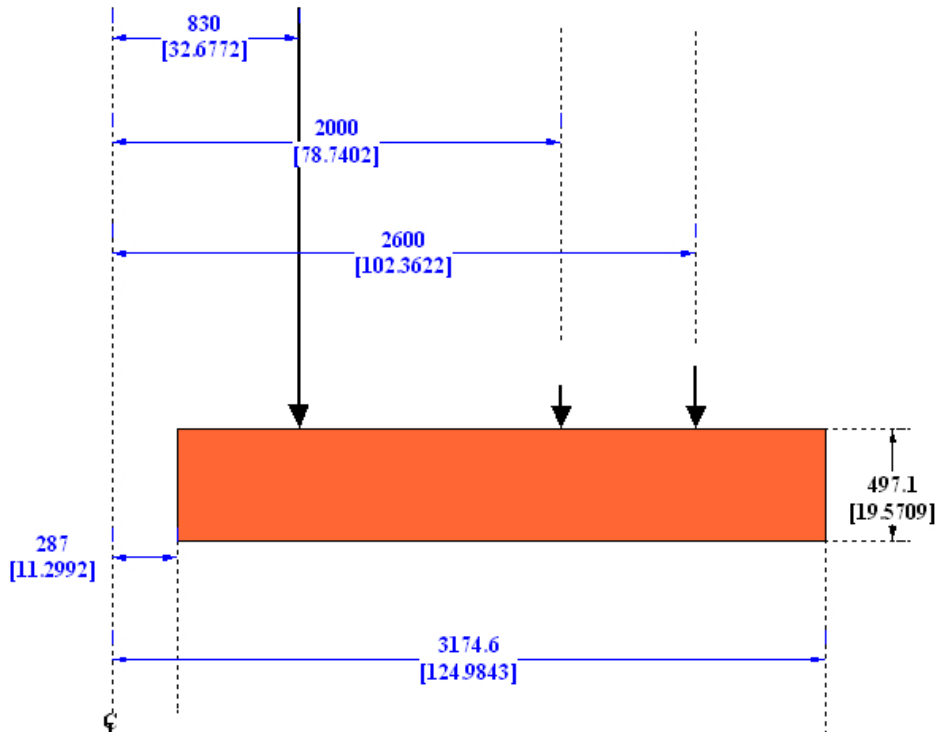
Figure 3.4.36: Beam Calculation In-Plane Restraints For TF Upper Radial

Table 3.4.2a: TF Upper Radial Vertical Forces of Restraint and Deflections

Point Number	Radial Location (m)	Vertical Restraint Force (MN)	Vertical Deflection Of Restraint With Respect To Inner Joint (mm)	Vertical Deflection Of Restraint With Respect To Outer Joint (mm)
0	R=0.287	0	0	-0.7702
1	R=0.83	-1.8546	0.0229	-0.7473
2	R=2.0	-0.1923	0.4202	-0.3570
3	R=2.6	-0.2750	0.6463	-0.1239
4	R=2.926	0	0.7702	0

Therefore, a design goal for the TF inplane support system is that under full TF load it should deform to approximately match the deflections listed in the right hand column of the above table, thus canceling out the extension of the TF Outer Legs due to loading. It should be noted that this requires the vertical deflections to be in the direction *opposite* to local vertical forces. Such a design requires more analysis than a brute force approach which simply makes a structure stiff and strong. It requires careful tuning of elastic constants in the structure to achieve this result, which in effect cancels out some deflections by using other deflections. If achieved, then the inner TF electrical joint will be relatively insensitive to TF loading changes without requiring extremely massive supports (like the floor) or locally bolted joints . It turns out that it can be achieved by exploiting elastic deformations which conically reshape the umbrella like a dish.
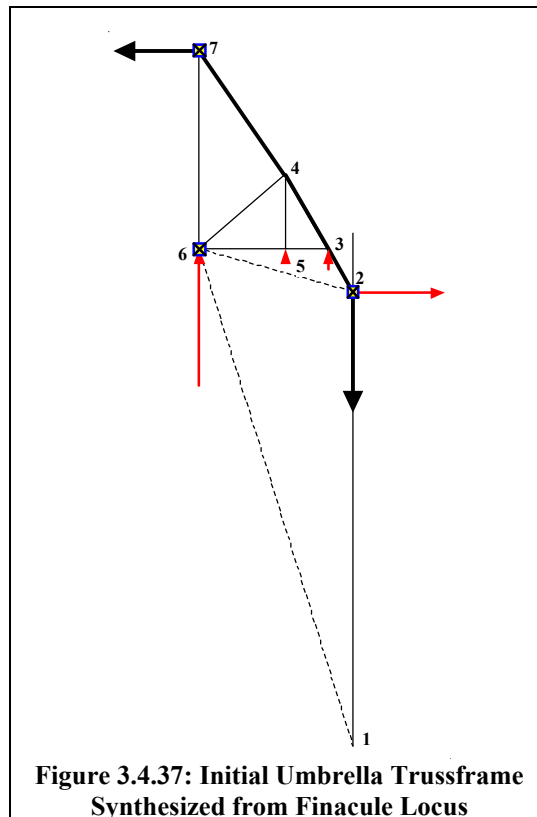
Figure 3.4.37: Initial Umbrella Trussframe Synthesized from Finacule Locus

In pursuit of this goal, the finacular curve was calculated for the three resultant concentrated vertical forces which are equivalent to the distributed electromagnetic forces and their lines of action. The funicular polygon vertices were as follows:

Table 3.4.2b: Funicular Polygon Vertices For Inplane Support of TF Upper Radial

Vertex	R (m)	Z (m)
a	0.83	9.5118
b	2.00	7.7822
c	2.60	6.8033
d	2.926	6.2000

These were used as the starting point to define a supporting trussframe as shown in the above diagram. Here, the diagram's nodes 1 and 2 represent respectively the bottom of the TF Outer Leg and the TF Outer Leg's upper pin. The finacule, shown in bold black,

includes nodes 2, 3, 4, and 7, and it terminates with a horizontal force at the inboard top and a downward force in the TF Outer Leg. The ring at node 7 provides the inward horizontal force for the finacule's end. The rings at nodes 2 and 6 were added later for trimming functions not initially modeled. The resultants of the electromagnetic forces to be supported by this trussframe are shown by the red vectors.

A MATLAB m-file was developed (see the Appendix) to solve for forces in 2D poloidal trusses incorporating toroidal rings, including solving for statically indeterminate force systems when needed using elastic compliance information. Using this m-file to analyze the initial truss layout showed that like any finacular curve it succeeds in supporting the loads while keeping bracing members inactive. Calculated results for this shape and loading showed approximately zero tension (or compression) in the bracing links directly connecting node 6 with nodes 1, 2, 4, 5, and in the bracing link connecting nodes 5 and 3. However, when reasonable values for the spring constants of links and rings were inserted, the results showed that the TF Upper Radial's inner joint would deflect upwards relative the TF Central Bundle by an amount excessive for an electrical joint. To eliminate this relative motion, rings were added at nodes 2 and 6 while the vertical relief of the trussframe above the pin location was linearly scaled. In addition, spring constants of truss members were increased to values corresponding to reducing average steel stresses to 14 MPa, with the objective of increasing the truss's elastic stiffness. Also, nodes 5 and 6 were raised slightly to be 0.05 m above the top of the TF Upper Radials in order to avoid interferences. With these changes including the stiffer spring constants, it was found that a vertical scaling factor of about 1.1, i.e., increasing the umbrella height by 10% beyond the funicular design, was sufficient to eliminate relative vertical motion at the TF upper inner joints. Some of the results from these calculations appear below: It turns out that the ring at node 2 resists about 9% of the radial force there while providing the necessary trimming so that TF inner joint vertical deflections are eliminated over the TF operating range. The ring at node 6 provides very little force but will be incorporated anyway as the mounting point for high pressure gas spring cylinders which will provide preload keeping the TF inner joints closed at low currents.

We note that in order to obtain this excellent calculated response from the umbrella structure it is necessary that its various truss spring constants be tuned properly. The solution calculated here is not the only design with this property, but many inadequately tuned designs would cause excessive relative motion of the TF upper inner joints. For this particular design, the large steel cross sections assumed are as follows.

Table 3.4.2c: Cross Sections For Elastic Compliance Response

Link or Ring #	Node	Node	Length (m)	Cross Section Area (steel) (m²)	Width (m) of square steel cross section member
2	2	3	0.68577	0.19094	0.437
3	3	4	1.1482	0.17364	0.417
5	4	5	0.97891	0.013935	0.118
8	4	7	2.0881	0.1619	0.402
9	6	7	2.7085	0.13439	0.367
10 (ring)	7	-	0.83 =radius	0.09028	0.300

The following diagram depicts the in-plane umbrella supports following these parameters. The pins shown are 200 millimeters in diameter, which as stated earlier leads

to pin bending stresses consistent with Inconel material. Widths of steel structural members have been scaled to approximately match the calculated cross-sections. The primary structural ring located at the top provides 90% of the radial restraint to the upper pin in each TF Outer Leg. The much smaller structural ring provides other 10% of the radial restraint, and an even smaller ring provides radial support for gas cylinders to hold TF inner joints closed. The sketch also shows the TF Radials slanting into the inner joints, a feature which provides favorable forces and flexibility.

Not discussed so far is the additional ring located above the outer upper TF joint. Together, the two outer rings play a role in supporting out-of-plane forces, as discussed in the next sections.

It may perhaps be possible to obtain similarly good structural response using truss members with smaller cross sections. The issue of alternative designs and design optimization was not investigated due to limited time. However, the important result here is the conclusion that at least one practical solution does exist for the umbrella's in-plane support structural design that is not excessively massive and provides good support of the

Figure 3.4.38: Concept Sketch for In-Plane Supports

TF Upper Radials and the TF upper inner electrical joints.
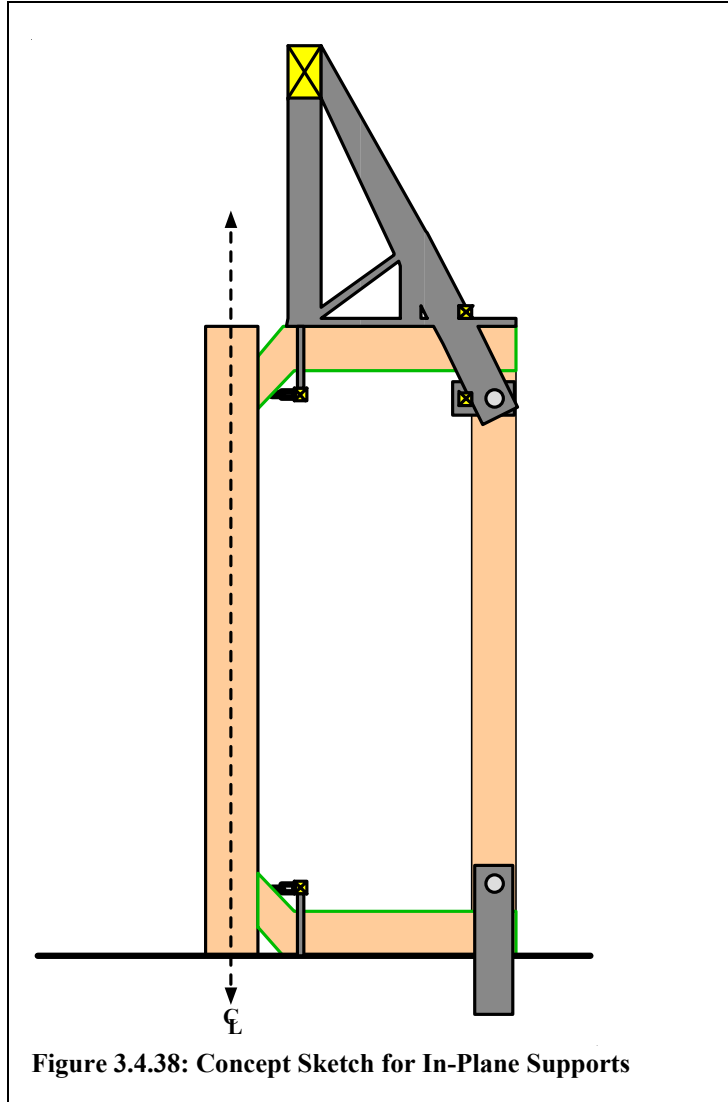
3.4.2.7 TF System Forces In The Toroidal Direction (i.e., Out-Of-Plane Forces)

TF Out-Of-Plane support is addressed in three parts. First, the distributed magnetic forces are estimated. Second, the ability of TF modules to withstand without excessive deformation or stress the distributed magnetic forces while being restrained at only concentrated support locations is evaluated. Third, the support system's ability to provide the concentrated restraining forces is considered.

The present section analyzes the out-of-plane forces exerted on the TF Radials and TF Outer Legs by expected poloidal fields. MATLAB calculation routines are used, as described in MSWORD/MATLAB notebook calculations documented in the Appendix. Calculation results are summarized in the following tables and plots.

For the four plasma scenarios, the calculated out-of-plane magnetic pressure profiles on the upper and lower TF Radials are shown in the following plots. Note that the maximum local pressure in any of the scenarios does not exceed 800 kPa, which is about 8 times atmospheric pressure (i.e., slightly less than about 120 psi).
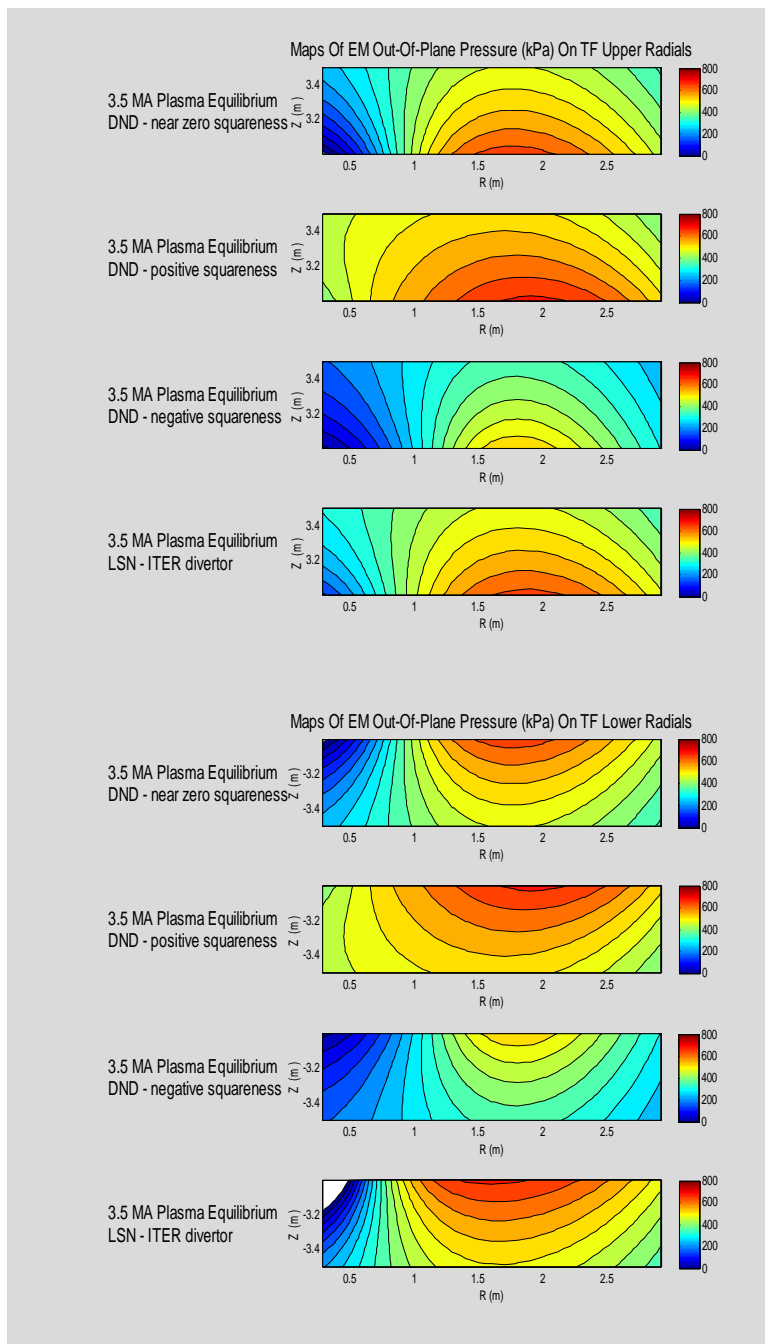
Figure 3.4.39: Out-of-Plane Magnetic Pressure On TF Radials Vs Plasma Equilibria

If each of these pressure profiles is vertically integrated to calculate the out-of-plane linear force density, the following eight curves result.
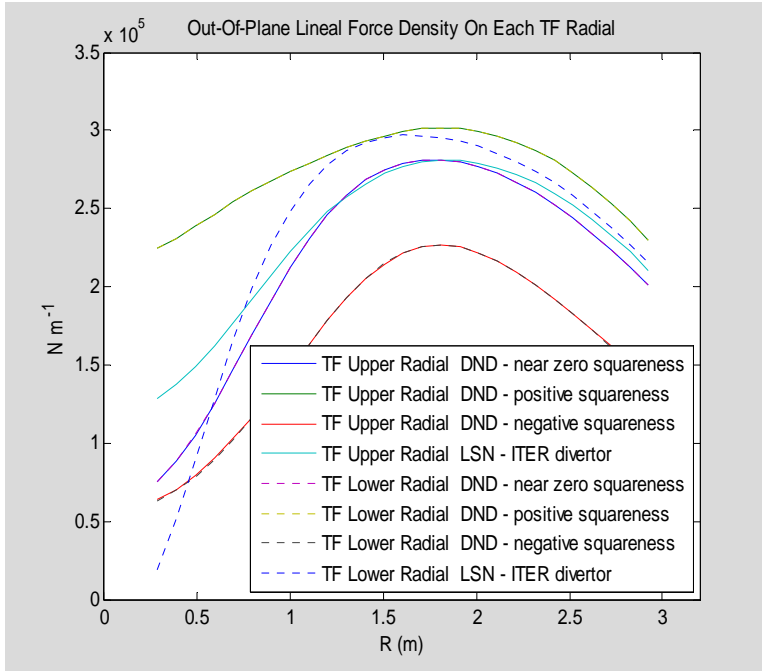
Figure 3.4.40: Linear OOP Force Density On TF Radials Vs Plasma Equilibrium

Only 5 curves are clearly visible here since the curves for upper and lower TF radials overlay each other in the Double Null Divertor (DND) cases. The following tables summarize total force and its moment about the NHTX machine's central axis, obtained by further numerical integration.

Table 3.4.3: E-M Force On Each TF Radial During 3.5 MA Plasma Operations

Plasma Scenario	Total E-M Force Per TF Upper Radial	Total E-M Force Per TF Lower Radial
DND-near zero squareness	$5.9060 *10^5$ N	$5.9060 *10^5$ N
DND-positive squareness	$7.2391 *10^5$ N	$7.2393 *10^5$ N
DND-negative squareness	$4.4676 *10^5$ N	$4.4646 *10^5$ N
LSN-ITER divertor	$6.2105 *10^5$ N	$6.2848 *10^5$ N

Table 3.4.4: E-M Moment About Central Axis From TF Radial During 3.5 MA Plasma Operations

Plasma Scenario	E-M Moment Per TF Upper Radial	E-M Moment Per TF Lower Radial
DND-near zero squareness	$1.0258 *10^6$ N-m	$1.0258 *10^6$ N-m
DND-positive squareness	$1.1760 *10^6$ N-m	$1.1761 *10^6$ N-m
DND-negative squareness	$0.7793 *10^6$ N-m	$0.7791 *10^6$ N-m
LSN-ITER divertor	$1.0560 *10^6$ N-m	$1.0951 *10^6$ N-m

The TF Outer Legs develop additional contributions to the overall overturning moment which must also be structurally resisted. They are calculated later.

3.4.2.7.1 TF Module Internal Stiffness Considerations For Out-Of-Plane Support

As discussed earlier, each TF Lower Radial and its associated TF Outer Leg will be mounted directly on the steel beams embedded in the pedestal floor, separated from the steel by a thin layer of solid electrical insulation. Each will be mechanically restrained from sliding in any horizontal direction by robust clamps which will be rigidly attached to the steel floor beams. Because of the extreme strength and stiffness of the massive floor structure, horizontal deflections of the TF Lower Radials or of the base of the TF Outer Legs will be negligible.

The NHTX structural support system will include a system of toroidal X-braces connecting the steel beams in the floor with the pair of outer toroidal ring located near the top of the TF Outer Legs. This system of X-braces will resist the total overturning moment and limit the ring's rotation about its symmetry axis under maximum loading conditions. Additional structural components will prevent the TF Upper Radials from rotating toroidally relative to that ring by providing toroidal restraints to each TF Upper Radial at concentrated location. This scheme requires that the internal stiffness of each TF Upper Radial component must provide the needed resistance to prevent excessive toroidal deformation or excessive localized mechanical stress.

In order to quantitatively estimate the TF Upper Radials' toroidal deflections with respect to the ring and their associated stresses, the one dimensional differential equations for ideal straight-beams are invoked. As presented by Popov the follow are valid for small deflections:

$$\frac{dV}{ds} = q(s)$$

$$\frac{dM}{ds} = V(s)$$

$$\frac{d\theta}{ds} = \frac{M(s)}{EI(s)}$$

$$\frac{dy}{ds} = \theta(s)$$

Here, the position of a particular cross section perpendicular to the beam's straight length is denoted by the independent variable, s, which represents distance along the beam's axis. The lineal force density of the perpendicular loading applied to the beam at location s is q(s). The total shear force acting across a particular cross section is V(s), and the bending moment, M(s), characterizes how axial tension or compression varies linearly across that cross section. The small angle of deflection from the unloaded axis of the beam is $\theta(s)$ in radian units, and the actual deflection distance of the beam at location s is

y(s). The material comprising the beam has a Young's elastic modulus value of E, and the shape of the beam's geometrical cross section is characterized by its moment of inertia, I.

To apply this model it is necessary to include in q(s) all forces applied to the beam including the forces of restraint, since both the net force and the net moment statically equivalent to q(s) must each be zero. It is also necessary to specify four boundary conditions in order to obtain a particular solution.

A difficulty is encountered because the TF Upper Radial design is not uniform. Since the upper part of the TF Outer Leg will move slightly radially, and since that motion must be permitted and retained since it is used in the in-plane support scheme to reduce vertical deflections at the TF inner joints, it follows that the TF Upper Radial's length must change slightly as the TF is ramped up. To accommodate this, it is planned that the TF Upper Radials will have a section in which the conductors are divided into many electrically paralleled thin flexible pieces bent into an S-shaped curve.   Flex conductors have been used in many previous designs but these may be the first set of water-cooled flexes capable of high current steady operation.

The difficulty is that the beam equations may be a poor approximation for the mechanical behavior of the TF Upper Radials in their flex conductor region, which will extend approximately over the major radius range from R=2.1 to R=2.6 meters.   If that region simply divided the conductor into many sheets, the beam equations could still be accurate provided the moment of inertia were reduced appropriately for the delamination state. However, the fact that the pieces are bent into S-shaped curves introduces other phenomena.

The approach followed here will simply use the beam equations with the appropriate modification to the moment of inertia in the flex section, but to totally ignore the force interactions of the S-shaped bends with the magnetic fields. It is simply hoped that since the two turns in each TF Upper Radial have their S-shaped bends in opposing directions, that perhaps some of the unmodelled interactions will cancel.   Obviously, a more detailed analysis will need to be conducted in later NHTX design phases.

The design plan is to externally restrain each TF Upper Radial against out-of-plane forces at three locations, two of which will be on the edges of the flex region. The use of three restraint locations effectively divides the assembly into two disjoint portions. Although two external restraint forces could be uniquely calculated for any loading, three statically equivalent forces can be found in an infinitude of different combinations. Thus, to calculate restraining forces for the two separate portions requires invoking some other constraint in order to determine the restraining forces at three support locations. The approach taken here involves the beam differential equations by requiring that beam deflections be zero at the three support locations. The beam ordinary differential equations have four free boundary conditions to set, of which two, i.e., the moment and shear at the inner end of the TF radial, will be set to zero. Thus, if the beam is supported at restraint locations r1, r2, r3 with restraint forces there of f1, f2, f3 and deflections there

of y1, y2, y3, then we will have five parameters to choose in order to set five resulting calculated quantities. The five parameters to choose and enter into the beam calculations are as follows:
(1) f1, the restraint force at the first support point,
(2) f2. the restraint force at the second support point,
(3) f3, the restraint force at the third support point,
(4) y0, the deflection at the inner end of the TF radial,
(5) θ0, the angular rotation at the inner end of the TF radial.
The five desired result values from the beam calculations are as follows:
(1) y1=0   (deflection at first support point)
(2) y2=0   (deflection at second support point)
(3) y3=0   (deflection at third support point)
(4) f1+f2+f3=Fem   (restraint force =electromagnetic force)
(5) r1*f1+r2*f2+r3*f3=sum (r*fem)   (restraint moment=electromagnetic moment)

Because the beam equations are linear, the 5X5 matrix of influence coefficients connecting inputs to outputs can be numerically calculated by running the beam model five times with perturbed inputs. Then the resulting matrix can be inverted and its inverse can premultiply the desired output vector to find the necessary input values.

This approach was followed here. In the flexes region, 2.0<R<2.6 meters, the moment of inertia of the cross section was adjusted to model the copper of the two turns being divided into a total of 72 separate flexes. This corresponds to using a 3/16 inch thick copper sheet for each flex, a thickness chosen because it would be difficult to provide steady edge cooling for thinner copper sheets. The resulting solutions to the beam equations meeting the above boundary conditions were then plotted versus radial position for each of the four plasma equilibrium scenarios previously calculated by J. Menard.

These MATLAB beam calculations, as documented in the Appendix, show that the maximum calculated out-of-plane deflection of the TF Upper Radial due to its own toroidal deformation perpendicular to the poloidal plane occurs in and beyond the flex region and is less than 2 millimeters. The following plot displays the results of these beam calculations for the four plasma scenarios. Stresses implied by these results are modest. The conclusion is that restraining the TF Upper Radials in only these three locations, which coincide with the chosen vertical restraint locations, provides an adequate design approach.
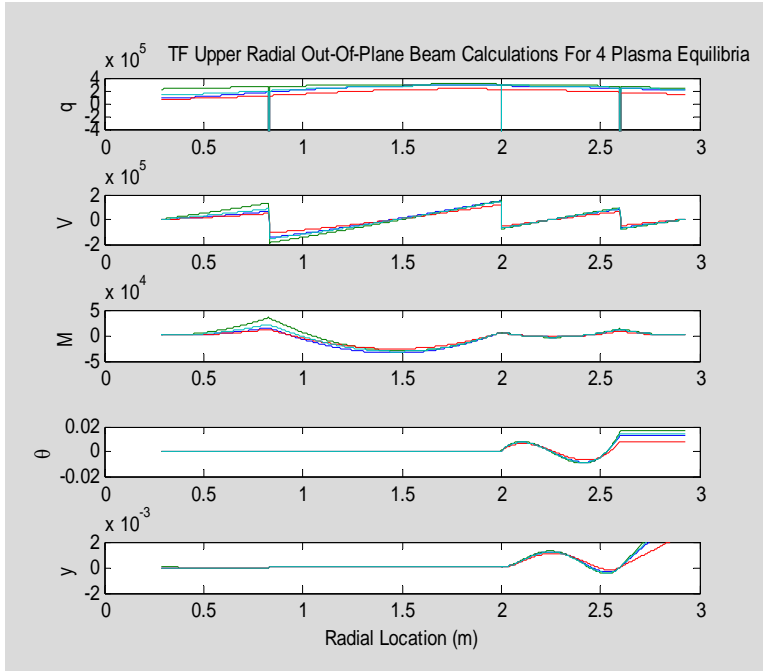
Figure 3.4.41: Out-of-plane Deformation of TF Upper Radials Vs. Plasma Scenario
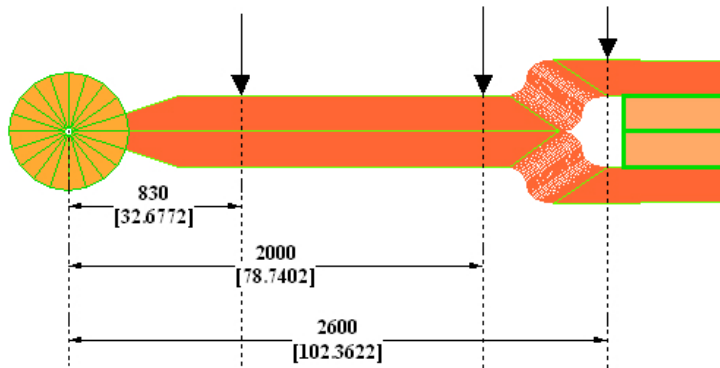
Figure 3.4.42:Out-of-plane Restraints of TF Upper Radials

3.4.2.8   *TF Out-Of-Plane Supports*

The Out-Of-Plane supports for the upper TF must provide firm sideways support for the TF Upper Radials at the three chosen support locations, i.e., at R=0.83 m, at R=2.0 m, and at R=2.6 m.   The three support locations for each TF Upper Radial transfer the toroidally directed electromagnetic forces to the outer rings located just inside the TF Outer Legs, above and below the TF Upper Radials.   These two toroidal rings are connected together in the regions between TF Outer Legs using "X-shaped" welded diagonal braces which effectively transmit torque between them.   In turn, the rings are restrained from rotation about the symmetry axis by X-braces attached to the pedestal floor. The connection between the rings and the X-braces involves a vertical pin on the X-braces sliding into a vertical hole attached to the rings, so that the X-braces do not interfere with vertical expansion of the TF Outer Legs.

Because the outer rings' torques are adjacent to the TF Outer Legs and they cross above and below the TF Upper Radials near the R=2.6 m location, torque can be easily transmitted to them there. Both the TF Outer Legs and the TF Radials are directly restrained by local clamps mounted on these rings.

However, the other two support locations require more extensive force transfer hardware for the out-of-plane restraints. Two different approaches are used, each one of which incorporates quick release features for easy demountability.

At the TF Upper Radials' middle out-of-plane support location at R=2.0 m, a mechanical clamp squeezing between different TF Upper Radials transmits torque to the outer rings at toroidal locations centered between the TF Outer Legs, as shown in the following sketch. Here, a radially moveable link operates each clamp, which employs link plates and hinge pins.
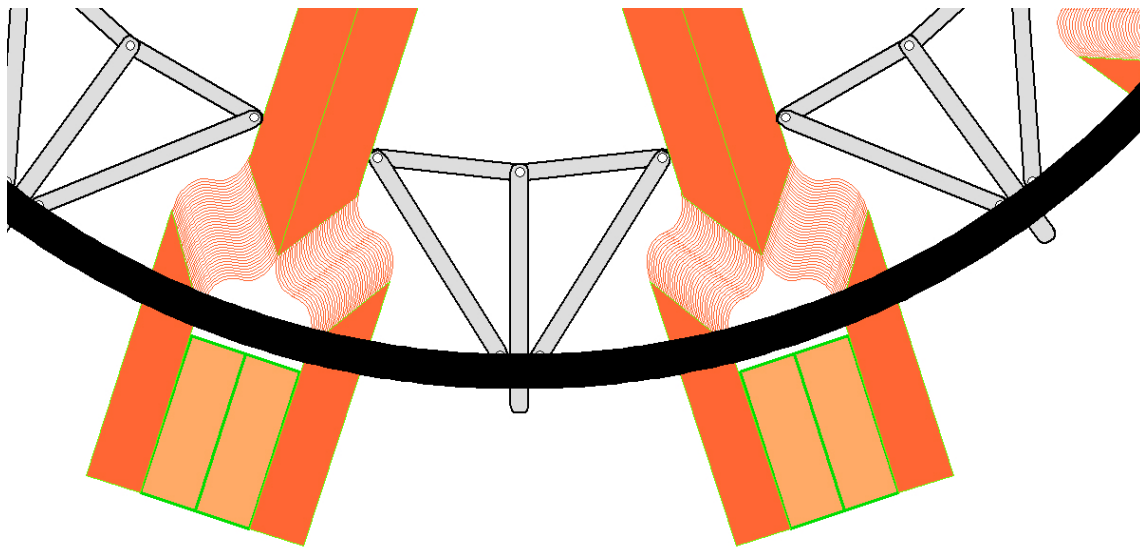
Figure 3.4.43: Out-of-plane Clamp Supports For TF Upper Radials at R=2.0 meters

As shown, each clamp's two outer link plates are mounted between the two vertically separated outer rings on vertical hinge pins which in the sketch are hidden by the upper ring. When each clamp's middle link plate is radially withdrawn, the two side link plates rotate away from the sides of the two TF Radials on either side of the clamp. Conversely, when the middle link plates are radially inserted they push the clamp's outer hinges firmly against the sides of the two TF Radials.

At the innermost support location, i.e., at R=0.83 m, the TF Upper Radials are restrained in the toroidal direction by radially inserted wedges which fill the gaps between the TF Upper Radials and web components of a strong metal hubspool assembly which extends above and below them. It is important to note that the wedges, which are inserted and withdrawn at times when the sideways magnetic force is zero, are not inserted with excessive force. As long as they completely fill the gaps their job is done. In the following conceptual sketch the wedges are shown in green, the hubspool webs are

shown in black, and the lower annular disk of the hubspool is shown in grey. The upper annular disk of the hubspool is not shown.
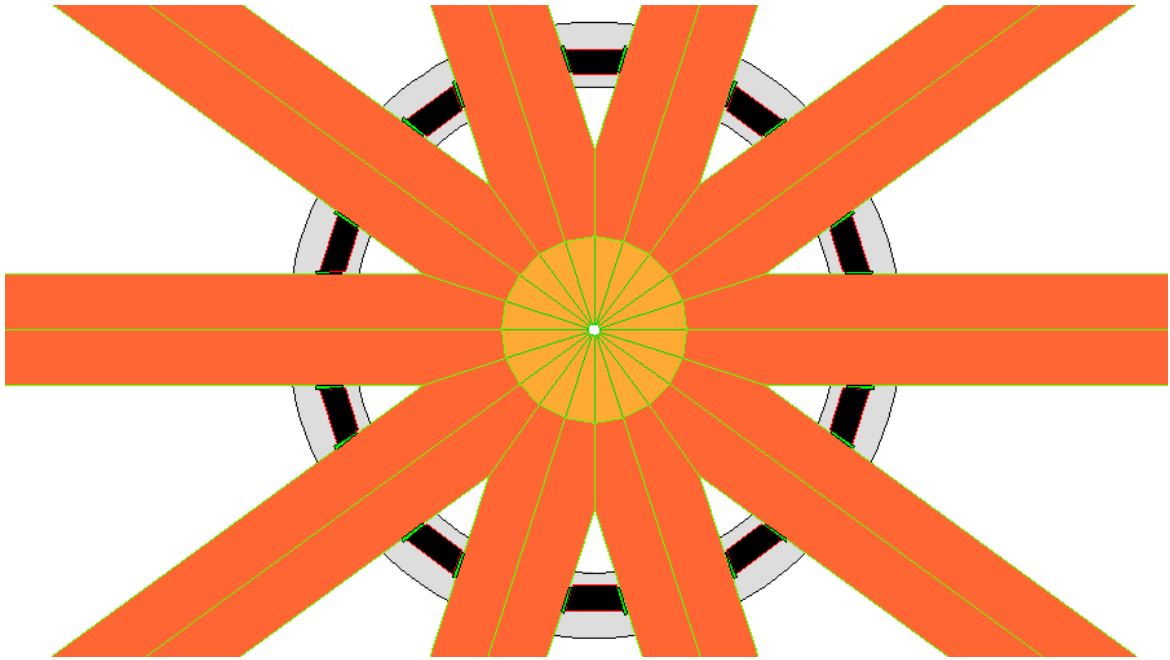
Figure 3.4.44: Out-of-Plane Wedge Supports for TF Upper Radials at R=0.83 meters

When out-of-plane forces are electromagnetically produced in TF Upper Radials, the gap-filling wedges transfer them as torques about the central axis of NHTX to the webs forming part of the hubspool. In turn, the hubspool's upper and lower annular disks are restrained by spokes running in nonradial directions which connect them to the two outer rings, similar to the way that spokes in the rear wheel of a bicycle transmit torque between its hub and its rim. The system of spokes is depicted in the following conceptual sketch, which shows them organized into two vertical levels, with spokes below the TF Upper Radials running clockwise outwards while those above run counterclockwise.
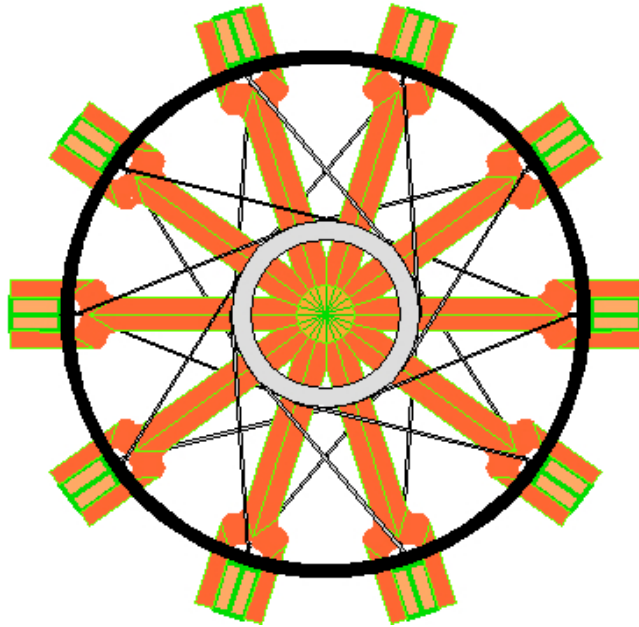
Figure 3.4.45: Hub, Rim, and Spokes Concept to Radially Transfer Out-of-plane Torques

A 3D sketch of these two out-of-plane support schemes follows. Although in-plane TF support structures are not shown, the sizes and 3D arrangements of components have been adjusted to be more consistent with force and elastic compliance requirements and to not spatially interfere with each other.
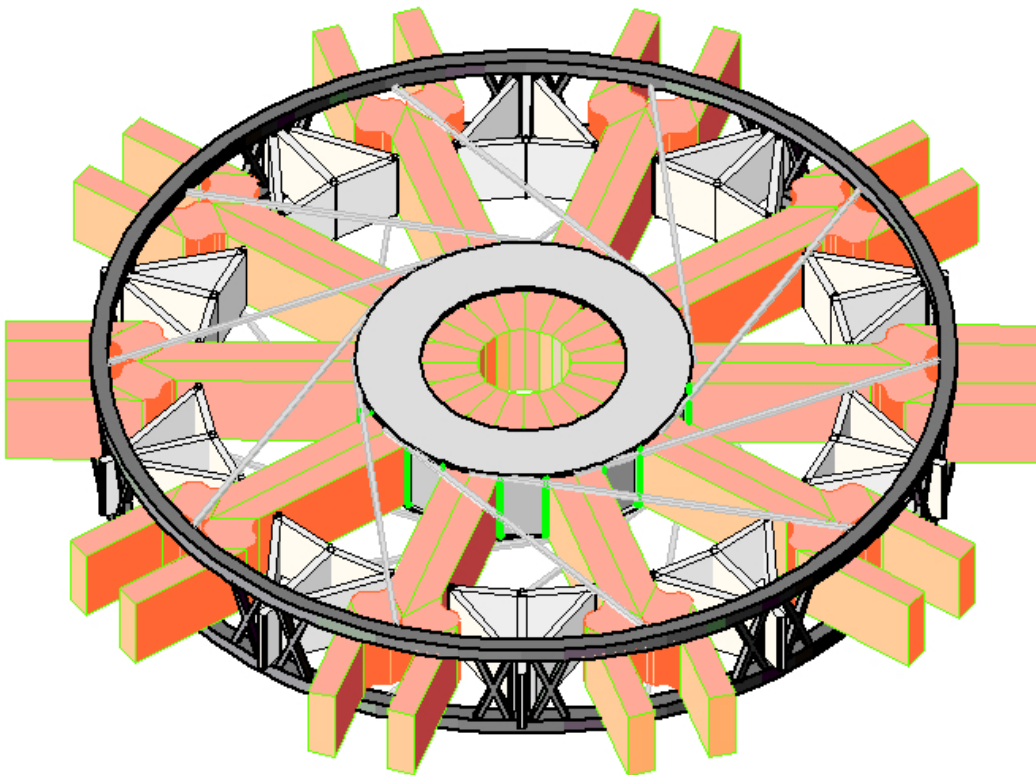
The third out-of-plane support location is formed by mechanical clamps (not shown) which are mounted on the two outer rings and which squeeze the outer TF electrical joints between the TF Upper Radials and the TF Outer Legs. These clamps transmit out-of-plane forces arising in the TF Outer Legs as well as in the TF Upper Radials to the two outer rings, from where the out-of-plane forces are transmitted to the floor through a system of tall X-braces which mates with the lower outer ring.

The lower portions of the TF system are not designed with quick release features for easy removal and replacement. The following 3D sketch depicts these lower portions, including the TF Central Bundle, TF Lower Radials, and TF Outer Legs. The sketch shows the lower 0.2 m diameter removable pins through the TF Outer Legs as being held down by clevis components which go through penetrations to the basement in order to transmit upwards forces to the steel beams in the basement ceiling. Each tall X-brace runs between locations radially just inside each TF Outer Leg at their tops or bottoms, skipping the adjacent location to meet the next TF Outer Leg. Cylinders topping each X-brace slide into holes in the lower of the outer rings to receive their out-of-plane torques. This X-brace scheme minimally restricts access by neutral beams and line-of-sight plasma diagnostics to a diamond-shaped pattern in which there are no obstructions in a midplane-centered zone more than 3 meters tall between each TF Outer Leg pair.
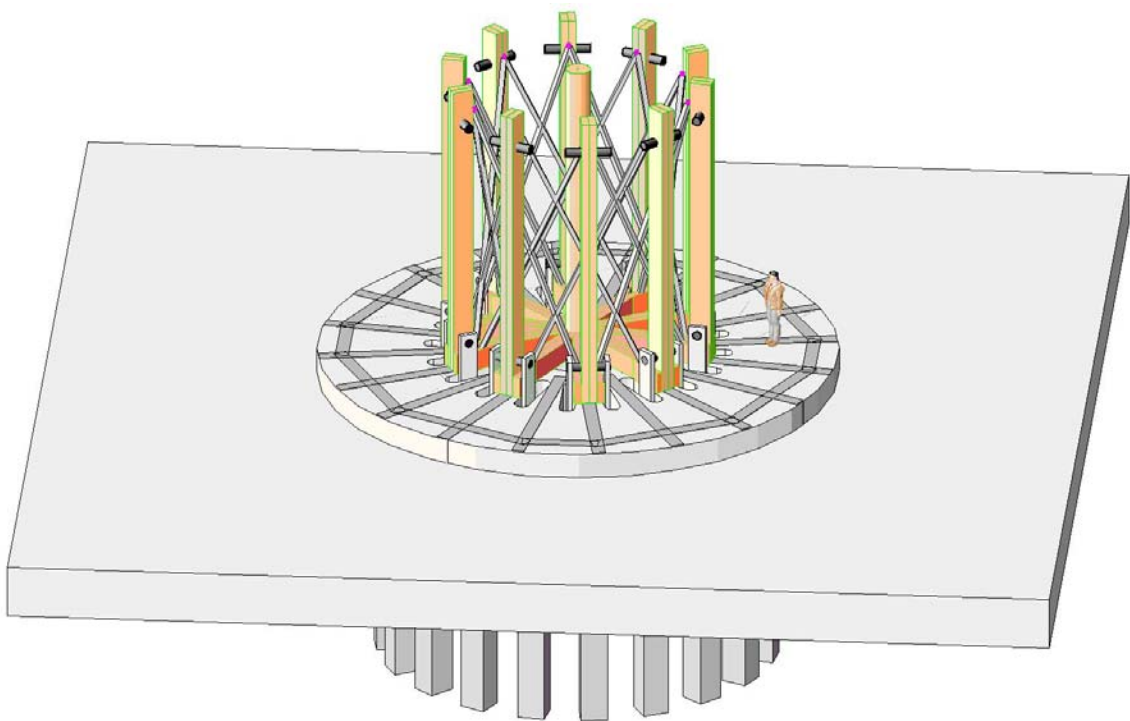
Figure 3.4.46: 3D View of Demountable TF System with Top Removed

A feature of all of the clamping arrangements is that they can be quickly released, after which the TF Upper Radials can slide radially outwards to clear the TF Central Bundle in preparation for removing the entire umbrella structure from the top of the NHTX machine.

The full removable umbrella structure also includes links and a massive topmost ring which together provide firm in-plane TF support so that the inner upper joints do not slide. The following 3D sketch shows it with these structures. However, this sketch still does not show spatial details of the TF inner joint shaping, the gas cylinders and ring which clamp the inner joints closed at zero field, the upper inner PF coils mounted on the bottom of the umbrella structure, water cooling manifolds, or electrical buswork.
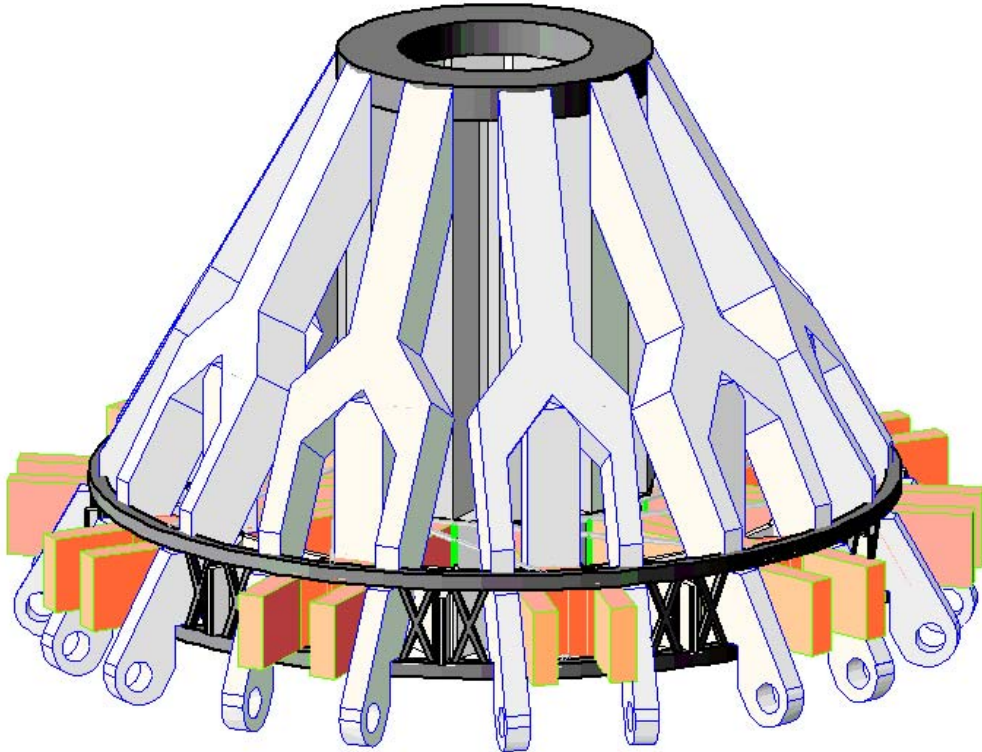
Figure 3.4.47: Removable Umbrella Structure With Upper TF Components

The following 3D sketch depicts the entire NHTX TF system and its support structure, with its removable umbrella mated to the lower components
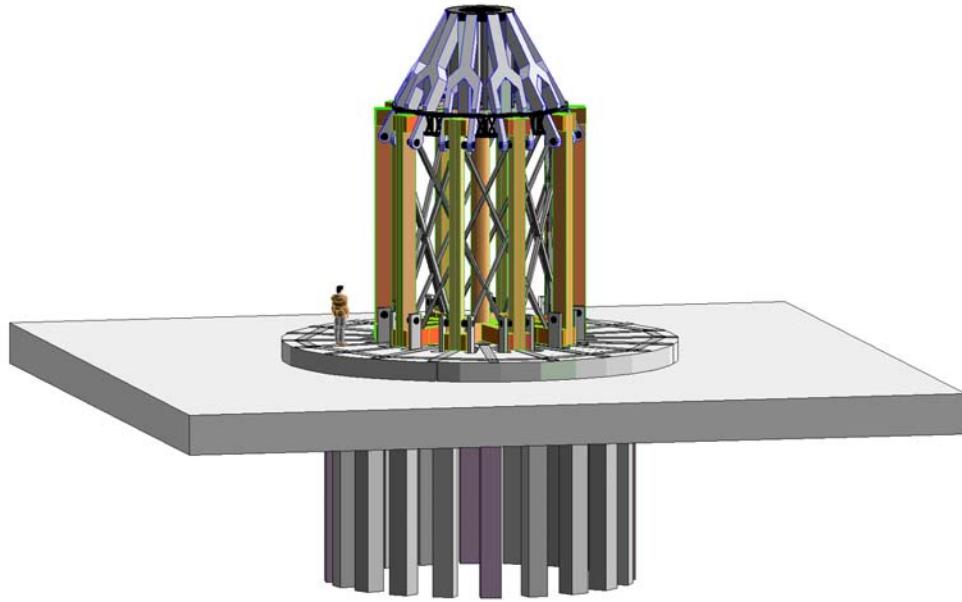
Figure 3.4.48: Assembled TF and Support Systems

3.4.2.9 TF System Inductance Calculations

An estimate of the energy and thus of the self-inductance of the TF (toroidal field) system can be made by hand calculations using an approximate axisymmetric model of TF currents to estimate the dependence of toroidal magnetic field on position, then spatially integrate the energy content of that magnetic field. This procedure is followed below.

We will use the cylindrical coordinate system to denote spatial locations by the triplet, (r,ϕ,z). For axisymmetric functions which in the present model include the toroidal field system threading current and the toroidal field strength, the dependence is only on (r,z) since there is no dependence on ϕ.

The spatial density of energy stored in a magnetic field, in joules per cubic meter, is $\dfrac{B^2}{2\mu_0}$ where B is the magnetic field in Tesla and μ_0 is the magnetic permeability which for free space is $4\pi*10^{-7}$ henries/meter. The total energy stored in a magnetic field is the integral of the energy density over all space, so for an axisymmetric magnetic field,

$$E \equiv \iiint \frac{B^2}{2\mu_0} d^3\vec{r} = \frac{\pi}{\mu_0} \iint_{(r,z)} r(B(r,z))^2 dr dz$$

Here, axisymmetry has been invoked to integrate over ϕ, so the remaining double integral is taken over the poloidal half-plane. Denoting $I(r,z)$ to represent the net TF system poloidal current (in ampere-turns) which threads upwards through a hypothetical circular loop coaxial with the cylindrical coordinate system and located at (r,z), the resulting toroidal field is

$$B(r,z) = \frac{\mu_0 I(r,z)}{2\pi r}$$

so the energy integral becomes

$$E = \frac{\pi}{\mu_0} \iint\limits_{(r,z)} r\left(\frac{\mu_0 I(r,z)}{2\pi r}\right)^2 drdz = \frac{\mu_0}{4\pi} \iint\limits_{(r,z)} \frac{(I(r,z))^2}{r} drdz$$

Since the threading current is zero outside the TF system, the integration can be restricted to the finite region of the poloidal plane including the TF system. The NHTX TF system's region can be subdivided into

        (1) The enclosed vacuum region,
        (2) The central bundle region
        (3) The outer leg region
        (4) The upper and lower radials regions.

This subdivision is useful because each of these subregions has a different spatial variation of the threading current function. Thus, the stored energies in each of these subregions are separately calculated, then added together to obtain the total stored energy.

$$E = E_{Region(1)} + E_{Region(2)} + E_{Region(3)} + E_{Region(4)}$$

In the enclosed vacuum region there are no TF conductors so the threading current function is a constant there which does not vary with spatial position, i.e., $I_{(1)}(r,z) = N_{TF} I_{TF}$. This simplifies the calculation since the constant threading current can be taken outside the integral:

$$E_{(1)} = \frac{\mu_0}{4\pi} \iint\limits_{Region(1)} \frac{(I(r,z))^2}{r} drdz = \frac{\mu_0 N_{TF}^2 I_{TF}^2}{4\pi} \int\limits_{Region(1)} dz \int\limits_{Region(1)} \frac{dr}{r}$$

$$= \frac{\mu_0 N_{TF}^2 I_{TF}^2}{4\pi} \left(Z_{max(1)} - Z_{min(1)}\right) \ln\left(\frac{R_{max(1)}}{R_{min(1)}}\right)$$

$$= \frac{\left(4\pi * 10^{-7}\right)\left(20\right)^2 \left(5 * 10^5\right)^2}{4\pi} (2)(3.0029) \ln\left(\frac{2.6775}{0.287}\right)$$

$$= 1.341 * 10^8 \text{ Joules}$$

In the central bundle region we approximate the TF system current as having everywhere a constant vertical direction and a constant current density. With those assumptions it follows that the threading current at any location is a fraction of the total TF ampere turns, with the fraction being the ratio of the area of the location's enclosed circle to the cross sectional area of the entire TF central bundle. Thus, in this region we have

$$I_{(2)}(r,z) = \left(N_{TF} I_{TF}\right)\left(\frac{r}{R_{CentralBundle}}\right)^2$$

and a total energy of

$$E_{(2)} = \frac{\mu_0}{4\pi} \iint\limits_{\text{Region}(2)} \frac{(I(r,z))^2}{r} dr dz = \frac{\mu_0 N_{TF}^2 I_{TF}^2}{4\pi R_{\text{CentralBundle}}^4} \int\limits_{\text{Region}(2)} dz \int\limits_{\text{Region}(2)} r^3 dr =$$

$$= \frac{\mu_0 N_{TF}^2 I_{TF}^2}{4\pi R_{\text{CentralBundle}}^4} \left(Z_{\max(2)} - Z_{\min(2)} \right) \frac{R_{\text{CentralBundle}}^4}{4} = \frac{\mu_0 N_{TF}^2 I_{TF}^2}{16\pi} \left(Z_{\max(2)} - Z_{\min(2)} \right)$$

$$= 1.501 * 10^7 \text{ Joules}$$

In the outer leg region we ignore the fact that the TF current flows in ten spatially distinct outer legs and instead model the outer legs as a complete axisymmetric cylindrical shell in which TF current flows vertically with a constant current density. The total cross sectional area of that hypothetical cylindrical shell is $\pi\left(R_{\text{OLmax}}^2 - R_{\text{OLmin}}^2\right)$. The threading current function must vary in the shell from $N_{TF}I_{TF}$ at its inner edge to zero at its outer edge. At any location within the shell, the fraction of total cross sectional area inboard of that location is $\dfrac{R_{\text{OLmax}}^2 - r^2}{R_{\text{OLmax}}^2 - R_{\text{OLmin}}^2}$, so we assume the threading current function in the shell is as follows:

$$I_{(3)}(r,z) = \left(N_{TF}I_{TF}\right)\left(\frac{R_{\text{OLmax}}^2 - r^2}{R_{\text{OLmax}}^2 - R_{\text{OLmin}}^2} \right)$$

Then the energy stored in the outer legs region's magnetic field is estimated as:

$$E_{(3)} = \frac{\mu_0}{4\pi} \iint\limits_{\text{Region}(3)} \frac{(I(r,z))^2}{r} dr dz$$

$$= \frac{\mu_0 N_{TF}^2 I_{TF}^2}{4\pi} \int\limits_{\text{Region}(3)} dz \int\limits_{\text{Region}(3)} \frac{1}{r}\left(\frac{R_{\text{OLmax}}^2 - r^2}{R_{\text{OLmax}}^2 - R_{\text{OLmin}}^2} \right)^2 dr$$

$$= \frac{\mu_0 N_{TF}^2 I_{TF}^2}{4\pi} \left(Z_{\max(3)} - Z_{\min(3)} \right) \int\limits_{R_{\text{OLmin}}}^{R_{\text{OLmax}}} \frac{1}{r}\left(\frac{R_{\text{OLmax}}^2 - r^2}{R_{\text{OLmax}}^2 - R_{\text{OLmin}}^2} \right)^2 dr$$

$$= \frac{\mu_0 N_{TF}^2 I_{TF}^2}{4\pi} \frac{\left(Z_{\max(3)} - Z_{\min(3)} \right)}{\left(R_{\text{OLmax}}^2 - R_{\text{OLmin}}^2 \right)^2} \int\limits_{R_{\text{OLmin}}}^{R_{\text{OLmax}}} \frac{1}{r}\left(R_{\text{OLmax}}^4 - 2R_{\text{OLmax}}^2 r^2 + r^4 \right) dr$$

$$= \frac{\mu_0 N_{TF}^2 I_{TF}^2}{4\pi}\left(Z_{\max(3)} - Z_{\min(3)}\right)*$$

$$\left(\frac{R_{OLmax}^4}{\left(R_{OLmax}^2 - R_{OLmin}^2\right)^2}\ln\left(\frac{R_{OLmax}}{R_{OLmin}}\right) - \frac{\left(3R_{OLmax}^2 - R_{OLmin}^2\right)}{4\left(R_{OLmax}^2 - R_{OLmin}^2\right)}\right)$$

$$= 3.7056 * 10^6 \text{ Joules}$$

Within the upper and lower TF Radials the toroidal field at any particular vertical section is modeled as varying linearly from its value at the boundary with other regions to zero at the external edge of the TF Radial. Since in regions (1), (2), and (3) the toroidal field strength is independent of z, the magnetic field in each TF Radial is modeled to be consistent with constant current density, as follows:

$$B_{(4)} = \frac{\left|z - Z_{(123)}\right|}{Z_{(4)max} - Z_{(123)max}} B_{(123)}(r)$$

where the subscripts denote boundaries with other regions. Then

$$E_{(4)} \equiv \iiint_{Region(4)} \frac{B^2}{2\mu_0} d^3\vec{r} = \frac{\pi}{\mu_0} \iint_{(r,z)_{(4)}} r\left(B(r,z)\right)^2 drdz$$

$$= \frac{\pi}{\mu_0} \iint_{(r,z)_{(4)}} r\left(\frac{z - Z_{(123)}}{Z_{(4)max} - Z_{(123)max}}\right)^2 \left(B_{(123)}(r)\right)^2 drdz$$

$$= \left(\int_{Region(4)} \left(\frac{z - Z_{(123)}}{Z_{(4)max} - Z_{(123)max}}\right)^2 dz\right)\left(\frac{\pi}{\mu_0} \int_{Regions(123)} \left(B_{(123)}(r)\right)^2 rdr\right)$$

$$= \frac{2}{3}\left(Z_{(4)max} - Z_{(123)max}\right)\left(\frac{E_{(1)} + E_{(2)} + E_{(3)}}{Z_{(123)max} - Z_{(123)min}}\right)$$

$$= \frac{2}{3}\left(\frac{Z_{(4)max} - Z_{(123)max}}{Z_{(123)max} - Z_{(123)min}}\right)\left(E_{(1)} + E_{(2)} + E_{(3)}\right)$$

$$= \frac{2}{3}\left(\frac{3.5 - 3.0029}{(2)(3.0029)}\right)*$$

$$\left(1.341 * 10^8 + 1.501 * 10^7 + 3.7056 * 10^6\right)\text{Joules}$$

$$= 8.432 * 10^6 \text{ Joules}$$

Total magnetic energy in the toroidal field is then

$$E = E_{Region(1)} + E_{Region(2)} + E_{Region(3)} + E_{Region(4)}$$

$$= 1.341 * 10^8 + 1.501 * 10^7 + 3.7056 * 10^6 + 8.432 * 10^6$$

$$= 1.612 * 10^8 \text{ Joules}$$

The estimated toroidal field system inductance, L_{TF}, is then obtained by

$$E = 1.612 * 10^8 \text{ Joules} = \frac{L_{TF}}{2} I_{TF}^2$$

or

$$E = 1.612 * 10^8 \text{ Joules} = \frac{L_{TF}}{2} I_{TF}^2$$

$$L_{TF} = \frac{2E}{I_{TF}^2} = \frac{(2)(1.612 * 10^8)}{(5 * 10^5)^2} = 0.00129 \text{ henry}$$

$$= 1.29 \text{ millihenry}$$

This error in this L_{TF}=1.29 millihenry estimate is expected to be near 10%, and to arise mainly because of the modeling assumption of axisymmetry. While this assumption is good in the high field strength regions, it is quite inaccurate in the larger volumes with lower field strength in the vicinity of the outer legs.

3.4.3   Poloidal Field (PF) Magnet System

The PF coil set initially proposed by J. Menard was evaluated and adjusted to optimize the match with the existing Transrex power supply system and to maximize the space available in tight inboard regions of the machine, with due consideration of thermal performance. The fields and forces for the adjusted PF coil set were analyzed and assessed.

3.4.3.1   Refinement of PF Coil Geometry Within.Power Supply Constraints

Four plasma equilibria were initially calculated for NHTX (by J.Menard) consistent with a PF coil geometry found to provide ample flexibility for controlling plasma shape. This geometry is summarized in Table 3.4.5 in terms of each coil's current center, width and height. Figure 1 plots their cross sections in the (r,z) poloidal half-plane.

Table 3.4.5: Initial PF Coil Geometry As Assumed in Plasma Equilibria Calculations

Coil Index	Coil Name	r (m)	dr (m)	z (m)	dz (m)
1	OH	0.33	0.04	0	4.5
2	PF1U	0.42	0.08	1.6	0.4
3	PF2U1	0.51	0.24	2.05	0.3
4	PF2U2	0.51	0.24	2.4	0.3
5	PF3U	0.9	0.24	2.4	0.3
6	PF4U	1.25	0.3	2.08	0.24
7	PF5U2	2.1	0.4	1.4	0.2
8	PF5U1	3.425	0.45	1.2	0.4
9	PF5L1	3.425	0.45	-1.2	0.4
10	PF5L2	2.1	0.4	-1.4	0.2
11	PF4L	1.25	0.3	-2.08	0.24
12	PF3L	0.9	0.24	-2.4	0.3
13	PF2L2	0.51	0.24	-2.4	0.3
14	PF2L1	0.51	0.24	-2.05	0.3
15	PF1L	0.42	0.08	-1.6	0.4
16	Plasma	1.0	0.89	0	
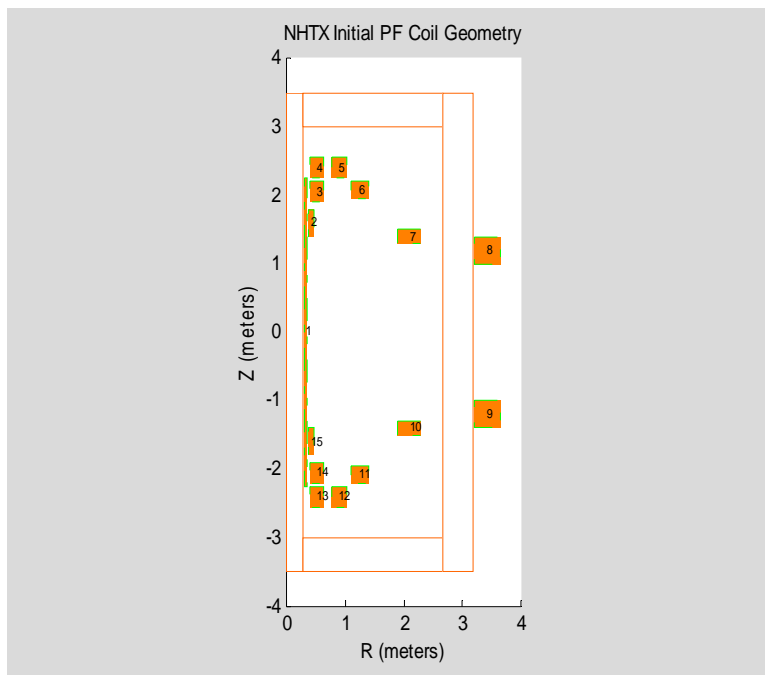
Figure 3.4.49: Initial PF Coil Geometry For NHTX Plasma Equilibria Calculations

Table 3.4.6 lists coil currents for each equilibrium normalized to 3.5 MA plasma current..

Table 3.4.6: Initial Plasma Equilibria PF Coil Currents Scaled To 3.5 MA Plasma Current.

Index	Coil Name	Plasma Equilibrium Name: DND - near zero squareness (kA-turns)	DND - positive squareness (kA-turns)	DND - negative squareness (kA-turns)	LSN - ITER divertor (kA-turns)
1	OH	0	0	0	0
2	PF1U	292	0	330	0
3	PF2U1	155	280	576	155
4	PF2U2	10	106	165	10
5	PF3U	15	181	373	-102
6	PF4U	1015	276	1015	135
7	PF5U2	-1210	62	256	-1210
8	PF5U1	-1219	-2238	-1219	-2532
9	PF5L1	-1216	-2354	-1216	-2533
10	PF5L2	-1212	132	256	-1212
11	PF4L	1008	-105	1008	-105
12	PF3L	22	175	373	-102
13	PF2L2	13	992	992	13
14	PF2L1	157	1121	1121	157
15	PF1L	292	-609	330	-609
16	Plasma	3500	3500	3500	3500

Existing thyristor rectifier power supplies remaining from the TFTR project include 37 identical independently controllable power systems, each of which contains two identical electrically isolated power supply sections. Each of these 74 sections provides output power with bidirectional dc voltages controllable in the ±1000 volt range and unidirectional dc currents ranging up to 30,000 amperes. Since these sections are electrically isolated, their dc outputs can be interconnected in series/parallel combinations to develop higher voltages or higher currents, or they can be used in different circuits.

However, the maximum output current per section is thermally limited based on pulse duration and duty cycle. Although brief 30 kA pulses are possible, the section current rating is only 24 kA for pulses lasting 3 seconds and is lower for longer duration pulses, declining to the steady-state dc current rating of only 3.25 kA. A thermal analysis (by C.Neumeyer) has concluded that with 1000 second pulses repeated once per hour for an 8 hour run period each day, the allowable dc current per power supply section is 6.5 kA.

Due to apparent source impedance within the power supplies, the full dc output voltage capability is reduced below 1 kV as output current is increased. This voltage droop is significant at 30 kA but small at 6.5 kA. However, because of it the maximum steady power that NHTX can extract from a single power supply section for each 1000 second pulse is reduced below (1kV)(6.5 kA)=6.5 MW to slightly more than 6 MW.

The design of the NHTX PF coils should assign numbers of turns to each PF coil in such a way that this existing set of power supplies remaining from TFTR will suffice for

NHTX PF and OH coils. That requires taking into account the section current limitation to 6.5 kA, the section voltage limitation to slightly less than 1 kV and the resistive voltage drop needed to drive the steady coil currents through both PF coils and also through external PF buswork and power cabling. Some useful guidance results from considering the maximum coil power dissipations, which can be calculated from the data of Tables 3.4.5-6 independent of how the numbers of coil turns are assigned. Table 3.4.7 presents the resulting calculated resistive power dissipated in each coil for each of the four equilibria, assuming only that the coils are 80% OFHC copper by volume and that their average copper temperature is 75C.

Table 3.4.7: Power Dissipated In Initial PF Coil Set For Plasma Equilibrium At 3.5 MA Plasma Current
(Assuming 0.80 packing factor and 75C Average Copper Temperature)

Equilibrium Name=		DND_0SQ	DND_PSQ	DND_NSQ	ITER_LSN	Maximums
index	Coil	MW	MW	MW	MW	MW
1	OH	0.000	0.000	0.000	0.000	0.000
2	PF1U	0.233	0.137	0.181	0.000	0.233
3	PF2U1	0.125	0.382	0.028	0.090	0.382
4	PF2U2	0.031	0.004	0.000	0.013	0.031
5	PF3U	0.282	0.021	0.000	0.066	0.282
6	PF4U	0.154	0.051	2.906	0.215	2.906
7	PF5U2	0.155	0.279	6.243	0.016	6.243
8	PF5U1	13.579	19.828	4.595	15.482	19.828
9	PF5L1	13.578	19.830	4.572	17.127	19.830
10	PF5L2	0.155	0.279	6.264	0.075	6.264
11	PF4L	0.154	0.052	2.868	0.031	2.868
12	PF3L	0.282	0.021	0.001	0.062	0.282
13	PF2L2	0.031	0.004	0.000	1.132	1.132
14	PF2L1	0.125	0.382	0.028	1.446	1.446
15	PF1L	0.233	0.137	0.181	0.791	0.791
Total PF System Power=		29.118	41.408	27.868	36.547	41.408

In Table 3.4.7 the steady coil power dissipations reflecting NHTX Plasma Equilibrium calculations are listed for each equilibrium and for each coil, and their maximum dissipation values for each coil are listed in the highlighted right hand column. One can immediately observe that many of the coil maximum power levels are considerably less than 6 megawatts. These include each of the 10 coils for PF1 through PF4, i.e., coil indices 2 through 6 and 11 through 15. A single power supply section would be more than adequate to power each of these PF coils, provided that the proper number of turns is chosen and that each power supply section is connected in the appropriate polarity.

Each of the Table 3.4.7 projected maximum dissipations for the 4 PF5 coils (i.e., for coil indices 7 through 10) exceeds 6 megawatts. With 74 power supply sections available for use, it is appropriate to provide some margin for these by assigning 2 power supply sections each to the PF5U2 and PF5L2 coils and 4 power supply sections each to the PF5U1and PF5L1 coils.

.

After further consideration of space requirements for the vacuum vessel and TF systems, it became apparent that it would be beneficial to reduce the heights allocated for the PF coils with indices 4, 5, 12, and 13. For coil indices 5 and 12 this improves divertor access while for coil indices 4 and 13 this allows improved TF joints. Table 3.4.8 summarizes the resulting modified PF coil geometry, and Figure 3.4.50 plots the revised coil cross sections in the (r,z) poloidal half-plane. Since current centers of the PF coils are unchanged, the coil currents needed for plasma equilibrium do not change much.

Table 3.4.8: Revised NHTX PF Coil Geometry

Coil Index	Coil Name	r (m)	dr (m)	z (m)	dz (m)
1	OH	0.33	0.04	0	4.5
2	PF1U	0.42	0.08	1.6	0.4
3	PF2U1	0.51	0.24	2.05	0.3
4	PF2U2	0.51	0.24	2.4	0.15
5	PF3U	0.9	0.24	2.4	0.15
6	PF4U	1.25	0.3	2.08	0.24
7	PF5U2	2.1	0.4	1.4	0.2
8	PF5U1	3.425	0.45	1.2	0.4
9	PF5L1	3.425	0.45	-1.2	0.4
10	PF5L2	2.1	0.4	-1.4	0.2
11	PF4L	1.25	0.3	-2.08	0.24
12	PF3L	0.9	0.24	-2.4	0.15
13	PF2L2	0.51	0.24	-2.4	0.15
14	PF2L1	0.51	0.24	-2.05	0.3
15	PF1L	0.42	0.08	-1.6	0.4
16	Plasma	1.0	0.89	0	3.0
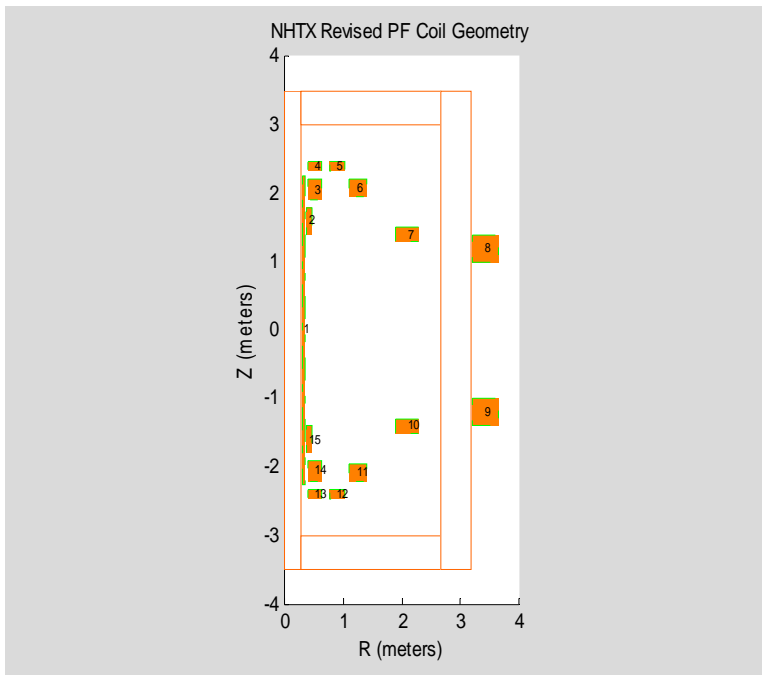
Figure 3.4.50: Revised PF Coil Geometry For NHTX

Table 3.4.9 lists revised coil power dissipations calculated using coil currents for the different plasma scenarios.

Table 3.4.9: Power Dissipated In Revised PF Coil Set For 3.5 MA Plasma Current
(Assuming 0.80 packing factor and 75C Average Copper Temperature)

Equilibrium Name=		DND_0SQ	DND_PSQ	DND_NSQ	ITER_LSN	Maximums
index	Coil	MW	MW	MW	MW	MW
1	OH	0.000	0.000	0.000	0.000	0.000
2	PF1U	0.233	0.137	0.181	0.000	0.233
3	PF2U1	0.125	0.382	0.028	0.090	0.382
4	PF2U2	0.063	0.009	0.000	0.026	0.063
5	PF3U	0.565	0.042	0.001	0.132	0.565
6	PF4U	0.154	0.051	2.906	0.215	2.906
7	PF5U2	0.155	0.279	6.243	0.016	6.243
8	PF5U1	13.579	19.828	4.595	15.482	19.828
9	PF5L1	13.578	19.830	4.572	17.127	19.830
10	PF5L2	0.155	0.279	6.264	0.075	6.264
11	PF4L	0.154	0.052	2.868	0.031	2.868
12	PF3L	0.564	0.042	0.002	0.124	0.564
13	PF2L2	0.063	0.009	0.000	2.264	2.264
14	PF2L1	0.125	0.382	0.028	1.446	1.446
15	PF1L	0.233	0.137	0.181	0.791	0.791
Total Power=	PF	29.745	41.459	27.870	37.820	41.459

Table 3.4.9 shows that no additional PF power supply sections are needed since maximum power dissipations in the four revised PF coils remain well below 6 MW each.

3.4.3.1.1 Assignments of Numbers of Turn and Power Supply Sections to PF Coils

Provisional assignments of the numbers of turns in each PF coil are summarized in Table 6. They were made based on considerations of matching the coil's current per turn and resistive voltage drop to the current and voltage ratings of power supply sections powering them, while maintaining up/down symmetry in the design of coil pairs. It was decided that multiple sections powering a single coil would operate electrically in parallel since that reduces the number of turns, thus simplifying both coil construction and coil cooling. Table 3.4.10 also lists the maximum steady turn currents for the plasma equilibria and their projected maximum resistive voltage drops per coil. With these assignments, none of the steady PF coil currents needed for any of the four different plasma equilibria reaches the full 1000-second current capability of assigned power supply sections. Maximum expected resistive voltage drops in the coils are also well within power supply capabilities. In Table 3.4.10, these turn assignments are called provisional because it is not necessary to precisely adhere to them in the detailed coil design. Since neither coil voltages nor currents are at power supply limits, these provisional assigned numbers of turns can be increased or decreased slightly if necessary for the detailed coil design without causing impedance mismatch difficulties with the power supply.

Table 3.4.10: NHTX PF Coil Turn Assignments, Turn Currents, and Coil Voltage Drops

(Assuming 0.80 packing factor and 75C Average Copper Temperature)

index	Coil	Assigned Number Of Power Supply Sections	Provisional Number Of Turns Per Coil	Largest Turn Currents For Tabulated Plasmas	Largest Coil Resistive Voltage Drops For Tabulated Plasmas
				(kA)	(Volts)
1	OH		860	[24]*	0
2	PF1U	1	108	3.058	59
3	PF2U1	1	200	2.880	103
4	PF2U2	1	180	0.916	26
5	PF3U	1	66	5.649	39
6	PF4U	1	180	5.638	399
7	PF5U2	2	110	-10.999	-439
8	PF5U1	4	110	-23.023	-666
9	PF5L1	4	110	-23.023	-666
10	PF5L2	2	110	-11.017	-440
11	PF4L	1	180	5.602	396
12	PF3L	1	66	5.647	77
13	PF2L2	1	180	5.509	318
14	PF2L1	1	200	5.605	200
15	PF1L	1	108	-5.639	-108

* OH Operates Only For An Initial Brief Pulse; Its Steady Current Is Zero

3.4.3.1.2 General Considerations For Constructing Steady Water-Cooled PF Coils

For low duty cycle pulsed PF coils relying on thermal inertia to limit temperature rise, and also for coils operating at steady but low power levels, a single extruded hollow conductor may be used directly to form a winding pack, yielding adequate active cooling without further complications. Chilled cooling water flows into the cooling hole at one end of the conductor along with the electrical current and exits along with the current from the hole at the other end. Indeed, this design approach will be followed for the NHTX OH solenoid coil which only carries current briefly to initiate the plasma, then has an entire hour to cool down before operating again. However, if a coil's steady electrical current and resulting power dissipation are increased sufficiently, this simple design becomes inadequate as the bulk temperature of its internally flowing cooling water becomes too hot. Some relief may be obtained by increasing the cooling channel's cross section or the cooling water's pumping pressure in order to increase flow, but those avenues are limited by the increases either in electric power dissipation as cross section is converted from conductor to cooling channel, or in pumping power.

A more effective general design strategy for steady high power density coils is to abandon forcing all cooling water through the entire coil and instead divide the coil winding into distinct parts for cooling purposes, with different water flowing in the different parts. There are two ways to accomplish this. In one approach, multiple hollow conductors are wound together to construct the winding pack, using a winding technique

commonly known as "two-in-hand" if only two separate conductors are used. The separate conductors in the winding are then externally jumpered to be connected electrically in series but hydraulically in parallel.

In the other approach, which is illustrated by the Figure 3.4.51 cartoon, a single hollow conductor is hydraulically tapped to form one or more "tee" external water connections along its length.   Each of these water taps and the cooling channel holes at the conductor's two ends are hydraulically connected either to the cooling water's supply manifold or to its low pressure return manifold, with these external water connections alternating so that all conductor regions have flowing water.
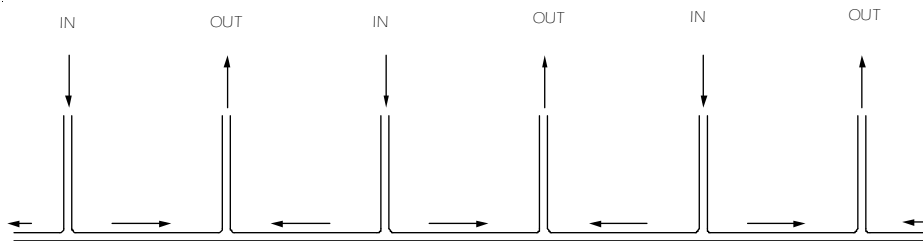
Figure 3.4.51: Hollow Conductor Cooling Augmentation Via External Tee Connections

It is also possible to combine the two approaches for even higher power density coils, as indeed is done in the NHTX PF coil designs.

For extremely high power density requirements it can become necessary to subdivide coils into multiple physically separated modules in order to provide sufficient cooling water access. Initial design calculations indicate this is not essential for NHTX, although it should be considered as an alternative design option for the PF5 coils.

Most hollow conductor coil designs arrange rectangular conductors into a rectangular array winding pack cross section. Conductors are then accessible for external water connections at the sides of each winding pack. However, if there are more than two rows and more than two columns in the rectangular array then locations exist which are not externally accessible.   To make sure that steady cooling is adequate for those "buried" parts of a winding pack it is necessary to consider the turn winding sequence.

Coils are wound either radially or axially, so that successive turns through a cross section are displaced from each other in either the radial or the axial direction. The result of winding a single conductor in a radial plane is a spiral pancake in which successive turns are displaced radially by one step. Double pancake windings typically use a single hollow conductor to form two axially adjacent spiral layers with a cross-over at their common inner radius and with their two leads brought out from their common outer radius. Double pancake windings with two separate conductors wound together two-in-hand are also common, and it is feasible to wind more than two conductors together provided that their interlayer cross-overs are well-spaced toroidally. If a winding is two-in-hand, successive turns are displaced 2 steps in the winding pack's cross section. In a 3-in-hand winding they are displaced by three steps. Radial winding schemes are also readily extended to more than two axially adjacent pancake layers, but usually the

number of axial layers is even so that the two electrical leads can easily exit together. As opposed to radial windings, a single layer wound in the axial direction forms a helical cylinder. This type of winding is commonly used to construct long solenoid coils, but it can equally well be used to form a square cross section PF coil. As with radial windings, the number of layers used is usually a multiple of two so that the external electrical leads can easily exit together. Axially wound coils can also be wound two-in-hand, or even more than two conductors may be used providing that there is room for their multiple interlayer transitions. Successive turns in axially wound coils are axially adjacent if one conductor is used, axially displaced by two steps if two-in-hand winding is employed, and displaced axially by three positions if three conductors are wound together. Thus, for each of the two winding directions, successive turns march across the coil's cross section with step sizes matching the number of conductors wound together.

As an example, for a hypothetical 144 turn coil wound with one conductor to form a square 12-by-12 array, the most aggressive cooling possible would provide external taps into the cooling passage at its layer transition locations on two opposing sides of the coil's surface. Because of the turn winding sequence these would divide the coil into 12 different 12-turn regions each of which would be separately cooled by its own water flow. Although this scheme would provide far more cooling than a single untapped 144 turn flow path, it would still limit power to a level that can be accommodated by 12-turn flow paths. However, if the example were changed to employ two separate conductors wound two-in-hand, then each conductor would be accessible to be externally tapped at intervals of only 6 turns, with the additional taps at a different toroidal location. This would double the net water cooling flow while cutting the necessary water pumping pressure drop in half so that pumping power remains unchanged. Winding 3-in-hand or 4-in-hand would provide even more toroidal locations to tap into the cooling channels, further increasing net cooling water flow while further decreasing the required pumping pressure. This example demonstrates that it is important to know for each coil design the length of conductor that can be steadily cooled while carrying the rated coil current, within practical limits on cooling channel size, water flow speeds, and water temperature.

It should be mentioned that an actual 12-by-12 coil array may have fewer than 144 turns because of transitions. However, clever 3-D design can minimize the discrepancy.

For extremely high power cooling requirements the option remains to split the coil into several two-layer subcoils physically separated by aisle spaces. This option eliminates all buried turn locations, providing external access to every turn along its entire length so that single-turn, half-turn or even quarter-turn cooling using the scheme combining Figures 3.4.51 through 3.4.53 becomes feasible. Although this approach has attractive features, the space needed to form its cooling access aisles decreases its net packing factor thus increasing its power consumption, and it also needs additional mechanical support structures to resist the attractive forces between its subcoils. If this design approach is taken it is reasonable to fit as many turns as possible facing each water cooling access aisle, leading to the use of elongated conductor cross sections in the form of thin strips. These are most easily wound radially so double pancakes wound from thin strips are the natural configuration. A central cooling hole in thin strips would be

difficult to extrude accurately and it would also be difficult to reliably tap into it at many locations along the strip's edge for external water connections. Therefore, edge cooling is the natural choice for this type of design. With edge cooling it is not necessary to extrude the conductor to form cooling water passages since it is easy to solder a copper tube into a slot machined in the strip's edge.

With single-edge cooling of thin copper conductor strips much wider than their thickness, the temperature gradient developed in the conductor across each strip's width becomes the limiting design consideration. Accurate analysis of single-edge cooling in this 1-D heat flow situation requires modeling the redistribution of electrical current across the strip's cross-section due to the nonlinear temperature dependence of electrical resistivity and of thermal conductivity. Analysis using this model shows that hot-spot temperature depends on only two quantities, i.e.:
(1) the temperature of the water-cooled conductor surface and
(2) the ratio of the steady current to the conductor thickness.
The second of these is not current per unit cross sectional area, the true current density. For this type of 1-D cooling situation the effect of conductor width on dissipated power due to electrical current density precisely cancels out its effects on thermal conduction so that the resulting hotspot temperature depends on the product of width and true current density, which is simply the ratio of current to conductor thickness. Figure 3.4.52 shows the dependence of cross-conductor temperature *rise* on these two quantities.
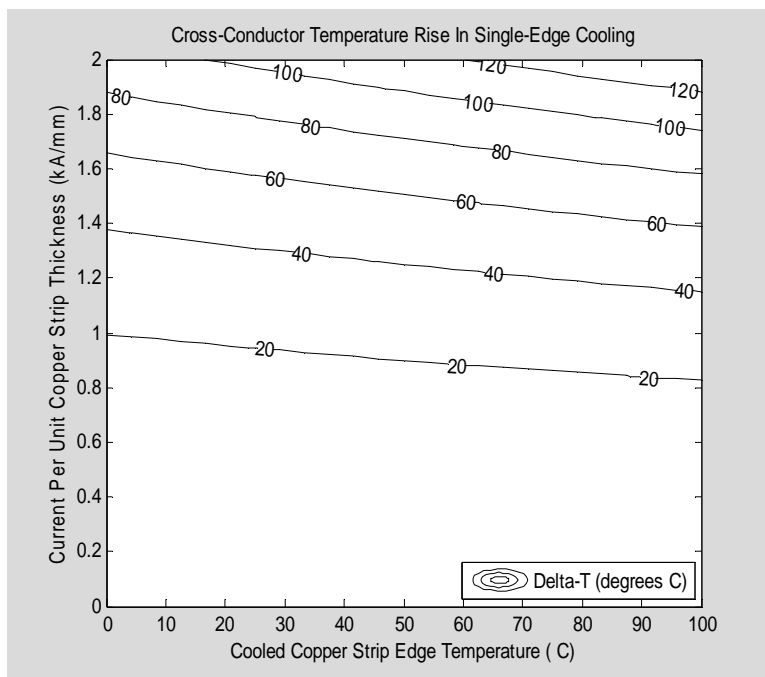
Figure 3.4.52: Dependence of Cross-Conductor Temperature Rise In Single-Edge Cooling

As shown in Figure 3.4.52, the temperature *rise* from the single cooled edge to the uncooled edge of a strip does not depend much on the cooled edge's temperature. Current per unit thickness values of one kiloampere per millimeter produce an acceptable cross-conductor temperature rise of about 20C while 2 kA/mm produces a large

temperature rise exceeding 100C. Therefore, with single edge cooling the conductor turn currents should be nominally about 1 kA per mm of the turn's radial thickness, i.e., about 26 kA per inch.
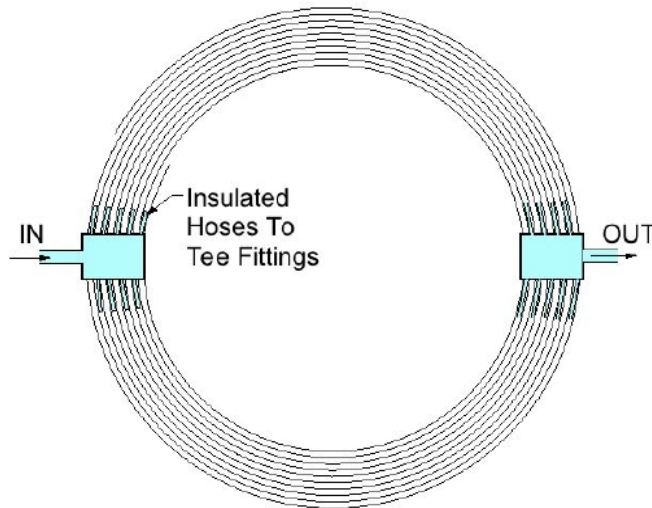
Figure 3.4.53: Example Of Strip-Wound Edge-Cooled PF Coil With Half-Turn Cooling

If the PF5 U1 and PF5L1 coils were to be implemented in this single edge-cooled manner with steady cooling adequate up to the full 26 kA 1000 second pulse capability of the four power supply sections driving each, then three double pancakes wound from one inch thick copper strip would be required. These three subcoils would need to be vertically stacked but separated by gaps forming the cooling access aisles.   However, it turns out that these coils can instead be implemented in a more conventional manner.

3.4.3.1.3 Winding Pack Design Configurations Selected For NHTX PF Coils

For the tabulated plasmas, the PF coil currents per turn as listed all correspond to power supply section currents slightly less than their 6.5 kA sustained power supply capability for 1000 second NHTX pulses. It is appropriate that steady cooling provisions provided for PF coils should instead match the slightly greater 6.5 kA capability of the power supply sections. To this end, Table 3.4.11 presents results of calculations of the cooling passage length for which cooling water introduced at 10C and flowing at 10 m/s reaches a bulk temperature of 60C at exit. For these calculations it was assumed the average conductor temperature is 75C, the power supply operates at its full sustained current limit, the cooling hole represents 15 % of the coil conductor's cross sectional area, and the copper conductor's overall packing fraction is 80%.

Table 3.4.11: NHTX PF Coil Cooling Parameters For Full Steady Turn Current

Index	Coil	No. of Turns In Coil	Total XSect Area Per Turn	Cooling Hole Diameter (15% of Turn XSect)	Cooling Water Volume Flow Rate Along Turn (*)	Steady Turn Current Rating	Power Per Turn At The Steady Turn Current Rating (**)	Resulting Calculated Maximum Coolable Length of Coolant Passage (***)
		(turns)	(cm^2)	(mm)	(liter/s)	(kA)	(kW)	(turns)
1	OH	860				0	0	0
2	PF1U	108	2.96	7.52	0.44	6.5	7.78	14.27
3	PF2U1	200	3.60	8.29	0.54	6.5	7.78	17.35
4	PF2U2	180	2.00	6.18	0.30	6.5	14.00	5.36
5	PF3U	66	5.45	10.21	0.82	6.5	9.06	22.57
6	PF4U	180	4.00	8.74	0.60	6.5	17.16	8.74
7	PF5U2	110	7.27	11.79	1.09	13.0	63.43	4.30
8	PF5U1	110	16.36	17.68	2.45	26.0	183.92	3.34
9	PF5L1	110	16.36	17.68	2.45	26.0	183.92	3.34
10	PF5L2	110	7.27	11.79	1.09	13.0	63.43	4.30
11	PF4L	180	4.00	8.74	0.60	6.5	17.16	8.74
12	PF3L	66	5.45	10.21	0.82	6.5	9.06	22.57
13	PF2L2	180	2.00	6.18	0.30	6.5	14.00	5.36
14	PF2L1	200	3.60	8.29	0.54	6.5	7.78	17.35
15	PF1L	108	2.96	7.52	0.44	6.5	7.78	14.27

(*) Assumes 10 m/s speed in a cooling passage which is 15% of conductor XSection
(**) Packing Factor 80%; Average Copper Temperature 75C
(***) Length (In Turns) Set By Limiting Coolant Temperature Rise From 10C To 60C

The right hand column of Table 3.4.12 shows that the smallest coolable lengths as measured in turns are for the PF5 coils, but that each of them is several turns. There are no coils with maximum coolable lengths less than one turn, a situation which would justify using multiple edge-cooled thin strip double pancakes separated by cooling access aisles.

Table 3.4.13 summarizes the cooling scheme adopted for each coil and its associated winding pattern. It turns out that conventional extruded hollow conductor designs can be adapted for the NHTX PF coils by combining the two approaches, i.e., by both using multiple hydraulic taps per hollow conductor and also winding multiple hollow conductors together. Apparently it is not necessary to split any of the PF coils in order to access each turn, although the PF5 coils do approach that situation.

Steady cooling with water does require a great increase in the number of water connections per coil. The average number of water connections assigned to each PF coil is more than 36, whereas for typical pulsed coils there are usually only two. With so many hydraulic connections per coil it is appropriate to provide local water manifolds as part of each coil assembly.

Table 3.4.12: NHTX PF Coil Winding Pack Design Configurations

Index	Coil	No. of Turns In Coil (turns)	Coolable Length of Coolant Passage (turns)	Winding Direction	Array Height	Array Width	No. In Hand	No. Water Leads Plus Taps	Actual Coolant Passage Length (turns)	No.Sides Of Winding Pack Used For Cooling
1	OH	860	0	Axial	430	2	1	2	860	1
2	PF1U	108	14.27	Axial	18	6	3	12	12	1
3	PF2U1	200	17.35	Axial	10	20	2	22	10	1
4	PF2U2	180	5.36	Axial	10	18	2	76	5	2
5	PF3U	66	22.57	Radial	6	11	1	4	22	1
6	PF4U	180	8.74	Radial	20	9	2	22	9	1
7	PF5U2	110	4.30	Axial	8	14	2	60	4	2
8	PF5U1	110	3.34	Axial	8	14	2	60	4	2
9	PF5L1	110	3.34	Axial	8	14	2	60	4	2
10	PF5L2	110	4.30	Axial	8	14	2	60	4	2
11	PF4L	180	8.74	Radial	20	9	2	22	9	1
12	PF3L	66	22.57	Radial	6	11	1	4	22	1
13	PF2L2	180	5.36	Axial	10	18	2	76	5	2
14	PF2L1	200	17.35	Axial	10	20	2	22	10	1
15	PF1L	108	14.27	Axial	18	6	3	12	12	1

3.4.3.2   *PF coil system magnetic field, flux, and force calculations*

Poloidal fields, fluxes, and then forces were numerically calculated for the NHTX design. The objective was to calculate 2-D mesh arrays covering the NHTX machine's poloidal cross-section with normalized values saved for each meshpoint. That is, for each meshpoint location, values would be calculated and stored for the radial and vertical components of the poloidal magnetic field per ampere and the flux per ampere, for each PF coil or plasma current. Then, for any operating scenario, summing the products of these matrices with the corresponding coil or plasma currents results in a global picture of the magnetic situation, which can be plotted in various forms by MATLAB. It can also be used to evaluate forces on PF or TF coils.

The magnetic field and flux calculations could be accomplished in various different ways.   Each method has its own tradeoff between accuracy, coding setup effort, and computer resources.   The approach taken here was chosen to maximize use of already-coded routines and thus minimize the investment of labor. MATLAB m-file subroutines for field and flux calculation previously coded and debugged by the author included one named "poloidal_fieldx". This m-file calculates the magnetic field components, br and bz, and also the total magnetic flux included inside the complete 2π radian circle(s) about the z-axis passing through location(s) specified by (rho, zeta). Providing they have the same array sizes, rho and zeta may be specified either as single scalars, as 1-D vectors, as

2-D matrices, or even as ND-arrays with 3 or more dimensions.   The calculated field is modeled as though it is produced by current flowing in a set of coaxial circular loops passing through location(s) (r, z), where r and z have the same array sizes as each other and also may be single scalars, as 1-D vectors, as 2-D matrices, or even as ND-arrays with 3 or more dimensions. Obviously, r and rho may have completely different sizes. The model assumes one ampere of current is equally *divided* between the different loops specified in (r, z), so that the total modeled current flowing is 1 ampere.

This m-file routine employs exact formulae for the magnetic field components and the enclosed magnetic flux of an idealized circular filament, employing Elliptic Integral functions exactly as given in Smythe's textbook on Electromagnetism.   Thus, this routine implements the Greens function approach for a finite number of circular filaments, to an accuracy limited only by the computational machine's precision. On the other hand, to use this approach for actual PF coils we must first represent each PF coil by a finite number of coaxial circular filaments.   This introduces approximation errors in representing continuous distributions of electrical current. Using a single filament is pretty accurate far from the coil, but its error increases at locations closer to the coil. To obtain better accuracy close to a coil, the coil could be represented by multiple nearby filaments.   The filament's field strength theoretically approaches an infinite limit at a sequence of field evaluation locations approaches the filament's location, whereas an actual PF coil's field remains finite at all locations including inside the coil. If you ask this coded m-file to calculate field at a current loop's precise location, the m0file returns MATLAB's NaN symbol (i.e., Not a Number) instead of a numerical value for that evaluation location, and it also warns about dividing by zero.

To automate the generation of multiple filaments to represent PF coils, another m-file subdivides each rectangular coil cross-section into a rectangular array of identical subrectangle cross-sections and then specify the (r,z) locations of the centers of each subrectangle.   With this multiple filament approximation of PF coils, magnetic fields and fluxes calculated close to, but outside of, PF coil bodies appear to be very accurate provided that several filaments are used to represent each coil. However, that is not true for arbitrary field evaluation locations inside the PF coils. Arbitrary internal locations for field evaluation may approach modeled current filaments arbitrarily closely. For field evaluation locations arbitrarily close to one of the modeled filaments, the calculated field strength may thus be arbitrarily large. The direction of the calculated magnetic field may also vary wildly between nearby locations inside a grid of circular filaments representing a constant current density PF coil.   Therefore, for arbitrary locations inside PF coils, the magnetic field as numerically calculated by summing contributions from a finite number of nearby filaments may be wildly in error.

An alternative approach using FEA methods to provide a numerical solution to the electromagnetic PDEs would avoid this particular inaccuracy.   However, FEA methods have their own problems, including a loss of accuracy for points more distant from a coil. A 2-step computational approach was taken instead.   Since the filaments representing a PF coil are located at the centers of tiled subrectangles, in the first step the field is evaluated at the *corners* of those same tiling subrectangles. Thus, if the PF coil cross

section partition was into an m-by-n array of subrectangles and thus resulted in m*n filament locations, then this approach defines an associated rectangular mesh of (m+1) by (n+1) locations within the coil with fields there calculated by summing the fields from filaments. Assuming that the calculation error is small at locations exactly midway between filaments in the rectangular grid of filaments representing a PF coil, this approach is expected to avoid much of the error. In the second step, 2-D interpolation of those meshpoint field values is used to estimate the field at any intermediate locations, even including locations precisely matching the modeling filaments.

This two-step scheme was implemented in a simply coded MATLAB script. All the MATLAB codes used is these calculations are documented in the Appendix.

All NHTX PF currents were modeled as having constant current density rectangular cross-sections, which is clearly a distortion of reality when applied to the plasma. Magnetic fields and fluxes were calculated, as documented in the Appendix, for each of the four plasma equilibria previously calculated by J.Menard, Resulting MATLAB contour plots of the calculated flux for these equilibria follow.
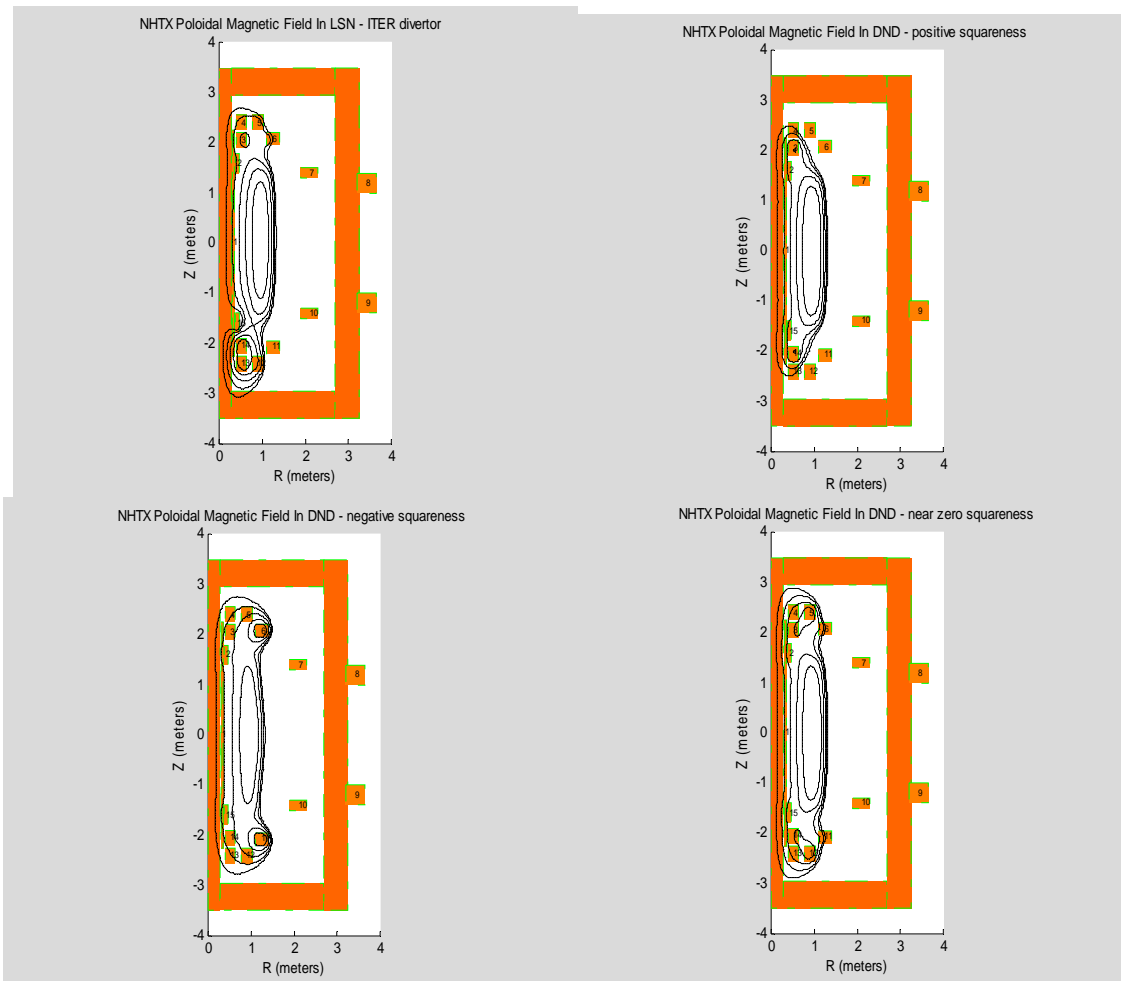
Figure 3.4.54: Poloidal Magnetic Field Patterns For Plasma Equilibria

Vertical forces were also calculated using MATLAB to implement Greens function filament methods as documented in the Appendix, for each of the four plasma equilibria previously calculated by J.Menard,   Results were as follows:

Table 3.4.13: Vertical Forces on PF Coils

Calculated Total Vertical Forces (Newtons) On PF Coils	Steady Sustained Plasma Scenario			
PF Coil	DND-near zero squareness	DND-positive squareness	DND-negative squareness	LSN-ITER divertor
OH	0	0	0	0
PF1U	19760	18860	770	0
PF2U1	-2070	-120440	-25690	3120
PF2U2	-51780	-29120	-2700	-27500
PF3U	-76900	23820	-6480	-37760
PF4U	12250	-19800	61550	-8060
PF5U2	-24890	32700	-173920	8320
PF5U1	-339980	-484250	-126550	-402120
PF5L1	339980	484240	126350	399440
PF5L2	24890	-32690	173760	-14930
PF4L	-12240	19810	-63610	2540
PF3L	76880	-23820	9330	31040
PF2L2	51780	29110	3420	688890
PF2L1	2080	120430	25300	-903940
PF1L	-19760	-18860	-1130	277010
Modeled Plasma	0	10	890	39440

Nonzero vertical forces calculated for the plasma arise because the plasma was approximated as a rectangular cross-section PF coil with constant current density, which is clearly not accurate.   If the actual current distribution calculated as part of the computed plasma equilibria had instead been used the calculated vertical force on the plasma would have been zero.   Thus, the nonzero force calculated for the plasma provides an estimate of the total error in the vertical force calculated for the PF coils.

The largest calculated force in the above table is $-9.0394*10^5$ Newtons, i.e., equivalent to 202,925 pounds.   Most calculated PF coil forces are far smaller than this value. By way of comparison, the total *vertical* force pushing all the upper TF radial limbs upwards is $2.35*10^7$ Newton= 23.5 MN, which is equivalent to about 5.27 million pounds.

Since it is hoped to support five PF coils from the umbrella structure, i.e., PF1U, PF21U, PF22U, PF3U, and PF4U, it follows that the sum of their vertical forces in various modes is important. These coils represent the 2nd through the 6th entries in the above matrix of calculated forces.   Their sums are as follows:
  (1) $-0.9874*10^5$ Newton (in DND-near zero squareness mode)
  (2) $-1.2668*10^5$ Newton (in DND-positive squareness mode)
  (3) $+0.2745*10^5$ Newton (in DND-negative squareness mode)
  (4) $-0.7020*10^5$ Newton (in LSN-ITER divertor mod

In conclusion, the largest magnitude among these net vertical PF coil forces on the umbrella is about *one quarter of one percent* of the vertical force developed on the umbrella due to the TF currents in the upper radial TF limbs. **Thus, these calculations justify ignoring the contribution of PF coil vertical loads on the umbrella in comparison to the much larger loads from the TF coil system.**

3.5   Power systems

3.5.1   Power systems design considerations

Two features of the NHTX electrical load represent a significant departure from the TFTR load for which the existing PPPL power system infrastructure was originally designed. First, the NHTX pulse length is ~ 100 times greater than TFTR such that the use of existing local energy storage to supply the full load is impractical. Second, the TF coil current is ~ 10 times greater, such that the connection of a large number of the existing Transrex AC/DC converters in parallel in the FCPC building and delivering very high current to the test cell a long distance away would be unwieldy and inefficient. Therefore the following solutions are adopted for NHTX.

     a. Utilize AC power directly from the grid to the maximum practical level, namely 300MW, by connected relatively quiescent loads (heating and TF) and implementing reactive compensation to achieve ~ unity power factor.

     b. Install a new 138kV substation at D-site, bringing the grid power directly to the load.

     c. Install a new high current TF AC/DC converter in available space west of the TFTR test cell, close to the load.

     d. Power the OH and PF loads, which tend to be more transient, lower power factor, and higher in harmonic content than the TF and heating loads, from the existing TFTR MG set. Supplement the MG stored energy and motor input energy as necessary using back-to-back AC/DC converters connected via a DC link.

System configuration is given in Figure 3.5.1.
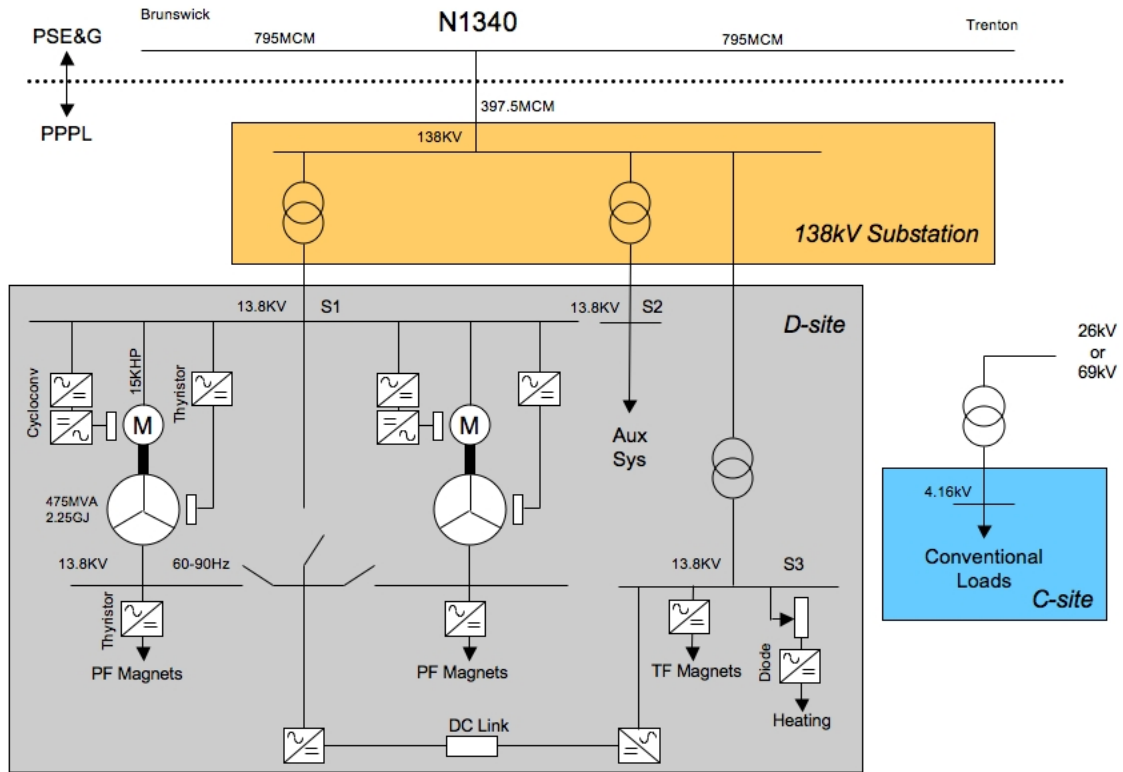
Figure 3.5.1 – Simplified One-line diagram of Power Systems for NHTX

A grid load limit of 300MW was assumed in the systems code study based on prior levels of power approved by the local utility operator, PSE&G, in the past as given in Table 3.5.1.

Table 3.5.1: Comparison of Electric Power Requirements For Past Proposed Projects

Parameter	BPX	TPX	TPX (upgrade)
Base Load (MW/MVAr)	24/21	31/23	31/23
Pulsed Load (MW/MVAr)	300/306	66/34	197/101
Peak Load (MW/MVAr)	324/327	96/57	228/125
p.f. Correction (MVAr)	400	0	100
Pulse Ramp (sec)	25	0	0
Pulse Flat Top (sec)	8	1000	1000
Pulse Period (sec)	3600	4500	4500
Flicker*	1%	0.5%	0.5%

The NHTX design point loads are given in Table 3.5.2

Table 3.5.2: NHTX Design Point Electrical Power Loads

	Ramp				Flat Top		
	P[MW]	Q[MVAR]	S[MVA]	W[MJ]	P[MW]	Q[MVAR]	S[MVA]
TF	96	72	120		88	83	120
OH	308	71	316	59	0	0	0
PF	100	0	100	50	37	93	100
NBI/RF	0	0	0		166	96	191
BOP	10	7.5	12		10	7.5	12
				Tot-->	300		

Typical grid loading profiles are given in the following figures. Figure 3.5.2 shows the initial rise in the load and figure 3.5.3 the duty cycle of the load. Here it is assumed that:

    a. reactive compensation results in a net p.f. of 0.95
    b. TF forcing factor (ratio of power supply voltage to I*R drop) equal to 1.1
    c. Ip ramp rate 5MA/sec
    d. Aux heating power applied in 12 steps during Ip ramping
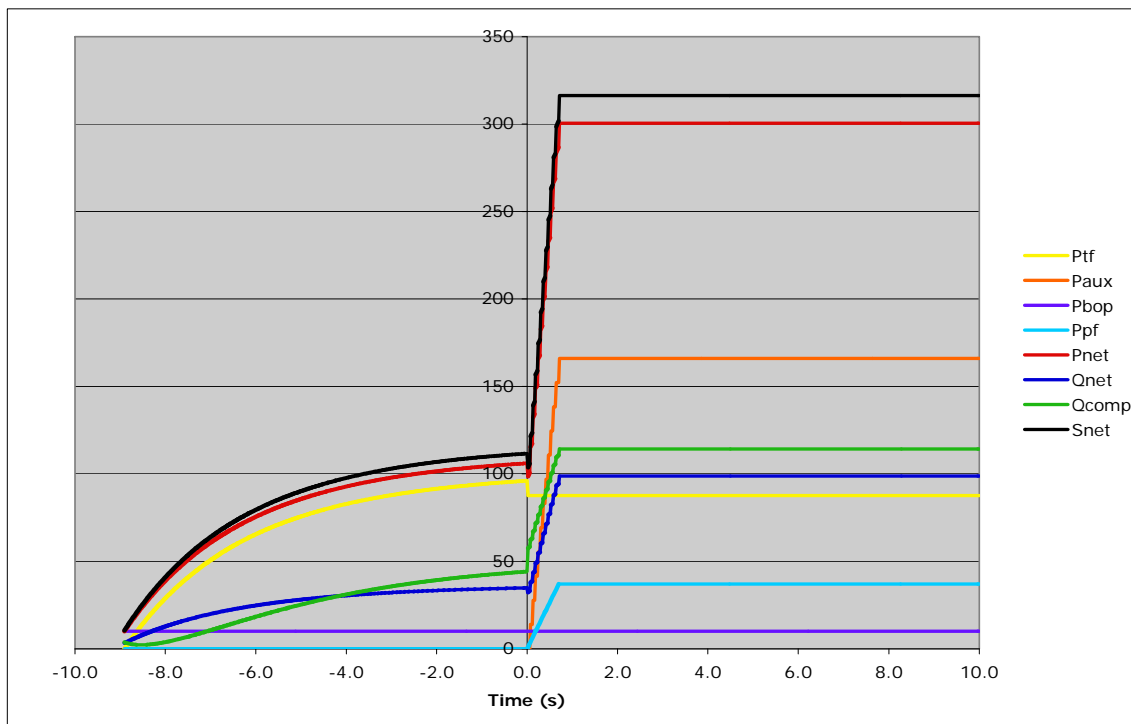
Figure 3.5.2 – Typical NHTX Load to Grid During Start of Pulse
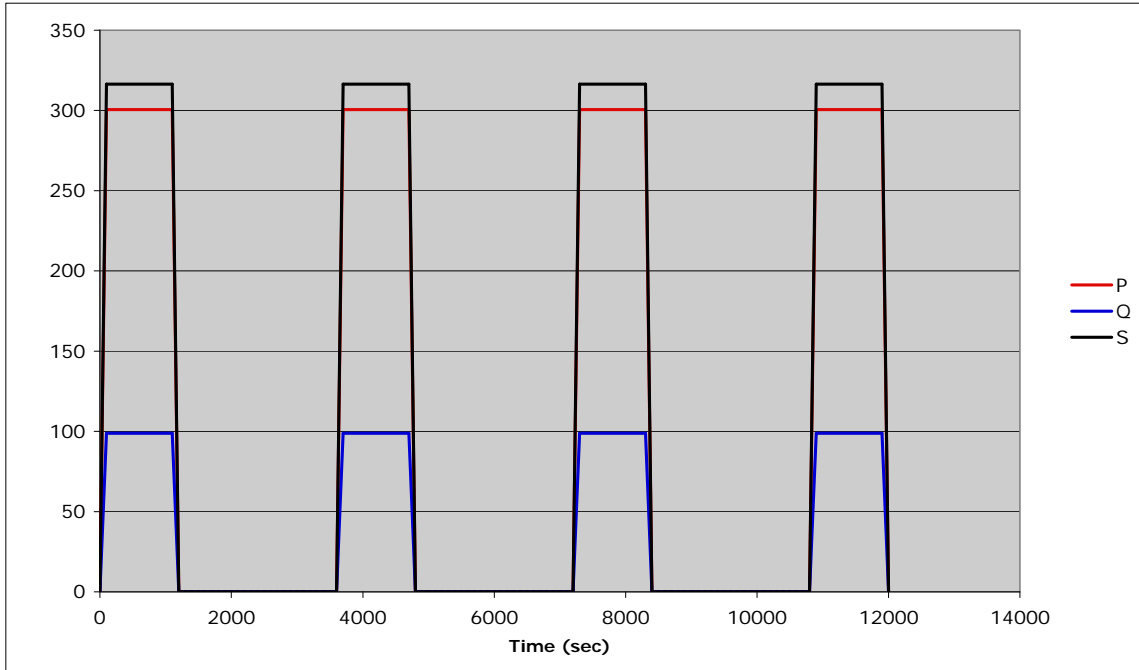
Figure 3.5.3 – Typical Train of NHTX Pulses

3.5.2 Long pulse capacity of existing power system components

Components of the existing PSE&G/PPPL power system infrastructure to be used for NHTX include the 138kV transmission line, the MG sets, the 13.8kV variable frequency distribution system, the FCPC converter transformers, the Transrex AC/DC converters, and miscellaneous DC circuit elements such as cables, current limiting reactors, disconnect switches, etc.. The long pulse capacity of these elements was assessed and the results are summarized in the following sections.

3.5.2.1 138kV transmission line

PPPL is fed from a tap off of the N1340 138kV transmission line which runs between Brunswick and Trenton substations. The conductor is 795MCM ACSR which has an ampacity 900A rms based on Westinghouse T&D Handbook table 2A p. 50. The tap is a 397.5MCM ACSR line running from Dey Road Plainsboro substation to PPPL, with ampacity of 600A rms based on Westinghouse T&D Handbook table 2A p. 50. Typical conductor ratings are given in Table 3.5.3[34].

---

[3] cccc

[4] SKM web site http://www.skm.com/Equipment%20Damage%20Curves%20Conductors.shtml

Table 3.5.3: Typical conductor operating temperature limits

Table 1 Typical conductor operating temperature limits

Type	Insulation	Voltage	Short Circuit 0.01 < t < 10 sec.	Emergency 10 sec. < t < ~1-6 hrs	Normal t > ~1-6 hrs
Al or Cu	TW	600V	150°C	85°C	60°C
Al or Cu	THWN	600V	150°C	90°C	75°C
Al or Cu	THHN	600V	150°C	105°C	90°C
Al or Cu	XLP	5-15kV	250°C	130°C	90°C
Al or Cu	EPR	5-15kV	250°C	130°C	90°C
AAC	Air	All	340°C	150°C	100°C
ACSR	Air	All	645°C	150°C	100°C

The thermal performance of these conductors was simulated based on a single time constant thermal model with the heat capacity based on the properties of copper and the thermal resistance based on the fact that the aforementioned current ratings are based on a 60C rise over a 40C ambient. The results given in figures 3.5.4 and 3.5.5 show that, at a typical NHTX load level of 297MW/330MVA corresponding to 1.38kA in the 138kV conductors, the 397.5MCM conductors cannot operated at pulse length greater than 250 seconds, assuming a 1 hour repetition period. On the other hand, the 795MCM conductors are adequate for this load for the desired 1000 second pulsing.
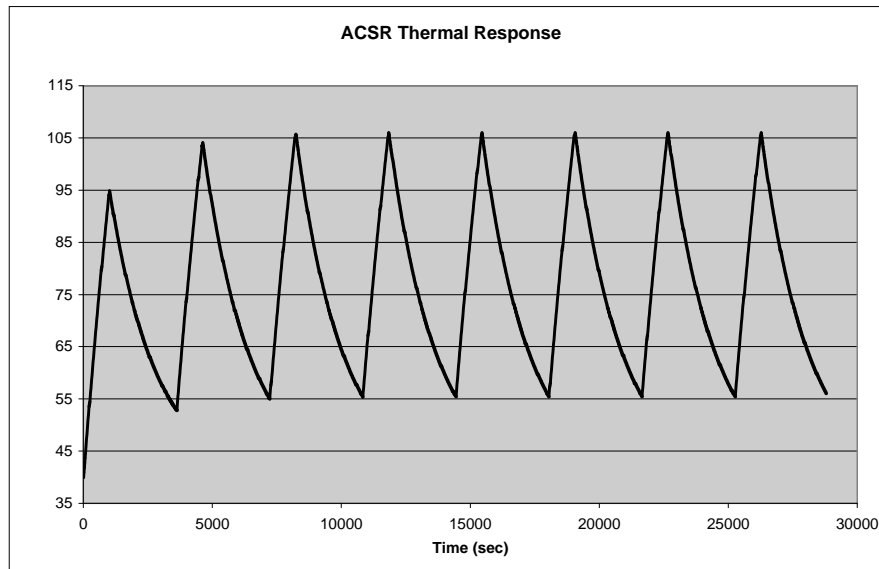
**Figure 3.5.4 – Thermal response of 397.5MCM (600A) ACSR conductor at a load of 297MW/330MVA corresponding to1.38kA-250s/3600s
@ 8 hours**

ACSR Thermal Response
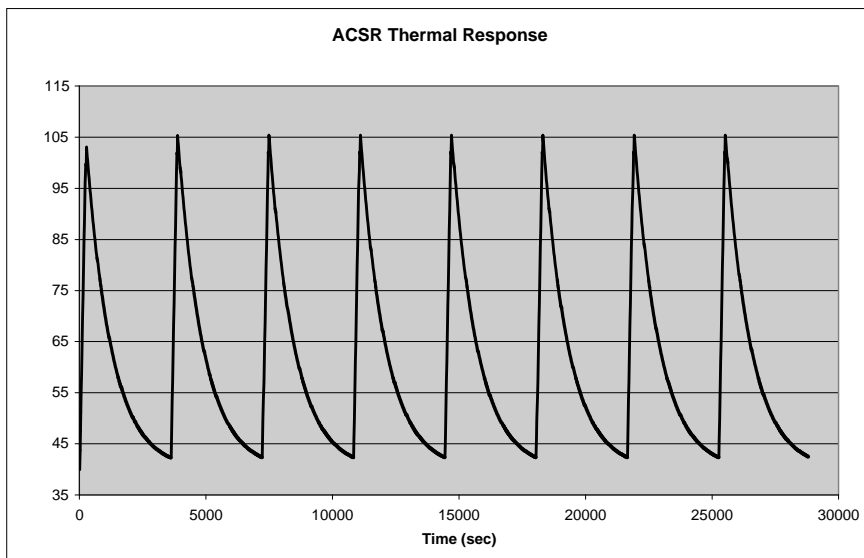
Figure 3.5.5 – Thermal response of 795MCM (900A) ACSR conductor at a load of 297MW/330MVA corresponding to1.38kA-1000s/3600s @ 8 hours

The conclusion is that the 397.5MCM conductors must be upgraded to 795MCM to achieve pulse lengths greater than 250 seconds. However, this upgrade is feasible and not extremely expensive. It should be noted that these calculations are based on a simple thermal limit and do not consider the conductor sag issue which could be limiting.

3.5.2.2 Motor-Generator (MG) sets

The two existing MG sets are each rated 475MVA, 0.7 p.f. for 6.77 second pulse duration, and release 2.25GJ in slowdown from 87.5Hz to 60Hz. The input power is supplied by wound rotor induction motors each rated 15kHp (11.2MW) at zero slip. Losses are primarily due to windage and friction, amounting to 2765kW at full speed, and approximately proportional to the speed cubed. For NHTX operation the MG sets will supply a relatively large load (~ 400MW) to the OH and PF systems during plasma initiation and ramping, and a reduced load due to the PF only (< 50 MW) during plasma sustainment. The MG sets will gradually slow down over the 1000 second period due to the PF load. Although not calculated as part of this study, it is assumed that this pulse duty is acceptable for the various elements of the MG sets (stator, rotor, exciter, breaker, etc.) The MG load current will depend on the power factor of the PF load, but assuming a p.f. such that the PF demand is 100MVA, the following is a comparison of the rms current loading of the TFTR basis and the NHTX load.

Table 3.5.4: – Comparison of TFTR and NHTX MG Loading

	TFTR	NHTX
Apparent power (MVA)	950	100
Ipulse (kA)	39.7	4.2
tpulse (s)	6.8	1000.0
Trep (s)	300.0	3600.0
Irms (kA)	6.0	2.2

It remains to be confirmed that the time dependant thermal behavior of the various elements of the MG sets is acceptable under this load condition.

The MG is used to power the OH and PF coils. The OH energy consumption is of order 60MJ, and the PF power load is of order 40MW. Assuming windage and friction losses ~ 2MW, and assuming both motors operating with a contribution of 22MW input, the MG system can supply NHTX for pulses up to a duration of ~ (4500-60)MJ/(40-22-2)MW = 250 seconds. Beyond this duration, supplementary input power is needed and for NHTX will be supplied via back-to-back Transrex rectifiers operating through a DC link as shown in the following figure. An additional input of about 12.6MW is needed to extend the pulse length to 1000 seconds, which would require that each power supply section operate at 6.3kA, which is well matched with the 1000 second pulse capability.
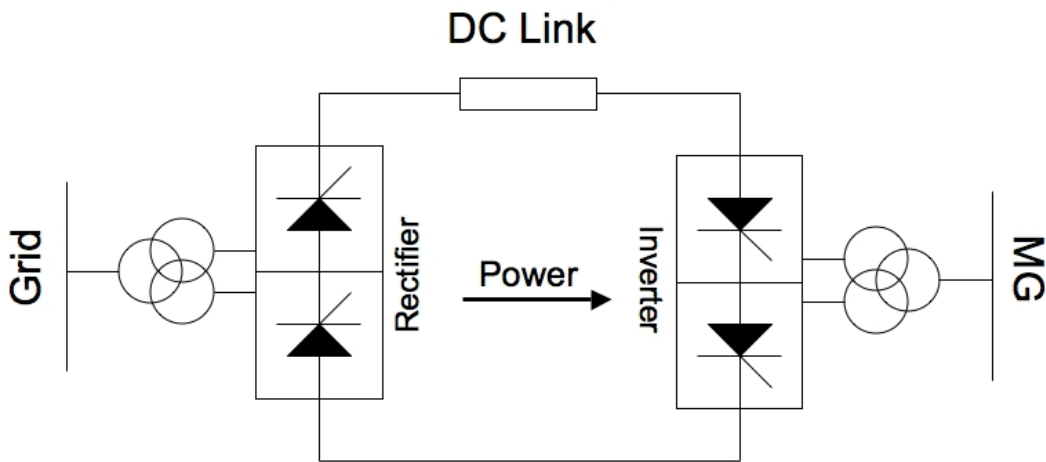
Figure 3.5.6 – DC Link to Supply Additional Energy to MG

3.5.2.3   13.8kV variable frequency distribution system

Feeder loads are set by the Transrex AC/DC converter loading and by the number of converters per feeder. The NHTX loading assumption for the Transrex AC/DC converters is 6.5kA DC, which yields an rms current the same as the original TFTR rating as indicated in the following table.

Table 3.5.5 – Comparison of TFTR and NHTX DC Pulse Current Ratings

	TFTR	NHTX
Ipulse (kA)	24.0	6.5
tpulse (s)	6.0	1000.0
Trep (s)	300.0	3600.0
Irms (kA)	3.4	3.4

It remains to be confirmed that the time dependant thermal behavior of the various elements of the variable frequency distribution system (CLRs, cables, switchgear, etc.) is acceptable. In case it is found to be too high, the loading can be reduced by changing the feeder configuration to supply one Transrex 12-pulse power supplies per feeder instead of two, or by reducing the loading per power supply section.

3.5.2.4 FCPC converter transformers

Based on data supplied by the transformer manufacture, GE[5], the thermal response to the NHTX loading was simulated and found to be acceptable with 6.5kA DC per Transrex power supply section as shown in the following figure.
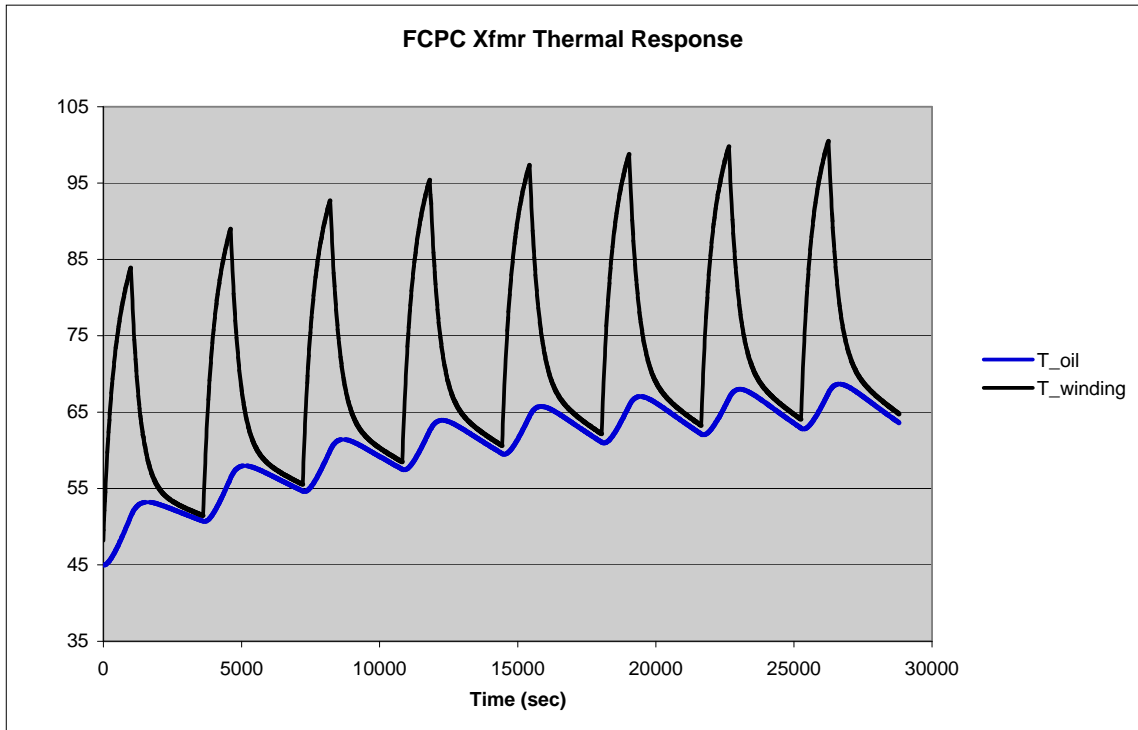
Figure 3.5.7– Thermal response of FCPC transformers due to Transrex Power Supply Loading of 2x 6.5kADC-1000s/3600s @ 8 hours

---

[5] GE Conversion Transformer Study, 24 June 1986, PPPL Req. 297-51743

3.5.2.5 Transrex AC/DC converters

A key aspect of the Transrex ampacity is that of the water cooled thyristors. Per the Transrex Final Design Review documentation[6], the continuous current carrying capacity of the water cooled thyristors is 15.5kA, well in excess of the NHTX load. It remains to be confirmed that the time dependant thermal behavior of the other current carrying elements of the power supplies (internal bus bars, fuses, etc.) is acceptable. In case it is found to be too high, it can be reduced by reducing the loading per power supply section. However, since the NHTX rms loading is the same as for the original design, a significant de-rating is not anticipated.

3.5.2.6 Miscellaneous DC circuit elements

As mentioned in prior sections, the rms current of the NHTX load matches the original rms rating of the equipment based on the TFTR load. However, the time dependant thermal behavior all the current carrying elements will need to be confirmed. As an example, the 750MCM cable loading was evaluated based on the heat capacity of the conductor copper and the thermal resistance based on the NEC rating of the cable of 685 amp, yielding a thermal time constant of 23 minutes. The cable is an important element because it would be impractical to have to utilize more than six cables per pole which was the original design and for which physical space and connection pads have been sized. The following figure confirms that the NHTX loading is acceptable from the cable ampacity point of view.

---

[6] Final Design Review, Ebasco Services Subcontract 7277-0411-131, August 1979, section 4.3.5
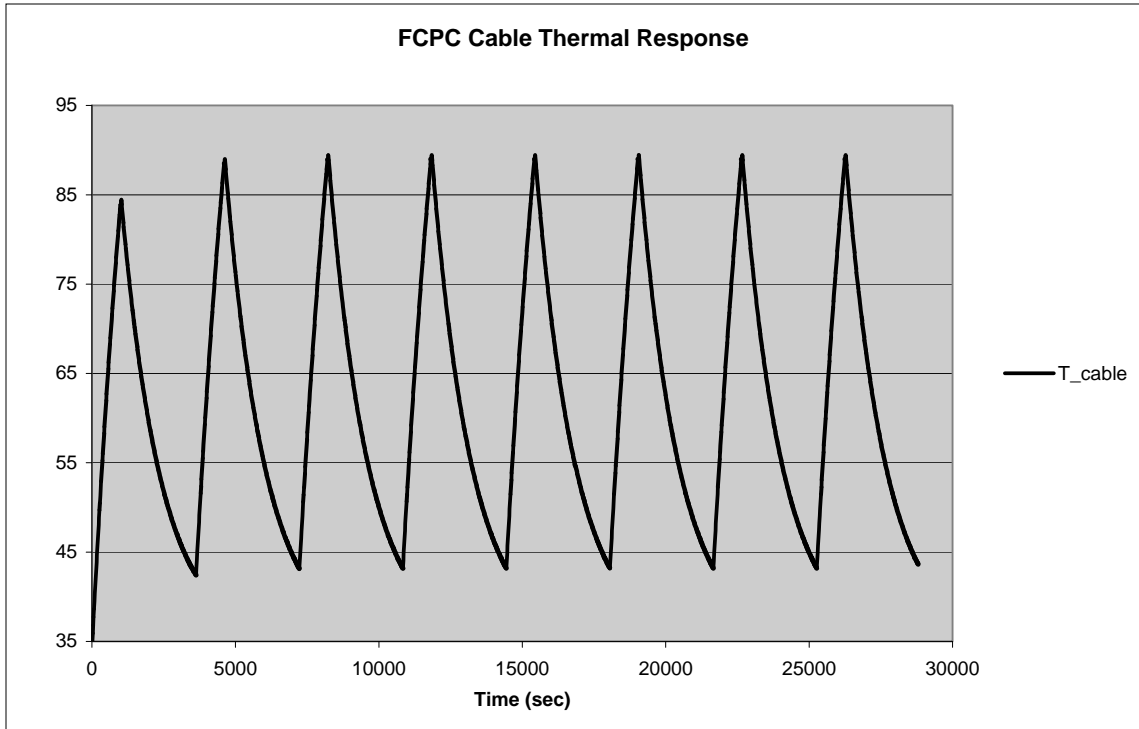
**Figure 3.5.8– Thermal response of FCPC power cables due to Transrex Power Supply Loading of 2x 6.5kADC-1000s/3600s
@ 8 hours**

3.5.3   AC power sources

One line diagrams are given in the following figures.
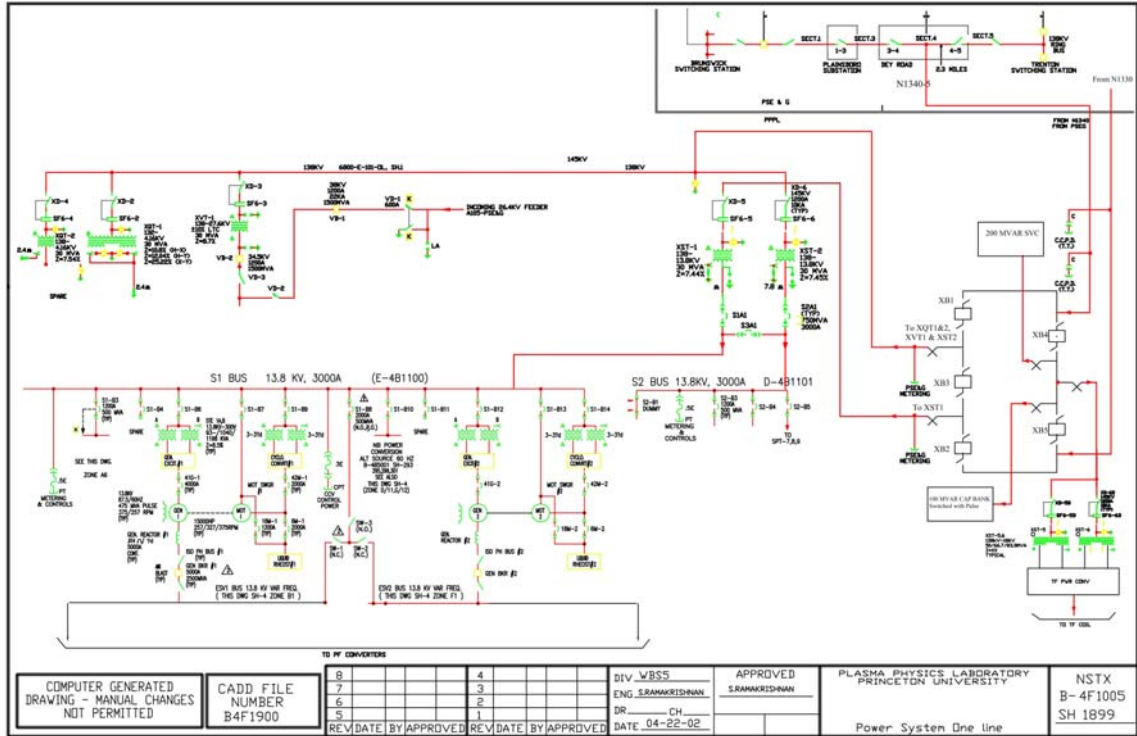
Figure 3.5.9 – One Line Diagram Of PPPL Power Systems for NHTX
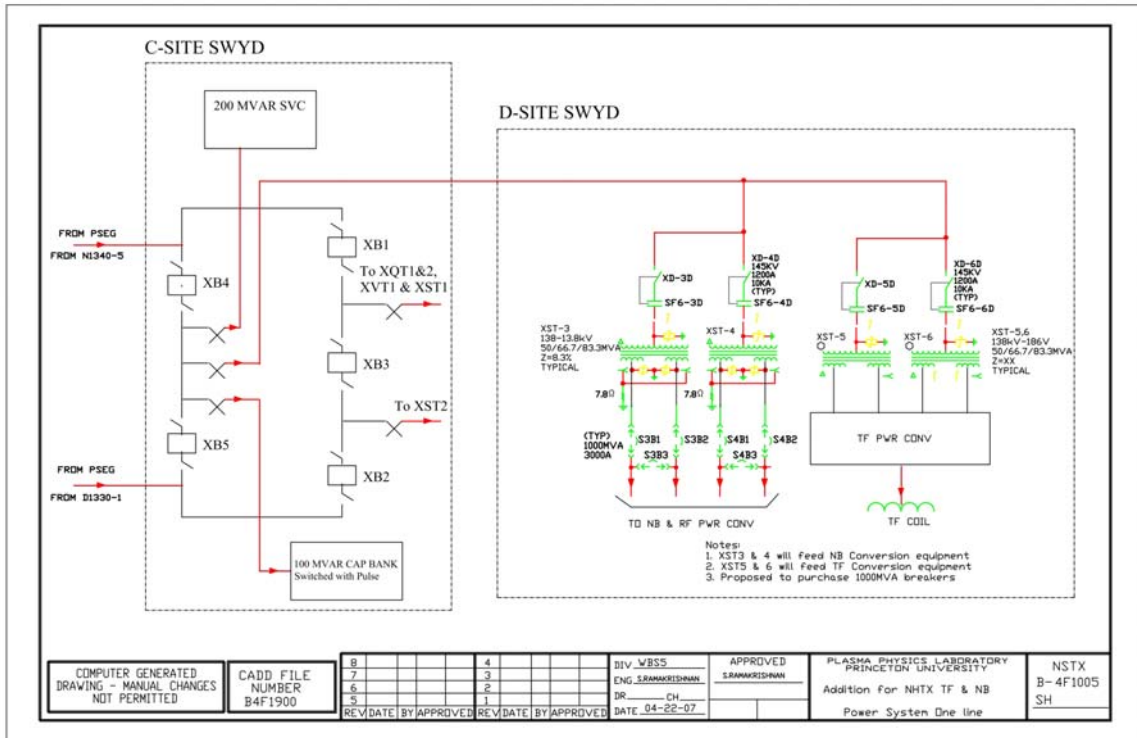
Figure 3.5.10 – One Line Diagram New D-Site Substation

3.5.3.1   Features

a. The present conditions of the supply of AC power to PPPL is derived from the N1340 138kV transmission line which connects the Public Service Electric & Gas (PSE&G) substations at Brunswick and Trenton. The continuous ampacity of the 397.5 MCM line which taps the N1340 line at Dey Road in Plainsboro and delivers the power to the PPPL substation is roughly 600A (corresponding to 140MVA). This will be upgraded as required to meet the NHTX loads.

b. In case of an outage of the 138kV system, the 26kV feed at A-site derived from a PSE&G 26kV transmission line separate from the PSE&G 138kV system is available to meet the essential loads in the facility.

c. Emergency power is supplied to a limited number of critical D-site loads including those related to the NHTX facility via a diesel generator rated 2600kW @ 0.8 p.f..

d. Under normal conditions the 138/13.8kV, three winding transformers XST1 & XST2 are used to power the PF part of the experimental and house power loads at D-site related to the NHTX experiment. The NHTX TF will be fed from the Grid via a new 138kV substation in D-Site.

e. Experimental power for NHTX is supplied primarily by:

> i) XST1 & XST2 to the S1 & S2 buses and by the D site MG equipment via SV1 & SV2 buses. Only one of the two D-Site generators is needed for NHTX.
> ii) Via a new D-Site 138kV substation.

f. Part of the RF sources are powered from existing C- Site from the Utility Grid via 138kV/4.16kV transformer XQT1 or 2 and fed by 4.16kV bus Q6 bus. Additional RF sources will be fed via the new D-Site sub-station.

g. House power and cooling water systems pumps for NHTX are supplied by XST2 to the Q10 and Q11 buses.

3.5.3.2   Layout

a. AC power at 138kV is received at the C-site substation, where it is transformed to the 26kV, 13.8kV and 4.16kV distribution voltage levels. 480 V distribution voltage is transformed at D-Site.

b. The NHTX loads are located in the D-site TFTR Test Cell, MG building, the FCPC building, NBPC building, and Pump Room. Only part of the RF feed is provided from the existing facilities in C- Site.

c. An MG control room is provided to house all the protection and control of the AC Distribution system equipment.

d. A new D-Site substation will be built to feed the NHTX TF and NHTX heating loads i.e. the Neutral Beams and part of RF Loads.

3.5.3.3 Component design features

All of the equipment associated with the AC power systems 480V and above that exists in place has been in service (under conditions less than of equal to the NHTX duty) for several years. The AC System equipment comprises of MG units, Generator main leads, Current limiting reactors, transformers and switchgear. Following specifications were used to procure the existing major components:

Table 3.5.6: List of TFTR Equipment Specifications applicable to NHTX

Equipment	Spec. # / Manufacturer
MG Units	PPPL- 0403 (RFP-255)
15 kV Power Cable	PPPL- 0415
Generator Main Leads	PPPL- 0421
2500 MVA Generator Breaker	PPPL- 0420
Current Limiting Reactors	PPPL- 0424
13.8 kV Switchgear (60 Hz)	PPPL- 0401
13.8 kV Switchgear (Variable Frequency)	PPPL- 0404
ACDS Board	PPPL- 0405
Protective Relay Board	PPPL- 0429
Low Voltage Power & Control Cables	PPPL-0431
Diesel Generator	PPPL-0406
Power Transformers XST1 & XST2 (C-Site)	RTE/ ASEA 4.B.2 -- TRA* RFP-285 Part IIC
13.8 kV 750 MVA Switchgear (C-Site)	Federal Pacific P.E.S. -- 47**

Salient features are as follows:

3.5.3.3.1 Input transformers

Each of the two power transformers XST1 & XST2 are rated 30/40/50 MVA, 138 kV/ 13.8 kV, 60 Hz. They are located in C- Site. The 13.8 kV outputs of XST1 & XST2 are fed to the S1 & S2 Buses in D- Site via 750 MVA Switchgear located in C- Site. The S1 & S2 buses comprise of 13.8 kV, 500 MVA, 1200 Amps Switchgear. Bus S1 feeds the D-Site MG loads including the induction motors, cycloconverters, and the generator static excitation system. Bus S2 serves the auxiliaries.

3.5.3.3.2 Motor Generator Sets

a. There are two MG sets each consisting of a drive motor, cycloconverter and 13.8kV generator with built-in flywheel. Only one set will be run for NHTX. Static excitation systems are provided for the generators. Each Generator is driven by an induction motor. The motors are doubly fed wound rotor induction motors with speed control by a cycloconverter system. A liquid rheostat is used to start up the motor to the base speed after which the cycloconverter takes over control. Main specifications of the MG sets are given in Table xx

Table 3.5.7: D-site MG Specifications
(per generator)

Parameter	Value	Units
Motor Power	15000	Hp
Synchronous Speed	327.27	rpm
Maximum Speed	375	rpm
Minimum Speed	257.14	rpm
Overspeed rating	424.29	rpm
Motor Stator Voltage	13.8, 3 Ph.	kV
Input voltage frequency	60	Hertz
Continuous Torque rating	240,625	Ft.lbs.
Generator Voltage	13.8, 3 Ph.	kV
Generator Peak Pulse Current	19.873	kA
Generator Power Factor	0.7	
Generator Peak Pulse Power	475	MVA
Maximum Operating Frequency	87.5	Hertz
Minimum Operating Frequency	60	Hertz
Generator Peak Pulse ESW	6.77	sec
Generator Peak Pulse Duty Cycle	2.257	%
Generator Sub-transient Reactance	0.156	Per Unit
Static Excitor rating	304	kW
Deliverable Energy	2250	M Joule

b. The mechanical construction of the MG sets and related auxiliaries were given consideration due to the pulsed nature of the load. The synchronous generators were built by General Electric and first operated in 1981. They have since been well maintained. How ever one of the MG units needs further repairs for welding cracks observed during routine check ups. Otherwise they are in good working order.

c. Windings are properly wedged and braced, and mechanical construction is designed conservatively for the life span and pulsed duty cycle. The rotating assembly is able to withstand 125% rated maximum speed without damage to any component.

d. The static excitation system for each generator consists of two oil-filled excitation transformers, three phase full wave thyristor rectifier bridges for 12 pulse operation and associated relays , controls and accessories.

e. Generators and exciters include all features for parallel operation.

f. The thyristor cycloconverter equipment is designed for use in the rotor circuit of each of the drive wound rotor induction motors. It is capable of operating with power flow and magnetizing current flow in either direction in any combination which does not exceed rated voltage and current. The thyristor system consists of six outdoor, oil-filled transformers, and three phase thyristor rectifier bridges as required for 12 pulse operation of cycloconverter.

g. One liquid rheostat is provided for each MG set to limit the inrush current of the induction motor during starting from 0 to 257 rpm.

h. A MG Relay Board is provided for each unit comprising of protective and control devices for the synchronous generator, wound rotor induction motor, cycloconverter, generator excitation system, and liquid rheostat.

i. Space heaters are provided in each motor and generator stator for protection against moisture condensation.

j. A DC tachometer generator coupled to the top end of the MG set shaft is provided to measure the rotational speed of the machine.

k. A sensor is mounted on the main generator shaft adjacent to the lower guide bearing for use with the digital speed devices.

l. Current transformers for metering and relaying are provided.

m. A free standing potential transformer and surge cubicles containing 14,400:120 volt potential transformers, 0.25μF surge capacitors, and 18 kV* class lightning arrestors are provided for metering and protection of each generator. (*upgraded from 15 kV class)

n. A screened indoor neutral grounding resistor rated 7.8 ohms, 1000 amperes for 10 seconds, and 8000 volts is connected for grounding the generator neutral.

o. The MG equipment was originally designed for 25 years of operation with a million pulses of deliverable energy. However only <100,000 pulses have been imposed on the sets since inception. Furthermore subsequent detailed analysis of the capability of the MG units indicates that the units are conservatively designed and is capable of operation up to 600 MVA.

3.5.3.3.3 Variable frequency bus

Buses SV1 & SV2 are fed from Generators 1 & 2 respectively. 5000 Amps (460kA momentary) Disconnect switches are provided to parallel the buses and to provide alternate feed from 60 Hz utility system bus S1. The output of each Generator is fed through a current limiting reactor, a generator air-blast circuit breaker, and finally to the feeder circuit current limiting reactors through an isolated phase bus duct. Connections from the feeder circuit breakers of the SV1 & SV2 buses are through 15 kV shielded cables to the transformers of Field coil power conversion system (FCPC) and the Neutral Beam Power Conversion (NBPC) system. There are twelve feeders in each of the SV1 & SV2 buses.

3.5.3.3.4 AC Protective Relaying

An AC Distribution Control System (ACDS) Board is located in the MG control room to provide control and metering of the MG sets and the 13.8 kV switchgears S1, S2, SV1, and SV2. The protective relaying for S1 & S2 buses are located in the ACDS board. The protection relaying for the SV1 & SV2 buses are provided in the Protective relay board which is also located in the MG control room.

3.5.3.3.5 D-Site substation (New)

A new substation with four 50/66.6/83.3 MVA , 138kV/13.8kV step down transformers (XST3,4) will be installed with all associated breakers and disconnects. XST3&4 will be used to feed Neutral Beam and additional RF loads. The TF power converter will be fed directly from the 138kV line through a step down transformer, along with the DC link rectifier.

3.5.3.4 Evaluation of grid loading

Present contractual arrangements with PSE&G allow for instantaneous peak power demand up to 120MVA without mention of power factor. The assessment of the capability of the grid to supply the power requires analysis which can only be performed in conjunction with the utility using appropriate analytic tools and extensive information about the power generation equipment in the grid, the transmission and distribution system, and the other loads. In recent years this type of analysis has been performed by PSE&G for the BPX (1991) and TPX (1993) experiments.

PSE&G was contacted and asked to evaluate the NHTX load. They confirmed the feasibility of a 300MW load and identified two options as follows.

Option 1

After a preliminary analysis, PSEG has conveyed that they can meet our requirements if suitable PF correction equipment is installed in PPPL & PSEG Trenton substation (at the cost of PPPL) and an additional parallel line is installed from Plainsboro to PPPL. The two lines will feed into a ring bus in PPPL and the loads will be tapped off from this ring

bus. Up to a total of 400MVAR of PF correction equipment may be needed. Details are as follows.

1. Provide an additional 138kV line to PPPL from Plainsboro. This line will be tapped off from the N1330 transmission line. (The existing line to PPPL is tapped off from N1340 Line). As per PSE&G this is to address thermal concerns with the additional load.
2. Install a 200 MVAR SVC in PPPL (at 138kV bus)
3. Install a 100 MVAR Cap Bank in PPPL. This will be switched on and off when NHTX gets pulsed.
4. Install a 100 MVAR Cap Bank in Trenton.

Option 2

Option items 2,3, and 4 above will all be implemented. How ever item 1 will be changed as follows:
PPPL has analyzed the thermal capability of the transmission line from Plainsboro to PPPL, Based on this analysis it appears that the existing conductor size may be just adequate to handle the NHTX pulsed loads. See Appendix 1. Thus another feed into PPPL may not be needed. This will eliminate the requirements of a ring bus with the associated 138kV breakers, within PPPL . According to PSE&G following are their stated concerns in this regard. PPPL suggested remedial measures are also indicated.

1. If (a) the Brunswick side of line or (b) the Trenton side of the line (N1340) trips the remaining half will not have the capability to handle the load.

PPPL feels that this can be addressed by tripping the PPPL feed in the event of the above.

2. PSEG would like to have the option to choose as to which generators to keep on line, for optimizing cost. They will loose this flexibility if the PPPL feed is only from one line. Such decisions are taken (according to them) by dispatchers on an hour-to-hour basis; that it becomes difficult to coordinate.

PPPL feels that NHTX can essentially be on a standby mode or in a mode of operation with certain limits imposed for the intake of Power, and thus will not affect PSE&G options to run generators of their choice.

3. PSEG conveyed that the short run from Plainsboro to PPPL can only take (a) 179MVA continuous (b) 212 MVA for four hours. In their assessment, 300 MVA pulsed load is on the borderline from their point of view.

PPPL analysis is in agreement with the PSE&G statement, except that it would advocate an upgrade to the conductor using the existing towers from Plainsboro to PPPL.

Option 2 has not been thoroughly discussed with PSE&G and has to be addressed when the project gets approved.

Finally, it is noted that harmonic filters will be provided as needed based on final simulations and analysis.

For the record, detailed minutes of a PPPL/PSE&G meeting are given below.

MINUTES OF THE MEETING WITH PSE&G ON JUNE 01 2007

Present:

PPPL

C. Neumeyer   (Project Engineer)   J. Menard   (Physicist)
R. Woolley   (Engineering)
S. Ramakrishnan (Engineering)

PSE&G

Esam Khadr   - Manager – Electric Delivery Planning
Shafique Mirza - Principal Staff Engineer – Transmission Planning
Glenn Catenacci – Principal Engineer, Asset Management
Craig D. Smith - Major Account Consultant

Summary of Discussions
Power requirements from the grid for the proposed new NHTX device were discussed. Charlie Neumeyer presented our requirements (see attached document) to PSE&G.

1. PSE&G performed a steady state load flow study using the PSSE program for delivering 300MW (PPPL Load at 100 MVAR) to PPPL. Their recommendations are based on the findings from the study. Transient study will be performed only after the project is finalized and is not needed at this stage. Their conclusions are very similar to their findings for the BPX project in 1991, which also required similar power levels. System upgrades are required to address the flicker problem which has to be limited to 1%. The voltage change at 138kV has to be under 5%. The upgrades are stated in the following paragraphs.
2. PSE&G conveyed that an additional 138kV line has to be run from Plainsboro to PPPL. The current feed is from the N1330 line. The second line will be tapped off from the N1340 line in Plainsboro. The tapping is easy (per PSE&G) since the lines N1330N & N1340 are in the same tower. This is to address the thermal limits of the line, keeping in view the line capability in the event either the New Brunswick side or the Trenton side trips putting the whole load on one side. This work will be performed by PSE&G with the cost borne by PPPL. PSE&G expects no problem in the reasonable sharing of the PPPL load, by the two parallel lines.
a) The present feed to PPPL is virtually devoted to PPPL (without any other tapped off loads) on the line running from Trenton to New Brunswick.

b) Even though the second line is tapped off from the N1330 Line which also feeds Plainsboro and Devilsbrook, PSE&G does not expect any flicker or other problems to the other connected loads in this vicinity, during NHTX pulsing.

(Post meeting note: The existing right of way to PPPL will be used and the present towers will be replaced with towers capable of carrying two lines. The scheme with two input lines to PPPL will necessitate a 138kV ring bus in PPPL to receive the lines. Thus two additional 138kV breakers will be needed.)

3. In addition to item 2 above, following PF correction equipment will be needed:

   a) 200 MVAR of active power factor correction equipment (SVC) will have to be installed at PPPL. (One of the D-Site MG can also meet this requirement by using it as synchronous condenser. This needs further study by PPPL).

   b) 100MVAR Cap bank has to be installed in PPPL. This needs to be switched on and off during NHTX pulsing.

   c) 100MVAR Cap bank has to be installed in Trenton. (The work will be performed by PSE&G. The cost for purchasing and installing this bank has to be borne by PPPL. Once installed, the maintenance will become the responsibility of PSE&G.)

   d) Installation of a 400MVAR SVC in PPPL will also meet the requirements – but this approach will be much more expensive.

4. PSE&G will furnish the cost for the upgrade on their side within couple of weeks. They conveyed that their proposed approach will be the least expensive.

5. The 138kV system within PPPL will have to designed with the required protective and control features in agreement and concurrence with PSE&G requirements.

6. PSE&G will provide an input to PPPL (from their recent past experience), the space requirements and cost for the SVC & Cap banks.

7. PSE&G conveyed that based on their generation capability in NJ, a large amount of Power has to come from the West.

8. PSE&G projected that with the proposed upgrade, the PPPL need of 300MW can be met based on their current study. This level may possibly increased to about 350MW by further addition of capacitive compensation. If PPPL power requirements is more than this level say 360-600MW, substantial cost has to be incurred (>100 million$).

9. It is assumed that PPPL will not operate NHTX during the months of June, July & August.

10. PSE&G conveyed that it will take about 3 years to complete the upgrade from the time approval is given.

11. With the proposed upgrade sudden load rejection will not be a problem.

12. If harmonic suppression is needed after a further thorough analysis (which will be performed if the project goes ahead) this also has to be implemented - however the cost for this additional equipment will be only a very small percentage of the total cost. Hence no further action is needed at this time.

(PS: If we install a state of the art converter for TF, this may not be needed at all)

13. PSEG will communicate the level of Fault MVA at the input to PPPL.
14. PSE&G engineers Esam Khadr & Glenn Catenacci were given a tour of the facility. They were also shown the 138kV lines into PPPL and the proposed location for the new substation in D-Site.

Conclusion:
1. The NHTX requirements of 300MW can be met by the Grid with following upgrades. This can probably be increased to 350MW with additional capacitive compensation. The proposed upgrades will be the least expensive.
   a) Provide an additional 138kV line to PPPL from Plainsboro. This line will be tapped off from the N1330 transmission line. (The existing line to PPPL is tapped off from N1340 Line.) This is to address thermal concerns with the additional load.
   b) Install a 200 MVAR SVC in PPPL (at 138kV bus)
   c) Install a 100 MVAR Cap Bank in PPPL. This will be switched on and off when NHTX gets pulsed.
   d) Install a 100 MVAR Cap Bank in Trenton.

2. For higher power intake of the order of 360-500 MW, expenses of the order of 100 million dollars may be necessary.
3. Estimated Cost for the Grid upgrade (other than the equipment and installation within PPPL) will be provided by PSE&G within couple of weeks. All the cost for the upgrade ((a) Additional line and (b) MVAR correction) has to be borne by PPPL. Once installed PSE&G will be responsible for maintenance of the equipment installed in their jurisdiction.

3.5.4   TF power supply

a. The NHTX TF Power Conversion System will be designed, purchased and installed in D-Site in the space west of the existing TFTR Test Cell. The rating is projected to be 250V at a load current of 500kA. By installing the converter close to the test cell, the lead lengths will be kept to a minimum for this high current feed. The area west of the TFTR Test Cell will be used to house the power supply.

b. The NHTX TF coil requires 177V with a pulse current of 500 kA for 1000 seconds every 3600 seconds. TF load is a simple inductive load with a ramp up , a flat top and a ramp down, and do not need fast changes and stringent controls during plasma operations. There are several options available for implementation. The most cost effective option will have to be adopted.

Option 1

In this option the system will be designed similar to the D-Site Power Conversion system. The 138kV will be stepped down to a medium voltage of 13.8kV, and will feed conversion transformers through medium voltage switchgear. Thyristor power supplies will then be provided to give a 24-pulse rectification system. On load tap-changer will be provided in the primary of the rectifier transformers to reduce the voltage during flat top, thereby keeping lower firing angle. This will decrease the ripple content and improve the power factor.

Option 2

Two conversion transformers 138kV/186V, 50/66.6/83.3 MVA will be installed. Thyristor rectifiers will be provided to feed TF. In this option the medium voltage switchgear is eliminated. On load tap-changer will be provided in the primary of the rectifier transformers to reduce the voltage during flat top, thereby keeping lower firing angle. This will decrease the ripple content and improve the power factor.

Option 3

Two conversion transformers 138kV/186V, 50/66.6/83.3 MVA will be installed. Diode rectifiers will be provided which will act as the DC Link to a set of IGBT choppers. In this option also, the medium voltage switchgear is eliminated. No on load tap-changer is necessary. This scheme will provide a power factor of 0.93 to 0.95.

c. The output of the TF converter will be fed to the NHTX TF coil via line switches for each parallel path and a ground switch.

3.5.5 PF power supply

a. The existing D-Site Power Conversion System will be used along with the associated line disconnect and grounding switches, ground fault detectors, cabling up to the South West corner of the TFTR Test Cell Basement, and hardwired control system modified to reflect the NHTX requirements. Additional disconnect and safety switches will be provided as needed. The power cabling will be modified as needed for NHTX. The power supplies are rated to pulse the coils for 1000 seconds every 3000 seconds.

b. The Converters will be re-configured to feed the NHTX PF circuits.

b. Additional bus work will be installed from the South West corner of the Test Cell Basement to the NHTX Test Cell.

c. All the power conversion equipment has been used in the past for the TFTR coils and later for NSTX coils and is functional.

3.5.5.1 Details of PF power supply equipment

a. The power conversion equipment comprises of conversion transformers and thyristor rectifiers, and DC reactors, Safety Disconnect Switches, Controls and Protective equipment. The transformers were manufactured by General Electric Co. The rectifiers were furnished by Transrex Division of Gulton Industries, Inc.. The SDS cabinets were furnished by Westinghouse. DC Reactors were manufactured by General Electric. Cables were manufactured by Okonite Co. Following specifications were used to procure the components:

Table 3.5.8: PF-1
List of D-Site Equipment Specifications
applicable to NHTX

Equipment	Spec. #
Conversion Transformers	PPPL-0410
Thyristor Rectifiers	PPPL-0411
DC Power Cable	PPPL-0414
5 kV Power Cable	PPPL-0430
Fault Detection Equipment	PPPL-0425
Precision Current transducers	PPPL-0426
Protective Relay Board	PPPL-0429
Metal Enclosed DC Equipment (SDS)	PPPL-0432
DC Reactors	PPPL-0436
Kirk Keys and stations	PPPL-0446

b) One three winding conversion transformer is provided to feed one power supply which was built by Transrex Division of Gulton Industries and were first put in service in 1982. The transformer windings are polygon/ delta-wye, with the polygon arranged to produce either + 7.5° or -7.5° phase shift depending on the phase sequence of the 13.8 kV input to the polygon. Thus an effective 24-pulse conversion is accomplished. The conversion transformer capability has been analyzed to meet the NHTX pulse duration and pulse period and determined to be able to meet the NHTX requirements.

c) One power supply comprises of two sections each with one Transrex rectifier rated 1 kV/24 kA-6sec/300sec . Each section consists of five parallel six-pulse bridges called power modules, and one parallel by-pass module. The power supplies are operated as phase controlled rectifier/ inverters, or may be bypassed from the load circuit by suppressing power module conduction and conducting the load current through the bypass module. The power supply can be also mechanically bypassed by a knife switch (manufactured by Pringle Co. and known as "Pringle Switch") provided for each of the 1 kV power supply section. The Transrex units accept digital commands for firing angle and thyristor (bridge and bypass) blocking; they do not include built in feedback control.
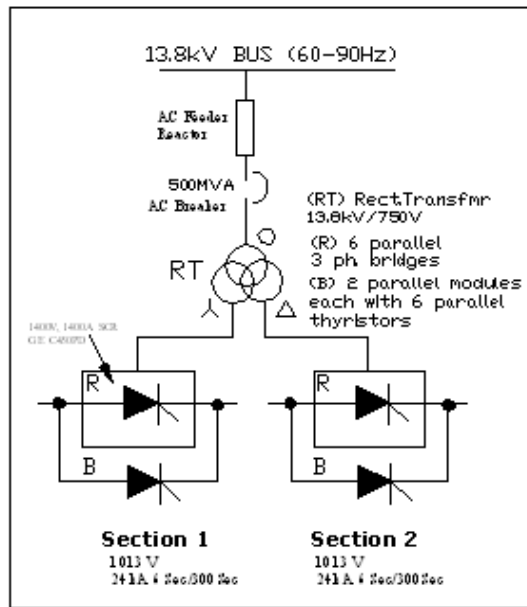
Table 3.5.9: Transrex Power Supply Ratings (per section)

Parameter	Value	Units
No Load Avg. DC Voltage	1012.85	volt
Maximum DC Current	30.0	kA
Nominal Pulse DC Current	24.0	kA
Nominal Pulse ESW	6.0	sec
Nominal Pulse Repetition Period	300.0	sec
Maximum Continuous DC Current as purchased	3.25	kA
Maximum 1000 second per hour DC Current as calculated	6.5	kA

c. Provision exists with bus links inside the SDS cabinets to accomplish current polarity reversal.

d. The existing line and ground switches will be utilized for test cell isolation, and will be interlocked with the access control system. This will be further integrated with the new TF Power feed isolation system to gain access to the Test Cell.

e. Feedback control of the current will be accomplished via the digital processor using a proportional-integral (PI) control law.

f. The ability to inject a hipot voltage on the coil system for daily pre-operational checks will be provided using the existing hipot system in the FCPC building. The new TF power loop will be integrated with the existing system.

g. Distribution of the PF power supply requirements in the PF load circuits is detailed in the PF coil section of this document.

3.6   Neutral Beam Injection (NBI)

3.6.1   Introduction

The NHTX NBI system would reuse the NBI technology which was originally provided for the Tokamak Fusion Test Reactor, and which is still in use on the National Spherical Torus Experiment, for relatively short pulses (<10 seconds duration). The technology requires an upgrade to 1000 second pulse length capability. The upgrade would be in large part identical to the upgrade to this technology planned for the Tokamak Physics Experiment as discussed in the TPX NBI Conceptual Design Review March 1993. The upgrade consists of bolstering power supplies to handle the pulse duration, upgrading all beam impinged surfaces with hypervapotrons for power handling capability, upgrading water systems to support the hypervapotrons, and upgrading the ion sources for pulse length and improved longevity. For many items in the NBI, upgrading to 1000 seconds essentially means CW operation.

The NBI system for NHTX consists of four beamlines using a total of 12 positive ion sources. Each source requires several different power supplies and a feedstock gas injection system to function. The sources create an ion beam which enters the beamline through a neutralizer section. The beamline consists of a beam box, neutralizer, bending magnet, ion dump, calorimeter and scrapers, cryogenic panels for pumping, vacuum and water services, and a support structure to bring the NBI centerline to the desired elevation on the vessel.

The beamline requires both liquid Nitrogen and liquid Helium for cryocondensation pumping of feedstock gas to limit reionization losses in the beamline. An existing 1070 Watt Liquid Helium Refrigerator in use on NSTX would be required to supply Liquid Helium. Deionized water systems provide cooling for power supplies, sources, and beam impinged surfaces in the beamline and duct. A high vacuum system roughs and maintains high vacuum conditions and provides cryopanel regeneration capability. An interconnecting duct attaches the NBI beamline to the torus vaccum vessel. A torus interface valve (TIV) in the duct bifurcates the vacuum boundary of the vessel and beamline.

The existing NBI ion source produces about 3 MW of neutrals to heat plasmas at a power density of approximately 4 kW per cm^2 on center. The existing beam impinged surfaces are water cooled copper plates so the pulse lengths are limited to a few seconds. For extended pulse lengths, hypervapotrons must be used to handle power densities. Hypervapotrons are commercially available units that have numerous applications comparable with the duty envisioned for the NHTX NBI, e.g. the JET NBI. Hypervapotrons have a front face with lateral grooves on the back. Water flows rapidly through the body of the unit. Some water swirls into the grooves. Bubbles from boiling form in the grooves and are scavenged into the main stream where they are condensed. The heat transfer characteristics of hypervapotrons are well studied.

A sulfur hexafluoride (SF6) distribution system provides pressurization and reclamation capability for insulating gas used in the source, transmission lines, high voltage enclosures, and power supplies. An extensive control system provides instrumentation, control, and data acquisition for operations and physics data.

3.6.2   Cryogenics

The existing liquid Helium refrigerator and liquid Nitrogen (LHe and LN) systems would be required to provide cryogenic pumping to the beamline. The systems are in use on NSTX and would require general maintenance. The cryogenic lines to connect the beamlines to the distribution systems would have to be fabricated on site and installed at time of operation.

3.6.3   Sources

The Common Long Pulse Ion Source has demonstrated reliable operation in deuterium and tritium for TFTR and deuterium operation for NSTX. The source consists of an arc chamber, grid mask, electrostatic accelerator, exit scraper, and Langmuir probes. The arc chamber will require an upgrade to the electron dump to achieve 1000 second pulse durations. The arc chamber will also require some protection to seams in plates to protect gaskets to improve longevity. The Langmuir probes will require additional testing or upgrade for longevity with more severe duty. The accelerator stage already reaches thermal equilibrium with present use so no upgrade is required. The exit scraper requires an upgrade to hypervaportrons.

3.6.4   Beamline

The NBI Beamline consists of a beam box made of stainless steel with a SS lid weldment from which are suspended six cryogenics panels. The cryocondensation panels could be upgraded to a cryosorption system but a feasibility study would be required. The TPX NBI CDR used cryocondensation panels with regeneration scheduled commensurate with pulse length and integrated run time.

Three sources rest on a source platform connected to the box. The 3 sources connect to an entrance flange in a fan array with the central source trajectory aligned with the horizontal centerline of the beam and the two outer sources at $\pm$ 4 degrees with a focal point at the exit of the duct. The neutralizer for each source collimates the beam, provides gun barrel to establish a gas crosssection appropriate for neutralization, and removes the heat associated with stray beam particles. The neutralizer aims through the bending magnet which deflects remaining unneutralized beam into the ion dump. Neutral beam particles proceed through the box to either the calorimeter if it is inserted into the beam path, or the interconnecting duct and vessel if injection is desired. Collimating scrapers exist fore and aft of the calorimeter and at the exit of the beamline to shield surfaces from divergent beam particles.

The beam box has a turbomolecular pump mounted to the source side of the beamline. A backing pump backs the turbo. A separate roughing pump can rough beamline, vacuum lines, and sources.

The ion source requires a feedstock gas injection system with enough capacity and control to deliver 1001 second pulses throughout an operating day.

The cryogenics panels consist of three panels each side. The outermost panel is a liquid Nitrogen shield panel. The liquid Helium panel is in the middle to minimize heat load. The liquid Nitrogen chevron panel is innermost and allows deuterium to be pumped by the Helium panel. The chevrons are designed to be 7 bounce angles. The pumping speed for the panels minimizes reionization after the neutral beam leaves the neutralizer.

The possibility exists to upgrade to cryosorption pumping with an associated improvement in efficiency that has been demonstrated on other fusion devices. This change would require an engineering feasibility and cost study.

The liquid Helium panels cryopump deuterium which must be regenerated at frequent intervals. A gaseous Helium regen system must be installed to spoil hard vacuum, warm the panels, and defrost them so the vacuum system can pump away the effluent.

All of the directly impinged beam surfaces will require upgrade to hypervapotrons, including the source exit scraper and neutralizer, ion dumps, and the collimating scrapers. The interconnecting duct will require hypervapotrons also because reionized beam can be focused in the duct by machine fields and can bore holes through any nonactively cooled surface. Each machine field and accel voltage configuration and TF and PF combination can produce a different focus and hot spot so the entire duct must be lined.

3.6.5 Duct and Aiming

The interconnecting duct consists of a spool section which attaches to the beamline exit flange, a Torus Interface Valve (TIV), a ceramic break to isolate the beam from vessel potentials, a bellows to account for vessel dimensional changes due to bakeout, a hypervapotron liner to handle reionized beam focused by machine fields into the duct walls. The 3 sources cross over at the focal point which is very near the exit of the duct where it bolts to the machine port. The beam requires adequate free aperature to avoid reionization losses causing wall heating, outgassing, and further runaway reionization.

3.6.6 Power Supplies

Six power supplies are required for ion source operation. These are: DC accelerator high voltage to 120 kV, DC gradient grid high voltage, negative DC high voltage for the suppressor grid, high current DC supply for filaments, high power (100kW) supply for arc, and a high current DC supply for the bending magnet.

The power supply for the accelerating voltage must produce 120 kV with 0.5% regulation, 70 Amperes of current, a rise time of 70 microseconds, and a turn off time for blocks and shot termination of 0.1 microseconds to protect grids from fault energy. At present, the gradient grid voltage is also supplied by the accel system using a gradient grid resistive voltage divider. Grad grid is usually about 15% lower than accel. The present system uses 13.8 kV 3 phase power supplied to an autotransformer for rough voltage selection, a stepup transformer/ rectifier, a capacitor bank and crowbar, and a tetrode based modulator/regulator. Several options exist to upgrade this system to 1000 second operation. The tetrode design has been tested to over an hour steady state operation at full current so for the TPX design an upgrade to the existing system was envisioned. With the development of IGBT technology and fast switching capability, a solid state accel system can now be envisioned. An engineering study would be required to determine the best and most cost effective course of action.

The suppressor grid supplies a negative potential at the exit of the accelerator grid system to create an electric field barrier against backstreaming electrons from the neutralizer region. The suppressor grid power supply must provide up to -5 kV at approximately 20 Amperes. IGBT technology readily provides a means to provide this power and switching capability.

The filament power supply provides heating current to the 32 source filaments to liberate electrons in the arc chamber. The present filament supply consists of a 480 VAC service, a Variable Voltage Transformer, an isolation transformer so the secondary can float to accel potential, a diode rectifier and associated cabling. The filament supply is not CW and will require upgrade.

The arc supply provides power to breakdown the feedstock gas and make a low temperature deuterium plasma from which ions are extracted. The present arc supply consists of a 480 VAC service, a Variable Voltage Transformer, an isolation transformer so the secondary can float to accel potential, a diode rectifier and associated cabling. The arc supply is not CW and will require upgrade.

The arc and filament supplies are referenced to the accel supply in a High Voltage Enclosure and supplied to the ion source via a transmission line. The ion source arc chamber is connected to the source grid of the accelerator and, in terms of electrostatic potential, it rises with the tide of the accel pulse. Because the ions are now floating at accel potential the grids extract and accelerate ions toward the ground grid and are focused by the source grid Pierce geometry into very parallel beamlets.

The High Voltage Enclosure also contains protection equipment and isolation transformers for the filament and arc supplies. The HVE requires upgrade because the heat exchanger for the SF6 is not CW and the upgrade required for the high voltage sections of the arc and filament supply will not fit within the HVE tank. A design for a high voltage deck with air isolation has been envisioned to upgrade to CW.

The transmission lines are not rated CW and require a design capable of standing off accel voltage while conducting full filament and arc current to the source. Development of new transmission lines will be required to upgrade to CW.

The bending magnet deflects ions that remain unneutralized upward into the ion dump. The bending magnet supply provides 1000 Amperes at up to 30 Volts CW. The existing supplies and magnets are CW and require no upgrade.

3.6.7   Services

The beamline and sources require high vacuum conditions to operate properly. The vacuum systems as designed can operate continuously. The vacuum system will require turbomolecular pumps, roughing and backing vacuum lines, large vacuum pumps and blowers, and associated valving and controls.

The deionized water systems service power systems, ion sources, and beamline water. A substantial upgrade to the previous system will be required to accommodate using hypervapotrons for 1000 second pulses.

SF6 is used as an insulating gas and must be reclaimed, distributed, and maintained at low dew point for effective use.

3.6.8   Controls

Because the NBI system is distributed throughout several buildings and about half of the equipment will be within the torus hall and inaccessible during operations, the controls for the NBI must provide remote and highly centralized instrumentation, control, and data acquisition for the NBI system to operate. A total upgrade of the controls will be required to take advantage of modern computing and software options but existing controls provide an adequate model.

3.7   Site Cooling Systems

The existing equipment for rejecting heat at the PPPL site remains from the TFTR project. The TFTR was designed to operate entirely from its two motor-generator energy storage systems which could hold up to 4.5 GJ or energy extracted in seconds during one brief plasma experiment then recharged from the local electric utility during the time between plasma experiments. Ultimately, most all of teh 4.5 GJ ended up after each experiment as heat in various cooling water systems which in turn passed their heat on to the site cooling towers. The equipment was designed to support one experiment every 300 seconds, so the local heat rejection capability is (4.5E9 J)/(300 s)= 15 MW.

The plan for the NHTX is to draw 300 MW from the local electric utility for 1000 second plasma experiments, and to conduct those experiments once per hour. Since again all this energy will be turned to heat in local water systems, the heat load will be (300 MW)*(1000 s)=300 GJ every 3600 seconds, i.e., a dissipation rate of (300E9)/(3600

s)=83.3 MW.   Since the initial 15 MW capability is still operable, the NHTX will require an additional 83.3-15=68.3 MW of cooling towers be installed to support its full pulse duty cycle rate.

The NHTX will also require additional cooling water storage capacity. The size required depends inversely on the allowable water temperature rise, which must be restricted if equipment is to be kept cool. To absorb 300 GJ in cooling water with a 50 C water temperature rise (e.g., from 10 C to 60 C) would require about 1450 m3 or water, i.e., almost 400,000 gallons. A reduction in the cooling water's temperature range would require proportionately more water volume.

While 400,000 gallons is a substantially sized tank it is not prohibitively large in comparison with community water towers. For instance, a 40 foot tall cylinder 40 feet in diameter would have almost exactly that volume. However, most of the cooling water would not need to be kept quite as clean as drinking water. A cooling water reservoir could be implemented as a concrete-lined outdoor pond with a suitable covering to avoid debris. On the other hand, it may be more cost-effective to implement this cooling water storage using multiple smaller tanks which can be shipped by truck and therefore would not require much on-site assembly.

Cooling water pumping will also need to be upgraded for the NHTX. In addition to more total pumping capacity, there is a need to provide more control of separate water cooling loops so that they can be throttled down for systens dissipating less power for a particular experiment and throttled off altogether between experiments

4   Radiological Issues

This section details those radiological parameters that will result in the operation of NHTX at PPPL. PPPL successfully operated TFTR in a D-T burning regime from 1993 to 1997. The PPPL site is well characterized for environmental conditions having had site-specific meteorological modeling performed by NOAA, and ground water modeling performed by the USGS. The site currently has in place an extensive radiological and environmental monitoring program. Environmental conditions at the site are stable with < 2 % variation from year to year. The PPPL site provides approximately $ 500 M in site credit infrastructure and provides a safe and robust platform for supporting a category 3 low hazard nuclear facility. The inclusion of NHTX will add value and scientific merit to this existing infrastructure, which includes, a well-shielded test cell, nuclear quality HVAC systems, appropriate utilities for supporting MFE nuclear operations, and a solid connection to the power grid.

4.1   Tritium

PPPL maintains a closed loop tritium fusion fuel cycle system, which is capable of delivering, processing, and recycling tritium at purities > 99 % for re-use in a D-T fusion device. The system has successfully processed ~ 100 grams of tritium in support of TFTR operations, including D&D, and is valued at ~ $ 25 M. The PPPL tritium facility includes; tritium storage, tritium delivery, tritium processing, isotope separation system (for cryogenic-distillation of hydrogen isotopes), analytical / monitoring capability, and ancillary components. The facility has the capacity to safely operate as a category 3 low hazard nuclear facility with tritium inventories at the 30 gram level as described in DOE Standard 1027. With minor modification to the existing system a 100% safety factor for the storage of tritium twice the category 3 low hazard nuclear facility can readily be implemented. In addition new stack scrubber technology for the removal of hydrogen isotopes are available and are planned to be installed in the station stack during NHTX D-T operation(s), thus furthering attenuating the release of tritium. A stack scrubber system with an effective operational DF of 500 for T is being investigated.

To support NHTX fuelling re-cycling requirements (on the order of hours) it would be possible to include multiple isotope separation systems running in parallel feeding multiple plenums, Employing multiple cryo-pumps capable of being isolated for real time regeneration would also support a rapid T recovery, re-cycling and purification. Laser rastering to remove T from first wall components would also provide efficient recovery of T for reuse in the device.

It should be noted that although TFTR had previously been limited to a 5-gram tritium inventory, Princeton University had previously agreed in principal to a 20-gram inventory regarding the CIT conceptual design. As was the case for TFTR, tritium will be delivered to NHTX via a U-bed loaded with 25kCi increments of tritium. During TFTR T was delivered in quantities as much as 2.8kCi to machine plenums prior to commencing D-T nuclear operations. The turn around time for T for TFTR was ~ 26 hours. Tritium fueling

of the plasma was mainly done through the neutral beam ion sources. At 27 torr liters/second/source, it took about 90Ci/source to initiate the arc and provide sufficient neutralizer line density, and then about 70Ci/source for a .75 second beam extraction. The amount of tritium needed by the ion sources is primarily governed by the requirement to provide adequate neutralizer efficiency

[Note: upgrades to the beam-line to allow a tritium ion beam to be neutralized via a separate introduction of deuterium have been discussed].

For NHTX, it is expected that plasma fueling will again be done via the beams. Although there are still ongoing discussions on pulse length, engineering efforts seem to be settling in on a nominal 60 seconds. Considering the above, a 60 second beam extraction would require about ~5.5kCi/source. Therefore a full D-T shot (6 D sources, 6 T sources) would use 33KCi or 3.3 grams of tritium.

It seems quite reasonable that we could develop a system to process tritium for re-use in less than a day. A more extensive beam-line modification is also possible, and could include a set of isolatable cryo-panels to pump gas only during the tritium shots. This would both speed up the process time (higher % of tritium on those panels) and allow processing to occur in parallel plasma operations.

Following is a footprint of the PPPL tritium facility. The tritium facility is located in the test cell basement on D-site is has been maintained (post TFTR) to support a category 3 low hazard nuclear facility.

PPPL Tritium Area

(2) 7.6m³ Tanks
(1) 1 m³ Tank

15' 0"x15' 0"

Gas Holding Tank Room

Tritium Purification System Room

16' 0"x21' 4"

TPS

Fumehood

48' 9"x26' 6"

Torus Cleanup System

Room Detritiation System

Tritiated Vent System

Glovebox Cleanup System

Tritium Cleanup Area

High Temp Oven
Vacuum System
Residual Gas Analyzer

Tritium Vault

16' 0"x24' 10.5"

1 Receiving/Analytical
GB with QMS
1 Vacuum Pump GB
1 Storage & Deliver GB
with 3 Ubeds

Tritium Waste Handling Area

325 w Nd:YAG Laser

45' 0"x14' 0"

Waste Handling Area Fumehood

Shower/
Eyewash
Station

Figure 4.1: PPPL Tritium Facility Floor Plan

4.2   Neutrons

Neutron dose (measured dose equivalent) at the site boundary resulting from the production of D-D neutrons is calculated to be 1.8 x 10⁻22 mrem / D-D neutron.
For D-T neutrons the dose is calculated to be 3.2 x 10⁻21 mrem / D-T neutron.

Therefore a 1 second NHTX D-T shot would result in an off-site dose of 5.6 E⁻3 mrem

Where; (NHTX D-T neutron flux = 1.77E⁺18 n / sec) (3.2E⁻21mrem / DT neutron) = 5.6E⁻3 mrem/ second

Thus 1000 seconds of D-T (shots) operations would result in 5.6 mrem at the site boundary.

The PPPL site limit is 10 mrem / year at the site boundary from all sources of radiation. This includes dose(s) from neutron radiation, prompt gamma radiation, activated components, activated air, tritium, and liquid effluent releases. Historically (during TFTR D-T operations including D&D) the pacing item for off-site doses was from tritium (see section 7).

Thus 1000 seconds of D-T operations would contribute > 50 % the annual boundary dose limit. As a result of the high NHTX neutron flux, localized shielding around the reactor core is required.   Currently the NHTX project team is investigating a water jacket (neutron shield) to be integrated into the outer co-axial wall of the reactor. The addition of localized neutron shielding in the NHTX will be required to maintain doses within the 10 mrem / year dose limit at the site boundary.

Analysis employing the ATTILA neutronics code is planned to determine the best shield configuration.

4.3   Activated Air

Activated air in the form of N-13 (9.9 minute half-life), N-16 (7.2 second half-life), S-37 (5.1 minute half-life), Cl-40 (1.5 minute half-life), and Ar-41 (1.8 hour half life) will be generated in the NHTX test cell atmosphere [assuming air is the major gaseous component surrounding the machine]. Ar-41 with a longer half-life, but generated at a much smaller fraction, could be delayed in the test cell by reconfiguration of the HVAC system during HPP operations. Another approach would be to backfill the test cell with an inert gas (N2) during HPP D-T operations to mitigate the production of Ar-41. Another area that components of activated gases would be found is cooling water flowing around the machine (magnets, diagnostics, pumps, etc). Access control procedures will be needed to ensure that personnel are kept away from the flow of this source term (pump room and ancillary flow lines) until it has time to go through ~ 10 half-life's. A second component of radioactive components in the cooling water will be from the activation was from corrosion products. This is addressed in section 5 of this report.

4.4 Gamma Radiation

The following items listed below are those activation components that can be expected due to NHTX D-T operations. There may be others based on the final composition of materials used in the vv, coils, and ancillary systems. Co-60 and Mn-54 will be the longer source terms limiting up-close (unshielded) machine access. A modest "cool down" period of several weeks may be required after HPP D-T operations. The employment of localized shielding, remote manipulation, and a cool down period would support machine access for maintenance and diagnostic servicing activities, in accordance with PPPL and DOE dose guidelines for radiation workers. The anticipated activation products include; Cu-62 (9.76 minute half life), Cu-64 (12.8 hour half life), Co-60 (5.26 year half life), Co-62 (13.9 minute half life), Cr-51 27.8 day half life), Mn-54 (312 day half life), Mn-56 (2.58 hour half life), Co-57 (270 day half life), Co-58 (71.3 day half life).

4.5 Doses to the Public

Doses to the public (commonly referred as off-site doses) for DOE fusion facilities is stated in DOE-STD -6003. For PPPL the annual off-site dose for normal operations, for all sources of radiation, is 10 mrem/ year at the site boundary. For accidental releases where there is no emergency evacuation plan in place the dose limit is 1 rem. Due to the NHTX plan to limit the releasable tritium at risk (under all conditions) to < 63.7 KCi there is no need for PPPL to have an off-site emergency evacuation plan during any aspect of NHTX operation.

DOE-STD - 6003-96 sets radiological criteria as depicted in the table below

	Fusion radiological Release requirement	Regulatory limit (evaluation guide)
Normal and anticipated operational occurrences	10 mrem/yr	100 mrem/yr
Off-normal conditions (per event)	1rem (no public evacuation)	25 rem

Table 4.1: Requirements for protection of the public from exposure to radiation

Environmental Releases / Environmental Doses

As stated (section 6) PPPL is limited to maintaining off-site doses from normal operations to ≤ 10 mrem / year. During TFTR D-T operations the largest contributor to the off-site dose was from tritium released from the facility stack. As detailed in section 2 of this report it is planned to install a hydrogen isotope scrubber in the NHTX stack to reduce the tritium going out the stack and into the environment. As described in section 3

of this report the pacing item for NHTX off-site doses appears to be from the D-T neutron source term. With appropriate shielding as described in the neutron section of this report the off-site dose values as described in table 4.1 for normal operations can be achieved in support of NHTX operations.

Following is historical data during the operation of TFTR in D-T and the components of dose based on the various source terms.

	CY1994`	CY1995	CY1996
n & g	.07	.08	.04
T	.12	.097	.32
AA	.11	.13	.07
Total dose	0.3 mrem	0.31 mrem	0.43 mrem

4.6   Meteorology

During the period of July 28, 1988 to September 21, 1998 the National Oceanic and Atmospheric Administration (NOAA) made ~ 50,000 measurements at PPPL to determine the site specific atmospheric dispersion characteristics of D-Site under a wide variety of meteorological conditions. The collection of these measurements resulted in site specific atmospheric concentrations (χ/Q) values for the release of radioactive materials. It was thus determined that for routine stack releases a χ/Q of $1.77 \text{ E}^- 5$ s/ m^3 should be used to determine radiological release concentration to the environment. For accidents resulting from a stack release (30 minute duration) a χ/Q of $1.70 \text{ E}^- 4$ s/ m^3 was established to reflect the atmospheric concentration. For ground level release accidents (2 hour duration) a χ/Q of $4.80 \text{ E}^- 4$ s/ m^3 is set.

Table 4.2: Radiological Summary

NHTX Classification	Category 3 Low Hazard Nuclear Facility
NHTX Safety Classification	High Hazard
Maximum T inventory	30 grams
Maximum T stack release	500 Ci / year
Maximum daily T stack release	10 Ci / day
Maximum release to sanitary system	1 Ci / year
Maximum annual dose to public	10 mrem / year
Maximum accidental release (ground)	63.7 KCi
Maximum accident dose	1 rem
Routine χ/Q	$1.77 \text{ E}^- 5$ s/ m^3
Accident χ/Q (stack)	$1.70 \text{ E}^- 4$ s/ m^3
Accident χ/Q (ground)	$4.80 \text{ E}^- 4$ s/ m^3
Site Boundary	176 meters from center of test cell

4.7 Hypothetical NHTX Pulse Spectrum, Flux, and Fluence

NEED TO UPDATE THE XL TABLE AND INSERT HERE

4.8 Section References

- Tokamak Fusion Test Reactor Final Safety Analysis Report (FSAR)

- PPPL - Report 3159 Annual Site Environmental Report for Calendar Year 1994

- PPPL - Report 3284 Annual Site Environmental Report for Calendar Year 1995

- PPPL - Report 3290 Annual Site Environmental Report for Calendar Year 1996

- DOE STD 1027 Hazard Categorization and Accident Analysis Techniques for Compliance with DOE Order 5480.23 Nuclear Safety Analysis Reports

- DOE-STD 6002-96 Safety of Magnetic Fusion Facilities Requirements

- " Hydrogeology, Ground-Water Quality, and the Possible Effects of a Hypothetical Radioactive-Water Spill, Plainsboro Township, New Jersey." US Geological Survey, Water-resources Investigations Reports 87-4092.

- Start, G., et al. " Atmospheric Diffusion for Airflows in the Vicinity of the James Forrestal Campus ". NOAA May 12, 1989

- PPPL Environmental Safety and Health Manual HSD 5008

- Code of Federal Regulations 10 CFR 835 "Occupational Radiation Protection"

5 Conclusions and Recommendations

The exploratory engineering assessment during FY2007 of the NHTX design point did not find any show-stopper concerns. Instead, it found that a quasi-steadystate toroidal plasma device closely approximating the NHTX design point can indeed be constructed at PPPL. With small additions and upgrades, existing site equipment can confine and heat its plasma for durations of up to 1000 seconds while achieving levels of the plasma's P/R ratio far beyond the capabilities of any other existing or planned facilities. The local electrical utility company can supply the requisite300 MW and slightly more if needed, without excessive capital costs for the upgrade. Magnet systems can use water-cooled copper technology without approaching any technological limits on mechanical stresses, power density, or heat removal.

Challenging design issues found included the difficulties of cooling high temperature plasma-facing surfaces and the difficulties of providing sufficient sustained vacuum pumping. For the first, it was found that removing heat using high temperature helium gas flowing at high pressure and high speed may perhaps be able to do the job but could be marginal without allocating more space inboard of the plasma for helium heat transfer.

For the second, there is not enough space around the NHTX divertor to install vacuum pumping ducts sufficiently large for sustained pumping by remotely located vacuum pumps. Instead, it is clear that some type of high speed high vacuum pump will need to be located adjacent to the divertor. A cryopump inside the vacuum vessel and integrated with the plasma divertor has been employed recently on other experiments, but does not extrapolate to a reactor for which high sustained radiation heat loads are incompatible with cryopump operation near absolute zero. None of the vacuum pump technologies commercially available today is appropriate for a fusion reactor, but the concept of a ceramic rotor turbomolecular pump which could operate in a high magnetic field would meet all needs if developed. This ceramic rotor approach, for which a prototype was successfully tested in Japan 20 years ago, should be pursued for NHTX.

This present engineering assessment did identify novel features worthy of further development and adoption as basic elements of the NHTX design. The vacuum vessel should incorporate two separate layers, i.e., an outer water-cooled vacuum vessel which operates near ambient temperature and a vacuum-insulated heated inner first wall which would operate at elevated temperatures. The outer vacuum vessel should also have a removable lid so that the crane can be used to remove and replace the internal first wall to accomplish different divertor experiments. Although features for fabricating, mounting, accessing, heating and cooling the first wall have been identified, more work should be invested into further developing the details of those features and scrutinizing them with more accurate 3D analyses of their optimized performances.

An improved scheme for the TF system's demountable inner electrical joints was also identified. It uses special shaping of the joints to generate magnetic forces which clamp the joints closed, which minimize peak out-of-plane forces on the joints, and which do

not concentrate current in abrupt corners. However, additional analysis work in the future is needed to choose the optimum joint shape from possible variations.

Continued future NHTX engineering investigations should consider small changes to the design point parameters. Improved heat removal from the plasma first wall using helium may require that the inner boundary of the vacuum vessel must move inwards, thus reducing the diameter of the TF Central Bundle and increasing its electrical power dissipation. Better access to the divertor for either high vacuum pumping or for backing forelines may require that the cross-sections of PF coils be reduced, further increasing electrical power dissipation.

A focus of future work should be choosing the detailed shapes and space allocations for the vacuum vessel, first wall, and other structures. This will require substantial 3D FEA modeling and also 3D structural design and drafting. Future work should also consider methods for constructing the designed components in order to optimize their cost. Finally, costs of the various efforts should be estimated.

Although there is considerable additional preliminary design work to do in the future, the conclusion of the FY2007 work is that the NHTX appears feasible at or near its design point parameters. It is recommended that the additional preliminary engineering work be pursued in the FY2008.

6   Appendix

This appendix contains MATLAB calculation scripts which were used in the analyses discussed in the main document. Although in an earlier draft version these scripts were interspersed within the main document, in this version they were segregated by relocating them into this appendix in order to improve readability of the main document while still maintaining some ability of readers to review how results were obtained.

The conductance of a circular duct of length L and constant diameter D is given by the following approximate dimensional formula [Roth]:

$$C = 0.381 \sqrt{\frac{T}{M}} \left(\frac{D^3}{L+1.33D} \right)$$

where C is the conductance in m^3/s, L and D are in meters, T is the gas temperature in Kelvins, and M is the molecular weight of the gas in atomic mass units. For helium or deuterium gas (M=4) at a temperature of 20 C, this becomes

$$C = 3.261 \left(\frac{D^3}{L+1.33D} \right)$$

Constant duct conductance contours are graphed versus duct length and diameter in the following plot, which was generated using the MATLEB computational cell .of Appendix A section 1.1.

```
d=0.1:.05:1;
l=0:0.05:5.0;
[D,L]=meshgrid(d,l);
C=3.261*D.^3./(L+1.33*D);
[c,h]=contour(L,D,C,[.01 .02 .04 .06 .1 .2 .4 .6 1 2],'-k');
clabel(c,h);
xlabel('Duct Length L (meters)')
ylabel('Duct Diameter D (meters)')
ylim([0 1])
title('D_2 or He  Conductance of Circular Cross-Section Duct @20C  ')
legend('m^3/s Conductance','Location','SouthEast')
interp2(D,L,C,0.3,3)

ans =
    0.0259
```
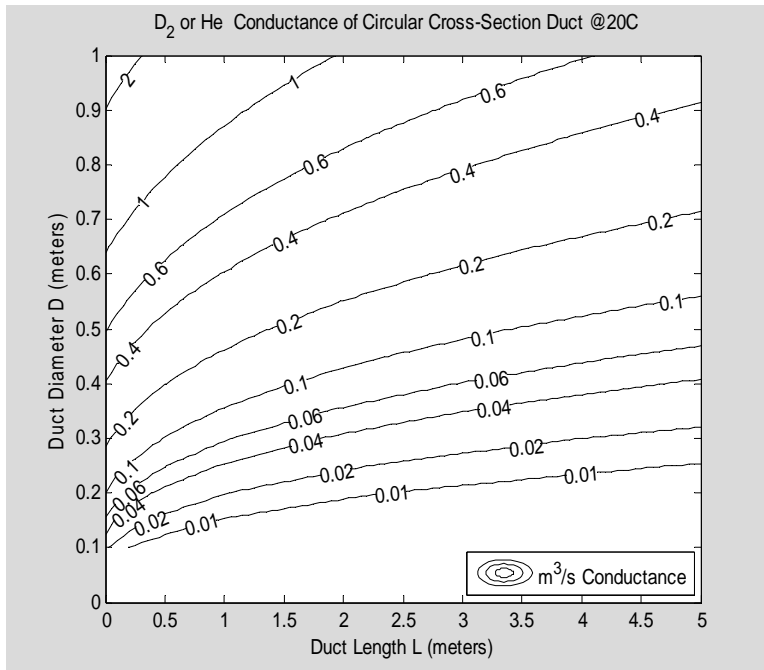
D_2 or He Conductance of Circular Cross-Section Duct @20C

Past practice in fusion research has usually located turbomolecular pumps remotely from magnetically confined plasmas but has sometimes also used passive magnetic shielding. To be outside the TF region implies a pumping duct length of several meters, and even more pumping duct length could be needed to attenuate poloidal fields. Locating turbomolecular pumps (or alternatively cryopumps) remotely from the tokamak at the end of long pumping ducts greatly reduces their effective pumping speeds. For a large turbomolecular pump with pumping speed 6 m^3/s, the effective pumping speed at the vacuum vessel varies as a function of duct size parameters as follows:

```
d=0.1:.05:1;
l=0:0.05:5.0;
[D,L]=meshgrid(d,l);
Sp=6;
C=3.261*D.^3./(L+1.33*D);
Se=C*Sp./(C+Sp);
[c,h]=contour(L,D,Se, [.01 .02 .04 .06 .1 .2 .4 .6 1 2],'-k');
ylim([0 1])
clabel(c,h);
legend('Pumping Speed (m^3/s)','Location','SouthEast');
xlabel('Duct Length L (meters)')
ylabel('Duct Diameter D (meters)')
title('Effective D_2 or He Pumping Speed of 6 m^3/s Pump At End Of
Circular CrossSection Duct')
```

Effective D$_2$ or He Pumping Speed of 6 m^3/s Pump At End Of Circular CrossSection Duct

----
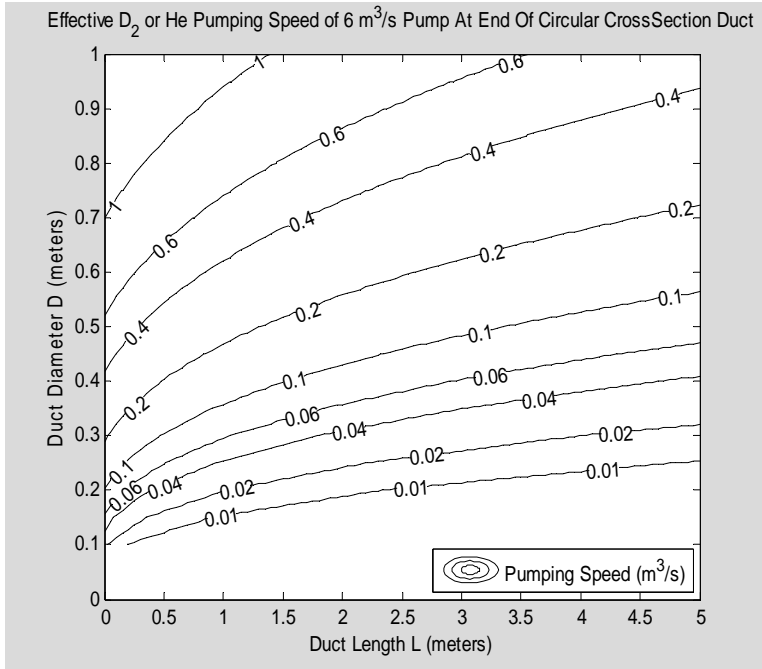
Solubility of Hydrogen Isotopes In Molten Lithium

Various investigators have measured this solubility curve. Shpil'rain's model [Ohse] is

$$\ln\left(n_H^{Sat}\right) = E - \frac{F}{T}$$

where the temperaure is in Kelvins. His regression fit values are as follows:

Isotope	E	F (Kelvins)	Exp. Range (Kelvins)
Protium	15.476	5360	523-775
Deuterium	15.047	5112	472-771

A MATLAB plot of his solubility model follows, as generated by a MATLAB cell in Appendix section 1.3:

```
E=[15.476  15.047];
F=[5360 5112];
 T=linspace(200,450)';
nsat=exp(ones(size(T))*E-ones(size(T))*F./((T+273)*[1 1]));
semilogy(T,nsat),xlabel('Lithium Temperature (Degrees C)'),
ylabel('Atom Parts Per Million (appm)'),title('Saturation Solubility of
Hydrogen Isotopes In Liquid Lithium')
legend('Protium','Deuterium')
```

Saturation Solubility of Hydrogen Isotopes In Liquid Lithium
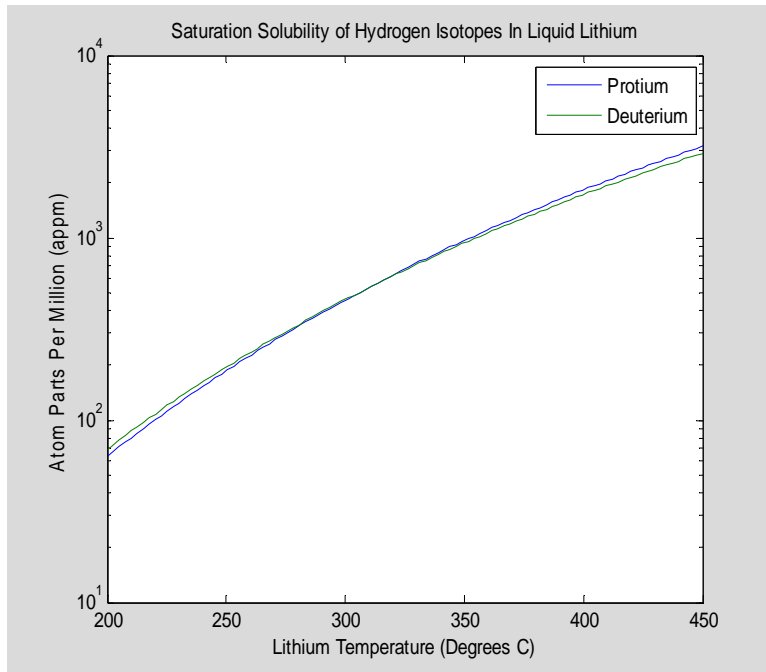
Heat Radiated From Hot First Wall To Water-Cooled Vacuum Vessel

The following graph shows the expected radiated heat rate versus first wall temperature, assuming that the emissivity of the first wall and the vacuum vessel surfaces facing it are each 0.5 and that the vacuum vessel is at 27 C.

```
T=linspace(300,1300);
RadiatedHeat=62*5.670e-8*(T.^4-300^4)*0.5;
plot(T-273,RadiatedHeat/1e6),ylabel('MW'),xlabel('First              Wall
Temperature (Degrees C)')
title('Expected Heat Radiated From NHTX First Wall To Vacuum Vessel')
```

Expected Heat Radiated From NHTX First Wall To Vacuum Vessel
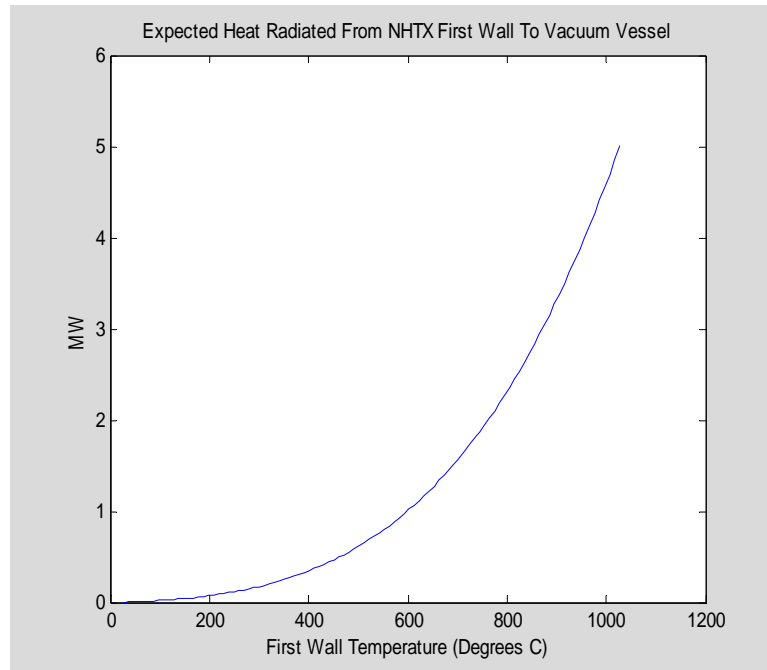
The following MATLAB m-file was developed to solve Saad's equations for 1-D flow of a gas (specifically, helium) in a constant area duct with friction and heat addition. It directly code's Saad's differential and conversion equations in ways compatible with the MATLAB numerical solver for non-stiff ordinary differential equations, ode45.

This m-file also contains code halting the integration of duct equations if and where the calculated gas flow reaches the speed of sound, which is detected as a Mach number of 0.9999 to avoid dividing by zero.   The sonic barrier breaking event is signaled to the user of the m-file by the last entry of the independent variable array, X, being less than the duct length, L, which the user spccified.   For this case, calculate duct profiles would be valid if the duct's length were reduced to match the last entry in the X array instead of L.

In an actual duct with length L, a "choked flow" situation would result in which a back pressure propagating back to the duct's inlet would lower the speed of the gas at the duct's inlet until the sound speed is not reached before the duct's exhaust outlet.   Thus, although any inlet gas speed value can be specified by the user as an input to this m-file, values exceeding the choked flow value resulting in reaching the sound speed at the duct exit are not physiically valid. However, choked flow analyses are not implemented herein.

```
function [mdot,Qdot,Pout,Ppump,T,To,P,V,M,dQdotdx,X]=FirstWallHxode1(D,L,Tw,Tin,Pin,Vin);
% Calculates helium gas duct flow with friction & heat addition via walls.
% Assumes constant duct wall temperature.
% Solves differential equations from Saad's text, COMPRESSIBLE FLUID FLOW.
% M-file inputs are the duct's hydraulic diameter D and length L (meters),
% the uniform wall temperature of the duct Tw, the helium gas temperature
% at the duct's inlet Tin, the helium pressure at the duct's inlet Pin,
% and the speed Vin (m/s).
```

```
% M-file outputs include some functions of position along the duct x,
% including true helium temperature T (Kelvins), helium stagnation temperature
% To, helium pressure P (Pascals), speed V (meters/sec), Mach number M, and the
% cooling profile dQdotdx in watts/meter along the duct length. Each of these
% outputs is a vector of corresponding values for different stations along
% the duct.  The m-file also outputs discrete values for total watts absorbed,
% Qdot, for the outlet pressure Pout, for mass flow rate mdot (kg/sec),
% and for the pumping power Ppump (watts).
% Coded by R. Woolley, June 2007
%
R=GasConstant('He');
cp=SpecificHeat('He',Tin);
kappa=cp/(cp-R);
csin=sqrt(kappa*R*Tin);
M20=(Vin/csin)^2;
rhogas0=Pin/Tin/R;
To0=Tin*(1+(kappa-1)/2*M20);
mdot=pi/4*D^2*rhogas0*Vin;
muTin=Viscosity('He',Tin);
Re0=4/pi*mdot/D/muTin;
y0=[M20 To0]';
options=odeset('Events',@events);
[X,Y,XE,YE,IE]=ode45(@f,[0 L],y0,options);
%-----------------------------------------
function [value,isterminal,direction] = events(x,y);
   isterminal=1;
   direction=0;
   value=y(1)-0.9999;  %detect Mach one
end %end nested function events
%-----------------------------------------
function dydx=f(x,y);
M2=y(1);
To=y(2);
T=To/(1+M2*(kappa-1)/2);
mu=Viscosity('He',T);
Re=4/pi*mdot/D/mu;
sqrt4f=1;
for i=1:10;
sqrt4f=1/abs(2*log10(Re*sqrt4f)-0.8);
end
f=sqrt4f^2/4;
Rgas=1/(4*mdot/D*f/2*cp);
dQdotdx=(Tw-To)/Rgas;
dTodx=2*f*(Tw-To)/D;
dM2dx=M2*dTodx/To*(1+(kappa-1)/2*M2)/(1-M2)*(1+kappa*M2+kappa*M2*2*To/(Tw-To));
dydx=[dM2dx dTodx]'  ;
end  % end nested function f
%------------------------------
M=sqrt(Y(:,1));
To=Y(:,2);
T=To./(1+(kappa-1)/2.*Y(:,1));
V=sqrt(Y(:,1)*kappa*R.*T);
P=sqrt(T./Y(:,1)*M20/Tin)*Pin;
dQdotdx=mdot*cp*fnval(fnder(csapi(X,To)),X);
Qdot=mdot*cp*(To(end)-To(1));
Pout=P(end);
Ppump=mdot*(Pin/rhogas0-T(end)*R);
end
```

MATLAB Notebook cells calculating the data and plots presented in the body of the present document are copied below.

First,, we analyze performance of a set of first wall cooling system designs using helium gas at 20 MPa=200 bar flowing in 6-meter lengths of quarter-inch O.D. tubing.

```
clear all;
D=0.004572;L=6; Tw=873; Pin=2e7;
m=15;n=24;
tin=linspace(273,823,n);
vin=linspace(10,150,m);
[Tin,Vin]=meshgrid(tin,vin);
Mdot=Vin;Qdot=Mdot;Pout=Mdot;
for i=1:m;
for j=1:n;
TIN=Tin(i,j);
VIN=Vin(i,j);
[mdot,qdot,pout,Ppump,T,To,P,V,M,dQdotdx,X]=FirstWallHxode1(D,L,Tw,TIN,
Pin,VIN);
if(X(end)==L)
Mdot(i,j)=mdot;
Qdot(i,j)=qdot;
Pout(i,j)=pout;
else
Mdot(i,j)=NaN;
Qdot(i,j)=NaN;
Pout(i,j)=NaN;
end
end
end
Ntubes=5e7*ones(size(Qdot))./Qdot;
LNtubes=L*Ntubes;
Coverage=0.00635*LNtubes;;
Mdottotal=Mdot.*Ntubes;
RHe=GasConstant('He');
PumpPower=-RHe*Tin.*log(Pout/Pin).*Mdottotal;


[C1,h1]=contour(Tin-273,Vin,Coverage,[10 15 20 30 40 50 70 100 140 200
300],'-k');
clabel(C1,h1);
ylim([0 150])
xlim([0 600])
hold on
[C2,h2]=contour(Tin-273,Vin,PumpPower*1e-6,[1 2 3 4 5 6 8 10 12],'-
.r');
clabel(C2,h2,'Color','r');
xlabel('Helium Inlet Temperature (\circ C)');ylabel('Helium Inlet Speed
(m/s)')
hold off
legend('Coverage (m^ ^2)','PumpPower (MW)','Location','South')
title({'Performance Of 50 MW Helium First Wall Cooling Systems','Using
6-meter Lengths of ¼ Inch OD Tubing'})
```

Performance Of 50 MW Helium First Wall Cooling Systems
Using 6-meter Lengths of ¼ Inch OD Tubing

Next, we analyze performance of a set of designs using 200 bar helium flowing into 2-meter lengths of quarter-inch O.D. tubing.

```
clear all;
D=0.004572;L=2; Tw=873; Pin=2e7;
m=15;n=24;
tin=linspace(273,823,n);
vin=linspace(10,150,m);
[Tin,Vin]=meshgrid(tin,vin);
Mdot=Vin;Qdot=Mdot;Pout=Mdot;
for i=1:m;
for j=1:n;
TIN=Tin(i,j);
VIN=Vin(i,j);
[mdot,qdot,pout,Ppump,T,To,P,V,M,dQdotdx,X]=FirstWallHxode1(D,L,Tw,TIN,
Pin,VIN);
if(X(end)==L);
Mdot(i,j)=mdot;
Qdot(i,j)=qdot;
Pout(i,j)=pout;
else
Mdot(i,j)=NaN;
Qdot(i,j)=NaN;
Pout(i,j)=NaN;
end
end
end
Ntubes=5e7*ones(size(Qdot))./Qdot;
LNtubes=L*Ntubes;
Coverage=0.00635*LNtubes;;
Mdottotal=Mdot.*Ntubes;
```

```
RHe=GasConstant('He');
PumpPower=-RHe*Tin.*log(Pout/Pin).*Mdottotal;

[C1,h1]=contour(Tin-273,Vin,Coverage,[10 15 20 30 40 50 70 100 140 200
300],'-k');
clabel(C1,h1);
ylim([0 150])
xlim([0 600])
hold on
[C2,h2]=contour(Tin-273,Vin,PumpPower*1e-6,[1 2 3 4 5 6 8 10 12],'-
.r');
clabel(C2,h2,'Color','r');
xlabel('Helium Inlet Temperature (\circ C)');ylabel('Helium Inlet Speed
(m/s)')
hold off
legend('Coverage (m^ ^2)','PumpPower (MW)','Location','South')
title({'Performance Of 50 MW Helium First Wall Cooling Systems','Using
2-meter Lengths of ¼ Inch OD Tubing'})
```


Performance Of 50 MW Helium First Wall Cooling Systems
Using 2-meter Lengths of ¼ Inch OD Tubing

Next, the profiles are plotted for the 6 meter quarter-inch O.D. tubing duct example with 200 bar He at 100C and 100 m/s at the duct's inlet.

```
clear,clf;
D=0.004572;L=6; Tw=873;Tin=373; Pin=2e7; Vin=100;
[mdot,Qdot,Pout,Ppump,T,To,P,V,M,dQdotdx,X]=FirstWallHxode1(D,L,Tw,Tin,
Pin,Vin);
mdot
Qdot
Pout
Ppump
RHe=GasConstant('He')
PumpPower=Tin*RHe*log(Pin/Pout)*mdot
```

```
T(end)
To(end)
V(end)
M(end)
clf;subplot(3,1,1);plot(X,M),ylabel('MachNumber'),title({'Duct Flow
With Friction And Heat Addition','Inlet Helium 200 bar 100\circC 100
m/s, Duct Diameter 4.572 mm'})
subplot(3,1,2);plot(X,To-273),ylabel({'TotalTemperature','To
(\circC)'}); ylim([0 700])
subplot(3,1,3);plot(X,dQdotdx/1e3),ylabel({'CoolingRate','kW/m'})
xlabel('Distance From Duct Entrance (m)')
```

```
mdot =
    0.0424
Qdot =
  1.0983e+005
Pout =
  1.2742e+007
Ppump =
 -4.2900e+004
RHe =
  2.0771e+003
PumpPower =
  1.4803e+004
ans =
  860.3425
ans =
  872.9623
ans =
  362.0394
ans =
    0.2098
```
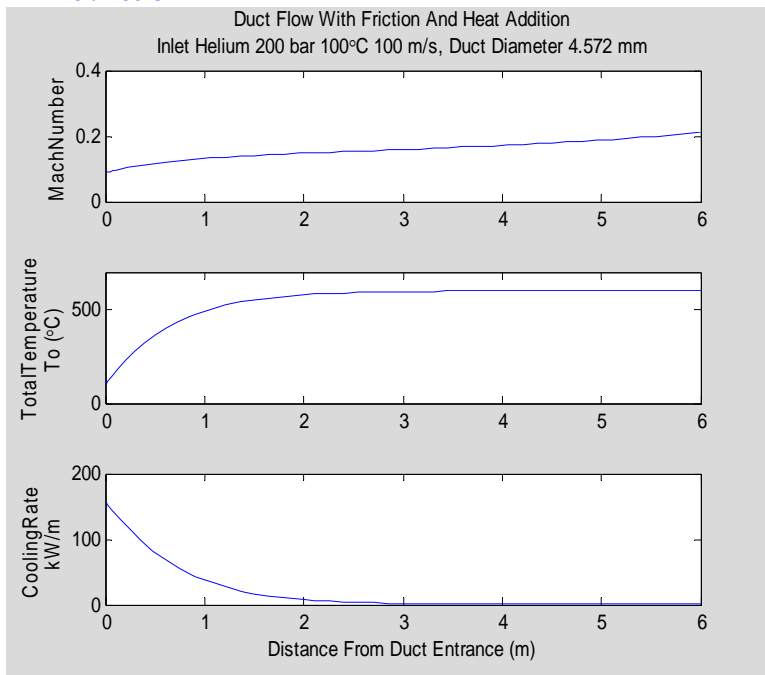
Water flows at 10 m/s speed in ¾ inch od tubes which have an id of 15.75 mm.   Thus, the total volumetric flow per tube is 1.948e-3 m³/s o= 1.943 liters/s which is about 1.943 kg/s.

Total power in each TF central bundle turn would be 2.96 MW.if the turn were 7 meters long and carrying its full current of 500 kA.   Since the specific heat of water is about 4,186 J/kg-Kelvin, if a single tube were to absorb this power the water temperature rise would be 2.96E6/1.943/4186=363.9 C, which is clearly too large. Using six tubes together would reduce this projected average water temperature rise to 363.9/6=60.7 C. The actual water temperature rise will be somewhat less and may be closer to 50 C since the TF turn does not conduct current for its full 7 meter length. The effective reduction in length is because the TF joints remove current from the central before it reaches the bottom and top.

The heat transfer coefficient between the TF Central Bundle turn's copper tubes and the flowing water inside them is estimated from the Dittus-Boelter correlation:

$$Nu = 0.023\,\mathrm{Re}^{0.8}\,\mathrm{Pr}^{0.4}$$

where Nu is the Nusselt number, Re is the Reynolds number and Pr is the Prandtl number. The Reynolds number is given by:

$$\mathrm{Re} = \frac{\rho VD}{\mu}$$

where ρ and μ represent water's temperature-dependent density and viscosity while V is the water speed and D is the water tube's inner diameter. Using 10 m/s as the water speed and 0.01575 m the id of each water tube, the Reynolds number varies with water temperature as plotted in the following figure. The variation is mostly due to the reduction in water's viscosity as its temperature is increased.

```
D=0.01575;
V=10;
T=linspace(273.15,473.15);
[PsatW,DensityW,CpW,ViscosityW,lambdaW,hfW,PrW]=LW_Properties(T);
Re=D*V*DensityW./ViscosityW;
plot(T-273.15,Re);
xlabel('Temperature (degrees C)')
ylabel('Reynolds Number')
title('Reynolds Number Vs Temperature for 10m/s Water in ¾" od Tube')
```

Reynolds Number Vs Temperature for 10m/s Water in ¾" od Tube
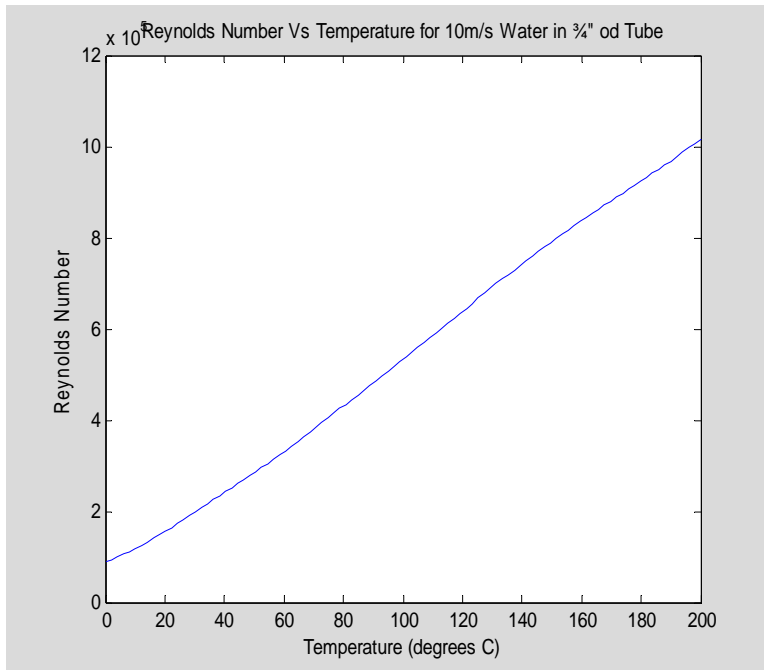
The Prandtl number is the product of viscosity and specific heat divided by thermal conductivity. For water it varies with temperature as follows:

```
PrW=ViscosityW.*CpW./lambdaW;
plot(T-273,PrW)
title('Prandtl Number Vs Temperature Water')
xlabel('Temperature (degrees C)')
ylabel('Prandtl Number')
```


Prandtl Number Vs Temperature Water
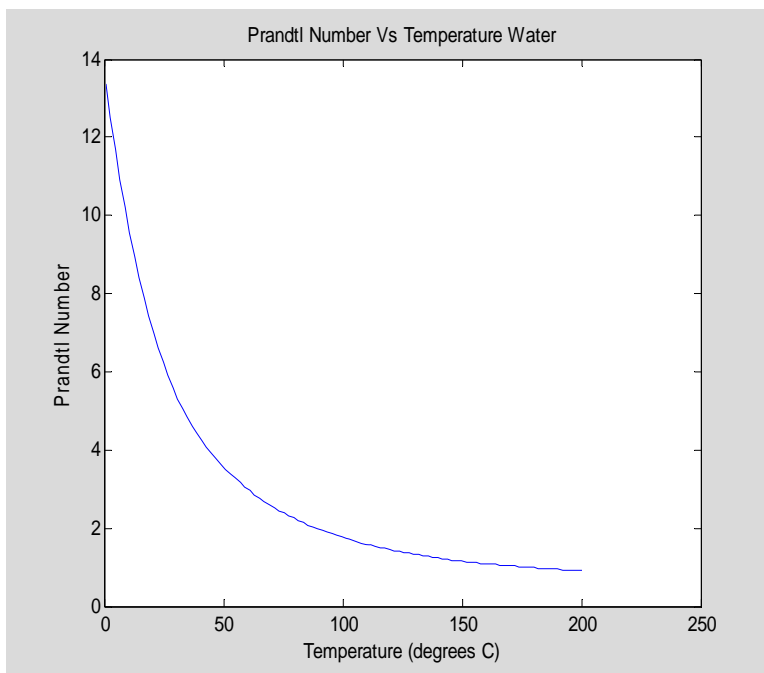
Combining these results, the Dittus-Boelter correlation asserts that for this flow situation the Nusselt number varies with temperature as follows:

```
Nu=0.023*Re.^0.8.*PrW.^0.4;
plot(T-273,Nu)
ylim([0 1500])
ylabel('Nusselt Number')
title('Nusselt Number Vs. Temperature for Water flow in ¾" od Tube')
xlabel('Temperature (degrees C)')
```
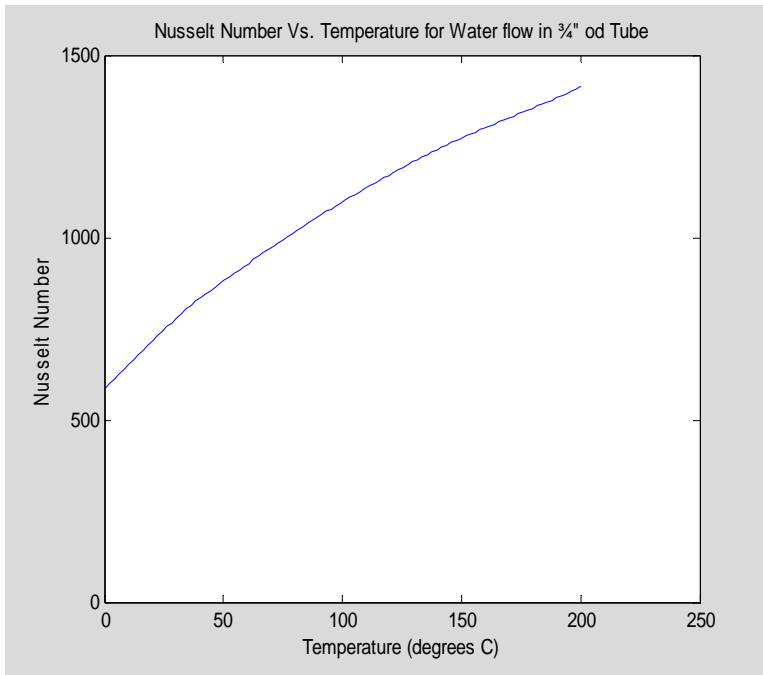

The heat transfer coefficient is defined in terms of the Nusselt number as follows:

$$h = \frac{k_w}{D} Nu$$

where kw is the thermal conductivity of water, another temperature dependent quantity. Using water properties and the previous results, the heat transfer coefficient for this situation is found to vary with water temperature as follows:

```
h=lambdaW.*Nu/D;
plot(T-273,h);
ylabel('W m^-^2 Kelvin^-1')
title('      Film Drop Heat Transfer Coefficient for 10 m/s Water
in ¾" od Tube')
xlabel('Temperature (degrees C)')
 xlim([0 200])
ylim([0 60000])
```

Film Drop Heat Transfer Coefficient for 10 m/s Water in ¾" od Tube
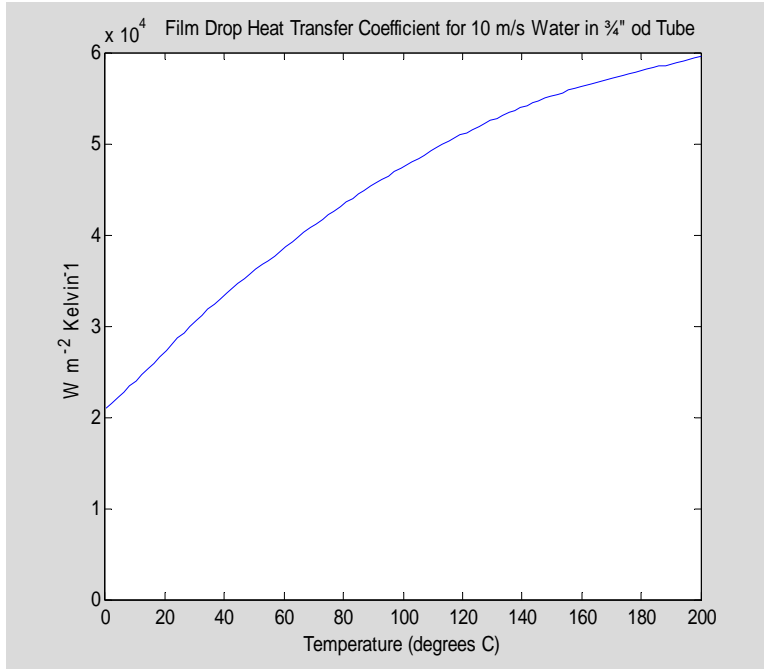
Approximating the average heat transfer coefficient as about 30,000 W/m^2-Kelvin, approximately its value for 40 degree C water which is the average water temperature if the inlet temperature is 10C, we note that the internal area of one tube is $(7)(.01575)\pi$=0.3464 m^2 , so six tubes would have a combined surface area of $(6)(0.3464$ m$^2)$=2.078 m^2 . Then the film temperature drop with 2.96 MW of heat per turn is:

DT=(2.96E6 W/turn)/((30000 W/m^2-Kelvin)(2.078 m^2/turn))=47.5 degrees C.

The following plots summarize results from a FEM analysis in MATLAB of 2D heat conduction and transfer in the initially assumed coolign hole configuration.

Temperature Rise Above Local Water Temperature

Temperature Rise Above Local Water Temperature(degrees C)
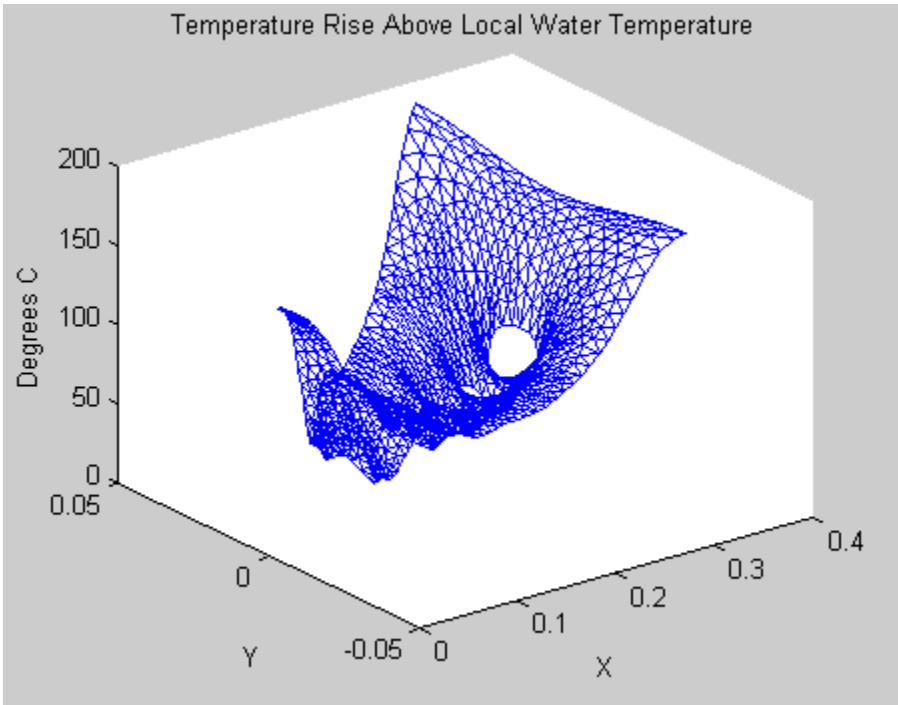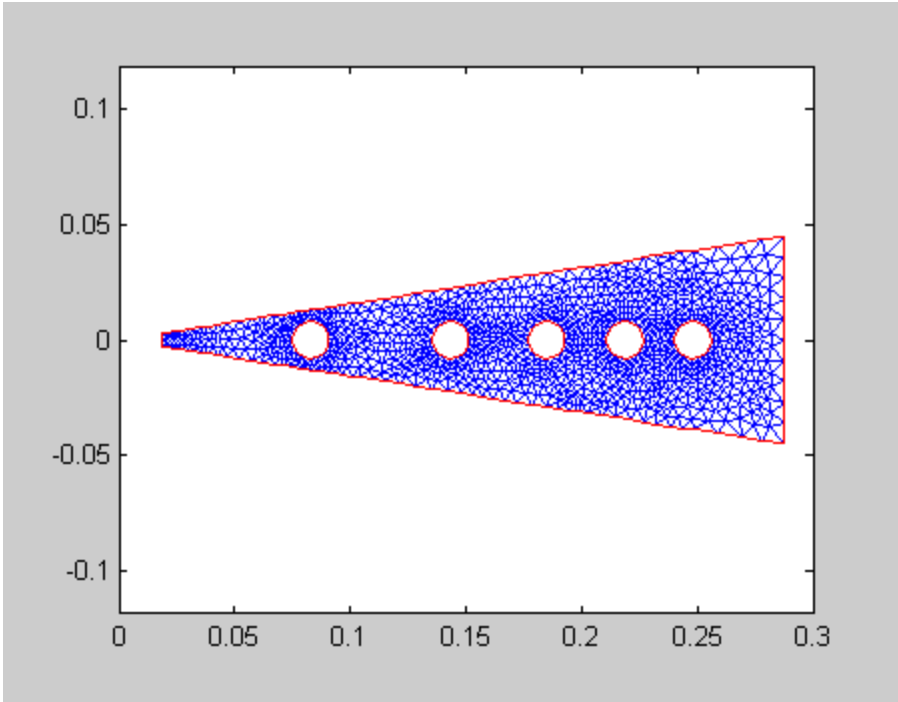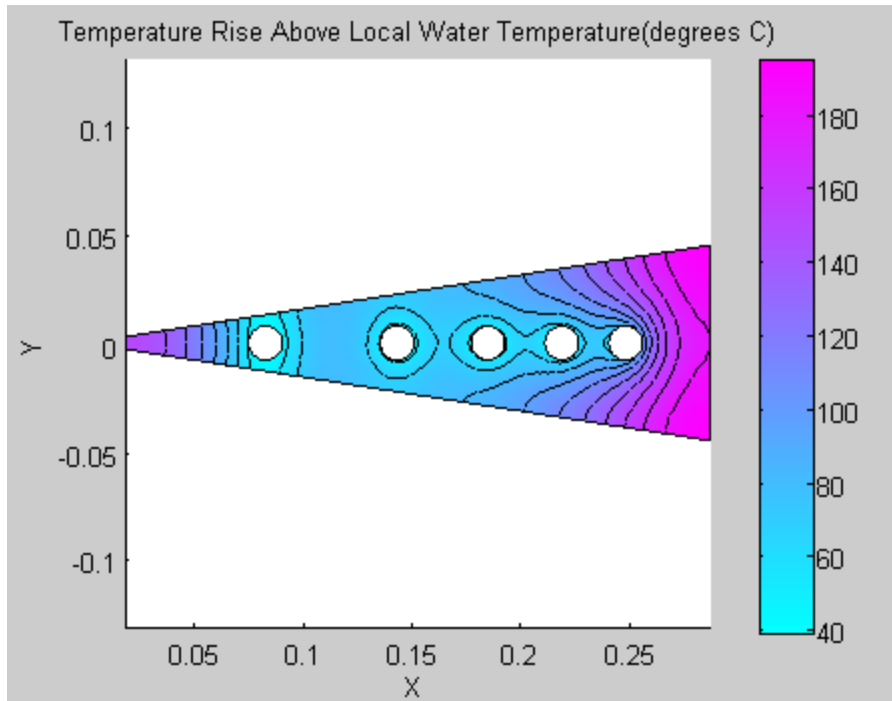
Clearly, this design is inadequate and must be changed.

As a tentative configuration to replace it, we consider 15 tubes of 0.50" outer diameter. Note that for standard Type K annealed copper tubing, this od is referred to as 3/8 inch tubing although its od is actually 0.5 inches. More importantly for this analysis, its inner diameter (id) is 0.402 inches which equivalently is 10.21 mm or 0.01021 meters. At 10 m/s with this id, each tube carries a volumetric flow of 0.81873 liters/s, so 15 such tubes carry a combined flow of 12.28 liters/s, which is enough to limit the bulk temperature rise to 57.6 degrees C while absorbing 2.96 MW of heat.

The od of this tubing is 12.7 mm.

Circle centers for the tubes within xsect of turn aligned with the X axis are as follows:

X	Y
54	0
90	0
115	0
135	0
153	0
170	±14
200	±16
225	±18
245	±20
265	±22

With this tubing the heat transfer coefficient is different. We recalculate it for this smaller tubing.

```
------------
D=0.01021;
V=10;
T=linspace(273.15,473.15);
[PsatW,DensityW,CpW,ViscosityW,lambdaW,hfW,PrW]=LW_Properties(T);
Re=D*V*DensityW./ViscosityW;
plot(T-273.15,Re);
xlabel('Temperature (degrees C)')
ylabel('Reynolds Number')
title('          Reynolds Number Vs Temperature for 10m/s Water in 1/2"
od Tube')
```
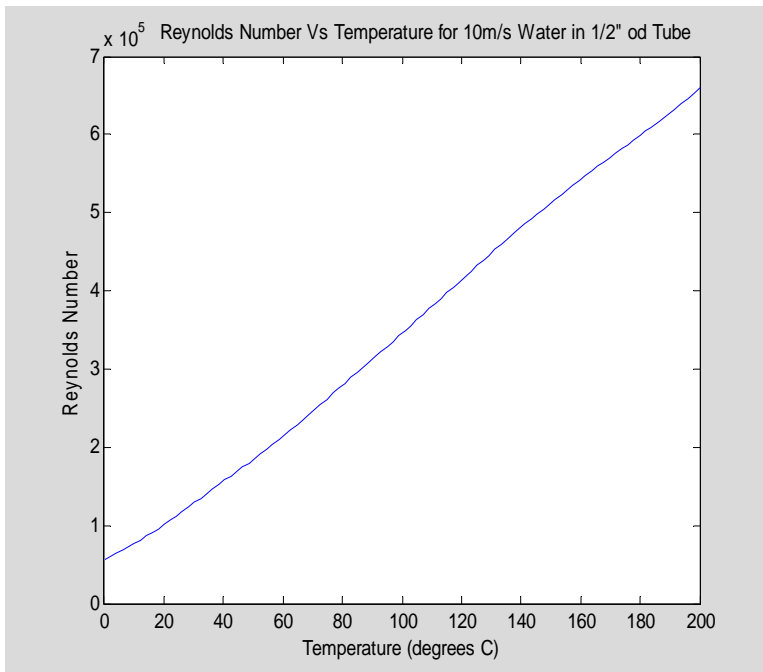

The Prandtl number vs temperature does not change from before.
Combining them, the Dittus-Boelter correlation asserts that for this flow situation the Nusselt number varies with temperature as follows:

```
Nu=0.023*Re.^0.8.*PrW.^0.4;
plot(T-273.15,Nu)
ylim([0 1500])
xlim([0 200])
ylabel('Nusselt Number')
title('Nusselt Number Vs. Temperature for Water flow in ½" od Tube')
xlabel('Temperature (degrees C)')
```

Nusselt Number Vs. Temperature for Water flow in ½" od Tube

Using water properties and the previous results, the heat transfer coefficient for this situation is found to vary with water temperature as follows:

```
h=lambdaW.*Nu/D;
plot(T-273,h);
ylabel('W m^-^2 Kelvin^-1')
title('          Film Drop Heat Transfer Coefficient for 10 m/s Water
in ½" od Tube')
xlabel('Temperature (degrees C)')
 xlim([0 200])
ylim([0 80000])
```

Film Drop Heat Transfer Coefficient for 10 m/s Water in ½" od Tube

The heat transfer coefficient has increased slightly due to the reduction in tube diameter. If we again use 40 degree C water as typical then we select 33,000 as an approximate value for the heat transfer coefficieint, h. The total heat transfer surface area is $(15)(7)(0.01021)\pi$=3.368 m^2, so the expected average temperature drop is (2.96E6 W)/(3.368 m^2)/(33,000 W/me/Kelvins) = 26.6 degrees C.

Using MATLAB's PDE toolbox, the temperature rise across a turn cross section was calculated with various tube arrangements. The best arrangement found appears below, along with the calculated temperature rise profile which includes both the film drop and the copper gradient drop.

Temperature Rise Above Local Water Temperature (degrees C)

jpg format:

Temperature Rise Above Local Water Temperature (degrees C)
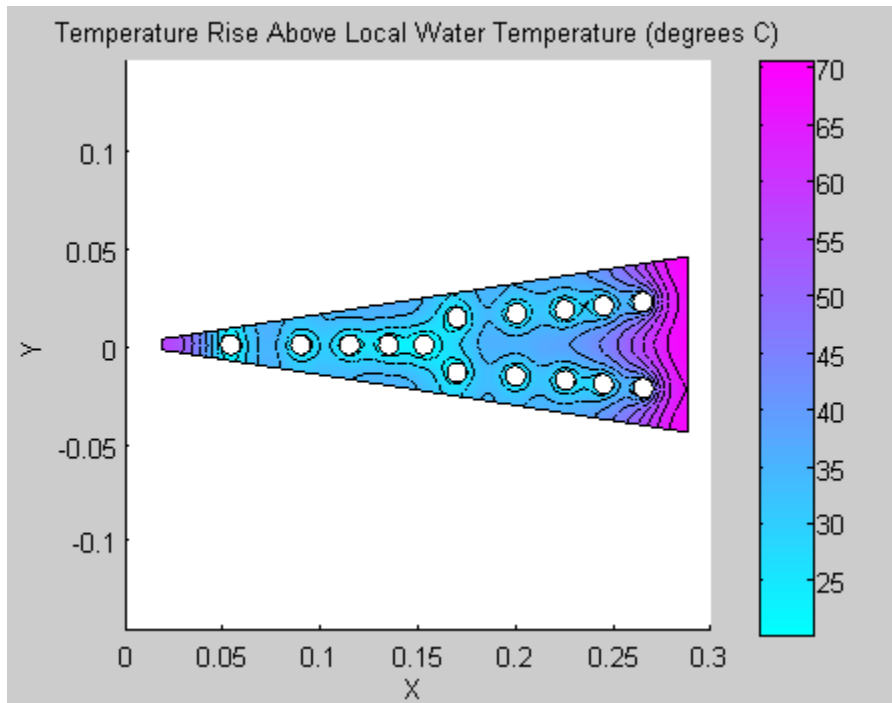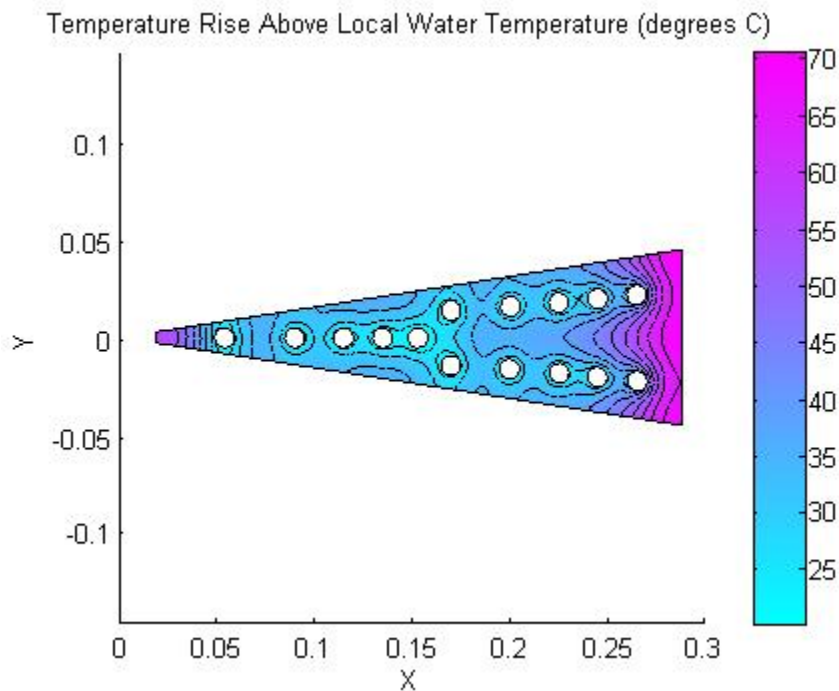
Peak copper temperature is about 70C above the temperature of the adjacent water. The hottest adjacent water occurs at the cooling water's exit point where it will be about 60C hotter than at the cooling water's inlet point. Assuming the inlet water temperature is 10C, the hottest copper is then 10C+60C+70C=140C.

We also see from the plot that although the peak copper temperature is 70C above the local water temperature, most of the copper cross section is much cooler, close to 30 or 35 degrees elevated above the local water temperature. Since the average bulk water temperature rise in the TF central bundle will be about 30 C, that implies the bulk average copper temperature will be near 10C+35C+35C=80C.

<u>TF Central Bundle Cooling Water Pressure Drop Calculation</u>
The pressure drop in the TF Central Bundle tubes is estimated via the Darcy-Weisbach head-loss formula:

$$\Delta p = f(\text{Re}, \varepsilon) \frac{L}{D} \frac{\rho V^2}{2}$$

where D, ρ, and V are as defined previously, L is the length of a tube, and f is a dimensionless friction factor which has been empirically studied and found to depend on Re, the Reynolds number of the flow and on ε, tubing's per unit surface roughness, in a manner summarized by Moody's well-known diagram. For turbulent flow (i.e., for Re>>3000) in smooth pipes (i.e., for ε=0), Moody's diagram may be approximated by VonKarmen's equation:

$$\frac{1}{\sqrt{f}} = 2\log_{10}\left(\text{Re}\sqrt{f}\right) - 0.8$$

Iteration is used to numerically solve for f given a particular value of Re.

The pressure drop calculation done here approximates the water temperature as a constant value along the tube (whereas actually the water temperature varies continuously along the tube's length). The result is as follows:

```
L=7;
f=ones(size(Re));
for i=1:20;f=1./((2*log10(Re.*sqrt(f))-0.8).^2) ;end
DeltaP=f*L/D.*DensityW*V^2/2;
plot(T-273.15,DeltaP/1e5)
ylim([0 7])
ylabel('Bar')
xlabel('Water Temperature (Degrees C)')
title('         TF Central Bundle Water Pressure Drop @ 10 m/s &
Constant Temperature')
```

TF Central Bundle Water Pressure Drop @ 10 m/s & Constant Temperature

This plot shows for 10 m/s water speed vs. the assumed constant water temperaure, the calculated pressure drop using Bar units, where 1 bar=10^5 Pascals is slightly less than one standard atmosphere.   Of course, the actual water temperature will not be a constant but instead will vary along the length of a coolant tube, so this plot is only approximate and requires interpretation. However, with inlet temperature 10 C and outlet temperatue 70 C, the true pressure drop will be between 5.0 bar and 6.5 bar, the plotted values corresponding to constant water temperatures of 10 C and 70 C respectively. A reasonable estimate of the true pressure drop may be the plot's prediction for the 40 C average temperature of entrained water, i.e about 5.6 bar (which is equivalent to about 81 psi).

TF Central Bundle Cooling Water Flow

As stated earlier, with 15 tubes per turn the cooling water flow per turn is 12.28 liters per second.   Thus the total water flow for all 20 turns of the TF Central Bundle is

   (20)(12.28 liters/sec)=245.6 liters/second = 0.2456 m^3/s.

In the US Customary units frequently used for water flow, this is 3,892.8 gpm.

Pumping Power
Mechanical power transferred to the water by a pump is the product of pressure drop times flow, i.e.,
(560000 Pa)(0.2456 m^3/s)=137.5 kW.

Electrical power for the pump is this mechanical power value divided by the net combined motor and pump efficiency, which together will be in the vicinity of 90%.

Thus, electrical power for pumping the cooling water through the TF Central Bundle will be about 150 kw.

Several schemes for constructing steady-state water-cooled electromagnet coils rely on edge-cooling, so the electro-thermal-hydraulic characteristics of edge-cooled conductors is the subject of this analysis. Edge-cooling is frequently inferior thermally to the use of extruded hollow conductors wound with short flowpath lengths, but is preferred nonetheless because of its simpler construction. For this reason it will be used in portions of the NHTX TF system and may be used in outer PF coils. There are also cases where its ability to use flowpaths with lengths less than one turn makes it superior thermally.

Figure 1 shows schematically the general geometry of an edge-cooled current-carrying conductor as analyzed herein, along with geometric variables used in the analysis. The conductor bar's height is denoted by h and its width is denoted by w. Locations along its height are denoted by the variable y which is zero at the bar's center. Locations along its width are denoted by the variable, x. Locations along the bar's length are denoted by the variable, z. A current of I amperes flows in the bar in the z direction. The blue regions shown in Figure 1 located above and below the bar represent cooling water flowing along the bar's edge, absorbing heat from the bar as it flows.

Figure 1: Geometry Of EdgeCooled Conductor
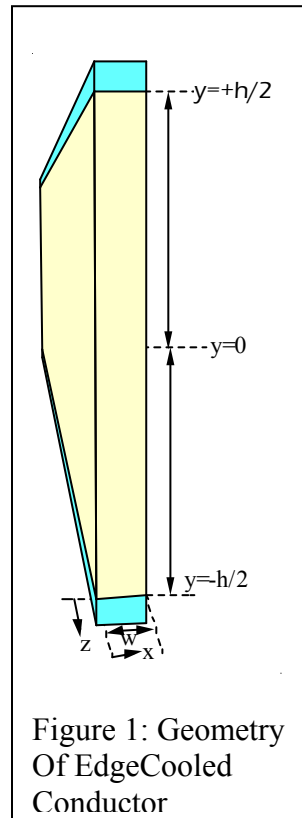
We note that the analyzed edge-cooled bar does not have any internal cooling passages. Such a conductor can be any bar stock available; it does not need to be a special extrusion. We note also that although Figure 1 shows a bar which is perfectly straight in the direction of current flow (i.e., the z direction), the analysis to follow does not depend on the straightness of the bar. Thus, an edge-cooled coil can be formed by bending the conductor into the form of a spiral to form a pancake which has both top and bottom edges accessible for edge cooling. To minimize the plastic flow of the metallic conductor sometimes called "keystoning", bars are typically bent in their narrower width direction rather than in their greater height direction.

In the present steady-state analysis, heat produced within the electrical conductor flows by thermal conduction to the water located at the conductor's top or bottom. Since there is no heat sink on the conductor's sides, there is no heat flow in the x direction. Although in reality there will be some small thermal gradient in the z direction, the resulting heat flow in the z direction is ignored in this analysis. Heat is modeled as entirely flowing in the y direction. As a result, the heat conduction problem becomes one dimensional, described by an ordinary differential equation with the single independent variable, y.

With possibly a large conductor temperature variation as a function of y at a particular z section, the electrical resistivity may be quite nonuniform across that section. The present analysis calculates how the current restributes itself as a function of this

resistance nonuniformaty. To do this, the assumption is made that across any cross-section there is a single electrical field value in the z direction, although that value is permitted to vary as a function of z.

Although the methodology could apply to any metallic conductor, for this analysis we assume the metal is OFHC copper. For copper, two nonlinear functions of temperature have been coded into MATLAB m-file subroutines, i.e., copper's thermal conductivity $K(T)$ and copper's electrical resistivity $\eta(T)$. They are plotted in Figures 2 and 3 below.

```
T=linspace(273,273+150);
RRR=100;
[eta,K]=Cu_Properties(T,RRR);
plot(T-273,K)
xlabel('Temperature (C)')
ylabel('Thermal Conductivity (W m^-^1 Kelvin^-^1)')
title('Thermal Conductivity of OFHC Copper with RRR=100 Vs.
Temperature')
ylim([0 405])
```
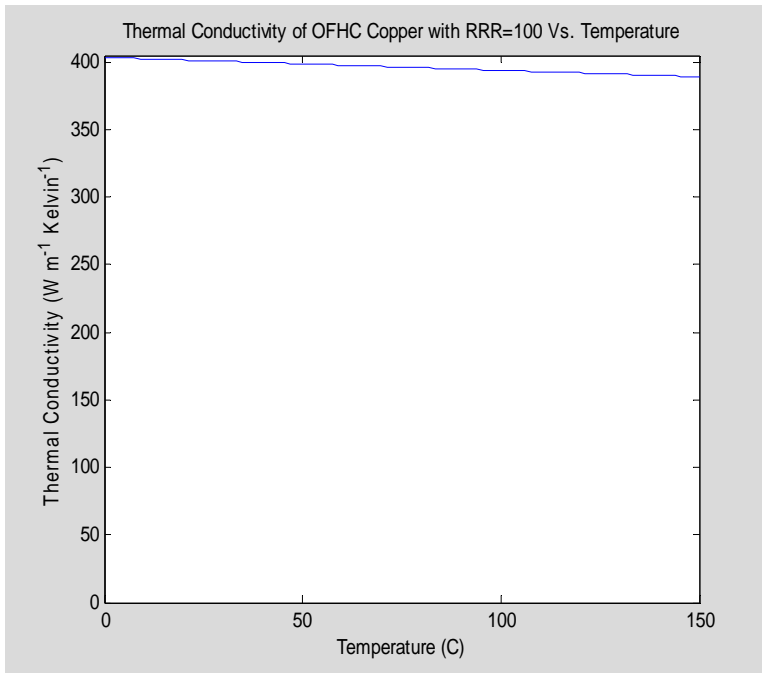

Figure 2: Thermal Conductivity Vs Temperature Of OFHC Copper With RRR=100

```
plot(T-273,eta*1e9)
xlabel('Temperature (C)')
ylabel('Nano-Ohm-meters')
title('Electrical Resistivity of OFHC Copper with RRR=100 Vs.
Temperature')
ylim([0 26])
```
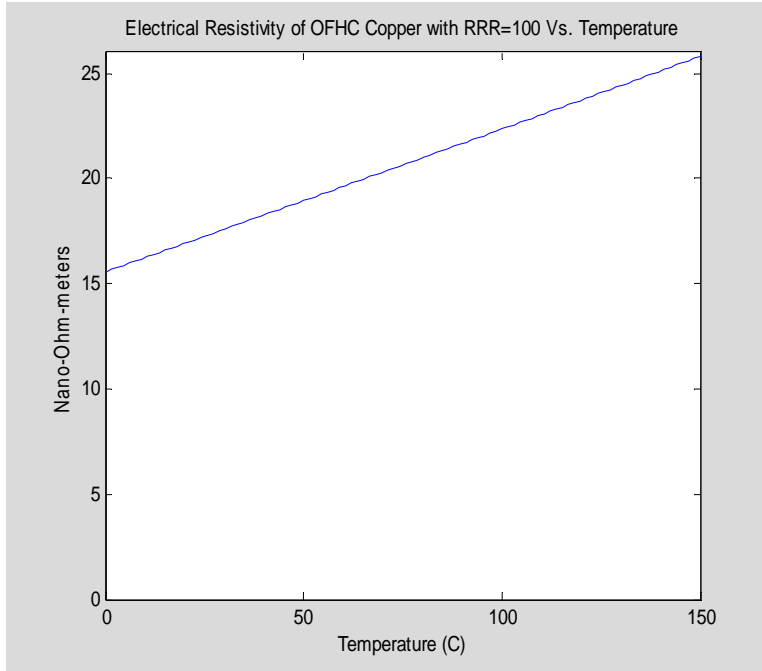
Figure 3: Electrical Resistivity Vs Temperature of OHFC Copper With RRR=100

The following differential and integral equation define the problem for any particular section, z. Heat conduction in the y direction is related to the thermal gradient as follows:

$$q(y) = -K(T(y))\frac{dT(y)}{dy}$$

$$q(0) = 0 \tag{1}$$

where zero heat flow through the center of the bar follows from symmetry.
The spatial rate of change of heat flow is the local electrrical heating, i.e.:

$$\frac{dq(y)}{dy} = \eta(T(y))(J(y))^2 \tag{2}$$

where J(y) is the local value of the nonuniform electrical current density, given by

$$J(y) = \frac{E}{\eta(T(y))} \tag{3}$$

The total current, I, obeys

$$I = w \int_{y=-h/2}^{y=+h/2} J(y) dy \tag{4}$$

so therefore it follows that the electrical field at any section is given by:

$$E = \frac{I}{w \int_{y=-h/2}^{y=+h/2} \frac{dy}{\eta(T(y))}} \tag{5}$$

Putting these equations together we arrive at the following single integrodifferential equation:

$$\frac{d}{dy}\left(K(T(y))\frac{dT(y)}{dy}\right) = -\left(\frac{I}{w}\right)^2 \frac{1}{\eta(T(y))\left(\int\limits_{y=-h/2}^{y=+h/2}\frac{dy}{\eta(T(y))}\right)^2}$$

$$(6)$$

with the two boundary conditions that

$$\frac{dT(y)}{dy}\bigg|_{y=0} = 0$$

$$T\left(y = \frac{h}{2}\right) = T_{edge}$$

$$(7a,7b)$$

We note that because of symmetry, T(y)=T(-y) so it is not necessary to numerically solve for the temperatures in the lower half of the conductor bar and the integral can also be taken over a nonnegative domain. Equation (6) is then replaced by the following:

$$\frac{d}{dy}\left(K(T(y))\frac{dT(y)}{dy}\right) = -\left(\frac{I}{w}\right)^2 \frac{1}{\eta(T(y))\left(2\int\limits_{y=0}^{y=+h/2}\frac{dy}{\eta(T(y))}\right)^2}$$

$$(7)$$

This system is numerically solved in the MATLAB algorithm below which uses Jacobi functional iteration. The solution scheme is as follows:

(1) Accept input values of h, I/w, Tedge.
(2) Set up grid of y values from 0 to h/2.
(3) Initialize vector of temperature values on that grid, setting all temperatures on the grid to T(y)=Tedge.
(4) Using grid temperatures and Cu properties, calculate grid of K(y)=K(T(y)) and η(y)=η(T(y)) values.
(5) Calculate the following function:

$$q(y) = \left(\frac{I}{2w\int\limits_{y=0}^{y=h/2}\frac{dy}{\eta(y)}}\right)^2 \int\limits_{y=0}^{y}\frac{dy}{\eta(y)}$$

$$(8)$$

(6) Calculate a new set of grid temperatures:

$$T^{(NEW)}(y) = \int\limits_{y=0}^{y=h/2}\frac{q(y)dy}{K(y)} - \int\limits_{y=0}^{y}\frac{q(y)dy}{K(y)} + T_{edge}$$

$$(9)$$

(7) Decide whether solution has converged by examining the change from the previous iteration.

$$\Delta = \left\|T^{(NEW)}(y) - T(y)\right\|$$

If Δ>threshold then set $T(y) \leftarrow T^{(NEW)}(y)$ and go back to step 4; otherwise exit.

This is implemented in the following MATLAB cell:

```
h=0.1; I=3e4; w=0.01; Tedge=20+273;
y=linspace(0,h/2)';T=Tedge*ones(size(y));
for i=1:100;
[eta,K]=Cu_Properties(T,100);sigma=1./eta;
q=cumtrapz(y,sigma)*(I/2/w/trapz(y,sigma))^2;
TNEW=Tedge+trapz(y,q./K)-cumtrapz(y,q./K);
D=max(abs(TNEW-T))
if D<1e-6;
break
else
T=TNEW;
end
end
i
plot(y,TNEW-273)
title('A Temperature Profile In A 1 cm X 10 cm Edge-Cooled Cu Conductor
At 30 kA')
xlabel('Vertical Location y Above Middle (m)')
ylabel('Temperature ©')


D =
   47.4064
D =
    4.5969
D =
    0.4747
D =
    0.0481
D =
    0.0049
D =
  4.9535e-004
D =
  5.0281e-005
D =
  5.1037e-006
D =
  5.1805e-007
i =
     9
```
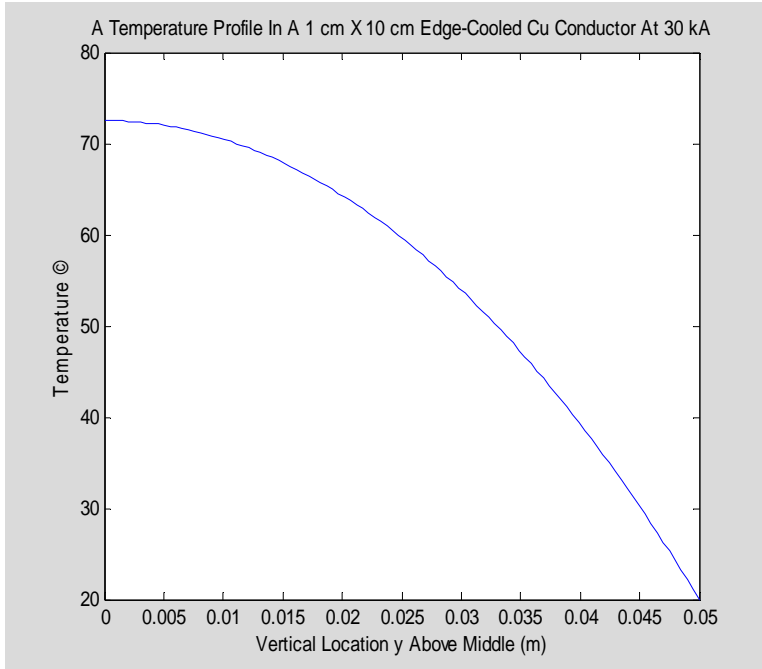
Figure 4: Conductor Temperature Vs Vertical Position In Top Half Of 10 cm Tall 1 cm Wide Copper Conductor Carrying 30 kA, With Edge Temperature 20 C.

We then commit this algorithm to an m-file form as follows:

```
function [Tmax,T]=EdgeCooledCopper(I,w,h,Tedge);
% Solves 1D electrical heating of edgecooled bar with current redistribution.
y=linspace(0,h/2)';T=Tedge*ones(size(y));
for i=1:100;
[eta,K]=Cu_Properties(T,100);sigma=1./eta;
q=cumtrapz(y,sigma)*(I/2/w/trapz(y,sigma))^2;
TNEW=Tedge+trapz(y,q./K)-cumtrapz(y,q./K);
D=max(abs(TNEW-T))
if D<1e-6;
break
else
T=TNEW;
end
end
Tmax=T(1)
```

Next, we use this m-file to investigate how the cross-copper temperature rise varies as a function of the bar height, h, keeping other inputs constant.

```
h=.01:.01:1;
Tedge=20+273;
w=0.01;
I=30000.;
Tmax=zeros(100,1);
for i=1:100;
[Tmax,T]=EdgeCooledCopper(I,w,h(i),Tedge);
end
plot(h,Tmax-273)
```

```
title('Peak Copper Temperature Vs Height Of 1 cm Wide Cu Bar Carrying
30 kA With Edges 20 C')
xlabel('Conductor Bar Height (m)')
ylabel('Peak Temperature ©')
```
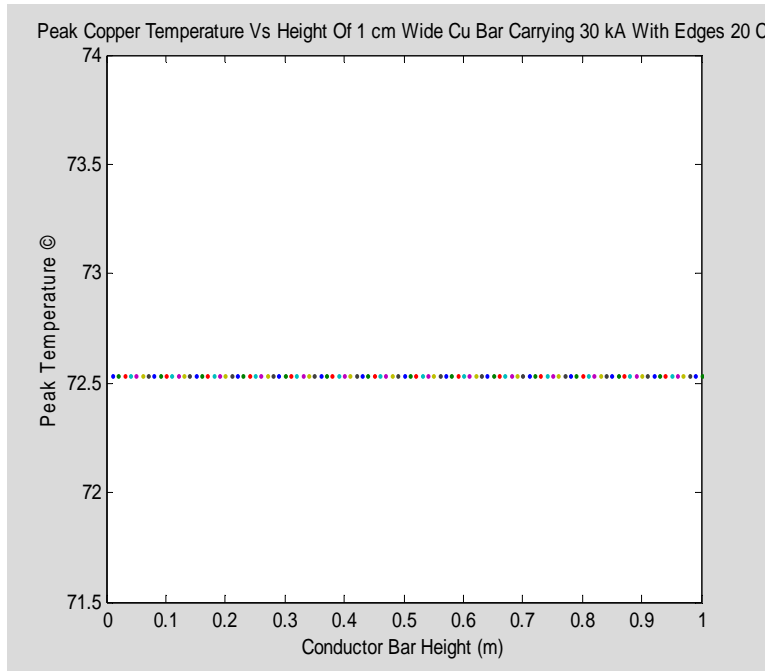

Figure 5: Example Showing <u>Insensitivity</u> To Conductor Bar Height

Figure 5 illustrates that the peak copper temperature does not depend on h, the height of the conductor. In this example, the same peak copper temperature of 72.53 C results regardless whether the bar carrying 30 kA is 1 meter tall, 1 cm tall, or any height between, provided it carries 30 kA, is 1 cm wide, and its top and bottom edges are maintained at 20 C temperature.

Equation (7) shows that the parameters I and w do not enter the problem as completely independent quantities. Instead, only their ratio, I/w, affects copper temperatures. For the example of Figure 5 this ratio is 30 kA/cm=3 MA/m, so with top and bottom edges held at 20 C the same peak temperature would result in 2 cm wide bars carrying 60 kA or 20 cm wide bars carrying 600 kA.

Peak copper temperature with edge cooling thus depends on only two quantities, the edge temperature Tedge, and the current per unit width, I/w. This dependence is shown by the following plots.

```
Tedge=linspace(0,100,25)+273;
Currentperwidth=linspace(0,4e6,20);
[TEDGE,CURRENTPERWIDTH]=meshgrid(Tedge,Currentperwidth);
TMAX=zeros(size(TEDGE));
for j=1:length(Tedge);
for i=1:length(Currentperwidth);
```

```
TMAX(i,j)=EdgeCooledCopper(Currentperwidth(i),1.0,1.0,Tedge(j));
end
end
surf(TEDGE-273,CURRENTPERWIDTH/1e6,TMAX-273);
xlabel('Edge Temperature ( C)')
ylabel('Current Per Width (MA/m)')
zlabel('Peak Temperature ( C)')
title('Peak Cu Temperature Vs Edge Temperature And Current Per Width')
```
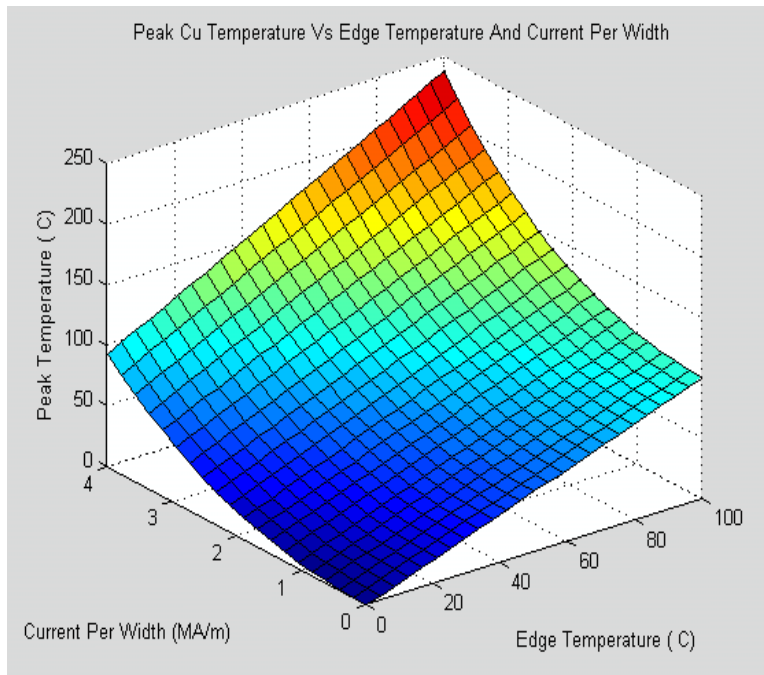

Figure 6: Surface Plot Of Peak Cu Temperaturee In Edge Cooling

```
[C,H]=contour(TEDGE-273,CURRENTPERWIDTH/1e6,TMAX-273,'-k');
clabel(C,H);
xlabel('Edge Temperature ( C)')
ylabel('Current Per Width (MA/m)')
title('Peak Cu Temperature Vs Edge Temperature And Current Per Width')
```
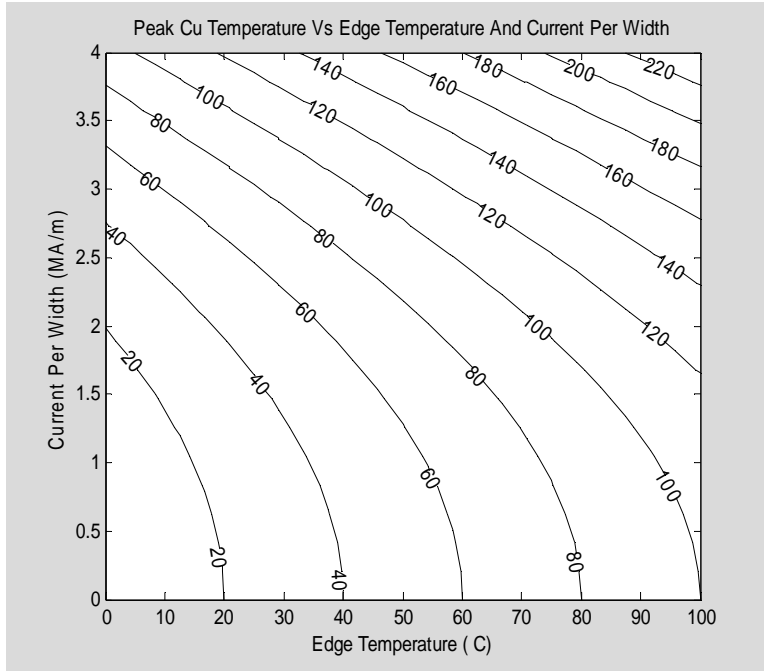
Figure 7: Contour plot of Peak Cu Temperaturee In Edge Cooling

For instance, Figures 6 and 7 show that at a current per width value of 3MA/m, keeping the upper and lower edge at 50 C results in a peak copper temperature of about 100 C.

It may be instructive to examine the temperature rise from the edge to the peak instead of the actual peak temperature.   This is plotted in Figure 7.

```
[C,H]=contour(TEDGE-273,CURRENTPERWIDTH/1e6,TMAX-TEDGE,'-k');
clabel(C,H);
xlabel('Edge Temperature ( C)')
ylabel('Current Per Width (MA/m)')
title('Conduction Temperature Rise Vs Edge Temperature And Current Per
Width')
```

Conduction Temperature Rise Vs Edge Temperature And Current Per Width
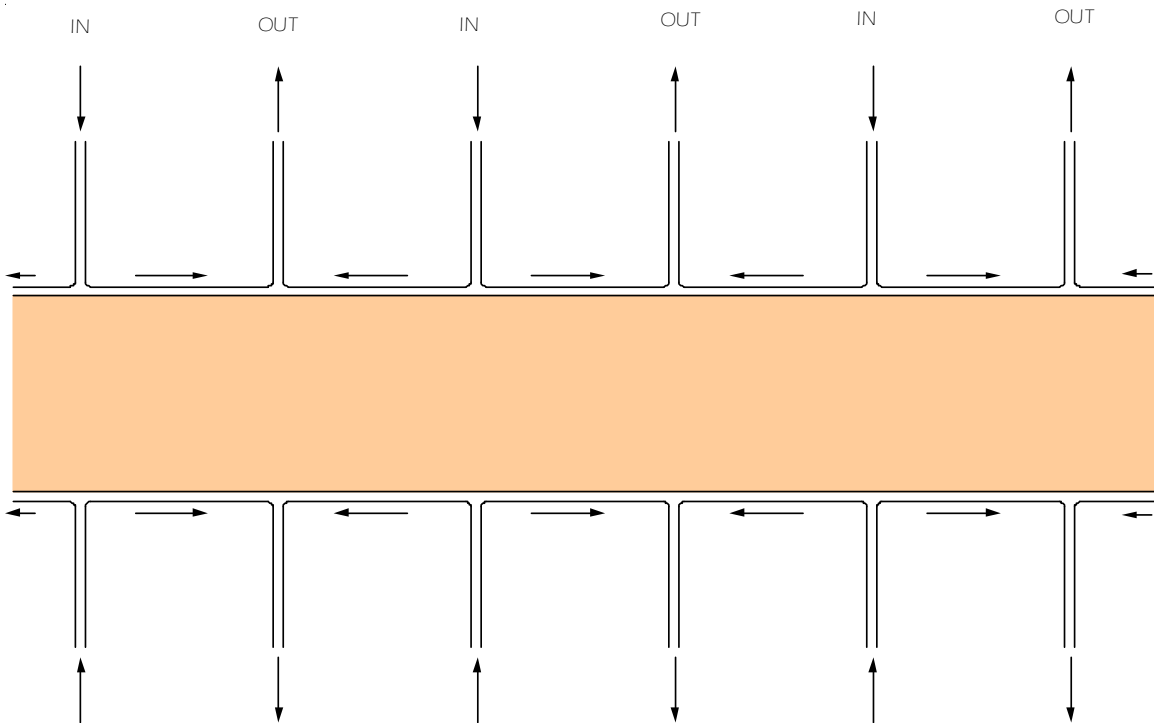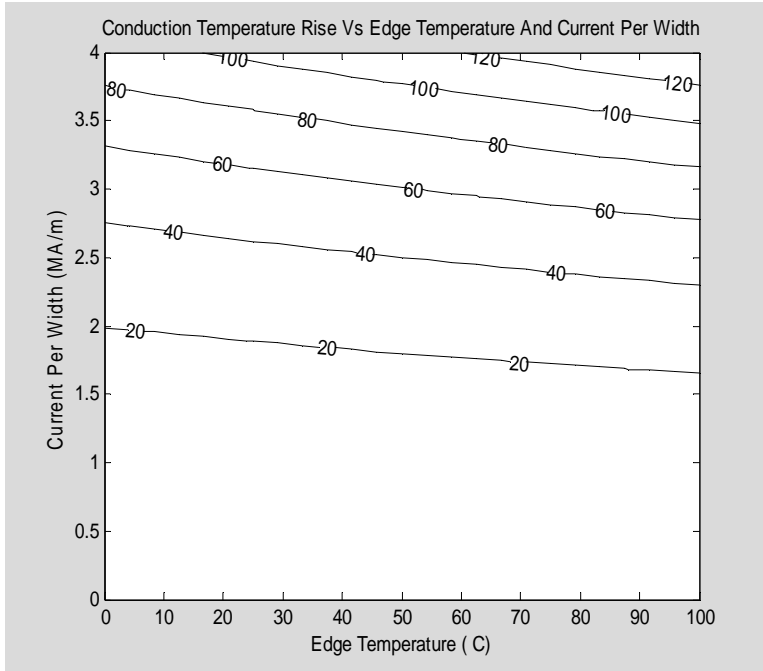
Alternatively we may be interested in how well single-ege cooling would work. The contour plot for it is simply related to the previous one.

```
[C,H]=contour(TEDGE-273,CURRENTPERWIDTH/2e6,TMAX-TEDGE,'-k');
clabel(C,H);
xlabel('Cooled Copper Strip Edge Temperature ( C)')
ylabel('Current Per Unit Copper Strip Thickness (kA/mm)')
title('Cross-Conductor Temperature Rise In Single-Edge Cooling')
legend('Delta-T (degrees C)','Location','SouthEast')
```
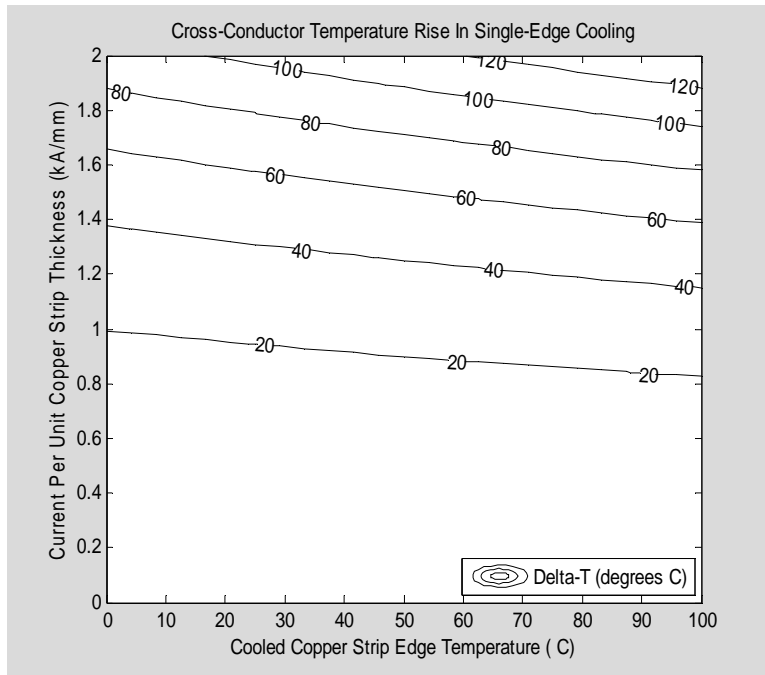
TF Radials Thermal-Hydraulic Calculations

The Reynolds number and heat transfer coefficients for this tubing are estimated as follows:

```
D=0.004826;
V=10;
T=linspace(273.15,473.15);
[PsatW,DensityW,CpW,ViscosityW,lambdaW,hfW,PrW]=LW_Properties(T);
Re=D*V*DensityW./ViscosityW;
plot(T-273.15,Re);
xlabel('Temperature (degrees C)')
ylabel('Reynolds Number')
title('              Reynolds Number Vs Temperature for 10m/s Water
in 1/4" od Tube')
```

Reynolds Number Vs Temperature for 10m/s Water in 1/4" od Tube
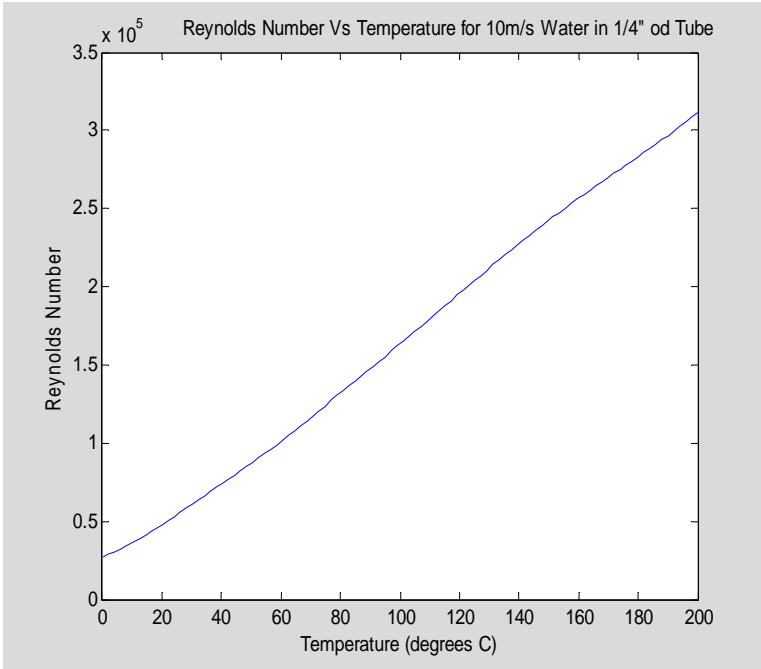
```
Nu=0.023*Re.^0.8.*PrW.^0.4;
plot(T-273,Nu)
ylim([0 1500])
ylabel('Nusselt Number')
title('Nusselt Number Vs. Temperature for Water flow in 1/4" od Tube')
xlabel('Temperature (degrees C)')
```
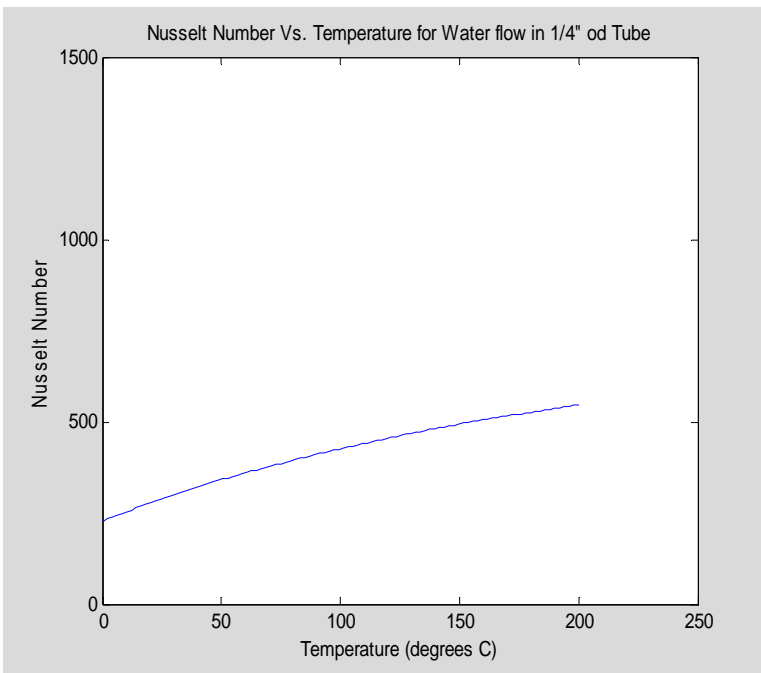

Nusselt Number Vs. Temperature for Water flow in 1/4" od Tube

```
h=lambdaW.*Nu/D;
```

```
plot(T-273,h);
ylabel('W m^-^2 Kelvin^-1')
title('          Film Drop Heat Transfer Coefficient for 10 m/s Water
in ¼" od Tube')
xlabel('Temperature (degrees C)')
 xlim([0 200])
ylim([0 80000])
```


Film Drop Heat Transfer Coefficient for 10 m/s Water in ¼" od Tube
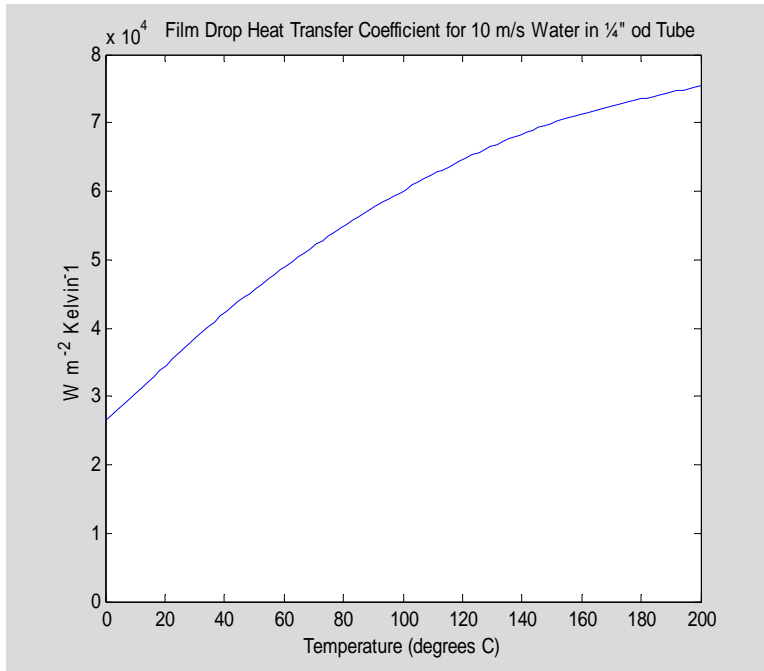
Calculation of Water Pumping Pressure Drop In TF Radials

```
L=2*2.888,
f=ones(size(Re));
for i=1:20;f=1./((2*log10(Re.*sqrt(f))-0.8).^2) ;end
DeltaP=f*L/D.*DensityW*V^2/2;
plot(T-273.15,DeltaP/1e5)
ylim([0 7])
ylabel('Bar')
xlabel('Water Temperature (Degrees C)')
title('          TF Radials Water Pressure Drop @ 10 m/s & Constant
Temperature')

L =
    5.7760
```

TF Radials Water Pressure Drop @ 10 m/s & Constant Temperature
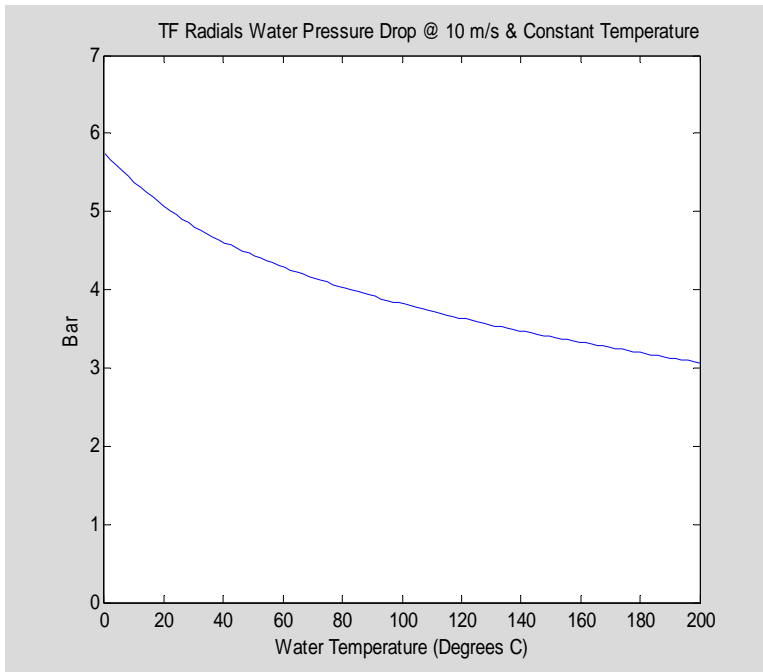
This shows the expected pressure drop in cooling water within each of the TF Radial turns is about 5 bars, i.e., about 72 psi.

```
L=7,
f=ones(size(Re));
for i=1:20;f=1./((2*log10(Re.*sqrt(f))-0.8).^2) ;end
DeltaP=f*L/D.*DensityW*V^2/2;
plot(T-273.15,DeltaP/1e5)
ylim([0 7])
ylabel('Bar')
xlabel('Water Temperature (Degrees C)')
title('        TF Radials Water Pressure Drop @ 10 m/s & Constant
Temperature')

L =
     7
```
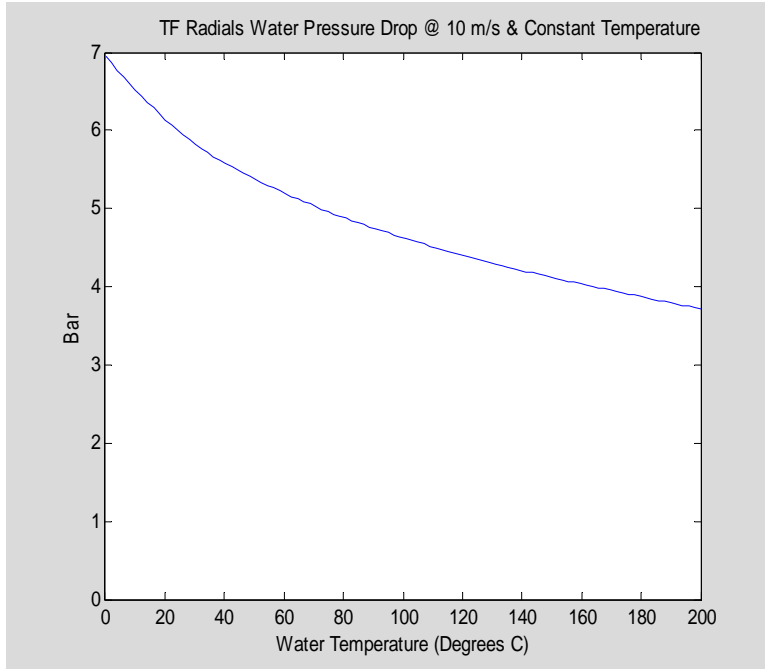
TF Radials Water Pressure Drop @ 10 m/s & Constant Temperature

Thus, the required pressure drop to pump coolant through the TF outer Leg cooling tubes will be about 6 Bar, i.e., about 87 psi.

In the following MATLAB cell, stress concentration data manually extracted from Peterson's stress concentration factor plot for pin-connected plates, which was tabulated in terms of the average stress in a section computed with the pin rem oved, is reformulated in terms of plate average stress without the pin removed and then replotted.

```
a_over_w=(0.15:0.05:0.75)';
Ktnb=[1.22 1.32 1.44 1.58 1.77 2.00 2.28  2.62 3.00 3.47 4.14 4.98
6.18]';
sigmamaxP_over_wh=Ktnb./a_over_w;
plot(a_over_w,sigmamaxP_over_wh,a_over_w,sigmamaxP_over_wh,'.')
xlim([0 1])
ylim([0 10])
xlabel('a/w=Pin Diameter/ Plate Width')
ylabel('Peak Stress / Average Stress Away From Pin')
title('Closely Fitting Pin Joint Stress Concentration Factor')
```
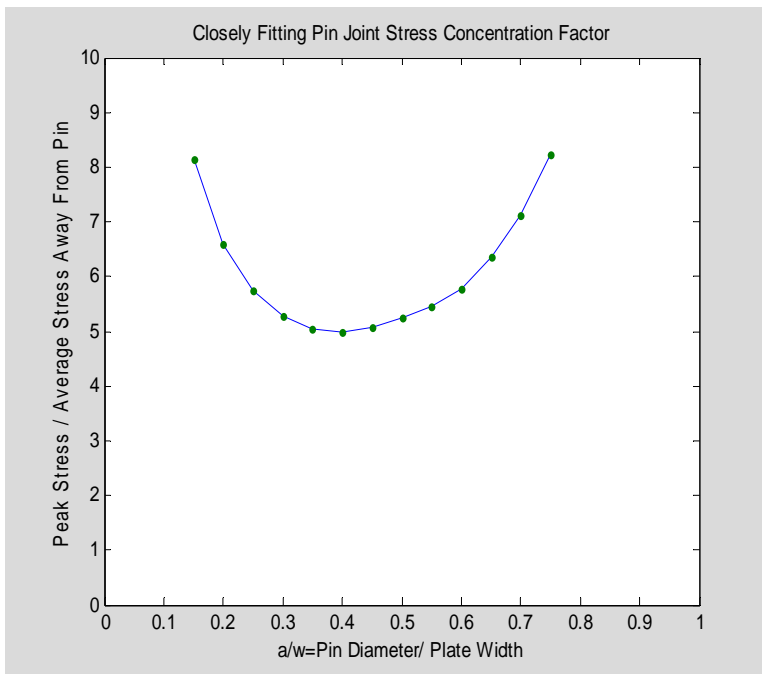

Peak bending in the TF outer leg pins is calculated here as a function of pin diameter.

```
D=0.2:0.01:0.49;
sigmamax = 4.455e6*ones(size(D))./D.^3;
plot(D,sigmamax/1e6);
ylabel('MPa');
xlabel('meters');
title('Peak Bending Stress In Pins Vs Pin Diameter');
```

NHTX Assessment FY2007 R1

Peak Bending Stress In Pins Vs Pin Diameter
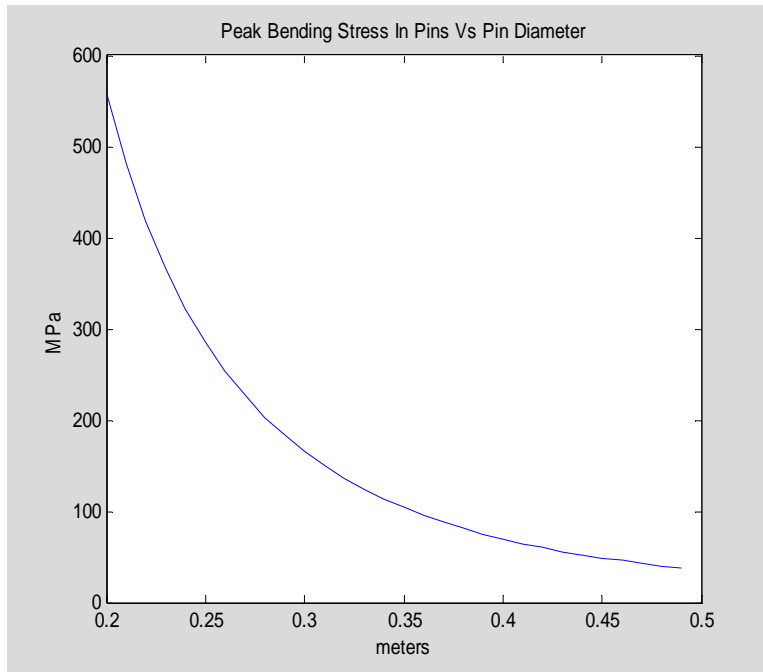
The following MATLAB code cell numerically solves the ordinary differential equation system for ideal beam stresses and deflections under arbitrary loading, as applied to radial deformation of the TF Outer Legs under full TF-only load.

```matlab
clf;
npoints=7001;
s=linspace (0,7,npoints)';
q=zeros(size(s));V=q;M=q;theta=q;y=q;
w=341758.;
for i=1:npoints;if s(i)>0.4971/2 & s(i)<(7-0.4971/2); q(i)=w;end;end;
emforce=trapz(s,q)
ffloor=(6.2-3.5)/(6.2-0)*emforce
fpin=(3.5-0)/(6.2-0)*emforce
I=0.3446*(0.4971)^3/12;
ds=s(2)-s(1)
q(2)=q(2)-ffloor/ds;
q(6201)=q(6201)-fpin/ds;
E=1.25E11;
V=cumtrapz(s,q);
M=cumtrapz(s,V);
yd=cumtrapz(s,cumtrapz(s,M))/E/I;
theta=(cumtrapz(s,M) )/E/I  -yd(6201)/6.2;
y=cumtrapz(s,theta);
subplot(5,1,1);plot(s,q);ylabel('q');
title('TF Outer Leg Ideal Straight Beam Calculations')
subplot(5,1,2);plot(s,V),ylabel('V')
subplot(5,1,3);plot(s,M),ylabel('M')
subplot(5,1,4);plot(s,theta),ylabel('\theta')
subplot(5,1,5),plot(s,y),ylabel('y')
xlabel('Distance Above Bottom (m)')
```

```matlab
max(abs(M))
max(y)
imax=find(y==max(y))
s(imax)
sigmamax=max(abs(M))*0.4971/2/I
```

```
emforce =
  2.2225e+006
ffloor =
  9.6784e+005
fpin =
  1.2546e+006
ds =
  1.0000e-003
ans =
  1.6100e+006
ans =
    0.0146
imax =
       3094
ans =
    3.0930
sigmamax =
  1.1344e+008
```
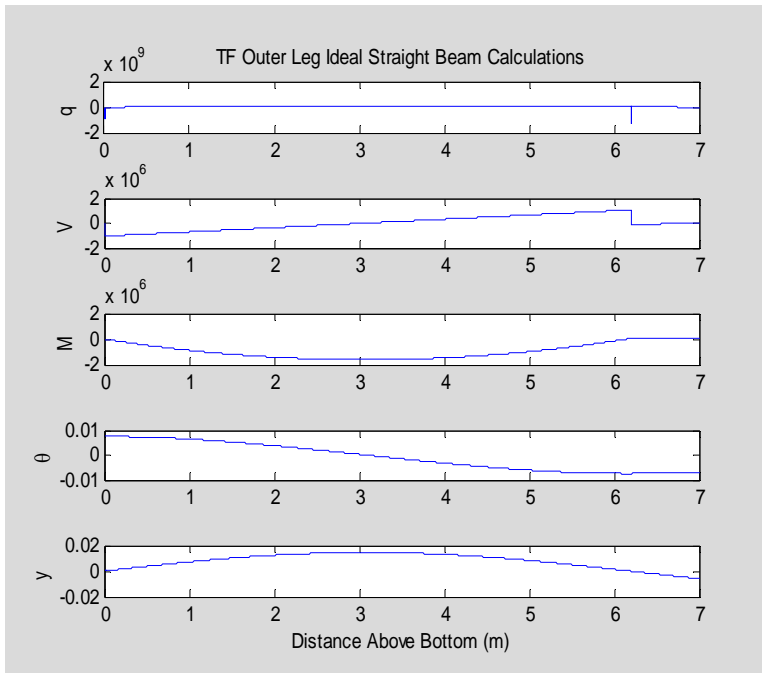
The following MATLAB code cell calculates an ideal finicular curve for the support of a TF Upper Radial under the action of TF-only forces.

.

```
clear;clf;
r0=0.287;
rol=2.926;
R=linspace(r0,rol,30)';
Z=(R.*log(R/r0)+r0-R);
H=-3.292/Z(end);Z=Z*H+2.429;
plot(R,Z,'-k','LineWidth',2)
hold on
stem(R,Z,'-g.')
xlabel('R (meters)')
ylabel('\DeltaZ =Z-Ztop (meters)')
title('Finicular Curve For TF Upper Radial Distributed Vertical Load')
xlim([0 3.5])
hold off
```


Finicular Curve For TF Upper Radial Distributed Vertical Load

----
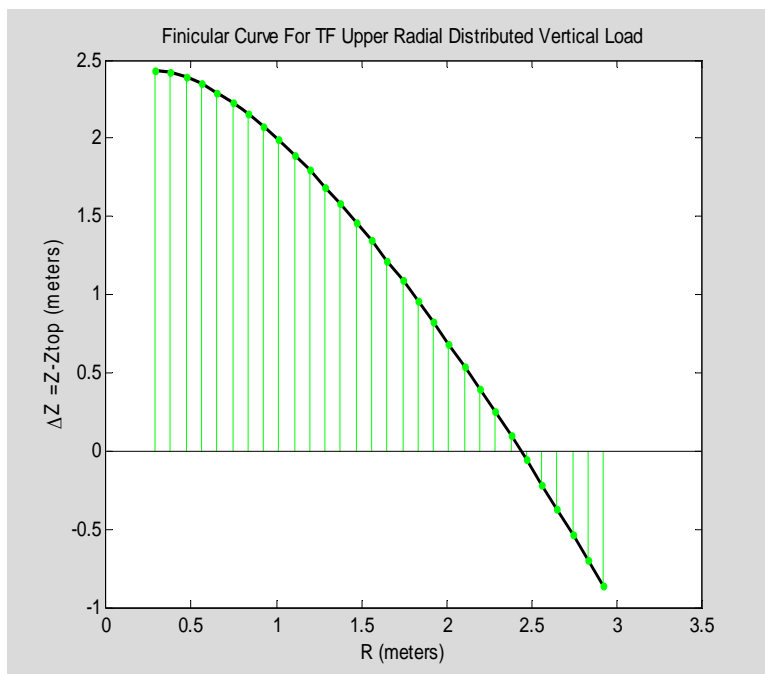
The actual in-plane support for the TF Upper Radial was designed through the use of the following MATLAB computational cell, which includes determination of equilibrium forces and also a deformation analysis using ideal straight beam theory.

These TF Upper Radial support calculations are implemented in a MATLAB computation cell in the Appendix, integrated with solution of the differential equations for deflections of a straoght beam representing the TF Upper Radial.

the following MATLAB cell, which also includes an ideal straight beam analysis of deflections.:

```
r0=0.287;r1=0.83;r2=2.0;r3=2.6; r4=2.926;;
```

```
fa=1e6*log(r2/r0);rfa=1e6*(r2-r0);
f1=(r2*fa-rfa)/(r2-r1);
f2a=(rfa-r1*fa)/(r2-r1);
fb=1e6*log(r4/r2);rfb=1e6*(r4-r2);
f2b=(r3*fb-rfb)/(r3-r2);
f3=(rfb-r2*fb)/(r3-r2);
f2=f2a+f2b;
[f1 f2 f3]
ftotal=f1+f2+f3
clf;
npoints=(r4-r0)/0.001+1
R=linspace (r0,r4,npoints)';
q=zeros(size(R));V=q;M=q;theta=q;y=q;I=q;
for i=1:npoints;q(i)=1e6/R(i);
I(i)=(0.4971)^3/12*min(0.3446, 2*R(i)*tand(18)-0.01);end;
dR=R(2)-R(1)
d1=abs(r1-R);i1=find(d1==min(d1));q(i1)=q(i1)-f1/dR;
d2=abs(r2-R);i2=find(d2==min(d2));q(i2)=q(i2)-f2/dR;
d3=abs(r3-R);i3=find(d3==min(d3));q(i3)=q(i3)-f3/dR;
E=1.25E11;
V=cumtrapz(R,q);
M=cumtrapz(R,V);
theta=(cumtrapz(R,M./I) )/E;
y=cumtrapz(R,theta);
subplot(5,1,1);plot(R,q);ylabel('q');
title('TF Upper Radial Ideal Straight Beam Calculations')
subplot(5,1,2);plot(R,V),ylabel('V')
subplot(5,1,3);plot(R,M),ylabel('M')
subplot(5,1,4);plot(R,theta),ylabel('\theta')
subplot(5,1,5),plot(R,y),ylabel('y')
xlabel('Radial Location (m)')
sigmamax=max(abs(M./I))*0.4971/2
imax=find(abs(M./I)*0.4971/2==sigmamax);Rmaxstress=R(imax)
ReactionLocations=[r1 r2 r3]
ReactionForces=[f1 f2 f3]
ReactionPointDeflectionsAndOL=[y(i1) y(i2) y(i3) y(end)]

ans =
  1.0e+006 *
    1.8546    0.1923    0.2750
ftotal =
  2.3219e+006
npoints =
       2640
dR =
    0.0010
sigmamax =
  2.3812e+007
Rmaxstress =
    0.8300
ReactionLocations =
    0.8300    2.0000    2.6000
ReactionForces =
  1.0e+006 *
    1.8546    0.1923    0.2750
ReactionPointDeflectionsAndOL =
  1.0e-003 *
```

TF Upper Radial Ideal Straight Beam Calculations
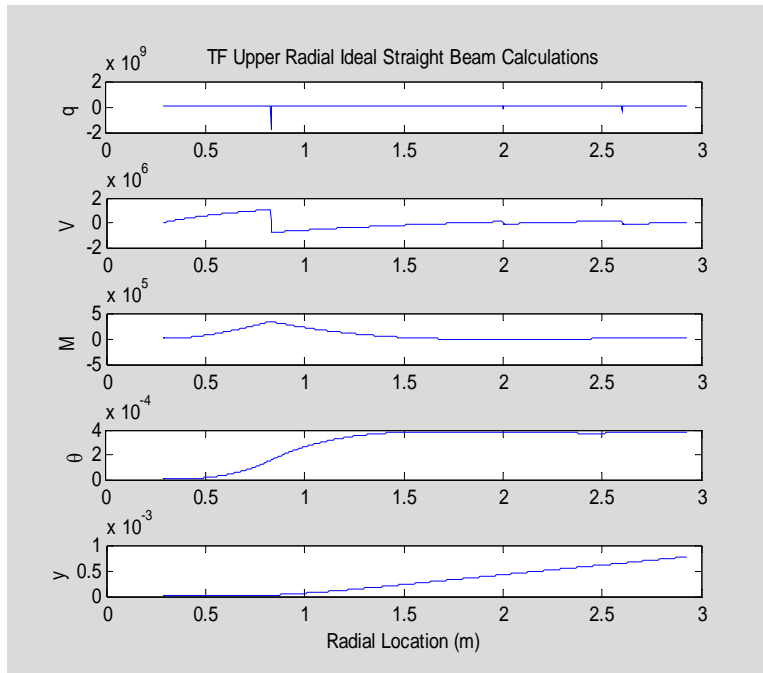
To support the TF Upper Radial and TF Outer Leg, it is necessary to synthesize a truss structure. Therefore, an m-file was developed to accompish analysis of forces and deflections in trusses incorporating planar link elements and toroidal ring elements. Its listing follows.

```
function [T, NodeResults]=trussframeRZ(nodes,fixednode,linksrings,loads)
% Mechanical analysis of 2D truss (aka frame) in cylindrical geometry.
% Model:
% Ideal link elements transmit tension/compression between ends in (R,Z)
% half-plane.  Ideal ring elements provide radial force from their hoop
% tension/compression.  Elements join at node which transmit forces only..
% External load forces are applied to the nodes.  By convention, node#1 is
% constrained to not move, so it develops additional forces of constraint.
% Input:
% The nodes array is dimensioned (N,2) where N is the number of nodes.  The
% (R,Z) coordiantes of the nodes without loading makes up its contents.
% fixednode identifies the single node with constrained (R,Z) position.
% The linksrings array is dimensioned (L,3)where L is the total number of links
% plus rings.  Its first two columns contain the node numbers of the two ends
% of each link,or the node number for each ring with a zero (0) in the
% other position.  These node numbers used correspond to the successive
% positions in the nodes array.
% Its third column contains the reciprocal spring constant for the link or ring.
% The loads array is dimensioned (N,2,C).  Its two columns contain the
% (R,Z) components of the external forces applied to the nodes as loads in
% each of C cases.
% Outputs:
% The T array, dimensioned (L,C) contains for each load case the link's
% tension or the poloidal plane ring's radial force.
% The NodeResults array, dimensioned (N,2,C), contains 2-element vectors
% calculated for each of the N nodes and for each of the C loads cases.
% For each loads case, the "fixednode" entries are the (R,Z) components of the
% additional force of constraint vector which must be externally applied at the
```

NHTX Assessment FY2007 R1   p 246

```
% constrained node in  order to satisfy static equilibrium condeitions, and the
% other 2(N-1) entries are the (R,Z) components of node displacements under
% loadig force conditions.
%   -Coded by R. Woolley, July 2007
%
[N,nvalue2]=size(nodes);[L,nvalue3]=size(linksrings);[NN,nvalue_2,C]=size(loads);
if nvalue2~=2 | nvalue3~=3 | N~=NN | nvalue_2~=2;
    error('An input array passed to trussframe.m is dimensioned improperly')
end
if fixednode<1 | fixednode>N
    error('fixednode does not specify a node in the range of defined nodes')
end
for j=1:L
    if linksrings(j,1)==linksrings(j,2)|linksrings(j,1)<1|linksrings(j,2)<0 ...
        |linksrings(j,1)>N|linksrings(j,2)>N;
      error('The linksrings input array refers to a nonexistent node')
    end
end
%
% Set up two lists for each node. The first lists the attached links or rings.
% The second lists the node number on the other end of each attached element.
indexpointers=cell(N,3);
for i=1:N;
    for j=1:L;
      if(linksrings(j,1)==i);
          indexpointers{i,1}=[indexpointers{i,1} j];
          indexpointers{i,2}=[indexpointers{i,2} linksrings(j,2)];
      elseif (linksrings(j,2)==i);
          indexpointers{i,1}=[indexpointers{i,1} j];
          indexpointers{i,2}=[indexpointers{i,2} linksrings(j,1)];
      end
    end
    indexpointers{i,3}=length(indexpointers{i,1});
end
%
% Set up matrix equation for the linear model. Variables to solve for
% include L tension values, (N-1) 2-component displacement vectors, and 1
% 2-component restraining force.
A=zeros(2*N+L);
for i=1:N;
    ri=nodes(i,:);
    J=indexpointers{i,2};
    LR=indexpointers{i,1};
    for k=1:indexpointers{i,3};
      j=J(k);
      lr=LR(k);
      if(j>0);   % link element
          rj=nodes(j,:);
          rij=rj-ri;
          rijhat=rij/norm(rij);
          A(2*i-1,lr)=rijhat(1);
          A(2*i,lr)=rijhat(2);
      else       % ring element
          A(2*i-1,lr)=-1;
          A(2*i,lr)=0;
      end
    end
end
for k=1:L;
    A(2*N+k,k)=-linksrings(k,3);
    i=linksrings(k,1);
    j=linksrings(k,2);
    if j~=0;
      rji=nodes(i,:)-nodes(j,:);
      rjihat=rji/norm(rji);
      A(2*N+k,L+2*i+[-1 0])=rjihat;
      A(2*N+k,L+2*j+[-1 0])=-rjihat;
    else
      A(2*N+k,L+2*i+[-1 0])=[1 0];
    end
```

p 247   NHTX Assessment FY2007 R1

```
end
%  Modify A-matrix for the fixednode:
A(2*N+(1:L),L+2*fixednode+[-1 0])=0;
A(2*fixednode-1,L+2*fixednode-1)=1;
A(2*fixednode,L+2*fixednode)=1;
% Next, reconfigure the loads array in preparation for solving.
Loads=[reshape(-permute(loads,[2 1 3]),[2*N C]);zeros(L,C)];
Results=A\Loads;
T=Results(1:L,1:C);
NodeResults=permute(reshape(Results(L+(1:(2*N)),1:C),[2 N C]),[2 1 3]);
```

The variables are explained as follows. The nodes3 array lists the undeflected (R,Z) coordinates (meters) of each of the trussframe's nodes. The linksrings4 array has a different row for each link or ring element used, with the first two columns listing the nodes connected to the element and the third column listing the element's *reciprocal* *s*pring constant in meters per newton. The loads array lists the external forces applied to each node while the Areas array lists the cross sectional areas (square meters) which each steel link must have in order to obtain the stated spring constants. The T2 array lists the calculated tensions (or compressions) in Newtons in each link or ring element. The NodeResults2 array gives for node 1 the calculated additional constraint force (Newtons) needed for equilibrium while for the other nodes it gives the calculated (R,Z) deflections (meters) from unloaded positions.

Examining the NodeResults array, we see that under full TF loading conditions node 2, i.e., the TF Outer Leg's upper pin, deflects vertically upwards by 0.69132 millimeters, but that the vertical deflection of node 6 is essentially zero at -0.002 millimeters.

```
nodes3,linksrings4,loads,Areas,linklengths,T2,NodeResults2


nodes3 =
        2.926              0
        2.926            6.2
          2.6         6.8634
            2         7.9397
            2           7.05
         0.83           7.05
         0.83         9.8413
linksrings4 =
            1              2   2.9773e-010
            2              3    1.735e-011
            3              4   3.1943e-011
            3              5         0.001
            4              5   3.3937e-010
            5              6   6.6982e-005
            4              6    0.00011947
            4              7   6.2307e-011
            6              7   9.7361e-011
            7              0   4.4413e-011
            6              2   1.1178e-005
            6              1   1.3075e-005
            2              0   2.2313e-008
```

```
          6              0         0.01
loads =
              0              0
      1254600              0
              0         275000
              0              0
              0         192300
              0        1854600
              0              0
Areas =
         0.1006
         0.19094
         0.17364
     8.4383e-008
         0.013935
     8.4383e-008
     6.1686e-008
         0.1619
         0.13439
         0.09028
     9.4261e-007
     1.6285e-006
         0.0006335
linklengths =
            6.2
         0.68577
         1.1482
            0.6
         0.97891
           1.17
         1.5255
         2.0881
         2.7085
           0.83
         2.1811
         4.4076
          2.926
T2 =
   2.3219e+006
   2.5872e+006
   2.3435e+006
       -2.9959
  -1.923e+005
       -2.8607
       -1.3472
   2.1776e+006
  -1.8546e+006
   1.1411e+006
        18.141
       -44.476
    1.135e+005
        0.20324
NodeResults2 =
      -12.675 -2.3219e+006
    0.0025326    0.00069131
   -0.0019274    -0.0014505
    0.0014391    0.00051193
```

```
     0.0018408    0.00057719
     0.0020324  -2.4264e-006
    5.068e-005   -0.00018299
```

TF OOP Force Calculations

It should be noted that the envelope of poloidal fields for the NHTX structural design
represents expected plasma operations.   Higher forces are theoretically possible if PF
coils were simultaneously mid-operated in the worst possible combinations, but those
combinations will not be accommodated in the design since they serve no experimental
purpose and they can readily be avoided by engineered protective features. The out-of
plane force situations which will be accommodated by the structure include the four
plasma equilibria initially calculated by J. Menard for the NHTX PF system design, and
also the plasma startup-scenario where the OH coil operates at its maximum "precharge"
flux while other PF coils and the plasma carry zero current.

The first step is to load previously prepared files containing information about J.
Menard's geometry for the NHTX PF coil system.

```
clear;clf;cla;
load NHTX_PFSystem
whos
  Name                Size                    Bytes  Class

   coil_dr            16x1                      128  double array
   coil_dz            16x1                      128  double array
   coil_index         16x1                      128  double array
   coil_name          17x1                     1172  cell array
   coil_r             16x1                      128  double array
   coil_z             16x1                      128  double array
```

The loaded data give the centers (r,z) and widths(dr,dz) of rectangles representing the OH
and PF coils and plasma for NHTX. There is one OH coil, 14 PF coils and one plasma,
making up 16 independent axisymmetric currents flowing in the toroidal direction.
While this representation is reasonably accurate for the OH and PF coils, it is not a good
representation for the plasma, which has a very non-rectangular shape and in addition has
a very nonuniform current density. However, the rectangular uniform current density
model of a plasma is used herein.

To calculate the toroidal component of the force density acting on TF components, we
shall determine the poloidal magnetic field at a grid of locations within them. The
toroidal force density is then the vector cross product JXB between the current density
and the poloidal field. For initial force calculations we will make the further somewhat
distorting approximation that current density is of uniform magnitude and direction
everywhere within a component.

We will calculate a NX16 set of force coeffients, f_{ij} , such that the toroidal force on coil
number i is given by

$$F_i = I_i \sum_j f_{ij} I_j$$

where I_i is the number of ampere-turns flowing in the ith coil and where F_i is the net vertical force on the coil in Newtons.

First, we create matrices giving the coordinates of bundles of filaments which will represent the coils. I shall make them all uniformly 50 locations tall and 5 locations wide, in the hope that this will be adequate to represent the OH coil accurately enough without causing too much time to be spent in the computations.

In the MATLAB code below, the calculated Br matrix holds the values of radial magnetic field at the ith set of internal coil (r,z) locations which is caused by one ampere-turn distributed between axisymmetric circular filaments at the similarly specified locations for the jth coil, where i and j are different. Each such calculated radial field value is then multiplied by the circumference of the local axisymmetric circle, then the resulting products are averaged over the ith coil body to form the ijth element of the matrix, f. The diagonal of f is zero. The plot following this is provided as a "sanity check". Covering a side-view of a TF Upper Radial, it superimposes a contour plot of the magnetic flux (in red) with a contour plot of the (in black) vertical magnetic field which causes the out-of-plane TF force there.

```
clf;
R=zeros(50,5,16);Z=R;
for i=1:16;
[R(:,:,i),Z(:,:,i)]= filamentize(coil_r(i)-
coil_dr(i)/2,coil_r(i)+coil_dr(i)/2,coil_z(i)-
coil_dz(i)/2,coil_z(i)+coil_dz(i)/2,50,5);
end
deltah=0.4971;
IZ=25; IR=27;
[Rtfuprradial,Ztfuprradial]=meshgrid(linspace(0.287,
2.926,IR),linspace(3.5-deltah,3.5,IZ));
[Rtflwrradial,Ztflwrradial]=meshgrid(linspace(0.287,
2.926,IR),linspace(-3.5,-3.5+deltah,IZ));
Brupr=zeros([size(Rtfuprradial) 16]);Bzupr=Brupr;Fluxupr=Brupr;
Brlwr=Brupr;Bzlwr=Bzupr;Fluxlwr=Fluxupr;
for j=1:16
[Brupr(:,:,j),Bzupr(:,:,j),Fluxupr(:,:,j)]=poloidal_field(Rtfuprradial,
Ztfuprradial,R(:,:,j),Z(:,:,j));
[Brlwr(:,:,j),Bzlwr(:,:,j),Fluxlwr(:,:,j)]=poloidal_field(Rtflwrradial,
Ztflwrradial,R(:,:,j),Z(:,:,j));
end
SQRTFluxupr=sqrt(Fluxupr);
contour(Rtfuprradial,Ztfuprradial,SQRTFluxupr(:,:,1),':r');
hold on
[C,H]=contour(Rtfuprradial,Ztfuprradial,1e6*Bzupr(:,:,1),'-k');
axis image
clabel(C,H)
hold off;
```
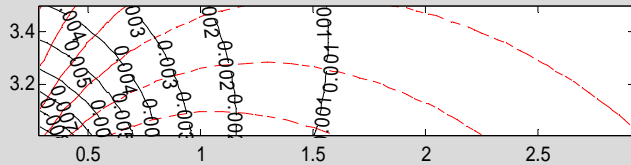
Four vectors of currents for the four plasma equilibrium modes previously had been
calculated by J. Menard were then loaded from the MATLAB command line, along with
their scenario names, as follows:

```
 ScenarioName
ScenarioName =
    'DND - near zero squareness'
    'DND - positive squareness'
    'DND - negative squareness'
    'LSN - ITER divertor'
Icurrents
Icurrents =
  1.0e+006 *
        0         0         0         0
    0.3303    0.2532    0.2917         0
    0.3297    0.5761    0.1555    0.2801
    0.1648    0.0625    0.0103    0.1057
    0.3728   -0.1020    0.0153    0.1806
    0.2333    0.1351    1.0149    0.2760
   -0.1908    0.2558   -1.2099    0.0618
   -2.0958   -2.5325   -1.2191   -2.2378
   -2.0957   -2.5326   -1.2160   -2.3537
   -0.1908    0.2557   -1.2118    0.1322
    0.2333    0.1352    1.0084   -0.1050
    0.3727   -0.1020    0.0221    0.1750
    0.1648    0.0625    0.0130    0.9917
    0.3297    0.5760    0.1568    1.1210
    0.3303    0.2532    0.2917   -0.6090
    3.5000    3.5000    3.5000    3.5000
```

For each of these current sets the vertical field in the TF Upper Radial and in the TF
Lower Radial were next calculated.

```
clf;
Bzupro=zeros(IZ,IR,4);
Bzlwro=Bzupro;
for l=1:4;
for k=1:16;
Bzupro(:,:,l)=Bzupro(:,:,l)+Bzupr(:,:,k)*Icurrents(k,l);
Bzlwro(:,:,l)=Bzlwro(:,:,l)+Bzlwr(:,:,k)*Icurrents(k,l);
end
end
[C,H]=contour(Rtfuprradial,Ztfuprradial,Bzupro(:,:,1),'-k');
axis image
clabel(C,H);
```
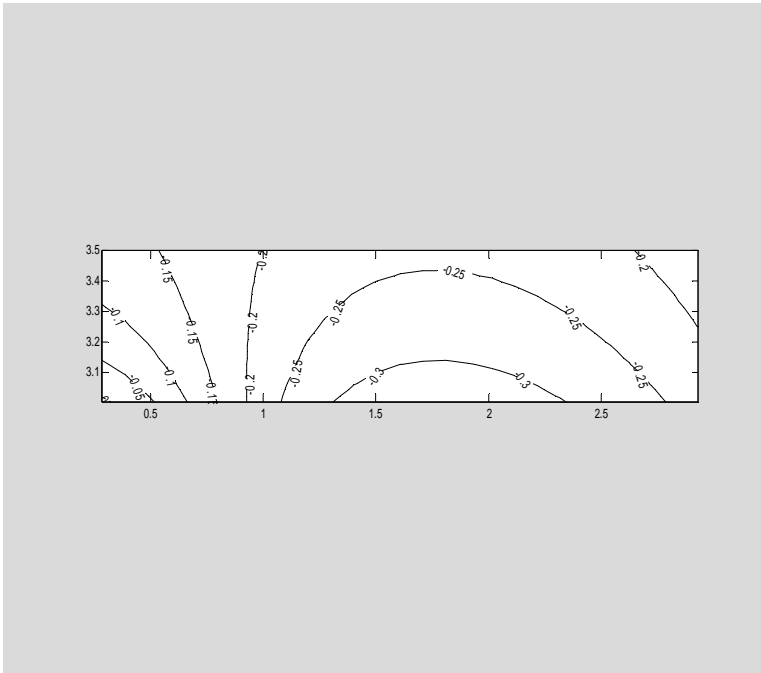


```
ITF=1e6;
Fdensityupr=zeros(IZ,IR,4);Fdensitylwr=Fdensityupr;
for k=1:4;
for l=1:16;
Fdensityupr(:,:,k)=Fdensityupr(:,:,k)+Bzupr(:,:,l)*Icurrents(l,k);
Fdensitylwr(:,:,k)=Fdensitylwr(:,:,k)+Bzlwr(:,:,l)*Icurrents(l,k);
end
end
Fdensityupr=-Fdensityupr*ITF/deltah;
Fdensitylwr=-Fdensitylwr*ITF/deltah;
```

Then, the toroidally directed force density distributions on the TF Radials for each of the four plasma modes were calculated. The filled contour plots below illustrate calculated lateral electromagnetic pressure (in kPa) on TF Radials for the four NHTX plasma equilibria thatt have been calculated, scaled to 3.5 MA of plasma current. The plotted pressure represents the total of both turns in a TF Radial, i.e., 1 MA-turn. They were calculated with the simplifying assumption that the TF current in each TF Radial is uniformly of constant density and is everywhere radial in direction. Although this is

likely an accurate approximation in most locations, it is clearly not accurate near the inner and outer ends of each TF Radial where the actual direction of the current changes.

The first plot shows the lateral pressure on the TF Upper Radial for the different plasma equilibria.

```
clf;cla reset;
currentfigurehandle=get(0,'CurrentFigure');
for k=1:4;
hlabel=subplot(4,3,(k-1)*3+1);
set(hlabel,'Visible','off')
text(0.01,0.5,['3.5 MA Plasma Equilibrium';
ScenarioName(k,:)],'FontSize',14 )
subplot(4,3,(k-1)*3+[2 3],'align')
[C,H,CF]=contourf(Rtfuprradial,Ztfuprradial,Fdensityupr(:,:,k)/1e3,0:40
:800);
currentaxeshandle=get(currentfigurehandle,'CurrentAxes');
set(currentaxeshandle,'CLim',[0 800]);
ylabel('Z (m)')
xlabel('R (m)')
axis image
colorbar
if k==1
 title('Maps Of EM Out-Of-Plane Pressure (kPa) On TF Upper
Radials','FontSize',14)
end
end
```
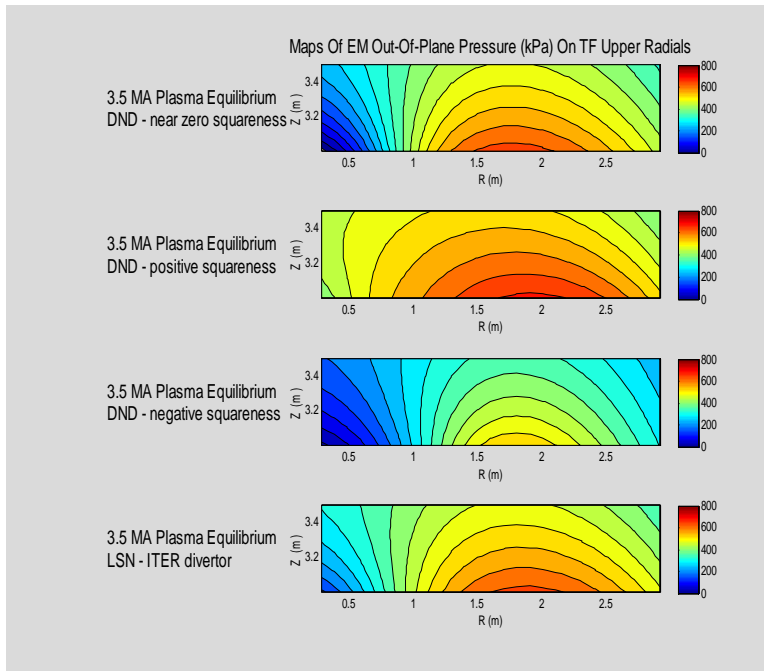
The next plot shows the lateral pressure on each of the TF Lower Radials for the same plasma equilibria.   It should be understood that the direction of this pressure on the lower TF Radials is opposite to the pressure on the upper TF Radials, so the signs of the lower pressure distributions have been reversed for plotting in order to simplify their comparison.

```
clf;cla reset;
currentfigurehandle=get(0,'CurrentFigure');
for k=1:4;
hlabel=subplot(4,3,(k-1)*3+1);
set(hlabel,'Visible','off')
text(0.01,0.5,['3.5 MA Plasma Equilibrium';
ScenarioName(k,:)],'FontSize',14 )
subplot(4,3,(k-1)*3+[2 3],'align')
[C,H,CF]=contourf(Rtflwrradial,Ztflwrradial,Fdensitylwr(:,:,k)/1e3,0:40
:800);
currentaxeshandle=get(currentfigurehandle,'CurrentAxes');
set(currentaxeshandle,'CLim',[0 800]);
ylabel('Z (m)')
xlabel('R (m)')
axis image
colorbar
if k==1
 title('Maps Of EM Out-Of-Plane Pressure (kPa) On TF Lower
Radials','FontSize',14)
end
end
```
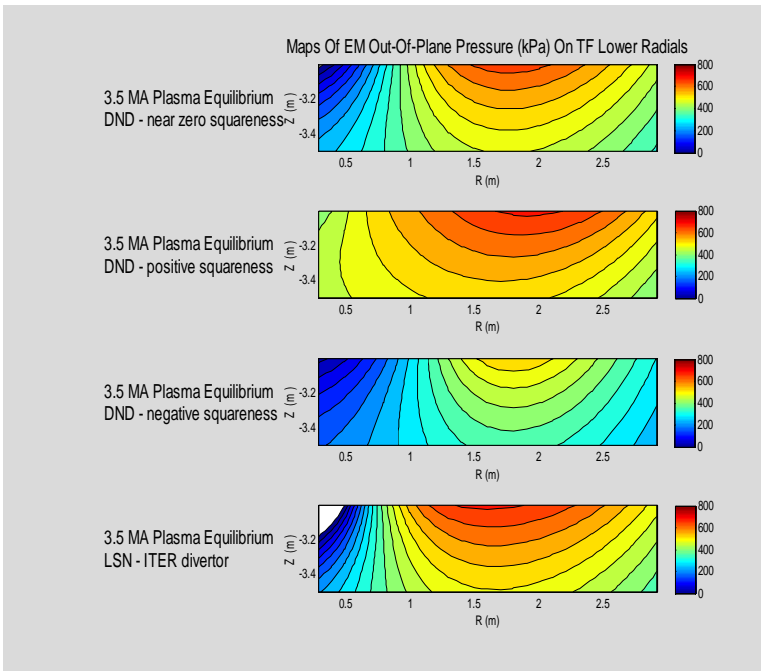

Inspection of these contour plots reveals that in all four of the plasma scenarios, the peak out-of-plane electromagnetic pressure on the TF radials occurs in a broad region between major radii of 1.5 m and 2.0 m. This out-of-plane pressure loading varies over the height

NHTX Assessment FY2007 R1

of a TF Radial by almost a factor of two, with the peak pressure developed on the edge closest to the plasma. Pressure profiles in upper and lower TF Radials have opposite directions but similar magnitudes, with the lower TF radials having a slightly stronger loading. Upper and lower pressure profiles are almost indistinguishable for the double-null divertor scenarios, but are slightly different for the LSN-ITER Divertor plots. The only profile with an internal direction reversal within a single plot is the TF Lower Radial's LSN-ITER Divertor plot, which shows a small reversal near its inner edge (where the assumption of uniform radial current made in calculating the plots is least accurate).

Next, we deliberately blur the details of the vertical variations of load by integrating pressure over the vertical extent of each TF Radial. This results in representing the out-of-plane loading as lineal force densities in Newtons per meter, which is the representation form typically used in simple ideal beam calculations.

```
clf;
Flinealupr=deltah*squeeze(mean(Fdensityupr,1));
plot(Rtfuprradial(1,:),Flinealupr)
title('Out-Of-Plane Lineal Force Density On Each TF Upper Radial')
xlabel('R (m)')
ylabel('N m^-^1')
ylim([0 3.5e5])
xlim([0 3.2])
legend(ScenarioName,'Location','SouthEast')
```
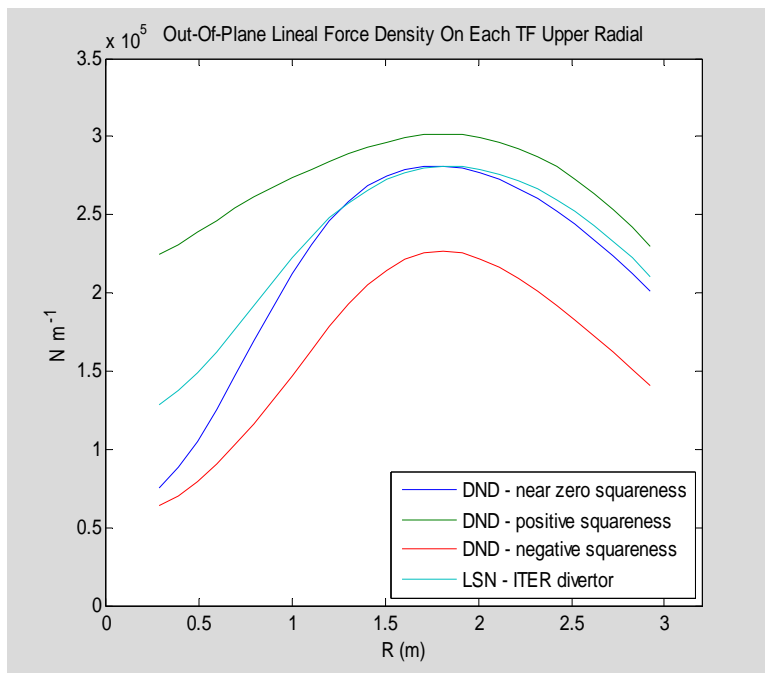


```
clf;
Flineallwr=deltah*squeeze(mean(Fdensitylwr,1));
plot(Rtflwrradial(1,:),Flineallwr)
title('Out-Of-Plane Lineal Force Density On Each TF Lower Radial')
xlabel('R (m)')
```

```
ylabel('N m^-^1')
ylim([0 3.5e5])
xlim([0 3.2])
legend(ScenarioName,'Location','SouthEast')
```
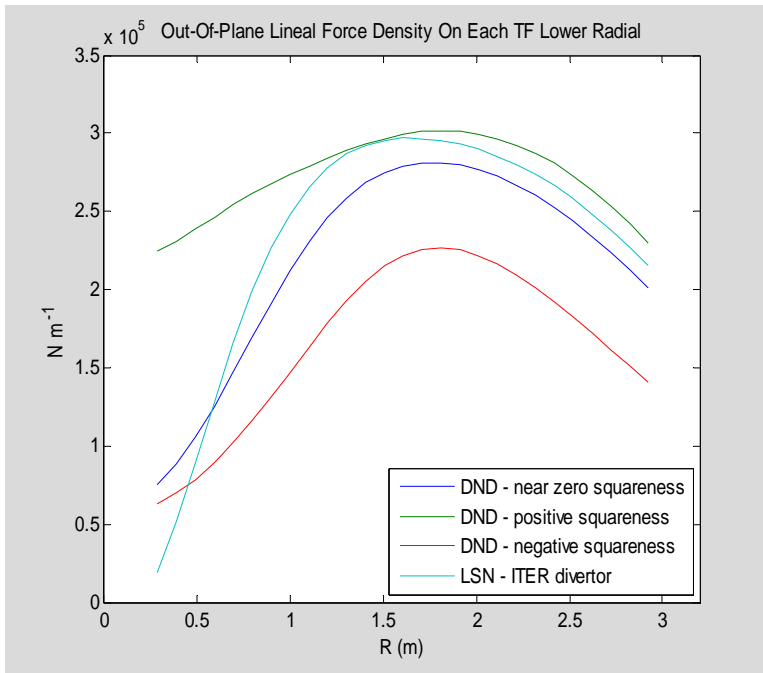

Next we compare the upper and lower linear force distributions on a single graph.

```
plot(Rtfuprradial(1,:),Flinealupr,'-',Rtflwrradial(1,:),Flineallwr,':')
title('Out-Of-Plane Lineal Force Density On Each TF Radial')
xlabel('R (m)')
ylabel('N m^-^1')
ylim([0 3.5e5])
xlim([0 3.2])
legend(
['TF Upper Radial  ' char(ScenarioName(1,:))],
['TF Upper Radial  ' char(ScenarioName(2,:))],
['TF Upper Radial  ' char(ScenarioName(3,:))],
['TF Upper Radial  ' char(ScenarioName(4,:))],
['TF Lower Radial  ' char(ScenarioName(1,:))],
['TF Lower Radial  ' char(ScenarioName(2,:))],
['TF Lower Radial  ' char(ScenarioName(3,:))],
['TF Lower Radial  ' char(ScenarioName(4,:))] ,'Location','SouthEast')
```
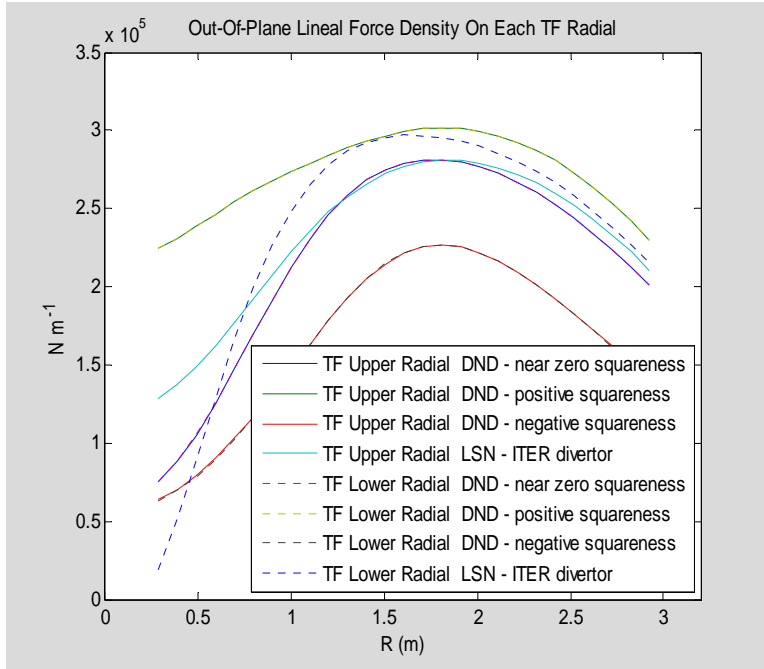
The plots for upper and lower out-of-plane lineal force densities overlay each other and are almost indistinguishable for the three double null Divertor (DND) plasma cases. This is not surprising since an examination of the PF coil currents for these three equilibria shows that they are essentially symmetric about the midplane. The upper and lower plots for the lower single null (LSN) ITER style of Divertor do differ from each other, with the lower TF radial receiving somewhat less loading than the upper TF radial on the inboard side but more in the middle.

Over all four plasma scenarios, the maximum local out-of-plane lineal force densities on upper and lower TF Radials are both about $3*10^5$ N/m.

The total force exerted on each TF Radial for each equilibrium can be found by integration of the lineal force densities, as follows:

```
Fupr=trapz(Rtfuprradial(1,:) , Flinealupr)
Flwr=trapz(Rtflwrradial(1,:) , Flineallwr)


Fupr =
  1.0e+005 *
    5.9060    7.2391    4.4676    6.2105
Flwr =
  1.0e+005 *
    5.9060    7.2393    4.4646    6.2848
```

Table XX: E-M Force On Each TF Radial During 3.5 MA Plasma Operations

Plasma Scenario	Total E-M Force Per TF Upper Radial	Total E-M Force Per TF Lower Radial
DND-near zero	5.9060 *10^5 N	5.9060 *10^5 N

squareness		
DND-positive squareness	7.2391 *10^5 N	7.2393 *10^5 N
DND-negative squareness	4.4676 *10^5 N	4.4646 *10^5 N
LSN-ITER divertor	6.2105 *10^5 N	6.2848 *10^5 N

The total overturning moment developed on each TF Radial is next calculated for each scenario by integrating the product of lineal force density with major radius. The results are as follows:

```
OTMupr=trapz(Rtfuprradial(1,:) , Rtfuprradial(1:4,:)'.*Flinealupr)
OTMlwr=trapz(Rtflwrradial(1,:) , Rtflwrradial(1:4,:)'.*Flineallwr)


OTMupr =
  1.0e+006 *
    1.0258    1.1760    0.7793    1.0560
OTMlwr =
  1.0e+006 *
    1.0258    1.1761    0.7791    1.0951
```

Out-Of-Plane Overturning Moments developed in each TF Radial are then as follows for the four plasma scenarios:

Table XX: E-M Moment About Central Axis From TF Radial During 3.5 MA Plasma Operations

Plasma Scenario	E-M Moment Per TF Upper Radial	E-M Moment Per TF Lower Radial
DND-near zero squareness	1.0258 *10^6 N-m	1.0258 *10^6 N-m
DND-positive squareness	1.1760 *10^6 N-m	1.1761 *10^6 N-m
DND-negative squareness	0.7793 *10^6 N-m	0.7791 *10^6 N-m
LSN-ITER divertor	1.0560 *10^6 N-m	1.0951 *10^6 N-m

Calculation of OOP capability of TF modules based on their internal stiffness

```
clear;clf;
deltah=0.4971;
load NHTX_TFRadial_PoloidalFields Brupr Bzupr Fluxupr Rtflwrradial
Ztflwrradial Brlwr Bzlwr Fluxlwr Rtflwrradial Ztflwrradial
load NHTX_PFSystem
load NHTX_Equilibria
IZ=25; IR=27;
[Rtfuprradial,Ztfuprradial]=meshgrid(linspace(0.287,
2.926,IR),linspace(3.5-deltah,3.5,IZ));
ITF=1e6;
Fdensityupr=zeros(IZ,IR,4);
for k=1:4;
for l=1:16;
Fdensityupr(:,:,k)=Fdensityupr(:,:,k)+Bzupr(:,:,l)*Icurrents(l,k);
end
end
Fdensityupr=-Fdensityupr*ITF/deltah;
Flinealupr=deltah*squeeze(mean(Fdensityupr,1));
%Fine grid interpolation to prepare for beam calculations:
npoints=round((Rtfuprradial(1,end)-Rtfuprradial(1,1))/0.001)+1;
R=linspace(Rtfuprradial(1,1),Rtfuprradial(1,end),npoints)';
Flu=csapi(Rtfuprradial(1,:)',Flinealupr',R)';

r0=R(1),r1=0.83,r2=2.0,r3=2.6, r4=R(end),
Nflexes=72,
dR=R(2)-R(1)
d1=abs(r1-R);i1=find(d1==min(d1));r1=R(i1),
d2=abs(r2-R);i2=find(d2==min(d2));r2=R(i2),
d3=abs(r3-R);i3=find(d3==min(d3));r3=R(i3),
R=linspace (r0,r4,npoints)';
I=zeros(npoints,1);
for i=1:npoints;
if(i<i2 | i>i3)
I(i)=0.4971*min(0.3446, 2*R(i)*tand(18)-0.01)^3/12;
else
I(i)=0.4971*(min(0.3446, 2*R(i)*tand(18)-0.01)/Nflexes)^3/12*Nflexes;
end;
end;
E=1.25E11;
LinearTransform=zeros(5,5);
dR=R(2)-R(1);

q=zeros(npoints,1);V=q;M=q;theta=q;y=q;
q(i1,:)=q(i1,:)+1e6/dR;
V=cumtrapz(R,q);
M=cumtrapz(R,V);
theta=cumtrapz(R,M./I)/E ;
y=cumtrapz(R,theta);
LinearTransform(:,1)=[y(i1) y(i2) y(i3) 1 r1]';

q=zeros(npoints,1);V=q;M=q;theta=q;y=q;
```

```
q(i2,:)=q(i2,:)+1e6/dR;
V=cumtrapz(R,q);
M=cumtrapz(R,V);
theta=cumtrapz(R,M./I)/E ;
y=cumtrapz(R,theta);
LinearTransform(:,2)=[y(i1) y(i2) y(i3) 1 r2]';

q=zeros(npoints,1);V=q;M=q;theta=q;y=q;
q(i3,:)=q(i3,:)+1e6/dR;
V=cumtrapz(R,q);
M=cumtrapz(R,V);
theta=cumtrapz(R,M./I)/E ;
y=cumtrapz(R,theta);
LinearTransform(:,3)=[y(i1) y(i2) y(i3) 1 r3]';

LinearTransform(:,4)=[1 1 1 0 0]';

q=zeros(npoints,1);V=q;M=q;theta=q;y=q;
V=cumtrapz(R,q);
M=cumtrapz(R,V);
theta=cumtrapz(R,M./I)/E+1e-3 ;
y=cumtrapz(R,theta);
LinearTransform(:,5)=[y(i1) y(i2) y(i3) 0 0]'/1e-3;

dR=R(2)-R(1);
q=Flu;V=q;M=q;theta=q;y=q;
V=cumtrapz(R,q);
M=cumtrapz(R,V);
theta=(cumtrapz(R,M./(I*ones(1,4))))/E ;
y=cumtrapz(R,theta);


fa=-trapz(R,Flu)/1e6;
rfa=-trapz(R,R*ones(1,4).*Flu)/1e6;
Linverse=inv(LinearTransform);

Inputs=Linverse*[-y(i1,:); -y(i2,: ); -y(i3,: );fa;rfa];
f1=Inputs(1,: )*1e6
f2=Inputs(2,: )*1e6
f3=Inputs(3,: )*1e6
y0=Inputs(4,: )
theta0=Inputs(5,: )
dR=R(2)-R(1);
q=Flu;V=q;M=q;theta=q;y=q;
q(i1,:)=q(i1,:)+f1/dR;
q(i2,:)=q(i2,:)+f2/dR;
q(i3,:)=q(i3,:)+f3/dR;
V=cumtrapz(R,q);
M=cumtrapz(R,V);
theta=(cumtrapz(R,M./(I*ones(1,4))))/E +ones(npoints,1)*theta0;
y=cumtrapz(R,theta)+ones(npoints,1)*y0;
subplot(5,1,1);plot(R,q);ylabel('q');ylim([-4e5 4e5])
title('                        TF Upper Radial Out-Of-Plane Beam
Calculations For 4 Plasma Equilibria')
subplot(5,1,2);plot(R,V),ylabel('V');
subplot(5,1,3);plot(R,M),ylabel('M');
subplot(5,1,4);plot(R,theta),ylabel('\theta');
```

```
subplot(5,1,5),plot(R,y),ylabel('y');ylim([-.002 .002])
xlabel('Radial Location (m)')
```

```
r0 =
        0.287
r1 =
         0.83
r2 =
     2
r3 =
          2.6
r4 =
        2.926
Nflexes =
    72
dR =
        0.001
r1 =
         0.83
r2 =
     2
r3 =
          2.6
f1 =
 -2.1296e+005 -3.2245e+005 -1.5626e+005 -2.4225e+005
f2 =
  -2.218e+005 -2.2578e+005 -1.7642e+005  -2.169e+005
f3 =
 -1.5604e+005 -1.7583e+005 -1.1421e+005 -1.6207e+005
y0 =
 -2.0544e-005  9.4242e-007 -1.5183e-005  -1.182e-005
theta0 =
  3.4475e-005  -1.043e-005  2.5288e-005  1.6582e-005
```


NHTX Assessment FY2007 R1   p 262
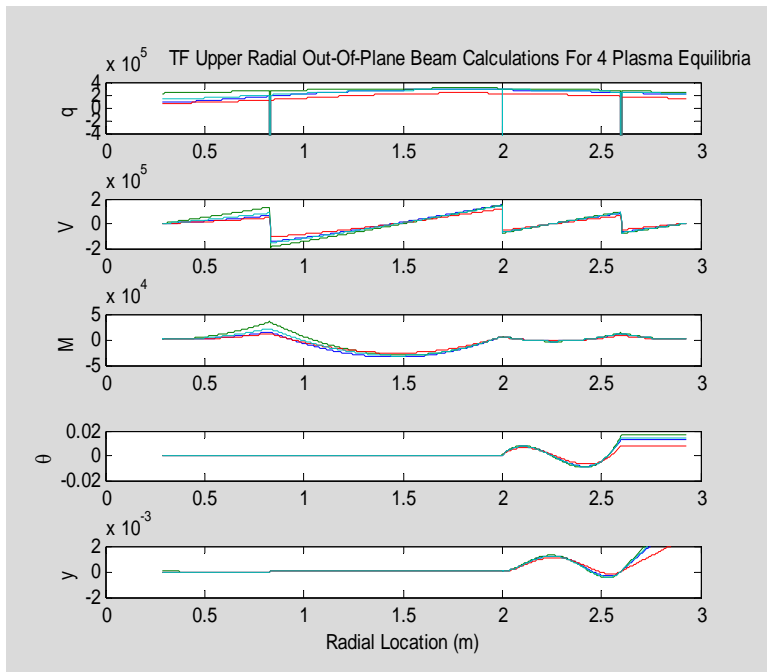
<u>Poloidal Field Field and Flux Calculations in MATLAB</u>

```
[num,txt] = xlsread('F:\NHTX\NHTX_PF_070115_copy.xls', 'B42:G58')


num =
     1.0000    0.3300    0.0400         0    4.5000
     2.0000    0.4200    0.0800    1.6000    0.4000
     3.0000    0.5100    0.2400    2.0500    0.3000
     4.0000    0.5100    0.2400    2.4000    0.3000
     5.0000    0.9000    0.2400    2.4000    0.3000
     6.0000    1.2500    0.3000    2.0800    0.2400
     7.0000    2.1000    0.4000    1.4000    0.2000
     8.0000    3.4250    0.4500    1.2000    0.4000
     9.0000    3.4250    0.4500   -1.2000    0.4000
    10.0000    2.1000    0.4000   -1.4000    0.2000
    11.0000    1.2500    0.3000   -2.0800    0.2400
    12.0000    0.9000    0.2400   -2.4000    0.3000
    13.0000    0.5100    0.2400   -2.4000    0.3000
    14.0000    0.5100    0.2400   -2.0500    0.3000
    15.0000    0.4200    0.0800   -1.6000    0.4000
    16.0000    1.0000    0.4400         0    3.0000
txt =
    'Coil'       'index'      'r'       'dr'      'z'       'dz'
    'OH'           ''          ''        ''        ''        ''
    'PF1U'         ''          ''        ''        ''        ''
    'PF2U1'        ''          ''        ''        ''        ''
    'PF2U2'        ''          ''        ''        ''        ''
    'PF3U'         ''          ''        ''        ''        ''
    'PF4U'         ''          ''        ''        ''        ''
    'PF5U2'        ''          ''        ''        ''        ''
    'PF5U1'        ''          ''        ''        ''        ''
    'PF5L1'        ''          ''        ''        ''        ''
    'PF5L2'        ''          ''        ''        ''        ''
    'PF4L'         ''          ''        ''        ''        ''
    'PF3L'         ''          ''        ''        ''        ''
    'PF2L2'        ''          ''        ''        ''        ''
    'PF2L1'        ''          ''        ''        ''        ''
    'PF1L'         ''          ''        ''        ''        ''
    'plasma'       ''          ''        ''        ''        ''


coil_name=txt(:,1)
coil_index=num(:,1)
coil_r=num(:,2)
coil_dr=num(:,3)
coil_z=num(:,4)
coil_dz=num(:,5)
```

```
coil_name =
    'Coil'
    'OH'
    'PF1U'
    'PF2U1'
    'PF2U2'
    'PF3U'
    'PF4U'
    'PF5U2'
    'PF5U1'
    'PF5L1'
    'PF5L2'
    'PF4L'
    'PF3L'
    'PF2L2'
    'PF2L1'
    'PF1L'
    'plasma'
coil_index =
     1
     2
     3
     4
     5
     6
     7
     8
     9
    10
    11
    12
    13
    14
    15
    16
coil_r =
    0.3300
    0.4200
    0.5100
    0.5100
    0.9000
    1.2500
    2.1000
    3.4250
    3.4250
    2.1000
    1.2500
    0.9000
    0.5100
    0.5100
    0.4200
    1.0000
coil_dr =
    0.0400
    0.0800
```

```
        0.2400
        0.2400
        0.2400
        0.3000
        0.4000
        0.4500
        0.4500
        0.4000
        0.3000
        0.2400
        0.2400
        0.2400
        0.0800
        0.4400
coil_z =
             0
        1.6000
        2.0500
        2.4000
        2.4000
        2.0800
        1.4000
        1.2000
       -1.2000
       -1.4000
       -2.0800
       -2.4000
       -2.4000
       -2.0500
       -1.6000
             0
coil_dz =
        4.5000
        0.4000
        0.3000
        0.3000
        0.3000
        0.2400
        0.2000
        0.4000
        0.4000
        0.2000
        0.2400
        0.3000
        0.3000
        0.3000
        0.4000
        3.0000

save NHTX_PFSystem.mat coil_name coil_index coil_r coil_dr coil_z
coil_dz


clear
load NHTX_PFSystem
whos
```

```
 Name                 Size                          Bytes  Class

  coil_dr              16x1                            128  double array
  coil_dz              16x1                            128  double array
  coil_index           16x1                            128  double array
  coil_name            17x1                           1172  cell array
  coil_r               16x1                            128  double array
  coil_z               16x1                            128  double array

Grand total is 173 elements using 1812 bytes
```

At this point, the NHTX PF coil data for the design documented in excel spreadsheet dated 16 January 2007 has been loaded into MATLAB. In preparation for the NHTX "unit field" calculations the NHTX global mesh grid is defined. In extends radially from the axis out to 4 meters and extends vertically 4 meters above and below the midplane. Initially, a resolution of 1 centimeter is chosen, so the grid has 801*401 points.

```
RMIN=0;RMAX=4;ZMIN=-4;ZMAX=4;RES=0.04;
M_GRID=round((ZMAX-ZMIN)/RES);
N_GRID=round((RMAX-RMIN)/RES);
R_GRID=linspace(RMIN,RMAX,N_GRID+1);
Z_GRID=linspace(ZMIN,ZMAX,M_GRID+1);
[RHO, ZETA]=meshgrid(R_GRID,Z_GRID);
BR=zeros(M_GRID+1,N_GRID+1,16);
BZ=BR;
FLUX=BR;
whos
```

```
  Name                 Size                          Bytes  Class

  BR                   201x101x16                  2598528  double array
  BZ                   201x101x16                  2598528  double array
  FLUX                 201x101x16                  2598528  double array
  M_GRID               1x1                               8  double array
  N_GRID               1x1                               8  double array
  RES                  1x1                               8  double array
  RHO                  201x101                      162408  double array
  RMAX                 1x1                               8  double array
  RMIN                 1x1                               8  double array
  R_GRID               1x101                           808  double array
  ZETA                 201x101                      162408  double array
  ZMAX                 1x1                               8  double array
  ZMIN                 1x1                               8  double array
  Z_GRID               1x201                          1608  double array
  coil_dr              16x1                            128  double array
  coil_dz              16x1                            128  double array
  coil_index           16x1                            128  double array
  coil_name            17x1                           1172  cell array
  coil_r               16x1                            128  double array
  coil_z               16x1                            128  double array
  xqxqxq1234           1x1                               1  logical array
  xqxqxq1235           1x3                               6  char array
```

```
Grand total is 1015536 elements using 8124691 bytes
```

Next, we calculate all the first-pass magnetics data. Note that this will require a significant time duration to complete these calculations.

```
for icoil=1:16;

rcoilmin=coil_r(icoil)-coil_dr(icoil)/2;
rcoilmax=coil_r(icoil)+coil_dr(icoil)/2;
zcoilmin=coil_z(icoil)-coil_dz(icoil)/2;
zcoilmax=coil_z(icoil)+coil_dz(icoil)/2;

mcoil=ceil((zcoilmax-zcoilmin)/RES);
ncoil=ceil((rcoilmax-rcoilmin)/RES);

[rcoil,zcoil]=filamentize(rcoilmin,rcoilmax,zcoilmin,zcoilmax,
mcoil,ncoil);

[rhocoil,zetacoil]=filamentize_corners(rcoilmin,rcoilmax,zcoilmin,zcoil
max, mcoil,ncoil);;

[br,bz,flux]=poloidal_fieldy(rhocoil,zetacoil,rcoil,zcoil);

[BR(:,:,icoil),BZ(:,:,icoil),FLUX(:,:,icoil)]=poloidal_fieldy(RHO,ZETA,
rcoil,zcoil);

[IFIND,JFIND]=find(rcoilmin<RHO & RHO<rcoilmax & zcoilmin<ZETA &
ZETA<zcoilmax);

if ~isempty(IFIND);
 BR(IFIND,JFIND,icoil)=interp2(rhocoil,zetacoil,br,RHO(IFIND,JFIND),
ZETA(IFIND,JFIND),'cubic');

 BZ(IFIND,JFIND,icoil)=interp2(rhocoil,zetacoil,bz,RHO(IFIND,JFIND),
ZETA(IFIND,JFIND),'cubic');


FLUX(IFIND,JFIND,icoil)=interp2(rhocoil,zetacoil,flux,RHO(IFIND,JFIND),
ZETA(IFIND,JFIND),'cubic');

end
 beep
save NHTX_globalfields.mat RHO ZETA BR BZ FLUX
end




load NHTX_PFSystem
load NHTX_globalfields.mat RHO ZETA BR BZ FLUX
clf
i=1;
ylim([-4 4]);
xlim([0 4]);
```

```
rectangle('Position',[0 -3.5 0.29 7.00] ,
'EdgeColor','g','LineWidth',0.1,'LineStyle','-.','FaceColor',[1 0.4 0])
rectangle('Position',[.29 -3.5 2.41,0.55] ,
'EdgeColor','g','LineWidth',0.1,'LineStyle','-.','FaceColor',[1 0.4 0])
rectangle('Position',[.29 2.95 2.41 0.55] ,
'EdgeColor','g','LineWidth',0.1,'LineStyle','-.','FaceColor',[1 0.4 0])
rectangle('Position',[2.7 -3.5 0.55 7.00] ,
'EdgeColor','g','LineWidth',0.1,'LineStyle','-.','FaceColor',[1 0.4 0])


for icoil=1:15
rcoilmin=coil_r(icoil)-coil_dr(icoil)/2;
rcoilmax=coil_r(icoil)+coil_dr(icoil)/2;
zcoilmin=coil_z(icoil)-coil_dz(icoil)/2;
zcoilmax=coil_z(icoil)+coil_dz(icoil)/2;
H(icoil)=rectangle('Position',[rcoilmin zcoilmin rcoilmax-rcoilmin,
zcoilmax-zcoilmin], 'EdgeColor','g','LineWidth',0.1,'LineStyle','-
.','FaceColor',[1 0.5 0]);
text(coil_r(icoil),coil_z(icoil),num2str(icoil),'FontSize',6)
end
hold on
contour(RHO,ZETA,sqrt(FLUX(:,:,i)),5,'k','LineWidth',.1); axis
image;xlim([0 4]),
hold off
xlabel('R (meters)'),ylabel('Z (meters)'),title('NHTX Poloidal Magnetic
Field With OH Current Only')
```
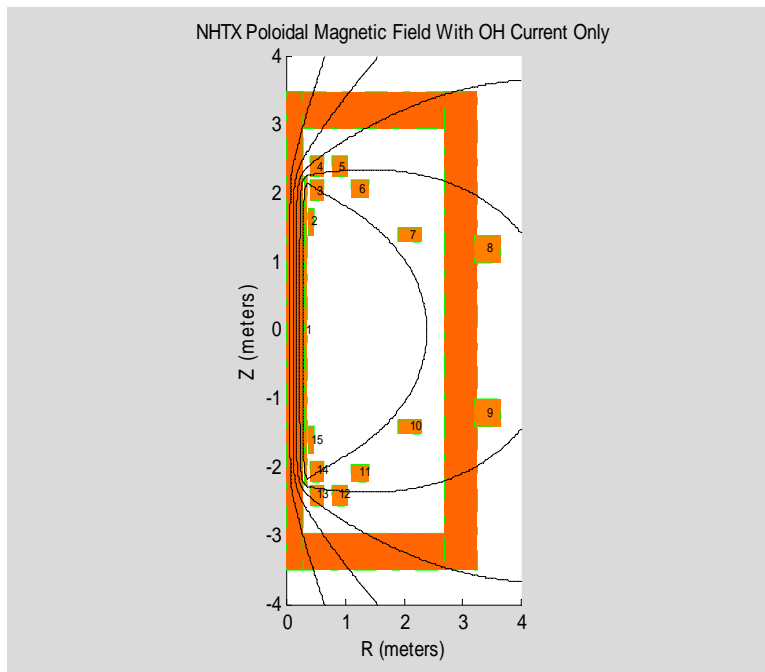

Next, plot the PF coil system without any flux lines or TF:

```
clf;
```

```
ylim([-4 4]);
xlim([0 4]);

TFEdgeColor=[1 0.4 0];TFColor=[1 1 1];
rectangle('Position',[0 -3.5 0.28 7.00] ,
'EdgeColor',TFEdgeColor,'LineWidth',0.1,'LineStyle','-
','FaceColor',TFColor)
rectangle('Position',[.287 -3.5 2.3905,0.4971] ,
'EdgeColor',TFEdgeColor,'LineWidth',0.1,'LineStyle','-
','FaceColor',TFColor)
rectangle('Position',[.28 3.0029 2.3905, 0.4971] ,
'EdgeColor',TFEdgeColor,'LineWidth',0.1,'LineStyle','-
','FaceColor',TFColor)
rectangle('Position',[2.6775 -3.5 0.4971 7.00] ,
'EdgeColor',TFEdgeColor,'LineWidth',0.1,'LineStyle','-
','FaceColor',TFColor)

for icoil=1:15
rcoilmin=coil_r(icoil)-coil_dr(icoil)/2;
rcoilmax=coil_r(icoil)+coil_dr(icoil)/2;
zcoilmin=coil_z(icoil)-coil_dz(icoil)/2;
zcoilmax=coil_z(icoil)+coil_dz(icoil)/2;
H(icoil)=rectangle('Position',[rcoilmin zcoilmin rcoilmax-rcoilmin,
zcoilmax-zcoilmin], 'EdgeColor','g','LineWidth',0.1,'LineStyle','-
.','FaceColor',[1 0.5 0]);
text(coil_r(icoil),coil_z(icoil),num2str(icoil),'FontSize',6)
end
axis image;xlim([0 4]),
xlabel('R (meters)'),ylabel('Z (meters)'),title('NHTX Initial PF Coil
Geometry')
```
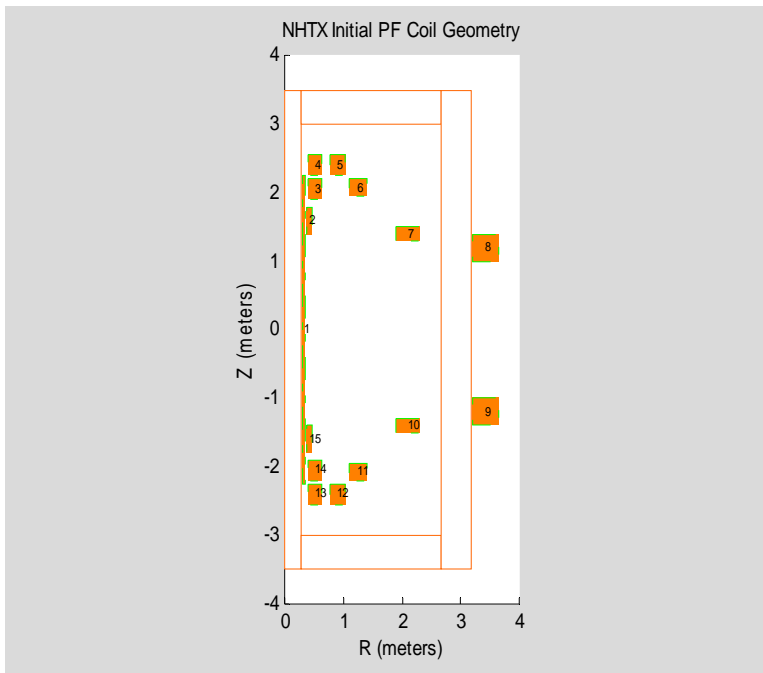
Next, reduce the heights of four PF coils to implement R.Woolley's PF Coil Geometry
Revision:

```
 coil_dz(4)=0.15 ;
 coil_dz(5)=0.15 ;
 coil_dz(12)=0.15 ;
 coil_dz(13)=0.15 ;
save NHTX_PFSystem1 coil_dr coil_dz coil_index coil_name coil_r coil_z

load NHTX_PFSystem1
```

Then redraw the PF coil system in its revised form:

```
clf;

ylim([-4 4]);
xlim([0 4]);

TFEdgeColor=[1 0.4 0];TFColor=[1 1 1];
rectangle('Position',[0 -3.5 0.28 7.00] ,
'EdgeColor',TFEdgeColor,'LineWidth',0.1,'LineStyle','-
','FaceColor',TFColor)
rectangle('Position',[.287 -3.5 2.3905,0.4971] ,
'EdgeColor',TFEdgeColor,'LineWidth',0.1,'LineStyle','-
','FaceColor',TFColor)
rectangle('Position',[.28 3.0029 2.3905, 0.4971] ,
'EdgeColor',TFEdgeColor,'LineWidth',0.1,'LineStyle','-
','FaceColor',TFColor)
rectangle('Position',[2.6775 -3.5 0.4971 7.00] ,
'EdgeColor',TFEdgeColor,'LineWidth',0.1,'LineStyle','-
','FaceColor',TFColor)

for icoil=1:15
rcoilmin=coil_r(icoil)-coil_dr(icoil)/2;
rcoilmax=coil_r(icoil)+coil_dr(icoil)/2;
zcoilmin=coil_z(icoil)-coil_dz(icoil)/2;
zcoilmax=coil_z(icoil)+coil_dz(icoil)/2;
H(icoil)=rectangle('Position',[rcoilmin zcoilmin rcoilmax-rcoilmin,
zcoilmax-zcoilmin], 'EdgeColor','g','LineWidth',0.1,'LineStyle','-
.','FaceColor',[1 0.5 0]);
text(coil_r(icoil),coil_z(icoil),num2str(icoil),'FontSize',6)
end
axis image;xlim([0 4]),
xlabel('R (meters)'),ylabel('Z (meters)'),title('NHTX Revised PF Coil
Geometry')
```

NHTX Revised PF Coil Geometry
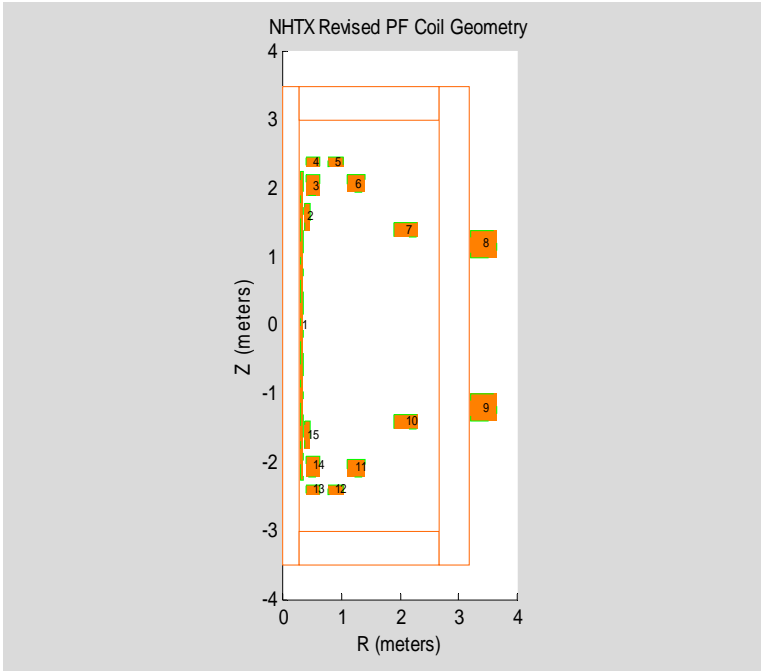
```
---------------------------------------------------------

Next, read in currents for J. Menard's four plasma scenarios.


[num,txt] = xlsread('F:\NHTX\NHTX_PF_070115_copy.xls', 'B04:J39')

num =
  1.0e+003 *
  Columns 1 through 7
    0.0010       NaN        0        0       NaN    0.0010       NaN
    0.0020       NaN    0.2831    0.0088    NaN    0.0020       NaN
    0.0030       NaN    0.2826    0.0039    NaN    0.0030       NaN
    0.0040       NaN    0.1413    0.0020    NaN    0.0040       NaN
    0.0050       NaN    0.3196    0.0044    NaN    0.0050       NaN
    0.0060       NaN    0.2000    0.0028    NaN    0.0060       NaN
    0.0070       NaN   -0.1636   -0.0020    NaN    0.0070       NaN
    0.0080       NaN   -1.7964   -0.0100    NaN    0.0080       NaN
    0.0090       NaN   -1.7963   -0.0100    NaN    0.0090       NaN
    0.0100       NaN   -0.1636   -0.0020    NaN    0.0100       NaN
    0.0110       NaN    0.2000    0.0028    NaN    0.0110       NaN
    0.0120       NaN    0.3195    0.0044    NaN    0.0120       NaN
    0.0130       NaN    0.1413    0.0020    NaN    0.0130       NaN
    0.0140       NaN    0.2826    0.0039    NaN    0.0140       NaN
    0.0150       NaN    0.2831    0.0088    NaN    0.0150       NaN
       NaN       NaN       NaN       NaN       NaN       NaN       NaN
```

```
      NaN          NaN          NaN          NaN          NaN          NaN          NaN
      NaN          NaN          NaN          NaN          NaN          NaN          NaN
      NaN          NaN          NaN          NaN          NaN          NaN          NaN
   0.0010          NaN            0            0          NaN       0.0010          NaN
   0.0020          NaN       0.2170       0.0068          NaN       0.0020          NaN
   0.0030          NaN       0.4938       0.0069          NaN       0.0030          NaN
   0.0040          NaN       0.0535       0.0007          NaN       0.0040          NaN
   0.0050          NaN      -0.0874      -0.0012          NaN       0.0050          NaN
   0.0060          NaN       0.1158       0.0016          NaN       0.0060          NaN
   0.0070          NaN       0.2193       0.0027          NaN       0.0070          NaN
   0.0080          NaN      -2.1707      -0.0121          NaN       0.0080          NaN
   0.0090          NaN      -2.1708      -0.0121          NaN       0.0090          NaN
   0.0100          NaN       0.2192       0.0027          NaN       0.0100          NaN
   0.0110          NaN       0.1159       0.0016          NaN       0.0110          NaN
   0.0120          NaN      -0.0874      -0.0012          NaN       0.0120          NaN
   0.0130          NaN       0.0535       0.0007          NaN       0.0130          NaN
   0.0140          NaN       0.4937       0.0069          NaN       0.0140          NaN
   0.0150          NaN       0.2170       0.0068          NaN       0.0150          NaN
  Columns 8 through 9
        0            0
        0            0
   0.2401       0.0033
   0.0906       0.0013
   0.1548       0.0021
   0.2366       0.0033
   0.0530       0.0007
  -1.9181      -0.0107
  -2.0174      -0.0112
   0.1133       0.0014
  -0.0900      -0.0013
   0.1500       0.0021
   0.8500       0.0118
   0.9608       0.0133
  -0.5220      -0.0163
      NaN          NaN
      NaN          NaN
      NaN          NaN
      NaN          NaN
        0            0
   0.2500       0.0078
   0.1333       0.0019
   0.0088       0.0001
   0.0131       0.0002
   0.8699       0.0121
  -1.0370      -0.0130
  -1.0449      -0.0058
  -1.0423      -0.0058
  -1.0387      -0.0130
   0.8643       0.0120
   0.0189       0.0003
   0.0112       0.0002
   0.1344       0.0019
   0.2500       0.0078
txt =
  Columns 1 through 5
       ''           ''         [1x26 char]                    ''        ''
    'Index'     'Coil'      'Current (kA)'     '|J| (MA/m^2)'       ''
```

```
              ''        'OH'                         ''                    ''         ''
              ''        'PF1U'                       ''                    ''         ''
              ''        'PF2U1'                      ''                    ''         ''
              ''        'PF2U2'                      ''                    ''         ''
              ''        'PF3U'                       ''                    ''         ''
              ''        'PF4U'                       ''                    ''         ''
              ''        'PF5U2'                      ''                    ''         ''
              ''        'PF5U1'                      ''                    ''         ''
              ''        'PF5L1'                      ''                    ''         ''
              ''        'PF5L2'                      ''                    ''         ''
              ''        'PF4L'                       ''                    ''         ''
              ''        'PF3L'                       ''                    ''         ''
              ''        'PF2L2'                      ''                    ''         ''
              ''        'PF2L1'                      ''                    ''         ''
              ''        'PF1L'                       ''                    ''         ''
              ''             ''                      ''                    ''         ''
              ''             ''                      ''                    ''         ''
              ''             ''              [1x25 char]                   ''         ''
        'Index'     'Coil'      'Current (kA)'     '|J| (MA/m^2)'          ''
              ''        'OH'                         ''                    ''         ''
              ''        'PF1U'                       ''                    ''         ''
              ''        'PF2U1'                      ''                    ''         ''
              ''        'PF2U2'                      ''                    ''         ''
              ''        'PF3U'                       ''                    ''         ''
              ''        'PF4U'                       ''                    ''         ''
              ''        'PF5U2'                      ''                    ''         ''
              ''        'PF5U1'                      ''                    ''         ''
              ''        'PF5L1'                      ''                    ''         ''
              ''        'PF5L2'                      ''                    ''         ''
              ''        'PF4L'                       ''                    ''         ''
              ''        'PF3L'                       ''                    ''         ''
              ''        'PF2L2'                      ''                    ''         ''
              ''        'PF2L1'                      ''                    ''         ''
              ''        'PF1L'                       ''                    ''         ''
        Columns 6 through 9
              ''             ''       'LSN - ITER divertor'                ''
        'Index'     'Coil'      'Current (kA)'          '|J| (MA/m^2)'
              ''        'OH'                              ''                ''
              ''        'PF1U'                            ''                ''
              ''        'PF2U1'                           ''                ''
              ''        'PF2U2'                           ''                ''
              ''        'PF3U'                            ''                ''
              ''        'PF4U'                            ''                ''
              ''        'PF5U2'                           ''                ''
              ''        'PF5U1'                           ''                ''
              ''        'PF5L1'                           ''                ''
              ''        'PF5L2'                           ''                ''
              ''        'PF4L'                            ''                ''
              ''        'PF3L'                            ''                ''
              ''        'PF2L2'                           ''                ''
              ''        'PF2L1'                           ''                ''
              ''        'PF1L'                            ''                ''
              ''             ''                           ''                ''
              ''             ''                           ''                ''
              ''             ''                   [1x25 char]               ''
        'Index'     'Coil'      'Current (kA)'          '|J| (MA/m^2)'
              ''        'OH'                              ''                ''
```

```
      ''      'PF1U'                    ''              ''
      ''      'PF2U1'                   ''              ''
      ''      'PF2U2'                   ''              ''
      ''      'PF3U'                    ''              ''
      ''      'PF4U'                    ''              ''
      ''      'PF5U2'                   ''              ''
      ''      'PF5U1'                   ''              ''
      ''      'PF5L1'                   ''              ''
      ''      'PF5L2'                   ''              ''
      ''      'PF4L'                    ''              ''
      ''      'PF3L'                    ''              ''
      ''      'PF2L2'                   ''              ''
      ''      'PF2L1'                   ''              ''
      ''      'PF1L'                    ''              ''


Currents=zeros(16,6);
Currents(1:15,1)=num(1:15,3)*1e3;
Currents(1:15,3)=num(20:34,3)*1e3;
Currents(1:15,2)=num(1:15,8)*1e3;
Currents(1:15,4)=num(20:34,8)*1e3;
Currents(16,1:4)=3e6;
Currents(1,5:6)=5e6;
Scenario=[
'DND - near zero squareness'
'LSN - ITER divertor       '
'DND - positive squareness '
'DND - negative squareness '
'Plasma Startup, OH-only    '
'Plasma Startup, OH+Others ']


Scenario =
DND - near zero squareness
LSN - ITER divertor
DND - positive squareness
DND - negative squareness
Plasma Startup, OH-only
Plasma Startup, OH+Others




clf
iscenario=1;

flux=FLUX(:,:,1)*Currents(1,iscenario);
for i=2:16
flux= flux+FLUX(:,:,i)*Currents(i,iscenario);
end
ylim([-4 4]);
xlim([0 4]);
```

```
rectangle('Position',[0 -3.5 0.29 7.00] ,
'EdgeColor','g','LineWidth',0.1,'LineStyle','-.','FaceColor',[1 0.4 0])
rectangle('Position',[.29 -3.5 2.41,0.55] ,
'EdgeColor','g','LineWidth',0.1,'LineStyle','-.','FaceColor',[1 0.4 0])
rectangle('Position',[.29 2.95 2.41 0.55] ,
'EdgeColor','g','LineWidth',0.1,'LineStyle','-.','FaceColor',[1 0.4 0])
rectangle('Position',[2.7 -3.5 0.55 7.00] ,
'EdgeColor','g','LineWidth',0.1,'LineStyle','-.','FaceColor',[1 0.4 0])


for icoil=1:15
rcoilmin=coil_r(icoil)-coil_dr(icoil)/2;
rcoilmax=coil_r(icoil)+coil_dr(icoil)/2;
zcoilmin=coil_z(icoil)-coil_dz(icoil)/2;
zcoilmax=coil_z(icoil)+coil_dz(icoil)/2;
H(icoil)=rectangle('Position',[rcoilmin zcoilmin rcoilmax-rcoilmin,
zcoilmax-zcoilmin], 'EdgeColor','g','LineWidth',0.1,'LineStyle','-
.','FaceColor',[1 0.5 0]);
text(coil_r(icoil),coil_z(icoil),num2str(icoil),'FontSize',6)
end
hold on
contour(RHO,ZETA,sqrt(flux),5,'k','LineWidth',.1); axis image;xlim([0
4]),
hold off
xlabel('R (meters)'),ylabel('Z (meters)'),title(['NHTX Poloidal
Magnetic Field In '  Scenario(iscenario,:)])
```



```
clf
iscenario=2;

flux=FLUX(:,:,1)*Currents(1,iscenario);
for i=2:16
```

```
flux= flux+FLUX(:,:,i)*Currents(i,iscenario);
end
ylim([-4 4]);
xlim([0 4]);

rectangle('Position',[0 -3.5 0.29 7.00] ,
'EdgeColor','g','LineWidth',0.1,'LineStyle','-.','FaceColor',[1 0.4 0])
rectangle('Position',[.29 -3.5 2.41,0.55] ,
'EdgeColor','g','LineWidth',0.1,'LineStyle','-.','FaceColor',[1 0.4 0])
rectangle('Position',[.29 2.95 2.41 0.55] ,
'EdgeColor','g','LineWidth',0.1,'LineStyle','-.','FaceColor',[1 0.4 0])
rectangle('Position',[2.7 -3.5 0.55 7.00] ,
'EdgeColor','g','LineWidth',0.1,'LineStyle','-.','FaceColor',[1 0.4 0])


for icoil=1:15
rcoilmin=coil_r(icoil)-coil_dr(icoil)/2;
rcoilmax=coil_r(icoil)+coil_dr(icoil)/2;
zcoilmin=coil_z(icoil)-coil_dz(icoil)/2;
zcoilmax=coil_z(icoil)+coil_dz(icoil)/2;
H(icoil)=rectangle('Position',[rcoilmin zcoilmin rcoilmax-rcoilmin,
zcoilmax-zcoilmin], 'EdgeColor','g','LineWidth',0.1,'LineStyle','-
.','FaceColor',[1 0.5 0]);
text(coil_r(icoil),coil_z(icoil),num2str(icoil),'FontSize',6)
end
hold on
contour(RHO,ZETA,sqrt(flux),5,'k','LineWidth',.1); axis image;xlim([0
4]),
hold off
xlabel('R (meters)'),ylabel('Z (meters)'),title(['NHTX Poloidal
Magnetic Field In '  Scenario(iscenario,:)])
```


NHTX Poloidal Magnetic Field In LSN - ITER divertor

```
clf
iscenario=3;

flux=FLUX(:,:,1)*Currents(1,iscenario);
for i=2:16
flux= flux+FLUX(:,:,i)*Currents(i,iscenario);
end
ylim([-4 4]);
xlim([0 4]);

rectangle('Position',[0 -3.5 0.29 7.00] ,
'EdgeColor','g','LineWidth',0.1,'LineStyle','-.','FaceColor',[1 0.4 0])
rectangle('Position',[.29 -3.5 2.41,0.55] ,
'EdgeColor','g','LineWidth',0.1,'LineStyle','-.','FaceColor',[1 0.4 0])
rectangle('Position',[.29 2.95 2.41 0.55] ,
'EdgeColor','g','LineWidth',0.1,'LineStyle','-.','FaceColor',[1 0.4 0])
rectangle('Position',[2.7 -3.5 0.55 7.00] ,
'EdgeColor','g','LineWidth',0.1,'LineStyle','-.','FaceColor',[1 0.4 0])


for icoil=1:15
rcoilmin=coil_r(icoil)-coil_dr(icoil)/2;
rcoilmax=coil_r(icoil)+coil_dr(icoil)/2;
zcoilmin=coil_z(icoil)-coil_dz(icoil)/2;
zcoilmax=coil_z(icoil)+coil_dz(icoil)/2;
H(icoil)=rectangle('Position',[rcoilmin zcoilmin rcoilmax-rcoilmin,
zcoilmax-zcoilmin], 'EdgeColor','g','LineWidth',0.1,'LineStyle','-
.','FaceColor',[1 0.5 0]);
text(coil_r(icoil),coil_z(icoil),num2str(icoil),'FontSize',6)
end
hold on
contour(RHO,ZETA,sqrt(flux),5,'k','LineWidth',.1); axis image;xlim([0
4]),
hold off
xlabel('R (meters)'),ylabel('Z (meters)'),title(['NHTX Poloidal
Magnetic Field In '  Scenario(iscenario,:)])
```

NHTX Poloidal Magnetic Field In DND - positive squareness

```
clf
iscenario=4;

flux=FLUX(:,:,1)*Currents(1,iscenario);
for i=2:16
flux= flux+FLUX(:,:,i)*Currents(i,iscenario);
end
ylim([-4 4]);
xlim([0 4]);

rectangle('Position',[0 -3.5 0.29 7.00] ,
'EdgeColor','g','LineWidth',0.1,'LineStyle','-.','FaceColor',[1 0.4 0])
rectangle('Position',[.29 -3.5 2.41,0.55] ,
'EdgeColor','g','LineWidth',0.1,'LineStyle','-.','FaceColor',[1 0.4 0])
rectangle('Position',[.29 2.95 2.41 0.55] ,
'EdgeColor','g','LineWidth',0.1,'LineStyle','-.','FaceColor',[1 0.4 0])
rectangle('Position',[2.7 -3.5 0.55 7.00] ,
'EdgeColor','g','LineWidth',0.1,'LineStyle','-.','FaceColor',[1 0.4 0])


for icoil=1:15
rcoilmin=coil_r(icoil)-coil_dr(icoil)/2;
rcoilmax=coil_r(icoil)+coil_dr(icoil)/2;
zcoilmin=coil_z(icoil)-coil_dz(icoil)/2;
zcoilmax=coil_z(icoil)+coil_dz(icoil)/2;
H(icoil)=rectangle('Position',[rcoilmin zcoilmin rcoilmax-rcoilmin,
zcoilmax-zcoilmin], 'EdgeColor','g','LineWidth',0.1,'LineStyle','-
.','FaceColor',[1 0.5 0]);
text(coil_r(icoil),coil_z(icoil),num2str(icoil),'FontSize',6)
end
hold on
contour(RHO,ZETA,sqrt(flux),5,'k','LineWidth',.1); axis image;xlim([0
4]),
```

```
hold off
xlabel('R (meters)'),ylabel('Z (meters)'),title(['NHTX Poloidal
Magnetic Field In '  Scenario(iscenario,:)])
```


NHTX Poloidal Magnetic Field In DND - negative squareness

```
clf
iscenario=5;

flux=FLUX(:,:,1)*Currents(1,iscenario);
for i=2:16
flux= flux+FLUX(:,:,i)*Currents(i,iscenario);
end
ylim([-4 4]);
xlim([0 4]);

rectangle('Position',[0 -3.5 0.29 7.00] ,
'EdgeColor','g','LineWidth',0.1,'LineStyle','-.','FaceColor',[1 0.4 0])
rectangle('Position',[.29 -3.5 2.41,0.55] ,
'EdgeColor','g','LineWidth',0.1,'LineStyle','-.','FaceColor',[1 0.4 0])
rectangle('Position',[.29 2.95 2.41 0.55] ,
'EdgeColor','g','LineWidth',0.1,'LineStyle','-.','FaceColor',[1 0.4 0])
rectangle('Position',[2.7 -3.5 0.55 7.00] ,
'EdgeColor','g','LineWidth',0.1,'LineStyle','-.','FaceColor',[1 0.4 0])


for icoil=1:15
rcoilmin=coil_r(icoil)-coil_dr(icoil)/2;
rcoilmax=coil_r(icoil)+coil_dr(icoil)/2;
zcoilmin=coil_z(icoil)-coil_dz(icoil)/2;
zcoilmax=coil_z(icoil)+coil_dz(icoil)/2;
H(icoil)=rectangle('Position',[rcoilmin zcoilmin rcoilmax-rcoilmin,
zcoilmax-zcoilmin], 'EdgeColor','g','LineWidth',0.1,'LineStyle','-
.','FaceColor',[1 0.5 0]);
```

p 279 NHTX Assessment FY2007 R1

```
text(coil_r(icoil),coil_z(icoil),num2str(icoil),'FontSize',6)
end
hold on
contour(RHO,ZETA,sqrt(flux),15,'k','LineWidth',.1); axis image;xlim([0
4]),
hold off
xlabel('R (meters)'),ylabel('Z (meters)'),title(['NHTX Poloidal
Magnetic Field In '  Scenario(iscenario,:)])
```

NHTX Poloidal Magnetic Field In Plasma Startup, OH-only

Next, I will iterate on matched startup currents in 4 and 13 until flux looks good

```
clf
iscenario=6;
Currents(4,6)=0.25e6;
Currents(5,6)=0.04e6;
Currents(6,6)=0.014e6;
Currents(7,6)=0.015e6;
Currents(8,6)=0.0033e6;
Currents(9,6)=Currents(8,6);
Currents(13,6)=Currents(4,6);
Currents(12,6)=Currents(5,6);
Currents(11,6)=Currents(6,6);
Currents(10,6)=Currents(7,6);
flux=FLUX(:,:,1)*Currents(1,iscenario);
for i=2:16
flux= flux+FLUX(:,:,i)*Currents(i,iscenario);
end
ylim([-4 4]);
xlim([0 4]);
```

```
rectangle('Position',[0 -3.5 0.29 7.00] ,
'EdgeColor','g','LineWidth',0.1,'LineStyle','-.','FaceColor',[1 0.4 0])
rectangle('Position',[.29 -3.5 2.41,0.55] ,
'EdgeColor','g','LineWidth',0.1,'LineStyle','-.','FaceColor',[1 0.4 0])
rectangle('Position',[.29 2.95 2.41 0.55] ,
'EdgeColor','g','LineWidth',0.1,'LineStyle','-.','FaceColor',[1 0.4 0])
rectangle('Position',[2.7 -3.5 0.55 7.00] ,
'EdgeColor','g','LineWidth',0.1,'LineStyle','-.','FaceColor',[1 0.4 0])


for icoil=1:15
rcoilmin=coil_r(icoil)-coil_dr(icoil)/2;
rcoilmax=coil_r(icoil)+coil_dr(icoil)/2;
zcoilmin=coil_z(icoil)-coil_dz(icoil)/2;
zcoilmax=coil_z(icoil)+coil_dz(icoil)/2;
H(icoil)=rectangle('Position',[rcoilmin zcoilmin rcoilmax-rcoilmin,
zcoilmax-zcoilmin], 'EdgeColor','g','LineWidth',0.1,'LineStyle','-
.','FaceColor',[1 0.5 0]);
text(coil_r(icoil),coil_z(icoil),num2str(icoil),'FontSize',6)
end
hold on
contour(RHO,ZETA,sqrt(flux),15,'k','LineWidth',.1); axis image;xlim([0
4]),
hold off
xlabel('R (meters)'),ylabel('Z (meters)'),title(['NHTX Poloidal
Magnetic Field In '  Scenario(iscenario,:)])
```


NHTX Poloidal Magnetic Field In Plasma Startup, OH+Others

<u>Poloidal Field Coil Force Vertical Calculations</u>

The first step is to load information about the NHTX PF coil system's geometry.

```
load NHTX_PFSystem
whos
[coil_r coil_dr coil_z coil_dz]
```

```
  Name              Size                      Bytes  Class

  ans               16x4                        512  double array
  coil_dr           16x1                        128  double array
  coil_dz           16x1                        128  double array
  coil_index        16x1                        128  double array
  coil_name         17x1                       1172  cell array
  coil_r            16x1                        128  double array
  coil_z            16x1                        128  double array
  xqxqxq1234        1x1                           1  logical array
  xqxqxq1235        1x3                           6  char array

Grand total is 241 elements using 2331 bytes

ans =
    0.3300    0.0400         0    4.5000
    0.4200    0.0800    1.6000    0.4000
    0.5100    0.2400    2.0500    0.3000
    0.5100    0.2400    2.4000    0.3000
    0.9000    0.2400    2.4000    0.3000
    1.2500    0.3000    2.0800    0.2400
    2.1000    0.4000    1.4000    0.2000
    3.4250    0.4500    1.2000    0.4000
    3.4250    0.4500   -1.2000    0.4000
    2.1000    0.4000   -1.4000    0.2000
    1.2500    0.3000   -2.0800    0.2400
    0.9000    0.2400   -2.4000    0.3000
    0.5100    0.2400   -2.4000    0.3000
    0.5100    0.2400   -2.0500    0.3000
    0.4200    0.0800   -1.6000    0.4000
    1.0000    0.4400         0    3.0000
```

```
coil_name
```

```
coil_name =
    'Coil'
    'OH'
    'PF1U'
    'PF2U1'
    'PF2U2'
```

```
'PF3U'
'PF4U'
'PF5U2'
'PF5U1'
'PF5L1'
'PF5L2'
'PF4L'
'PF3L'
'PF2L2'
'PF2L1'
'PF1L'
'plasma'
```

The loaded data give the centers (r,z) and widths(dr,dz) of rectangles representing the OH and PF coils and plasma for NHTX. There is one OH coil, 14 PF coils and one plasma, making up 16 independent axisymmetric currents flowing in the toroidal direction. While this representation is reasonably accurate for the OH and PF coils, it is not a good representation for the plasma, which has a very non-rectangular shape and in addition has a very nonuniform current density. However, the rectangular uniform current density model of a plasma will be used herein.

We will calculate a 16X16 matrix of coeffients, f_{ij}, such that the vertical force on coil number i is given by

$$F_i = I_i \sum_j f_{ij} I_j$$

where I_i is the number of ampere-turns flowing in the ith coil and where F_i is the net vertical force on the coil in Newtons.

First, we create matrices giving the coordinates of bundles of filaments which will represent the coils. I shall make them all uniformly 50 locations tall and 5 locations wide, in the hope that this will be adequate to represent the OH coil accurately enough without causing too much time to be spent in the computations.

In the MATLAB code below, the calculated Br matrix holds the values of radial magnetic field at the ith set of internal coil (r,z) locations which is caused by one ampere-turn distributed between

axisymmetric circular filaments at the similarly specified locations for the jth coil, where i and j are different. Each such calculated radial field value is then multiplied by the circumference of the local axisymmetric circle, then the resulting products are averaged over the ith coil body to form the ijth element of the matrix, f. The diagonal of f is zero.

```
R=zeros(50,5,16);Z=R;
for i=1:16;
[R(:,:,i),Z(:,:,i)]= filamentize(coil_r(i)-
coil_dr(i)/2,coil_r(i)+coil_dr(i)/2,coil_z(i)-
coil_dz(i)/2,coil_z(i)+coil_dz(i)/2,50,5);
end
f=zeros(16,16);
for i=1:16
for j=1:16
if i~=j;
Br=poloidal_field(R(:,:,i),Z(:,:,i),R(:,:,j),Z(:,:,j));
f(i,j)=mean(mean(2*pi*R(i).*Br)');
end
end
end
f

f =
  1.0e-006 *
  Columns 1 through 6
        0     0.0158     0.0736     0.0847     0.0500     0.0355
  -0.0124          0     0.6113     0.1795     0.1985     0.1490
  -0.0490    -0.5147          0     0.8834     0.4367     0.0200
  -0.0567    -0.1483    -0.8834          0    -0.0000    -0.1698
  -0.0186    -0.0938    -0.2601     0.0000          0    -0.5549
  -0.0095    -0.0510    -0.0086     0.0725     0.4150          0
  -0.0023     0.0036     0.0144     0.0162     0.0550     0.1324
  -0.0007     0.0009     0.0027     0.0033     0.0108     0.0197
   0.0007     0.0019     0.0023     0.0020     0.0061     0.0134
   0.0023     0.0031     0.0032     0.0025     0.0073     0.0168
   0.0095     0.0017     0.0017     0.0012     0.0036     0.0082
   0.0186     0.0010     0.0010     0.0007     0.0022     0.0050
   0.0567     0.0006     0.0006     0.0004     0.0013     0.0030
   0.0490     0.0009     0.0008     0.0006     0.0017     0.0040
   0.0124     0.0012     0.0011     0.0008     0.0022     0.0050
  -0.0000     0.0386     0.0350     0.0199     0.0496     0.1081
  Columns 7 through 12
   0.0146     0.0070    -0.0070    -0.0146    -0.0355    -0.0500
  -0.0176    -0.0077    -0.0151    -0.0155    -0.0050    -0.0022
  -0.0576    -0.0178    -0.0154    -0.0131    -0.0040    -0.0017
  -0.0647    -0.0218    -0.0132    -0.0101    -0.0030    -0.0013
  -0.1263    -0.0407    -0.0230    -0.0170    -0.0050    -0.0022
  -0.2179    -0.0534    -0.0365    -0.0282    -0.0082    -0.0036
        0    -0.0469    -0.0817    -0.0606    -0.0168    -0.0073
   0.0293          0    -0.1183    -0.0503    -0.0134    -0.0061
```

```
   0.0503    0.1183         0   -0.0293   -0.0197   -0.0108
   0.0606    0.0817    0.0469         0   -0.1324   -0.0550
   0.0282    0.0365    0.0534    0.2179         0   -0.4150
   0.0170    0.0230    0.0407    0.1263    0.5549         0
   0.0101    0.0132    0.0218    0.0647    0.1698   -0.0000
   0.0131    0.0154    0.0178    0.0576   -0.0200   -0.4367
   0.0155    0.0151    0.0077    0.0176   -0.1490   -0.1985
   0.0901    0.0330   -0.0330   -0.0901   -0.1081   -0.0496
  Columns 13 through 16
  -0.0847   -0.0736   -0.0158   -0.0000
  -0.0008   -0.0011   -0.0012   -0.0885
  -0.0006   -0.0008   -0.0009   -0.0664
  -0.0004   -0.0006   -0.0006   -0.0382
  -0.0007   -0.0010   -0.0010   -0.0550
  -0.0012   -0.0017   -0.0017   -0.0876
  -0.0025   -0.0032   -0.0031   -0.0441
  -0.0020   -0.0023   -0.0019   -0.0098
  -0.0033   -0.0027   -0.0009    0.0098
  -0.0162   -0.0144   -0.0036    0.0441
  -0.0725    0.0086    0.0510    0.0876
   0.0000    0.2601    0.0938    0.0550
        0    0.8834    0.1483    0.0382
  -0.8834         0    0.5147    0.0664
  -0.1795   -0.6113         0    0.0885
  -0.0199   -0.0350   -0.0386         0
```

save NHTX_PF_VertForceMatrix f

I next loaded Icurrents from the command line for the four plasma modes identified by J. Menard. They are as follows.

Icurrents

```
Icurrents =
  1.0e+006 *
        0         0         0         0
   0.2831    0.2170    0.2500         0
   0.2826    0.4938    0.1333    0.2401
   0.1413    0.0535    0.0088    0.0906
   0.3196   -0.0874    0.0131    0.1548
   0.2000    0.1158    0.8699    0.2366
  -0.1636    0.2193   -1.0370    0.0530
  -1.7964   -2.1707   -1.0449   -1.9181
  -1.7963   -2.1708   -1.0423   -2.0174
  -0.1636    0.2192   -1.0387    0.1133
   0.2000    0.1159    0.8643   -0.0900
   0.3195   -0.0874    0.0189    0.1500
   0.1413    0.0535    0.0112    0.8500
   0.2826    0.4937    0.1344    0.9608
   0.2831    0.2170    0.2500   -0.5220
   3.0000    3.0000    3.0000    3.0000
```

Then, we calculate PF coil forces for each of the four plasma modes.

F=Icurrents.*(f*Icurrents)


```
F =
  1.0e+005 *
          0         0         0         0
     0.1976    0.1886    0.0077         0
    -0.0207   -1.2044   -0.2569    0.0312
    -0.5178   -0.2912   -0.0270   -0.2750
    -0.7690    0.2382   -0.0648   -0.3776
     0.1225   -0.1980    0.6155   -0.0806
    -0.2489    0.3270   -1.7392    0.0832
    -3.3998   -4.8425   -1.2655   -4.0212
     3.3998    4.8424    1.2635    3.9944
     0.2489   -0.3269    1.7376   -0.1493
    -0.1224    0.1981   -0.6361    0.0254
     0.7688   -0.2382    0.0933    0.3104
     0.5178    0.2911    0.0342    6.8889
     0.0208    1.2043    0.2530   -9.0394
    -0.1976   -0.1886   -0.0113    2.7701
     0.0000    0.0001    0.0089    0.3944
```